REACTIONS OF NITRIC OXIDE WITH CARBONS : THE KINETICS OF NO CHEMISORPTION ON CARBON

Hsisheng Teng, E. M. Suuberg and J. M. Calo

Division of Engineering
Brown University
Providence, Rhode Island 02912

Keywords: Nitric Oxide, Carbon, Chemisorption

INTRODUCTION

The fact that NO formed during a combustion process can be heterogeneously reduced by carbonaceous solids is well known[1]. There have been a modest number of studies of various aspects of NO-char studies in the last 30 years(e.g. ref. 2~6). In general, the overall reaction has been reported to actually include the following stoichiometric reactions :

$$\begin{array}{lllll} C + 2\,NO \rightarrow & CO_2 + & N_2 \\ C + NO \rightarrow & CO + & 1/2\ N_2 \\ CO + NO \rightarrow & CO_2 + & 1/2\ N_2 \end{array}$$

It has been noted that the reaction of NO with char parallels in some respects the reaction of O_2 with chars, in that surface oxide intermediates play a role in the mechanism. For example, it has been reported[2] that at temperatures betwen 123 and 473 K, there are carbon-oxygen complexes formed on the char surface, with the release of N_2 as a gaseous product. The NO-char reaction studies reported by previous workers focus mainly on the investigation of the global kinetics during the pseudo steady state gasification. From the global kinetic results, one group[4] proposed a mechanism for the reaction of carbon with NO as follows :

$$\begin{array}{llllll} NO + C^* \rightarrow & C(O) + & 1/2\ N_2 & & (R1) \\ CO + C(O) \rightarrow & CO_2 + & C^* & & (R2) \\ C(O) \rightarrow & CO & & & (R3) \end{array}$$

This reaction scheme was used to derive a Langmuir-Hinshelwood type rate expression for the rate of NO consumption. The authors of this model noted its shortcoming in terms of failing to correctly predict an overall first order rate with respect to NO pressure. An alternative mechanism [2] is somewhat more elaborate :

$$\begin{array}{llll} 2\,NO + 2\,C^* \rightarrow & 2\,C(O) + N_2 & & (R4) \\ NO + C + C(O) \leftrightarrow & C(O..ON)C & & (R5) \\ NO + C(O..ON)C \rightarrow & CO_2 + N_2 + C(O) & & (R6) \\ NO + C(O..ON)C \rightarrow & CO_2 + N_2 + CO & & (R7) \\ 2\,NO + 2\,CO \rightarrow & 2\,CO_2 + N_2 & & (R8) \end{array}$$

The original presentation of this model included two reversible steps of form (R5), representing the formation of the two different types of C(O..ON)C complexes that react according to (R6) and (R7). There is general agreement that the first step is chemisorption of NO at almost any temperature of relevance. It probably involves addition of NO in an N-down configuration[7], followed by release of N_2 and formation of carbon oxide surface complexes , as suggested in (R4). In our recent study[6], we found that N_2 is a significant product during desorption from NO oxidized char even at high temperatures(> 1000 K). Although (R5) of the above mechanism represents the existence of long-lived N containing complexes on the surface, the C(O..ON)C complex with the weak physical bonding suggested by the authors[2] still most likely cannot represent the long-lived N containing complexes we have observed. It might then be possible that the C(O..ON)C complex is actually a chemisorbed complex, and that the desorption of N_2 we have observed involves the reverse of reaction (R5) followed by (R6), (R7) or (R8). We however see no evidence of desorption of NO as

such, except at low temperatures(see below). Thus we feel it most likely that the reaction (R4) does not proceed as indicated in a single step, and that there is some way of forming N containing surface species that can desorb as N_2 even in the absence of NO. Furthermore, the above model is deficient in not including a straight desorption route for formation of CO[6].

The validity of (R1) or (R4) as the route for NO sorption is thus in doubt. A more sophisticated sorption model should be constructed to explain the observations.This paper presents some results of NO-char sorption at low temperatures(< 523 K), at which the gasification of char is negligible.

EXPERIMENTAL

A standard thermogravimatric device(TGA) was used for the present study. Experiments were performed in a static system, in He/NO mixtures at 101 kPa total pressure. The volume of the vessel was large enough to ensure that under any reaction conditions, the consumption of NO was not significant. Pulverized char samples(50~100 mg) were held in a quartz bucket suspended in the heated zone of a quartz tube. A thermocouple placed within a few millimeters of the bucket served to indicate the temperature of the sample. The vessel could be purged following an experiment, and the contents analyzed by gas chromatography.

The chars used in present study were derived from phenol-formaldehyde resins. These resin have structure features similar to those in coals, but contain few catalytic impurities. These can be controlled to very low levels in synthesis. The resin char was prepared by pyrolysis of the phenol-formaldehyde resin in a nitrogen environment at 1323 K for 2 hours, then ground and sieved to give the desired particle size. The surface of the char was cleaned of oxides prior to NO sorption experiments by heating the sample to 1223 K in high purity helium for at least 2 hours.

NO sorption experiments were performed after surface cleaning by lowering the temperature of the sample from 1223 K to the desired sorption temperature, and then quickly introducing the desired NO/He mixture. Three sequences(I, II and III) were used to monitor the NO uptake. Sequence I started with a continuous monitoring of NO uptake for at least 24 hours until the mass gain is undetectable(i.e. $\pm$ 10 μg). Sequence II involved performing sorption, as in sequence I, to a constant mass uptake, followed by a series of changes in temperature, which affected the mass on the surface. Each temperature step lasted for 10 hours until there was no longer any detectable variation of the sample mass. Sequence III also involved performing sequence I, followed by an abrupt replacement of NO atmosphere by pure helium. After a period of monitoring the sample mass in helium, until there was no detectable mass variation, the original mixture of NO/He was reintroduced to the system, and the mass was monitored. Sequence III was performed under isothermal conditions.

RESULTS AND DISCUSSION

The NO uptake curves and the final mass uptake in sequence I sorption at different experimental conditions are shown in Fig. 1 and Table 1, respectively. The shape of the NO uptake curve is similar to that of O_2 chemisorption[8] on char. However it was found that the amount of NO uptake decreases with the increase of the temperature of char sample, while there was always an increase of the amount of O_2 uptake with increase in temperaure[8]. These results suggested that gasification of the char by NO might be occuring in this temperature range, and that the increase in the rate of sorption with increasing temperature might have been counterbalanced by an increase in the rate of a gasification step. However, no mass decline was observed after four days of sorption in an NO atmosphere, unlike the case in O_2 chemisorption when the rate of gasification ultimately overtakes the rate of chemisorption, as all the surface sites are filled. Furthermore, only small amount of CO_2 were formed (no CO was found) after the long period of chemisorption. These amount of CO_2 were negligible in comparison to the large decreases in mass seen with increasing temperature. Finally, according to our previous studies, the steady state gasification of char by NO proceeds at an undetectable level at temperatures lower than 673K. Therefore, we rule out gasification of char by NO in this temperature range. Combining the above results with the claim that there exist long-lived N containing complexes on the NO oxidized char surface, as shown in our recent studies[6], one can conclude that NO sorption on char with the simultaneous release of N_2, as described by (R1), is not the route for NO sorption on char. A better model to describe this chemisorption might be as follows

$$C + NO \rightarrow C(NO) \qquad (R9)$$
$$C(NO) \rightarrow C(O) + 1/2\,N_2 \qquad (R10)$$

In this model, both C(O) and C(NO) exist on the char surface. The C(NO) complex above can represent the N containing complex on NO oxidized char, and N_2 can be released through (R10) during desorption.The release of N_2 in (R10) would be activated by raising the temperature of the char sample, therefore the mass uptake during NO chemisorption on char would be less at higher temperature owing to the the N_2 release. The possibility of the backward reaction of (R9) to release NO should be also considered, and will be discussed later in this paper.

The results of sequence II sorption are given in Table 2. It shows that the mass of the sample decreased when the temperature was raised, and mass was regained on the sample when the temperature was lowered to the original value. The sequence is shown in Table 2. Mass is always lost with an increase in sample temperature. Returning to the same temperature results in a significant regain of mass (e.g. compare 5 and 6), but does not always restore the mass on the surface to the original values - compare steps 1 and 6, 4 and 8, 3 and 9, 2 and 10. The process appears to reach a measure of reversibility with continued cycling, however (compare 6 and 11). Experimental work on this this point continues. Thus the mass loss or gain of the sample was found to be somewhat reversible with respect to the temperature of the sample. It appears from these experiments that there may be a reversible pathway for NO chemisorption. This will be further supported below. Since there are some complexes that cannot be removed by these procedures, there must be an essentially irreversible pathway for sorption as well (recall that there are N-complexes stable up to > 1000 K). As mentioned above in discussing sequence I, no significant amounts of carbon oxides were found during sorption in this temperature range. Therefore, reaction (R10) is the candidate for the irreversible loss of mass during heating in this temperature range.

The results of sequence III are shown in Fig. 2 and Table 3. The mass variation was reversible with respect to the partial pressure of NO, and, therefore, contributed to by NO uptake or release.The results in Fig. 2 can be well described by the low pressure limit of Langmuir sorption isotherm and a temperature dependent equilibrium constant :

$$w = k_0 \cdot \exp[-Q/RT] \cdot P_{NO} \ ,$$

where k_0 is the preexponential factor in g/(m^2•kPa), w is the NO uptake in g/m^2, P_{NO} is NO partial pressure in kPa, and Q is the heat of reversible sorption in kJ/mole. From a plot of ln(w) vs. 1/T, the value $7.63 \cdot 10^{-13}$ g/(m^2•kPa)for k_0 and -41.7 kJ/mol (i.e. exothermic) for Q were determined. The temperature dependence of the data of Table 3 is ,incidentally, entirely consistent with that of the data of Table 2 considering only the reversible part of the chemisorption. The conclusion is that the reversible sorbate in sequence II is NO. Therefore, there must exist a reversible chemisorption pathway in addition to the irreversible (R9) :

$$C' + NO \leftrightarrow C'(NO) \qquad (R11)$$

with a value of 41.7 kJ/mol as the heat of exothermic sorption, as described above. The heat of sorption of this value is much higher than that of usual physisorption which is usually less than 20 kJ/mol. This might be attributable to the free radical nature of NO molecules and thus an ability to form bonds stronger than physical bonds.

Similar to the O_2 chemisorption[9], the chemisorption behavior of NO can also be well described by the Elovich equation :

$$dq/dt = b \cdot \exp[-a \cdot q]$$

where a and b are fitting parameters, and q is the amount of mass uptake normalized by the total amount of mass uptake at the end of the run. The results given in Table 4 were determined by subtracting the contribution of the reversible step (R11), assuming it to occur instantaneously at time zero. It is unclear whether this is strictly speaking justified, but the rate of the reversible step appears to be quite high, compared to the overall rate for sorption, so the approximation may not be bad. Table 4 clearly shows that the b value, the extrapolated sorption rate at zero coverage, is roughly

proportional to NO pressure in the case of 423 K sorption temperature. This suggests that the rate of irreversible NO chemisorption (R9) is proportional to NO pressure. The value of a is not a function of NO pressure in the case of 423 K sorption, suggesting that the variation of kinetics of irreversible sorption with coverage is unaffected by the changing of NO pressure. It is of interest to note that the b value decreases with the sorption temperatures, which would imply a negative activation energy for the initial chemisorption. There is no physical significance to this result, because the role of N_2 release through (R10) has been neglected in the calculation.This aspect of the process will receive further attention.

The apparent activation energies of chemisorption (including both irreversible and reversible routes) at different extents of surface coverage, determined from the rates of mass uptake at several sorption temperautres, are shown in Fig. 3. The increase of the apparent activation energy, as shown in Fig. 3, from negative to positive values in the course of site filling suggests that the rate of N_2 release slows down compared to that of NO uptake when there are more complexes accumulated on the char surface. The reasons for this are not yet fully understood, and experiments are under way to verify the role of the N_2 release processes.

CONCLUSIONS

The chemisorption of NO on char surface is not always immediately followed by the release of N_2 from the dissociation of the NO molecule. The complexes C(NO) as well as C(O), derived from NO chemisorption, can both exist on char surface. The rate of NO chemisorption on clean char surface is roughly proportional to NO pressure. There are both irreversible and reversible routes for chemisorption of NO on carbon.

ACKNOWLEDGEMENT

We gratefully acknowledge the support of the USDOE through grant DEFG22-87PC79929 and the experimental assistant of Mr. William D. Lilly.

REFERENCES

1. Pereira, F. J., Beer, J. M., Gibbs, B. and Hedley, A. B., 15th Symposium(International) on Combustion, The Combustion Institute, Pittsburgh, 1149(1974)
2. Smith, R. N.,Swinehart, J. and Lesnini, D., Journal of Physical Chemistry, 63, 544(1959)
3. Furusawa, T., Kunil, D., Oguma, A. and Yamada, N., International Chemical Engineering, 20, No. 2,239(1980)
4. Chan, L. K., Sarofim, A. F. and Beer, J. M., Combustion and Flame, 52, 37/45(1983)
5. Teng, H., Suuberg, E. M., Calo, J. M. and Hall, P. J., Proc. 19th Conf. on Carbon, 574 (1989)
6. Suuberg, E. M., Teng H. and Calo, J. M., 23rd Symposium(International) on Combustion, The Combustion Institute, in press(1990)
7. Zarifyanz, Y. A., Kiselev, V. F., Lezhnev, N. N., and Nikitina, O. V., Carbon, 5, 127(1967)
8. Suuberg, E. M., Calo, J. M. and Wojtowicz, M., ACS, Division of Fuel Chemistry, Preprint, 31(3), 186(1986)
9. Suuberg, E. M., Wojtowicz, M. and Calo, J. M., Carbon, 27(3), 431(1989)

Table 1. Total amount of mass uptake(q_f) for NO adsorption on char in sequence I

P_{NO}	10.1 kPa				4.04 kPa
Temperature(K)	523	473	423	423	423
q_f $(g/m^2)\cdot 10^5$	1.59	2.20	2.71	2.48	2.08

Table 2. Variation in mass of sorbed species (m) for the reaction sequence II at constant NO partial pressure of 10.1 kPa

Step	1	2	3	4	5	6	7	8	9	10	11
Temp.(K)	$m(g/m^2)\cdot 10^6$										
373	34.20					30.88					30.86
398		30.75								28.26	
423			28.73						27.30		
448				27.48				26.93			
473					26.90		26.90				

Table 3. Amount of reversible NO uptake(w) at different temperatures and NO pressures in sequence III

	$w\ (g/m^2)\cdot 10^6$		
P_{NO}(kPa)	10.1	4.04	2.02
Temperature(K)			
373	4.29	1.72	0.889
398	1.80	0.693	0.320
423	0.849	0.319	0.182
448	0.512		
473	0.297		

Table 4. The Elovich parameters for NO chemisorption on char

P_{NO}	10.1 kPa			4.04 kPa
Temperature(K)	523	473	423	423
* a	4.55	5.59	5.70	5.78
** b · 100	3.06	3.70	4.17	1.73

* a is a non-dimensional quantity. ** b is in units of min^{-1}

Fig. 1 The monitoring of NO chemisorption on char

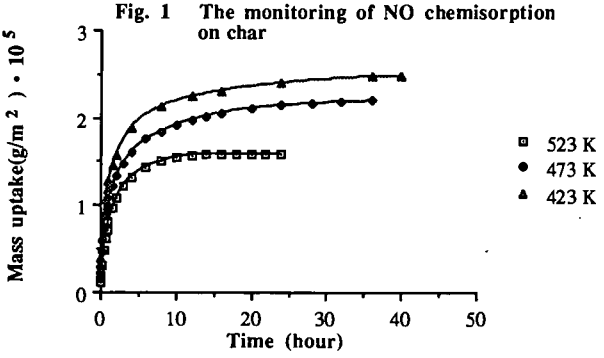

Fig. 2 Reversible NO uptake in sequence III

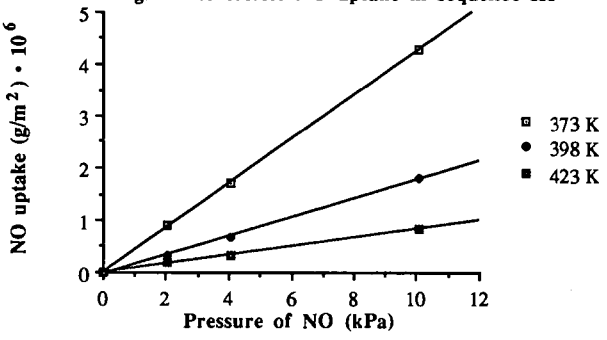

Fig. 3 Apparent activation energy of NO chemisorption on char at different surface coverages

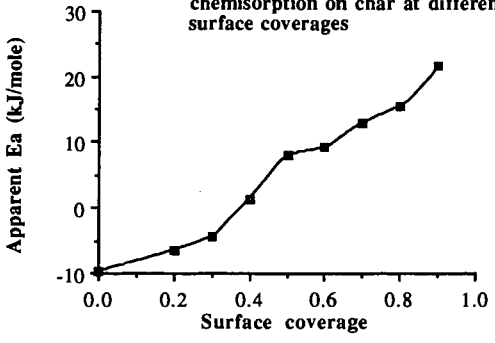

THE PREDICTION/CORRELATION OF CHAR REACTIVITY FROM DISTRIBUTIONS OF DESORPTION ACTIVATION ENERGIES

P.J. Hall and J.M. Calo
Chemical Engineering Program
Division of Engineering
Brown University
Providence, Rhode Island 02912

Keywords: Char gasification; carbon-oxygen surface complex energetics; temperature programmed desorption.

INTRODUCTION

Recently, in our laboratory, we have been concerned with the determination of distributions of desorption activation energies of oxygen surface complexes on carbons and chars from temperature programmed desorption (TPD) spectra. In the current communication we report on the application of probability density functions of desorption activation energies to the prediction/correlation of CO_2 gasification reactivities for chars produced from Wyodak coal and phenol-formaldehyde resin, which are desorption rate-controlled under the experimental conditions examined here. The resultant technique represents what we believe to be the first truly *a priori* prediction of CO_2 gasification reactivity as a function of temperature.

EXPERIMENTAL

Chars were prepared from Wyodak coal obtained from the Argonne Premium Coal Sample Bank, and phenol formaldehyde resin *via* pyrolysis in ultrahigh purity helium at 1273K with a soak time of 1 hour. The resin was synthesized in our laboratory according to a previously described procedure [1]. Care was taken to insure that contamination by any potentially catalytic impurities was kept to a minimum. Subsequent analysis by atomic absorption spectrometry revealed only nominal levels of alkali metal impurities.

The TPD apparatus and methods have been described elsewhere [2]. The most salient experimental details are as follows. Char gasification was performed in a TGA apparatus in 0.1 MPa CO_2 at the temperatures noted. Following cooling to room temperature in the TGA apparatus, the samples were transferred to a TPD reactor. Tests involving comparisons of TPD spectra obtained using this procedure with those following *in situ* oxidation in the TPD reactor have shown that transfer of the sample in this manner does not affect the resultant spectra.

The TPD reactor was constructed from a high-purity silica tube, 1-cm inside diameter, within which a close-fitting, circular silica sinter is used to support the sample. Ultrahigh purity helium

carrier gas is passed over the sample in downflow. Heating is accomplished electrically via nichrome wire wrapped around the outside of the silica tube, powered by a high current variable transformer. The heating regimen is controlled by a microcomputer. The resultant TPD reactor has a low thermal capacitance which allows linear heating rates of up to 500K/min.

Detection of desorbed species is accomplished with a quadrupole mass spectrometer (MS) which samples a small portion of the carrier flow. The MS output is fed to a microcomputer which also provides for multiple species detection via mass programming.

Typical sample sizes for the TPD measurements were ~10 mg. This size resulted in less than a monolayer coverage on the silica frit that was used as the sample holder in the TPD reactor. This, when combined with high helium carrier gas sweep rates, insured the absence of secondary interactions between the bulk gas species and the char samples.

Repeated experiments with char samples obtained from the same batch indicate that the reproducibility of gas desorption rates is approximately $\pm$10%. This error is attributable to a combination of effects arising primarily from sample inhomogeneity, sample size and MS calibration. For this reason, the spectra reported are representative, rather than averages.

THE APPROACH

The specific gasification reactivity, W, is given by:

$$W = -(1/C)\, dC/dt = k_d\, C_t\, \theta, \qquad [1]$$

where C is the amount of carbon, k_d is the desorption rate constant of oxygen surface complexes, C_t represents the total moles of active sites per mole of carbon, and θ is the fraction of the active carbon sites that are occupied by oxygen complex. For conditions where the surface is saturated with oxygen complex, θ =1 and Eq. [1] indicates that the specific gasification rate becomes desorption rate-controlled.

Eq. [1] applies explicitly to a homogeneous surface; i.e., one discrete surface complex with a single desorption activation energy. Actual char surfaces, however, are known to be distinctly heterogeneous, with a distribution of desorption energies. In a companion paper in this symposium [3], we present a method, based on the original work of Redhead [4], by which the the probability density function of desorption activation energies of oxygen surface complexes can be obtained by analysis of TPD spectra following gasification. The resultant transformation is given by:

$$d[CO]/dt = [C\text{-}O]_o\, S(E^*)\, dE^*/dt, \qquad [2]$$

where d[CO]/dt is the desorption rate of oxygen surface complexes as CO, $[C\text{-}O]_0$ is the total amount of oxygen surface complex initially on the char surface, S(E*) is the probability density function of desorption activation energies, and dE*/dt is the time derivative of the desorption activation energy during the TPD heating regimen. Since a TPD experiment yields the instantaneous d[CO]/dt directly, then knowledge of E* and dE*/dt defines the initial energetic distribution of surface complex, $[C\text{-}O]_0 S(E^*)$. The expression for E* and dE*/dt are given by [3]:

$$E^*/RT = [\ln (\nu_0 T/\beta) - 3.64], \qquad [3]$$

$$dE^*/dt = R\beta\,[E^*/RT] = R\beta\,[\ln (\nu_0 T/\beta) - 3.64], \qquad [4]$$

where ν_0 is the pre-exponential frequency factor for the desorption rate constant (assumed to be constant with energy and temperature), T is the temperature during desorption, and β is the local heating rate (constant for linear TPD).

The resultant energetic distribution can then be applied in a desorption rate-controlled reactivity expression similar to Eq. [1], with the exception that k_d must be energy-averaged over all surface complexes. In this case, the corresponding expression for W becomes:

$$W = \int_0^\infty \nu_0 \exp(-E^*/RT)\,[C\text{-}O]_0\,S(E^*)\,dE^*. \qquad [5]$$

RESULTS AND DISCUSSION

TPD spectra of oxygen complexes formed during burn-off of Wyodak and resin char samples at 850°C in 0.1 MPa CO_2 were compared after rapid quenching in helium, and after slow cooling in an atmosphere of CO_2. These experiments were performed in order to ascertain whether or not the surface was saturated with oxygen surface complex (i.e., θ=1) under these gasification conditions. It was reasoned that if θ is indeed a function of temperature, by cooling in CO_2 the resultant surface coverage would also change and differ from that obtained upon rapid quenching in helium. However, all the resultant spectra were virtually identical. This result implies that CO_2 gasification for these chars under these conditions is indeed desorption rate-controlled. This has also been concluded by other workers under similar conditions (e.g., see [5,6]).

Wyodak Coal Char. TPD spectra for a Wyodak subbituminous coal char sample are presented in Figure 1. In this figure, the rates of evolution of CO and CO_2 upon heating a Wyodak sample that has been gasified to 20% burn-off in CO_2 are presented as a function of temperature. As can be seen, the evolved gas is mostly CO, and its evolution is essentially continuous above a threshold temperature. The temperatures attained are quite high, indicating that the oxygen surface complexes from which the gases derive are quite thermally stable. The CO_2 evolved in

this case has been attributed to secondary reaction of desorbed CO with other surface complexes during TPD [2].

The energetic distribution, $[C\text{-}O]_o S(E^*)$, was obtained directly from these data using Eq. [2]. The result is presented in Figure 2. The prominent "bulge" on the leading edge of the distribution is also evident in the TPD spectra *ca.* 1000K. This feature has been attributed to catalytic mineral matter in the Wyodak char (most probably calcium oxide) in some of our work using demineralized samples. As is shown below, this feature accounts for practically all the reactivity of the char over the temperature range examined.

Since all the complex was not recovered in this experiment, due to the very high temperatures required, the entire distribution was also not determined. However, this could have been accomplished in principle by holding the sample at a final elevated temperature, T_f, until all the complex had desorbed. In any event, in order to predict the reactivity in the current temperature range of interest, knowledge of the entire distribution is not necessary, as explained below.

Predicted reactivities for the Wyodak coal char were determined from the preceding experimentally determined energetic distribution using Eq. [5]. The resultant parity plot of predicted versus measured reactivities (taken at 5% burn-off in other experiments in a TGA microbalance) is presented in Figure 3. As shown, the agreement between predicted and measured values is almost perfect for this char. It is noted that over the temperature range explored (i.e., 650-800°C), the gasification reactivity increased by three orders of magnitude, and Eq. [5] predicts the exact same behavior.

The reason for the large change in reactivity is clearly evident in Figure 4 which presents the differential reactivity over the distribution (i.e., the kernel of the integral in Eq. [5], along with the energetic distribution from Figure 2. As shown, as the temperature increases, an increasing number of surface complexes become involved in a highly nonlinear manner *via* the Arrhenius-dependent exponential term. It is also quite evident that gasification reactivity is controlled by only a very small fraction of the oxygen surface complexes located in the vicinity of the 1000K desorption feature; most of the complexes once formed are stable under these gasification conditions. Thus, this formulation shows in a very simple and graphic manner precisely why CO_2 gasification reactivity is so low at the lower temperatures and why it increases so precipitously with temperature.

Phenol-Formaldehyde Resin Char. In view of the suspected control of reactivity by mineral matter in the Wyodak coal char, we undertook some experiments with a "model compound" char produced from phenol-formaldehyde resin. A CO TPD from this char gasified to 11.7% in 0.1 MPa CO_2 at 1173K is presented in Figure 5. For this particular char, the amount of secondary CO_2 was negligible. As shown, the absolute amount of surface oxygen complex on this char is significantly less than for the Wyodak coal char gasified at even lower temperatures. In addition,

the CO spectrum is shifted significantly to higher temperatures than for the Wyodak char, and the low temperature "bulge," which controls the CO_2 reactivity for the Wyodak coal char, is noticeably absent.

The resultant energetic distribution of oxygen surface complexes, determined from Eq. [2], is shifted to higher energies than the Wyodak coal char. This fact should be directly reflected in significantly reduced predicted CO_2 gasification reactivity; and, indeed this is the case, as shown in the parity plot of predicted versus measured reactivities (taken at 5% burn-off in other experiments in a microbalance) presented in Figure 6. As shown, the agreement between predicted and measured values is quite good (to within a factor of two), although not as good as for the Wyodak reactivity predictions presented in Figure 3. It is noted that the CO_2 reactivity of the resin char is three orders of magnitude less than that of the Wyodak coal char at 1073K, and the current formulation predicts this considerable difference quite well.

It is also important to note that the oxygen reactivities measured for these same two chars at 623K in 0.1 MPa of oxygen are almost exactly the same on a total active surface area (ASA) basis, as measured by oxygen chemisorption. Therefore, it seems apparent that oxygen reactivity is not a good indicator of CO_2 reactivity, at least for these two chars. Therefore, it appears that correlations of char CO_2 reactivities according to ASA, as determined by low temperature oxygen chemisorption, can fail quite dramatically for certain chars.

CONCLUSIONS

We believe that this work represents the first truly *a priori* prediction of the CO_2 gasification reactivity of chars. With this method the reactivity of a char as a function of temperature can be predicted from a single TPD experiment following mild gasification at a single temperature. Currently, this prediction can be made for the case where gasification reactivity is controlled by the thermal desorption of oxygen surface complexes formed during gasification; however, the approach may be extended to arbitrary conditions as well. The implications of this work potentially affect all aspects of coal char behavior. It represents a foundation for the development of techniques for coal char characterization and reactivity prediction/correlation based upon knowledge of the energetic heterogeneity of the coal char surface as described by the appropriate probability density function.

Acknowledgement. This work was supported by the Morgantown Energy Technology Center of the Department of Energy under Contract No. DE-AC21-MC23284.

REFERENCES

1. Suuberg, E.M.; Wojtowicz, M.; Calo, J.M. *Carbon* **1989**, *27*, 431.
2. Hall, P.J.; J.M. Calo *Energy & Fuels* **1989**, *3*, 370.

3. Hall, P.J.; Calo, J.M. *ACS Div. Fuel Chem. Prepr.* **1990,** "Energetic distributions of oxygen surface complexes on porous carbons and chars," this symposium.
4. Redhead, P.A. *Vacuum* **1962,** *12*, 203.
5. Mentser, M., and S. Ergun, *A Study of the Carbon Dioxide-Carbon Reaction by Oxygen Exchange, 1973,* U.S.Bur.Mines Bull. 664.
6. Yang, R.T., in *Chemistry and Physics of Carbon,* **1984,** Volume 19, P.A. Thrower, ed., pp. 203-263, Marcel Dekker, NY.

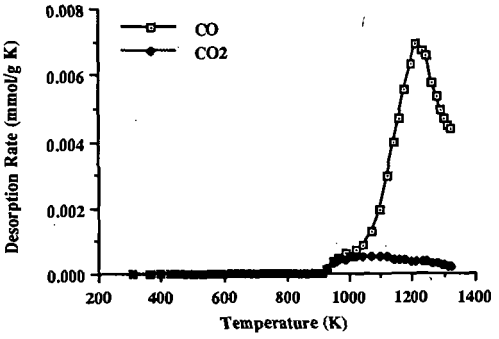

Figure 1. 100K/min CO and CO_2 TPD spectra from Wyodak coal char gasified to 20% burn-off in 0.1MPa CO_2 at 1173K, and cooled in ultrahigh purity helium.

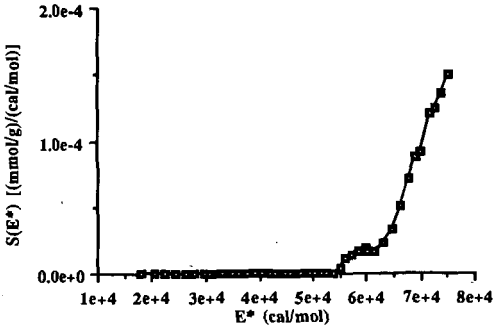

Figure 2. Probability density function of desorption activation energies, S(E*), for Wyodak coal char burned-off to 20% in 0.1MPa CO_2 at 1173K, and cooled in ultrahigh purity helium.

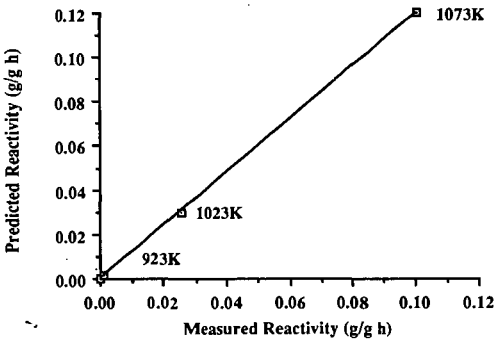

Figure 3. Parity plot of predicted *vs.* measured reactivities for Wyodak coal char in 0.1MPa CO_2 as a function of temperature.

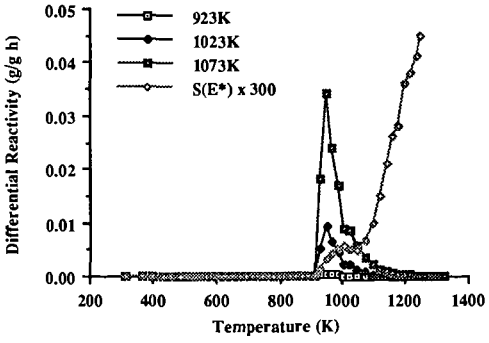

Figure 4. Differential reactivities as a function of temperature, and S(E*) for Wyodak coal char in 0.1MPa CO_2.

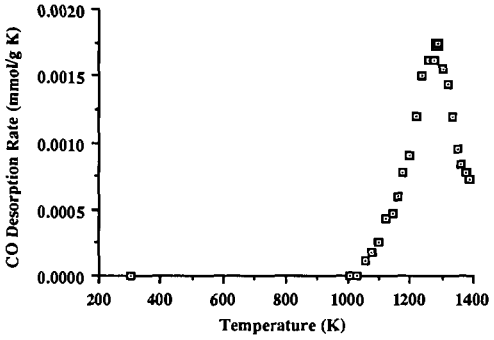

Figure 5. 100K/min CO TPD spectrum for resin char gasified to 11.7% burn-off in 0.1MPa CO_2 at 1173K, and cooled in ultrahigh purity helium.

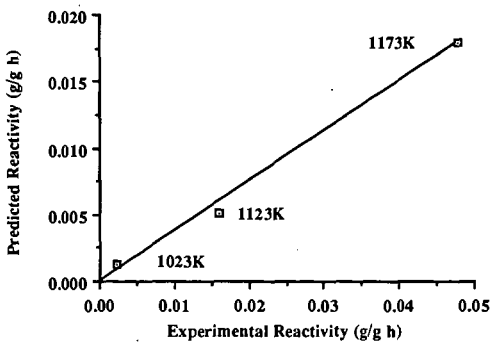

Figure 6. Parity plot of predicted *vs.*measured reactivities of resin char in 0.1MPa CO_2 as a function of temperature.

THE INFLUENCE OF COAL SURFACE CHEMISTRY ON THE ADSORPTION OF COAL CONVERSION CATALYSTS

Godfried M. K. Abotsi, Kofi B. Bota and Gautam Saha

Research Center for Science and Technology
Clark Atlanta University
Atlanta, GA 30314

Keywords: Adsorption, catalysts, coal surface charge.

INTRODUCTION

Prior to its gasification, coal is generally loaded with catalytic materials by mechanically mixing the coal with a solid catalyst precursor, by impregnation with a solution containing the catalyst precursor (incipient wetness technique), or by ion-exchange of the catalyst precursor metal ions with protons on the coal (1-3). For the same catalytic material, the various techniques typically produce different coal char reactivities under identical reaction conditions. The disparities in catalyst performance has been attributed to differences in catalyst dispersion, induced by differences in coal-catalyst contact.

Despite their significant influence on catalyst activity, the effects of interfacial phenomena on the adsorption of coal gasification metal catalysts has not been previously investigated. This paper describes the effects of coal surface charge on the adsorption of calcium and potassium ions from solution.

EXPERIMENTAL

The coals used in the study are a lignite (PSOC 1482) and a subbituminous coal (PSOC 1485), both of which were sealed in argon and supplied by the Penn State Coal Sample Bank. The ultimate and proximate analyses of the coals are provided in Table 1.

The surface charge properties of the coals were measured at room temperature using a Pen Kem Model 501 Lazer Zee Meter zeta potential instrument. Slurries were prepared by dispersing 300mg samples of each coal (equal proportions of -20 and -80 U.S. mesh sizes) in a liter of deionized water containing 10^{-3} moles l^{-1} $AgNO_3$ for ionic strength control. After the coal particles have been well-dispersed by

agitation in an ultrasonic bath, the sediments were separated from the suspended particles, the latter fraction was divided into 50.0 cm^3 portions, and the pH's of the dispersions were varied with nitric acid or ammonium hydroxide solutions. After 4h equilibration (by mechanical agitation), each sample was transferred to the zetameter and the zeta potential of the coal particles were measured.

The effect of coal surface charge on the adsorption of potassium and calcium ions was determined by dispersing 1.0g samples of coal in 10^{-2} or 10^{-3} moles l^{-1} of K^+ or Ca^{2+}. The samples were conditioned by shaking for 24h after which they were filtered and the filtrates analyzed for potassium or calcium with atomic absorption spectrophometry. Metals uptake were calculated as the difference in Ca or K content of the solutions prior to and after adsorption.

RESULTS AND DISCUSSION

The zeta potential results given in Figure 1 show that the surfaces of the lignite coal particles are negatively charged over a wide range of pH and that the isoelectric point (iep) occurs at about pH 1.9, the surfaces of the coal particles being positively and negatively charged, respectively, below and above this pH value. A review of the iep's of coals shows that the iep of coals occurs in the acidic range (4).

A striking feature of Figure 1 is that the negative charge density increases with increase in pH. A similar trend was observed for the subbituminous coal. These observations can be explained in terms of the surface functional groups on coal. It is well known that the surfaces of low-rank coals are dominated by oxygenated surface groups. Several studies [5-7] have shown that the surface chemistry of these coals is determined by these groups, although inorganic species also play a role [6]. In aqueous and basic environments, these acidic groups dissociate and the coal particles acquire negative charges, whereas the surface groups are protonated in acidic medium, reducing the negative charge density, and the surface may become positively charged in strongly acidic media [5,6]. The formation of surface charge on coals is depicted by equations (1)-(4) for carboxyl (COOH) and hydroxyl (OH) functional groups:

$$-COOH_{(s)} + OH^- \longrightarrow -COO^-_{(s)} + H_2O \quad (1)$$

$$-COH_{(s)} + OH^- \longrightarrow -CO^-_{(s)} + H_2O \quad (2)$$

$$-COOH_{(s)} + H^+ \longrightarrow -COOH_2^+{}_{(s)} \quad (3)$$

$$-COH_{(s)} + H^+ \longrightarrow -COH_2^+{}_{(s)} \quad (4)$$

where the subscript(s) designates the coal surface. Such reactions have also been reported for carbon surface oxygen functionality (8-10).

Figure 2 shows the quantities of calcium adsorbed by the lignite as a function of pH. It is observed that calcium uptake is not only inhibited in strongly acidic media (pH < 4), but calcium is actually extracted from the coal into solution, as indicated by the negative calcium values. However, calcium adsorption progressively increased as the pH's of the coal slurries increase. These trends are consistent with the surface charge properties of the coals. As the coal particles become more negatively charged, coal-Ca^{2+} interactions become more pronounced as a result of electrostatic interaction between the metal ions (Ca^{2+}) and the anionic coal surface. A similar trend was obtained for potassium adsorption onto the coals.

In synopsis, for the first time, it has been shown from the current study that coal surface charge exerts a predominant influence on the adsorption of coal gasification metal ions from solution. Metal ion adsorption is favored in highly alkaline solution, while it is suppressed in strongly acidic environments. Thus, efficient catalyst impregnation and improved catalyst dispersion and activity may be obtained by controlling the pH and the surface charge on coals.

REFERENCES

1. Wood, B. J., Sancier, K. M., Catal. Rev. - Sci. Eng. 1984, 26 (2), 233.

2. Radovic, L. R., Walker, Jr., P. L., Jenkins, R. G., *Fuel* 1983, 62, 209.

3. Johnson, J. L. *In Fundamentals of Coal Utilization: 2nd Supplementary Volume*, Elliot, M. A., Ed.; John Wiley: New York, 1981.

4. Quast, K. B., Readett, D. J. *Adv. Coll. Int. Sci.* 1987, 27(3-4), 169.

5. Kelebek, S. Salman, T.: Smith, G. W. *Canad. Metal. Quart.* 1982, 21, 205.

6. Fuerstenau, D. W.; Rosenbaum, J. M.; Laskowski, J. *Coll. Surf.* 1983, 8, 137.

7. Laskowski, J. s., Parfitt, G. D., In "Interfacial Phenomena in Coal Technology," Botsaris, G. D. Glazman, Y. M., Eds., Marcel Dekker, New York, 1988 p. 279.

8. Abotsi, G. M. K.; Scaroni, A. W. *Carbon '88 Proceedings* of Soc. Chem. Ind. (London), 1988, 422.

9. Abotsi, G. M. K.; Scaroni, A. W. *Carbon 1990*, 28, 000.

10. Abotsi, G. M. K., Osseo-Asare, K., Int. J. Miner. Process. 1986, 18, 217.

ACKNOWLEDGEMENT

Financial support for this work is provided by the U.S. Department of Energy Under Grant Number DE-FG22-89PC89760.

Table 1. Properties of Coals Used

Penn State Sample Number	PS0C-1482	PS0C-1485
Seam	Hagel	Rosebud
State	N. Dakota	Montana
Rank	Lignite	Subbit. B
Ultimate Analysis (daf, %)		
Carbon	71.34	75.78
Hydrogen	4.5	5.30
Nitrogen	1.14	1.19
Total Sulfur	0.79	0.99
Oxygen (by diff.)	22.24	16.75
Proximate Analysis (As Rec'd, %)		
Moisture	34.45	25.37
Volatile Matter	28.18	27.43
Fixed Carbon	31.80	38.67
Ash	5.57	8.54

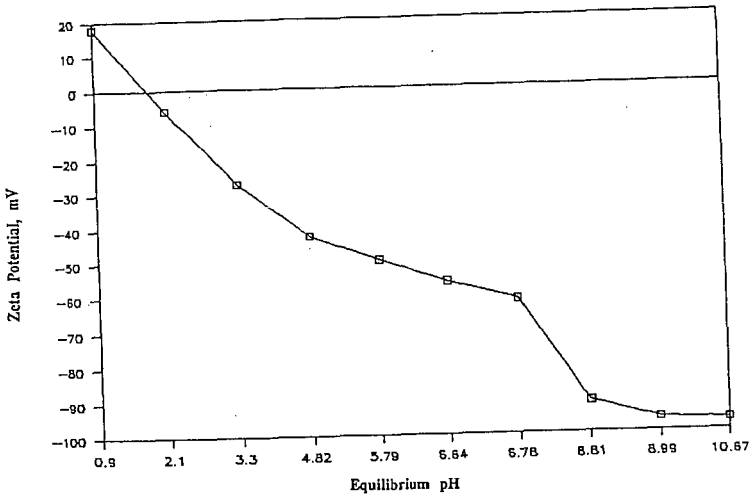

Figure 1: Dependence of Zeta Potential on pH for North Dakota (Hagel) Lignite (PSOC 1482). Ionic strength was controlled with 10^{-3} moles l^{-1} $AgNO_3$.

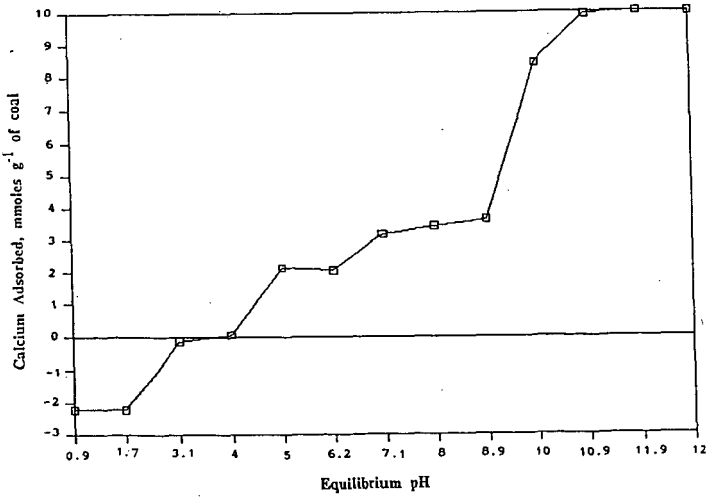

Figure 2: Calcium Adsorption as a Function of pH by Hagel Lignite (PSOC 1482).

HYDROTREATMENT OF COAL GASIFICATION LIQUID BY-PRODUCTS WITH A SOLID ACID CATALYST

Edwin S. Olson, Ramesh K. Sharma, and John W. Diehl
University of North Dakota Energy and Environmental Research Center
Box 8213 University Station, Grand Forks, ND 58202

KEY WORDS: hydrotreating, gasification, coal tar

INTRODUCTION

The production of transportation fuels by hydrotreatment of coal tars has been practiced for many years. Coal tars represent an important part of the products of coal gasification units, and as more of these units become operational, a large source of hydrocarbon fuels will be available. Three liquid by-products are produced at the Great Plains Gasification Plant. These include tar oil, crude phenol, and a light naphtha from the rectisol desulfurization unit. Mild gasification processes currently under study produce a liquid product in addition to the char and gas. Conversion of these tars to a transportation fuel requires removal of heteroatoms (nitrogen, sulfur, and oxygen) as well as hydrogenation and cracking of the larger aromatic and aliphatic components.

The production of a high density jet fuel from the Great Plains tar-oil by-product was investigated by hydrogenation with commercial supported bimetallic catalysts (1). The products contained large amounts of cyclohexane components from hydrogenation of the aromatics. For conversion to a gasoline fuel, hydrocracking of polynuclear aromatics in the tars is desired, but addition of hydrogen to single ring aromatics is not required. A new solid acid catalyst has been developed in our laboratory appropriate for the type of hydrotreating needed to produce a gasoline-type fuel with high single ring aromatic content. This catalyst consists of zinc chloride supported on and complexed with silica gel. Coal liquefaction and hydrodesulfurization with this new solid acid catalyst have been recently reported (2,3,4), and its effectiveness for hydrotreating tar samples is discussed in this paper.

EXPERIMENTAL

A tar oil sample resulting from the gasification of North Dakota lignite (Beulah) had the elemental analysis (5) shown in Table 1. The sample was hydrotreated at 400°C with 1000 psi hydrogen, as previously described (2) for hydrotreatment of liquefaction samples. The product slurry from the reaction of Great Plains tar oil with silica gel-zinc chloride catalyst was transferred into a centrifugation tube and separated into solid and liquid products.

The liquid product was analyzed by GC/FID and GC/MS analyses. Carbon and sulfur emission spectroscopy (GC/MS/AES) was used for the qualitative analyses of the reaction products. The solid product was washed with dichloromethane, vacuum dried, and weighed. Sulfur was analyzed with the Leco instrument, chlorine by the method in Vogel (2).

The second sample was a tar sample produced several years ago in the Grand Forks Energy Technology Center's slagging fixed-bed gasifier from a North Dakota lignite (Indian Head) This sample consisted of the residue after distillation of the light oil components shortly after collection of the tar. The sample was stored in a glass jar without any special precautions against oxidation. The elemental analysis of the sample is given in Table 1.

Hydrotreatment was carried out as described above, and the product distilled under vacuum (2 torr) to 250°C. The distillate was mixed with the appropriate internal standard and analyzed by GC/FID and GC/FTIR/MS/AED, as above. The solid residue was extracted with dichloromethane, and the soluble and insoluble fractions were weighed and analyzed by elemental analysis and infrared spectroscopy.

RESULTS AND DISCUSSIONS

The reactions of tar oil with a silica gel-zinc chloride catalyst were carried out at 400°C for 3 hours and in the presence of 1000 psig (repressurizations at 1-hour intervals) of molecular hydrogen. The product consisted entirely of distillable material (Table 2). Elemental analysis and mass balance indicated that the dichloromethane-insoluble product was essentially the recovered catalyst. No coke formation was observed.

The original tar oil contained 8% aliphatics, 48% aromatics, and 36% polar compounds (5). Aromatic components consisted of mostly alkylbenzenes and alkylnaphthalenes, but ranged from toluene to pyrene. Polar components consisted of phenolics, as well as dihydroxybenzenes and nitrogen bases. The hydrotreated product contained much fewer polar compounds, with no dihydroxybenzene and no nitrogen bases. The aromatic fraction of the hydrotreated product contained benzene, tetralins, and indanes and their alkyl substituted derivatives as the major components.

Major sulfur components of the original tar oil were alkylthiophenes, benzothiophenes, and a small amount of dibenzothiophene. The very sensitive sulfur emission determination of components by GC/AED showed that all thiophenes and benzothiophenes were removed and only a trace of dibenzothiophene remained in the hydrotreated product.

The dry tar sample was hydrotreated with the silica-gel-supported zinc chloride to give a similar slate of products (Table 2), but with higher average molecular weight. The distillate yield for the dry tar reaction product (82%) represented a substantial improvement over that obtained for the original dry tar.

The distribution of compound types in the original dry tar was 11% aliphatic compounds (alkanes/alkenes), 25% aromatic compounds, and 63% polar compounds. The major aromatic components of the original tar were three- and four-ring compounds. The polar components included a considerable amount of dihydroxybenzene and nitrogen bases.

The aliphatic fraction of the hydrotreated product distillate contained some cycloalkanes, and the distribution of larger alkanes (C_{14} to C_{33}) was essentially unchanged. The distillate still contained small amounts of aromatics such as phenanthrene and pyrene, however the majority of the product components were hydroaromatics, such as tetralin, and alkylbenzenes. The phenolic components consisted of phenol, cresols, and other alkylphenols, but no dihydroxybenzenes were present. No nitrogen components were observed in the distillate.

The major sulfur compound in the original dry tar was dibenzothiophene. The reconstructed sulfur emission chromatogram of the distillate indicated that only a trace of dibenzothiophene remained in the hydrotreated product, and no other organosulfur components were present.

The dichloromethane-soluble fraction of the residue represented 8 wt% of the starting material. This product was analyzed by elemental analysis (C, 77.4; H, 7.9; N, 0.31; S, <0.01; and O, 14.4). The dichloromethane-insoluble fraction was mainly recovered catalyst along with a small amount (6%) of organic material. Approximately 4% of starting material was converted to gas.

CONCLUSIONS

The silica gel-zinc chloride catalyst was effective in removing heteroatoms form the coal tars. Dihydroxybenzenes were converted to phenols and aromatics. Polynuclear aromatic components were hydrogenated to hydroaromatics, which were further cracked to smaller compounds, but hydrogenation of single ring aromatics was minimal. Retrograde coking reactions were also minimal. The products obtained were too heavy for gasoline; however, a distillate cut of the hydrotreated products containing components in the benzene to xylene range could be a gasoline additive. Further hydrocracking is need to convert the multi-ring components.

REFERENCES

1. Knudson, C.L. "Production of Jet Fuels from Coal-Derived Liquids"; Vol. XIV, Oxygenates Content of Coal-Derived Jet Fuels, AFWAL-TR-87-2042, 1990.

2. Sharma, R.K.; Diehl, J.W.; Olson, E.S. Prepr. Pap. - Am. Chem. Soc., Div. Fuel Chem., 1990, 35, 414-422.

3. Olson, E.S.; Diehl, J.W.; Sharma, R.K. Prepr. Pap. - Am. Chem. Soc., Div. of Fuel Chem., Preprints, 1990, 35, 563-569.

4. Sharma, R.K.; Diehl, J.W.; Olson, E.S. 3rd Int. Conf. on Proc. and Util. of High-Sulfur Coals; Ames, Iowa, Nov. 14-16, 1989.

5. Knudson, C.L. "Production of Jet Fuels from Coal-Derived Liquids"; Vol. II, Characterization of Liquid By-Products from the Great Plains Gasification Plant, AFWAL-TR-87-2042, 1988.

TABLE 1

ELEMENTAL ANALYTICAL DATA, WT%

Element	Tar Oil	Tar Residue
Carbon	83.76	83.12
Hydrogen	8.86	7.96
Nitrogen	0.52	0.88
Sulfur	0.39	0.32

TABLE 2

CATALYTIC HYDROTREATING REACTIONS

Reactants (g)			React. Cond.		Products (%)		
Sample	Cat.	Hydrog. (psi)	Temp. (°C)	Time (hr)	CH_2Cl_2-I	CH_2Cl_2-S	Dist.
Dry Tar 1.01	SZC 0.5	3 x 1000	400	3	6.0	8.0	82
Tar Oil 2.0	SZC 1.0	3 x 1000	400	3	0	0	98

BENCH-SCALE TEST RESULTS AND CALCULATION PROCEDURE FOR IN-SITU SULFUR CAPTURE VIA SORBENT ADDITION TO COAL SLAGS UNDER PARTIAL OXIDATION CONDITIONS

Mitri S. Najjar and Dick Y. Jung
Texaco Inc.
P. O. Box 509
Beacon, NY 12508

Keywords: in-situ desulfurization; coal gasification; optical basicity

SUMMARY

The addition of sorbents with the coal feed is being examined as a means to capture sulfur in-situ during the partial oxidation of coal in a Texaco gasifier operated in the slagging mode. To rapidly screen candidate sorbents for sulfur capture prior to their being tested in an experimental bench scale unit, a calculation scheme based on an extended use of the concept of optical basicity is being tested for estimating the solubility of sulfur in a given coal slag with and without added potential sorbents. This calculation method identified iron, calcium and sodium based compounds as well as combinations of these additives as potentially good sulfur-capturing sorbents for a coal slag. Experimental EDX data from bench-scale drop tube furnace runs with coal slag using these additive packages under simulated Texaco coal gasifier syngas conditions are presented which verify the predicted higher sulfur solubility in the resultant slag-additive mixtures.

INTRODUCTION

One of the most promising approaches for utilizing coal in an environmentally safe manner that has been recently demonstrated is the generation of electric power via partial oxidation of coal in an integrated gasification-combined cycle (IGCC) plant. To minimize emission of sulfur compounds, these processes typically separate the reaction step (where coal is converted to raw syngas under reducing conditions at high temperatures) from the acid gas removal step (where physical solvents are generally used to scrub hydrogen sulfide and carbonyl sulfide from the crude syngas). Currently, this approach requires cooling of the hot syngas to the low temperatures commonly needed for physical solvents and subsequent reheating of this cleaned syngas prior to its introduction into the gas turbine. Consequently, these heating and cooling cycles require significant capital investments as well as operating costs.

A potentially more efficient alternative is to combine coal combustion with the sulfur removal step in the same vessel. However, the total solubility of sulfur in coal slags is typically quite low (between 0.01 and 0.5 weight percent). One possible approach to enhance sulfur solubility in coal slags is the addition of sulfur-capturing sorbents along with the coal feed to the gasifier. The ideal sorbent would be an inexpensive additive that chemically reacts with the gas phase sulfur compounds (primarily hydrogen sulfide with smaller amounts of carbonyl sulfide) to form sulfide(s) that are encapsulated in a disposable slag-additive mixture but the addition

of this additive should not cause any complications for slag flow from the gasifier.

To rapidly screen candidate sorbents, a method to estimate the amount of sulfur captured by the mixture of coal slag with these potential additives would be quite useful to reduce the number of required experimental tests. Consequently, we have been exploring the use of an extended concept of optical basicity to estimate the sulfide capacity for mixtures of coal slag with various additives. This proposed calculation scheme estimates the sulfide capacity at a given temperature based solely on the elemental composition of the slag-additive mixture. With an estimate of the sulfur and oxygen partial pressures as well as the weight percentage of sulfur in the coal, the sulfur content in the slag mixture can then be approximated.

METHODS

Calculations

Slag basicity may be defined as being directly proportional to its free oxygen ion activity. Wagner[1] defined the basicity of a slag with respect to its "capacity" to absorb various constituents. For example, the main reaction that describes the sulfur-oxygen exchange behavior between slag and gas under reducing conditions is represented by the following reaction which has an equilibrium constant K_1:

$$[O^{-2}] + \tfrac{1}{2} S_2(g) = [S^{-2}] + \tfrac{1}{2} O_2(g) \quad (1)$$

where the brackets indicate that ions are present in the slag. Since the oxygen ion activity as well as the sulfide activity coefficient are difficult to measure in ionic melts, Fincham and Richardson[2] expressed the potential of a silicate slag to absorb sulfur in terms of a measured quantity called the sulfide capacity (C_s) that is related to the oxygen and sulfur partial pressures in the gas phase by:

$$C_s = [\%S] (P_{O2}/P_{S2})^{\frac{1}{2}} \quad (2)$$

where [%S] represents the concentration of sulfur as sulfide (sulfur solubility) in the slag mixture while P_{O2} and P_{S2} represent the oxygen and sulfur partial pressures in the gas phase, respectively. Utilizing the equilibrium constant expression for the reaction in Equation (1) and solving for the sulfide capacity:

$$C_s = K_1 (a_{O-2}/\gamma_{S-2}) = [\%S] (P_{O2}/P_{S2})^{\frac{1}{2}} \quad (3)$$

This equation ties the equilibrium constant and the sulfide capacity with the gas phase oxygen and sulfur partial pressures inside the gasifier. The sulfide capacity for a number of slag compositions has been measured[3] by classical physicochemical methods. However, the available literature data on sulfide capacity for slags are insufficient to cover the entire range of compositions that are of interest for in-situ sulfur capture.

An alternative approach is to estimate the slag's sulfide capacity using the concept of "optical basicity". Optical basicity (denoted by Λ) refers to a measure of basicity determined by spectroscopic methods that has been shown to be predictable from Pauling's electronegativity of the individual elements in a slag. For a large number of slag compositions at 1500°C, the relationship[4] between the optical basicity of a slag and its sulfide capacity is:

$$\log C_s = 12.6 \Lambda - 12.3 \quad (4)$$

To account for the effect of temperature on the equilibrium reaction, consider the calcium sulfide-oxide equilibrium reaction:

$$CaS(s) + \tfrac{1}{2} O_2(g) = CaO(s) + \tfrac{1}{2} S_2(g) \quad (5)$$

Based on this chemical equilibrium, a temperature-dependent correction

term (B) is introduced which gives the following temperature-corrected expression[5] for the sulfide capacity:

$$\log C_s = \log C_s^* + B \quad (6)$$

$$B = -4534\ (1773 - T)/\ (1773\ T) \quad (7)$$

where T is the temperature of interest in degrees Kelvin. The advantage of using optical basicity lies in the observation that it is simply extended to multicomponent systems by:

$$\Lambda = N_A\Lambda_A + N_B\Lambda_B + \ldots + N_Z\Lambda_Z \quad (8)$$

where N_i is the normalized "equivalent cation fraction" of the ith oxide in the solution based on the formula MO_y, i. e. the number of atoms of oxygen per metal in the oxide. Values of optical basicities[3,4] for several oxides commonly found in coal slags are available in the literature. Hence, it is possible to estimate the optical basicity for a slag-sorbent mixture knowing just its chemical composition.

It should be noted that these correlations were empirically developed based primarily on experimental data for metallurgical slags and have not been tested for coal slag mixtures with sulfur sorbents. Consequently, equilibrium drop tube furnace experiments using coal slags with selected additives were performed to check if the potential sorbent systems identified by this proposed calculation procedure would indeed capture sulfur.

Experiments

Bench scale tests were conducted at atmospheric pressure using temperatures and gas compositions selected to simulate gasifier conditions using the apparatus shown schematically in Figure 1. The principal units for high temperature testing are two identical LeMont Scientific quench furnaces capable of reaching 3000°F. Slag and sorbent samples (50-100 mg) were placed in a crucible that is suspended in the furnace by a thin platinum wire which is then equilibrated by exposure to a flowing gas mixture for at least 18 hours. Gaseous mixtures of CO, CO_2 and 1 vol %SO_2 in Argon were selected to simulate the S_2 and O_2 partial pressures at the desired temperatures and ambient pressure based on equilibrium calculations using a multiphase free energy minimization computer program, an in-house version of SOLGASMIX[6]. The suspended slag-sorbent sample was then rapidly quenched by dropping the crucible into a pool of water or simulated syngas. This was accomplished by passing an electrical current through the suspending platinum wire which causes the wire to break.

The quenched sample was recovered and characterized by petrographic examination using a Leitz Orthoplan microscope and electron microprobe analysis. An Amray 1645 scanning electron microscope equipped with secondary and backscattered electron detectors for imaging as well as a Tracor Northern TN-5500 energy dispersive X-ray microanalysis system with 40 MByte data storage capacity and color display were used to obtain SEM photomicrographs to show phase morphologies as well as EDX multielement semiquant chemical analysis to confirm phase identifications.

RESULTS

Calculations based on this extended use of the concept of optical basicity identified additive systems based on iron, calcium, and sodium compounds along with combinations of these compounds as potential sulfur-capturing sorbent systems under oxygen and sulfur

partial pressures found in Texaco coal gasifiers. For these additive packages, the sulfur solubility in the resultant mixture for these slag-additive systems are estimated to be substantially increased. A summary of several calculation results for Pittsburgh No. 8 coal slag with and without several additive packages are listed in Table 1. Note the increase in the predicted sulfur solubility in the resultant slag-additive mixtures depends on the chemical composition of the additive package.

The effects of gas composition and temperature on equilibrium in-situ sulfur capture were considered. For constant temperatures, calculations predict that a more reducing gas atmosphere (i. e. lower oxygen partial pressure) increases the sulfur solubility in the slag-additive mixture. Also, for constant sorbent composition, the sulfur solubility in the slag-additive mixture increases as the temperature decreases. Hence, the most favorable Texaco coal gasifier conditions for in-situ sulfur capture by these sorbents are expected to be at lower temperatures with a highly reducing gas atmosphere. However, several practical considerations (e.g. coal conversion and slag viscosity) place limits on the achievable operating conditions in Texaco coal gasifiers.

In addition, the effect of sorbent composition was also examined. The calculations indicate that sodium is incrementally more effective than either iron or calcium as a sulfur sorbent. Among the additive mixtures considered, calculations indicate that the iron-sodium package is expected to be the most effective with possible synergistic effects between the two components while the iron-calcium package is expected to be marginally better than a physical mixture of the two components.

To validate these predictions, experimental bench scale data using coal slag equilibrated with several of these proposed sorbent packages under simulated Texaco coal gasifier syngas environments were performed. Experimental sulfur solubilities in the slag's silicate phase as measured by EDX are shown as a function of temperature for bench scale runs for Pittsburgh No. 8 slag with a sodium additive are shown in Fig. 2. These experimental results qualitatively confirm the predicted increase in sulfur solubility for these resultant slag-additive mixtures as a function of temperature under simulated syngas conditions for a Texaco coal gasifier operated in a slagging mode with a coal-water slurry feed. In addition, several sorbent mixtures were tested that qualitatively confirm the estimated greater incremental effect of sodium-based sorbents versus either iron- or calcium-based sorbents as well as the synergistic interactions for a combined iron-sodium sorbent package. Hence, the extended use of the concept of optical basicity shows promise as a means to identify additive packages which can enhance the sulfur solubility in coal slag-additive mixtures under simulated Texaco coal gasifier syngas conditions.

CONCLUSIONS

A proposed calculation scheme based on an extended use of the concept of optical basicity was found to qualitatively identify several possible sorbent packages that could potentially capture sulfur in-situ under simulated Texaco coal gasifier syngas conditions. Experimental bench scale data confirm that addition of several of these additive packages enhance sulfur solubility in the resultant coal slag-additive mixtures. Consequently, this proposed calculation

scheme shows promise as a rapid method to identify potential sorbent packages which can enhance in-situ sulfur capture by the slag.

ACKNOWLEDGEMENTS

The authors gratefully acknowledge financial support for this work under the five year Texaco/Department of Energy Cooperative Program (Contract No. DE-FC21-87MC23277) on "Integration and Testing of Hot Desulfurization and Entrained Flow Gasification for Power Generation Systems" with METC's Dr. J. Beeson as Contract Manager. Mitri Najjar would like to thank Prof. John F. Elliot for several helpful discussions. Ron McKeon performed most of the experimental runs while Tris Laurion provided EDX analyses of the slag samples.

REFERENCES

1. C. Wagner, Met. Trans., 6B (1975) 405-409.
2. C. J. B. Fincham and F. D. Richardson, "The behavior of sulfur in silicate and aluminate melts", Proc. Roy. Soc. London, A223 (1954) 40-62.
3. J. A. Duffy and M. D. Ingram, "The Behavior of Optical Basicity Indicator Ions in Relation to the Ideal Optical Basicity of Glasses", Physics and Chemistry of Glasses, 16 (1975) 119-23.
4. I. D. Sommerville and D. J. Sosinski, "The Application of Optical Basicity Concept to Metallurgical Slags", in A. H. Fine and D. R. Gastell (Ed.), Second International Symposium on Metallurgical Slags and Fluxes, The Metallurgical Society, AIME, Warrendale, PA, (1984) 1015.
5. J. F. Elliot, Private communication.
6. G. Eriksson, Acta Chem. Scand., 25 (1971) 2651.

TABLE 1
Calculation results for Pittsburgh No. 8 coal slag with various additive packages based on extended use of optical basicity

Pittsburgh No. 8 slag Chemical Analysis (wt%)		Syngas Conditions
Na_2O	1.42	Temperature = 2200°F
CaO	5.04	Total Sulfur = 2.14 wt%
MgO	1.00	$P_{S2} = 4.09 \times 10^{-5}$ atm
Al_2O_3	22.33	
SiO_2	44.57	$P_{O2} = 2.59 \times 10^{-12}$ atm
FeO	24.17	Coal-water slurry feed
TiO_2	1.05	Air Gasification
P_2O_5	0.42	Slagging Mode

	Case I	Case II	Case III	Case IV
Additive, wt% slag	None	22wt% CaO	12wt% Na_2O 10wt% FeO	22% Na_2O
Optical basicity	0.61	0.65	0.68	0.71
log(Sulfide Capacity)	-5.10	-4.47	-4.20	-3.92
Sulfur Solubility in slag	0.03	0.14	0.25	0.47

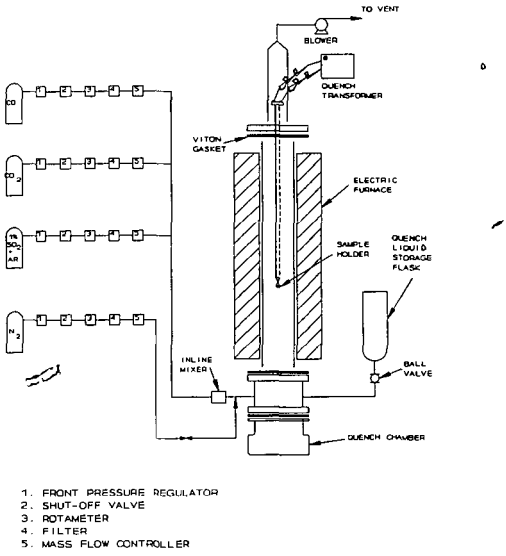

FIGURE 1 Schematic for Equilibrium Furnace

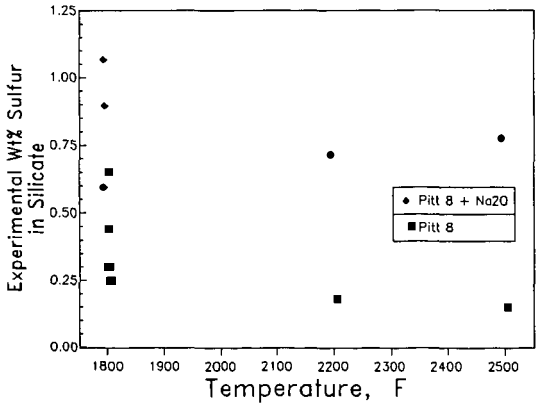

FIGURE 2 Effect of temperature and sodium addition on sulfur capture for Pittsburgh No. 8 slag under simulated Texaco coal gasifier slagging mode conditions

TRENDS IN THE EVOLUTION OF FLY ASH SIZE DURING COMBUSTION

Chris J. Zygarlicke, Donald L. Toman, and Steven A. Benson
Combustion and Environmental Research Center
University of North Dakota Energy and Environmental Research Center
Box 8213 University Station, Grand Forks, ND 58202

KEYWORDS Fly Ash, Particle-Size Distribution, Coalescence

ABSTRACT

Processes governing the evolution of the intermediate ash (inorganic gases, liquids, and solids) during pulverized coal combustion were examined in detail by combusting carefully sized fractions of Beulah lignite and Upper Freeport bituminous coals in a laminar flow drop-tube furnace. Char (partially combusted coal) and fly ash produced at various temperatures and residence times were analyzed using advanced scanning electron microprobe techniques. Fly ash was collected and sized in multicyclone and impactor devices. Work was focused on determining the relationship between the sizes of the original coal and coal minerals and the size of the resulting fly ash. Time-resolved size distributions of inorganic phases associated with chars show that Beulah and Upper Freeport phases exhibit some coalescence of inorganic phases with time. The Upper Freeport shows an initial increase in the amount of particles in the lower size ranges possibly due to fragmentation of minerals or the formation of smaller inorganic ash droplets from submicron minerals or organically associated inorganic constituents. The level of ash and coal minerals in size ranges greater than 3 microns is nearly equal for Upper Freeport, possibly indicating the influence of fragmentation. Size distributions of both the Upper Freeport coal minerals and resulting fly ash were larger than similar distributions for the Beulah. Both coals gave slightly smaller fly ash sizes for higher gas temperatures. In support of this observation, calculations revealed that both coals produced more fly ash particles per coal particle for higher combustion temperatures. The mechanism of fly ash formation for the Beulah was the result of partial coalescence of minerals and organically bound constituents. Upper Freeport ash revealed coalescence for the smaller (<3.0 μm) minerals. Using different coal sized fractions and the same gas temperature of 1500°C, larger fly ash particle size distributions were observed for the smaller-sized coal fractions.

INTRODUCTION

Today's coal energy technologies are being severely challenged by tighter pollution control regulations and demands to obtain higher yields from lower quality coals. Research on the chemical and physical transformations of inorganic components during combustion is a relevant branch of coal energy research geared to meet the challenge of today's demands because the results obtained pertain not only to emissions, but also to boiler efficiency. Intermediate inorganic components in combustion systems consist of inorganic gas, liquid, and solid phases produced during the combustion of coal. These inorganic components can cause significant problems in utility boilers, including:

fireside ash deposition on heat transfer surfaces, erosion and corrosion of boiler parts, and production of fly ash that is difficult to collect. The goal is to develop a means to predict the particle-size distribution and chemistry of the fly ash for a given coal, based on the character of the initial coal inorganic constituents and combustion conditions. In order to attain this goal, quantitative data is needed to describe the transformation of coal inorganic components to fly ash particulate, so that realistic predictive models can be devised. Carefully controlled laboratory-scale combustion regimes are being used, such as the laminar flow drop-tube furnace, which can simulate gas temperatures, particle residence times, and particulate stream flow rates in larger scale combustors. Also, more sophisticated analytical tools are now available which provide a more comprehensive means of quantifying inorganic constituents in coals, fly ash, and ash deposits (1,2).

Studies of fly ash particle sizes indicate a bimodal size distribution (3,4,5,6). The submicron size particles have an average diameter of about 0.1 micrometer. These small particles form as a result of the homogeneous condensation of flame-volatilized species. Flame-volatilized species may also condense heterogeneously on the surfaces of larger particles. Larger-sized particles are sometimes referred to as residual ash, which is largely derived from discrete mineral grains. The composition and size distribution of the larger particles are a result of the transformations and interactions between discrete mineral grains and organically bound inorganic components in the coal. Processes such as coalescence, fragmentation of minerals and char, and shedding of inorganic components all play a role in the final fly ash produced. Loehden et al., (7) indicate that three potential models for fly ash generation can be used to describe fly ash particle size and composition evolution. The first, "fine limit," assumes that each mineral grain forms a fly ash particle and that the organically associated elements form fly ash particles less than 2 μm. The second, total coalescence assumes one fly ash particle forms per coal particle. The third limit, partial coalescence, suggests that the fly ash composition and particle size evolves due to partial coalescence.

The focus of work presented in this paper was to observe trends of fly ash particle size evolution during combustion of low-rank Beulah lignite and higher-rank Upper Freeport bituminous coals. The approach was to carefully quantify the association and size of the inorganic constituents in the original coal and examine the combustion products quenched at successively longer residence times in an entrained laminar flow drop-tube furnace. In this way the stages of fly ash development can be discerned for coals of varying rank and composition. Accurate information of how ash particle sizes and compositions change with time and how specific coal inorganics and minerals are transformed and other new high-temperature products formed may lead to recognizing trends in fly ash evolution.

EXPERIMENTAL

Coal and Char Characterization

Sonically sieved fractions of Beulah and Upper Freeport coals (38-53-μm, 53-74-μm, and 74-106-μm fractions) were prepared. Extensive testing of these coal fractions and their combustion by-products were performed as part of a Department of Energy contract to study inorganic transformations during combustion. Computer-controlled scanning electron microscopy (CCSEM) (1,2) was

used to ascertain abundance and size distribution of minerals or inorganic phases in the coals and chars. Standard ash determination and bulk coal ash analyses were also performed on the coal fractions. Chemical fractionation analysis (8) of the Beulah lignite gave 92% of the sodium and 46% of the calcium as being organically bound in the coal matrix. Table 1 summarizes the initial coal characterization data for Beulah and Upper Freeport.

Production and Characterization of Ash Constituents

Time-resolved studies of the evolution of fly ash particle size were accomplished for the Beulah and Upper Freeport coals by tracking particle-size transformations beginning with the original coal minerals, progressing through short residence time chars, and ending in the near 100% carbon burnout. Fly ash and char were produced using an entrained flow-tube furnace, also known as a drop-tube furnace. The drop-tube furnace is a laboratory-scale furnace system that can simulate conditions in commercial combustors without the high cost associated with pilot-scale combustion testing. Figure 1 shows the drop-tube furnace used at the EERC. The combustion temperature, residence time, and gas cooling rate can be closely controlled and monitored (9).

Fly ash was collected using a Southern Research Institute Five-Stage Cyclone, equipped with a final filter, and a University of Washington Mark 5 Source Test Cascade Impactor. The multicyclone aerodynamically separates the fly ash into six stages or aerodynamic categories, while the impactor segregates the ash into twelve stages.

A short residence time probe was used to collect char samples at five residence time intervals: 0.05, 0.1, 0.2, 0.5, and 0.8 seconds. Particle-size distributions of original coal minerals and char phases were determined using CCSEM, and fly ash was sized using multicyclone and impactor collection devices attached to the drop-tube furnace. The effects of combustion temperature and coal particle size on the final fly ash size distribution were investigated as well.

Fly ash was produced at 1300, 1400, and 1500°C using 53-74 μm fractions of Beulah and Upper Freeport coals. The combustion parameters are given in Table 2. Near 100% carbon burnout was achieved under these conditions. The fly ash was cooled by means of a fly ash quenching probe and collected using the multicyclone. In addition, three size fractions of each coal were combusted at 1500°C and collected in the impactor to note changes in fly ash particle-size distribution with varying coal size (Table 3). Table 4 gives the combustion parameters used to produce chars from Upper Freeport and Beulah (53-74 μm) coals, respectively, at various residence times. Based on thermal gravimetric analysis, a steady decrease in carbon content was noted with increasing residence time for both coals, and by 0.8 seconds, near 100% burnout was achieved. The chars were analyzed using CCSEM to determine the size and composition of inorganic ash particles.

RESULTS AND DISCUSSION

Fly Ash Particle-Size Evolution

Detailed analysis was made of the Beulah and Upper Freeport inorganic components associated with the coal, char, and fly ash by observing area, weight, and number percent concentrations of inorganic components in different size categories. Number percent data refers to the number of particles in a particular size category, whereas weight percent data is a weighted average of the ash in different size categories which approximate a mass distribution. In effect, this gives a time-resolved look at the development of fly ash particle size which is helpful input into models which attempt to predict fly ash size and composition.

The analysis of Beulah char phases revealed that greater quantities of larger-sized particles were formed during char formation as compared to the original mineral size distribution (Figure 2). This may be evidence for coalescence of smaller inorganic particles to form larger ones.

The particle-size distribution for mineral phases in the Upper Freeport chars (Figure 3) shows an initial increase in the number of particles in the smaller size categories. By 0.8 seconds, however, larger quantities of phases are found in the >11.0 μm fraction than in the coal. This trend may indicate that, initially, fragmentation of mineral grains may be occurring with subsequent coalescence of ash particles as time in the hot zone progresses. Another trend noted for these coals is that the Upper Freeport, which had an overall larger mineral particle-size distribution than did the Beulah (Figure 4a), also produced a larger fly ash size distribution (Figure 4b). This may help answer the question as to whether the fly ash size distribution is heavily dependent on the size of the original discrete mineral phases.

The degree of coalescence in Beulah and Upper Freeport was examined by comparing the measured ash particle size-distributions with particle-size distributions at the extremes for total coalescence or no coalescence. The hypothesis is that the true fly ash size distribution should fall somewhere between ideal coalescence, where one ash particle is produced per coal particle, and no coalescence where each coal mineral grain remains intact as a separate particle. The predicted mean diameter (D_a) of an ash particle was derived using the ash % of the coal and the diameter (D_c) of the coal grains from Malvern (Equation 1). Assumptions made were that the coal particles were spheres

$$D_a = D_c \sqrt[3]{\%Ash} \qquad (1)$$

and that percent ash was evenly distributed throughout all the coal particles. The discrete minerals and the fly ash were sized using CCSEM. The size distribution curve for Beulah 0.8 second char, which closely approximates fly ash, falls between the mineral and predicted ash curves (Figure 5a). This is an indication of partial coalescence. Upper Freeport ash, on the other hand, follows very closely to the original coal size distribution for particles greater than approximately 3 microns (Figure 5b).

Both the Beulah and Upper Freeport showed some evidence of smaller fly ash particle size distributions at higher temperatures (Figure 6 a and b). Although the overall fly ash particle size was partially the result of coalescing mineral and organically bound constituents, early combustion stage char fragmentation may have occurred at higher temperatures resulting in finer-sized fly ash. To check the validity of smaller fly ash at higher temperatures, the number of fly ash grains produced per coal grain (F/C) was calculated for the fly ash size fractions in each multicyclone (Equation 2). The input variables needed to make the calculations were the mass of ash (m_n) in each multicyclone stage (n), total mass collected in the multicyclones (m_{tot}), density of the coal and ash (ρ_c and ρ_f), percent ash in the coal, and the diameters of the coal and fly ash grains (d_c and d_f). For simplicity, it was assumed that the coal and fly ash grains were spherical and had uniform densities of 1.4 and 2.7, respectively. Mean coal particle sizes (d_c) were obtained from Malvern sizing analysis, and the mean fly ash sizes (d_f) were calculated from the percent mass in each of the multicyclones. The same calculations apply for impactor data. The results

$$F/C = \frac{m_n \rho_c}{m_{tot} \rho_f} \left(\frac{\%Ash}{100}\right)\left(\frac{d_c}{d_f}\right)^3 \qquad (2)$$

of the calculations, given in Table 5a, are reported for fly ash grains greater than 1 μm. These very basic calculations verify the PSD data from the multicyclones that larger quantities of smaller fly ash particles are generated at higher temperatures. This may indicate that larger coal particles are reverting to the smaller-sized ash distributions dictated by the original coal mineral sizes as carbon matrix burns away.

Fly ash produced at 1500°C, using different Beulah coal size fractions and collected in the impactor, was larger for the smaller-sized coal fractions (Figure 7a). A similar result was achieved for Upper Freeport coal size fractions, especially for ash particles greater than 2.8 microns (Figure 7b). Calculations of fly ash particles generated per coal particle for the different coal size fractions showed more fly ash grains for the larger coal fractions, for both Beulah and Upper Freeport (Table 5b). Smaller minerals were observed earlier to experience a greater degree of coalescence. It may be that the smaller coal size fractions contain more smaller-sized minerals more apt to coalesce to form a larger ash particle.

CONCLUSIONS

Particle-size distributions of discrete mineral or amorphous phases in intermediates produced in the DTF for two coals were examined. Coal minerals and char inorganic phases approximately <3.0μm in the Beulah and Upper Freeport tend to coalesce with time. Upon combustion, the Upper Freeport shows an initial increase in the amount of particles in the lower size ranges, possibly due to fragmentation of minerals or the formation of smaller inorganic ash droplets from submicron minerals or inorganics. The Upper Freeport coal minerals PSD and resulting fly ash PSD are distributed over larger size ranges than the same PSDs for the Beulah.

The size distribution curve for Beulah ash falls between the mineral and predicted coalescence ash curves. This is an indication of partial coalescence.

Upper Freeport ash, on the other hand, follows very closely to the original coal size distribution for particles greater than approximately 3 microns. The mechanism may not necessarily be fragmentation of coal particles, but rather that as carbon matrix burns away, larger coal particles are reverting to the smaller-sized ash distributions as dictated by the original coal mineral sizes. Beulah, on the other hand, shows more coalescence influence, possibly due to the Na-Ca-rich phases from the organic bonding sites that envelop and react with aluminosilicates, resulting during combustion.

Particle-size distributions of the fly ash at three different temperatures showed slightly smaller fly ash sizes at the higher temperature for both coals. In support of this observation, both coals produced more fly ash particles per coal particle for higher combustion temperatures. Although the fly ash overall was a result of coalescing mineral and organically bound constituents, the early stage chars may have experienced more initial fragmentation at higher temperatures. Fly ash produced at 1500°C, using different coal size fractions and collected in the impactor, was larger for the smaller sized coal fraction.

The trends in fly ash formation observed here using empirical data are in agreement with various models of fly ash evolution and provide a good framework for verifying and testing future models.

ACKNOWLEDGEMENTS

This work was performed under contract to the Department of Energy under Cooperative Agreement No. DE-FC21-86MC10637. The authors thank the Contracting Officers Technical Representative, Mr. Philip M. Goldberg, for his support and permission to publish the results of this work.

REFERENCES

1. Jones, M.L., Kalmanovitch, D.P., Steadman, E.N., Zygarlicke, C.J., and Benson, S.A. "Application of SEM Techniques to the Characterization of Coal and Coal Ash Products", Advances in Coal Spectroscopy, in press, 1990.

2. Steadman, E.N., Zygarlicke, C.J., Benson, S.A., and Jones, M.L. "A Microanalytical Approach to the Characterization of Coal, Ash, and Deposits", ASME Seminar on Fireside Fouling Problems, Brigham Young University, Provo, Utah, April 1990.

3. Sarofim, A.F., Howard, J.B., and Padia, A.S. Combustion Science and Technology, Vol. 16, 1977, p. 187.

4. Flagan, R.C., and Friedlander, S.K. "Particle Formation in Pulverized Coal Combustion", Recent Developments in Aerosol Science, Ed. D.T. Shaw, Wiley, New York, 1978, Chapter 2.

5. Damle, A.S., Ensor, D.S., and Ranada, M.B. Aerosol Science and Technology, 1982, Vol. 1, p. 119.

6. Wall, T.F., Bailey, J.G., and Wibberley, L.J. "The Influence of Coal Properties and Combustion Conditions on the Size Distribution of Fly Ash", In Mineral Matter and Ash Deposition From Coal, Eds. Richard W. Bryers, Karl S. Vorres, Engineering Foundation Conferences Proceedings, Feb. 22-26, 1988, Santa Barbara, California, p. 249, 1990.

7. Loehden, D., Walsh, P.M., Sayre, A.N., Beer, J.M., and Sarofim, A.F. "Fly Ash Generation and Deposition in Pulverized Coal Combustion", In Mineral Matter and Ash Deposition From Coal, Eds. Richard W. Bryers, Karl S. Vorres, Engineering Foundation Conferences Proceedings, Feb. 22-26, 1988, Santa Barbara, California, p. 279, 1990.

8. Benson, S.A., and Holm, P.L. Ind. Eng. Chem. Prod. Res. Dev., 24, 145, 1985.

9. Zygarlicke, C.J., Steadman, E.N., and Benson, S.A. "Studies of the Transformations of Inorganic Constituents in a Texas Lignite During Combustion", Progress in Energy and Combustion Science: Special Issue on Ash Deposition, Pergamum Press, 1990, in press.

TABLE 1

INORGANIC CHARACTERIZATION OF BEULAH AND UPPER FREEPORT COALS

Coal Ash Analysis	Beulah	Upper Freeport
SiO_2	21.5	50.5
Al_2O_3	13.5	24.2
Fe_2O_3	10.8	12.8
TiO_2	1.0	1.3
P_2O_5	0.9	0.1
CaO	16.1	3.1
MgO	4.0	1.5
Na_2O	6.2	0.0
K_2O	0.2	3.7
SO_3	25.7	2.7
% Ash (Dry Basis)	6.9	19.6
CCSEM Mineral Analysis		
Quartz	17.5	12.6
Iron Oxide	1.6	1.9
Aluminosilicate	40.8	24.3
Ca-aluminosilicate	0.2	0.6
Fe-aluminosilicate	0.1	3.6
K-aluminosilicate	0.9	31.6
Pyrite	27.5	13.8
Gypsum	1.6	0.5
Barite	0.9	0.0
Calcite	0.1	1.1
Rutile	0.3	0.9
Pyrrhotite	0.7	1.3
Si-Rich	0.4	0.3
Unknown	6.7	6.9
Total Minerals (Coal Basis)	4.8	22.1

TABLE 2

DROP-TUBE FURNACE RUN CONDITIONS FOR MULTICYCLONE COLLECTION OF FLY ASH FOR BEULAH AND UPPER FREEPORT 53-74 μm COALS

	UPPER FREEPORT			BEULAH		
Run #	1	2	3	1	2	3
Gas Flow Rates (L\min):						
Primary air	1	1	1	1	1	1
Secondary air	4	4	4	3	3	3
Quench Gas (N_2)	4	4	4	3	3	3
Vacuum	10	10	10	10	10	10
Temperatures (°C):						
Secondary air	1000	1000	1000	933	930	930
Furnace Upper Wall	1298	1406	1498	1300	1400	1500
Furnace Lower Wall	--	1429	--	--	--	--
Coal Feed Rate (g/min)	0.13	0.09	0.06	0.29	0.45	0.31
Residence Time (sec)	2.5	2.4	2.3	2.5	2.4	2.3

TABLE 3

DROP-TUBE FURNACE RUN CONDITIONS FOR THE FORMATION OF FLY ASH FROM BEULAH AND UPPER FREEPORT COAL SIZE FRACTIONS

Coal Size, μm	38-53	53-74	74-106
Gas Flow Rates (L\min):			
Primary air	1	1	1
Secondary air	3-4	3-4	3-4
Quench Gas (N_2)	3-4	3-4	3-4
Vacuum	10	10	10
Temperatures (°C):			
Secondary air	980	990	980
Furnace 1 Upper Wall	1498	1500	1500
Furnace 1 Lower Wall	1530	1530	1510
Coal Feed Rate (g/min)	0.03-0.24	0.03-0.2	0.03-0.2
Residence Time (sec)	2.5	2.3	2.0

TABLE 4

DROP-TUBE FURNACE RUN CONDITIONS FOR CHAR COLLECTION
OF BEULAH AND UPPER FREEPORT 53-74 μm COALS

	Beulah				Upper Freeport				
Run #	1	2	3	4	1	2	3	4	5
Gas Flow Rates (L\min):									
Primary air	1	1	1	1	1.2	1.2	1.2	2	1.2
Secondary air	4	4	4	4	3	3	3	2.5	3
Quench Gas (N_2)	3	3	3	3	5	5	5	5	5
Vacuum	10	10	10	10	10	10	10	10	10
Temperatures (°C):									
Secondary air	1000	1000	1000	1000	982	982	983	982	992
Furnace 1 Upper Wall	1467	1470	1475	1442	1502	1498	1497	1503	1499
Furnace 1 Lower Wall	1487	1480	1478	1434	1572	1570	1563	1552	1545
Coal Feed Rate (g/min)	0.08	0.08	0.29	0.34	0.06	0.06	0.06	0.05	0.06
Residence Time (sec)	0.1	0.2	0.5	0.8	0.05	0.1	0.2	0.5	0.8

TABLE 5

CALCULATED FLY ASH GRAINS PER COAL GRAIN
(PARTICLES > 1 MICRON)

(a) Varied Temperature and 53-75 μm Coal

	Temperature °C		
	1300	1400	1500
Beulah	6.3	5.9	9.0
Upper Freeport	16.5	21.6	26.3

(b) Varied Coal Size

	Coal Size (μm)		
	38-53	53-74	74-106
Beulah	14	66	147
Upper Freeport	159	134	316

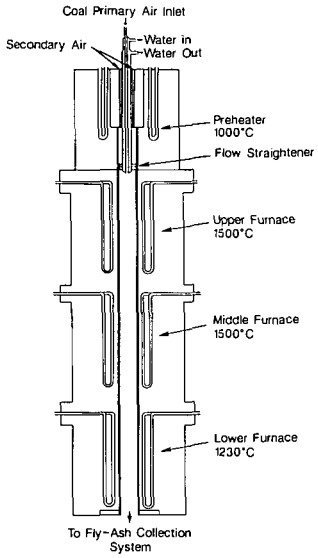

Figure 1. Schematic drawing of the EERC drop-tube furnace.

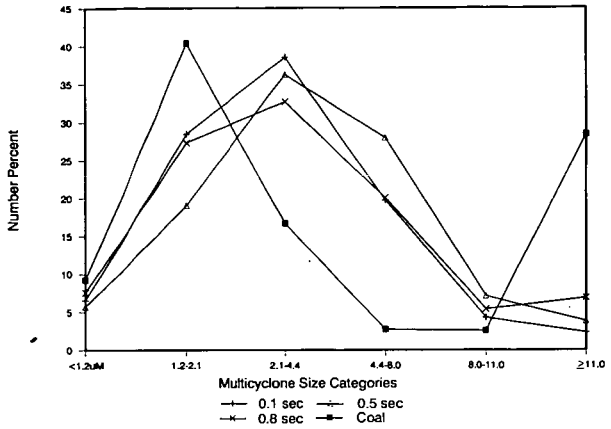

Figure 2. Particle-size distribution of inorganic particles in Beulah chars based on the numbers of particles in each size category determined using CCSEM of whole grain mounts.

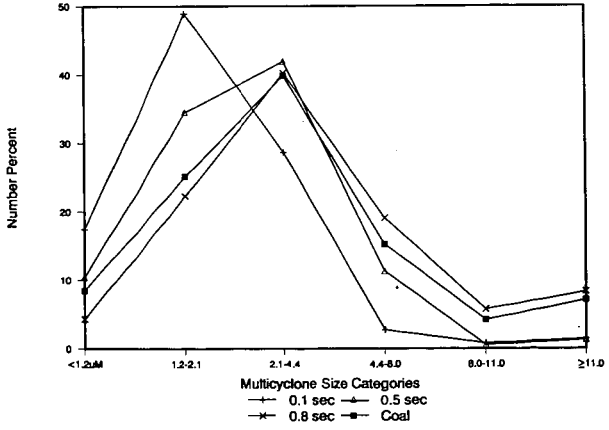

Figure 3. Particle-size distribution of inorganic particles in Upper Freeport chars based on the number of particles in each size category determined using CCSEM of whole grain mounts.

(a)

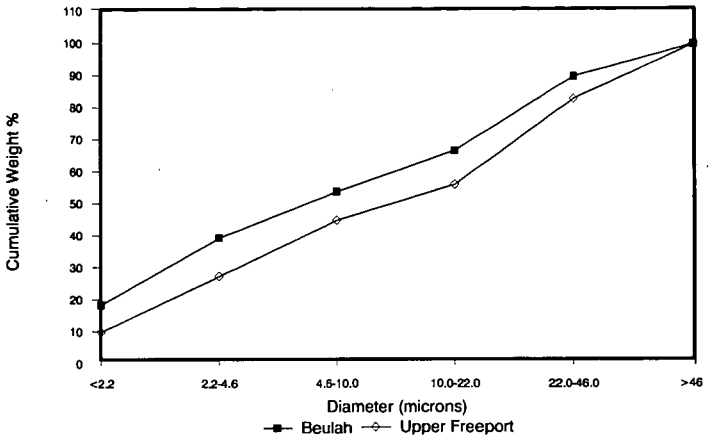

(b)

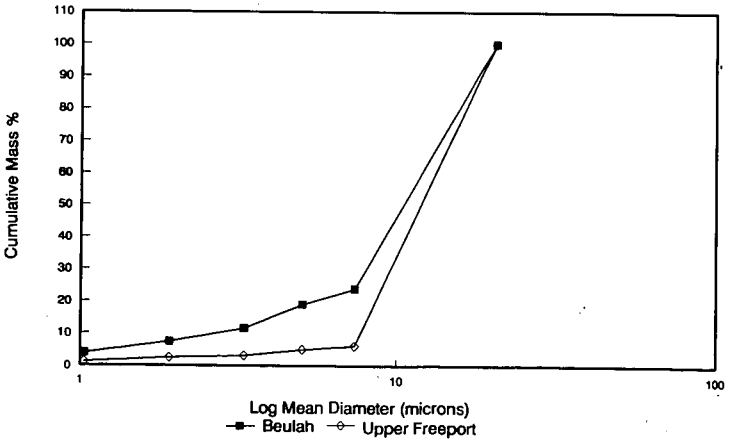

Figure 4. (a) Size distribution of minerals in Beulah and Upper Freeport 53-75 µm.
(b) Size distribution of fly ash in Beulah and Upper Freeport generated at 1500°C on the 53-74 µm fraction.

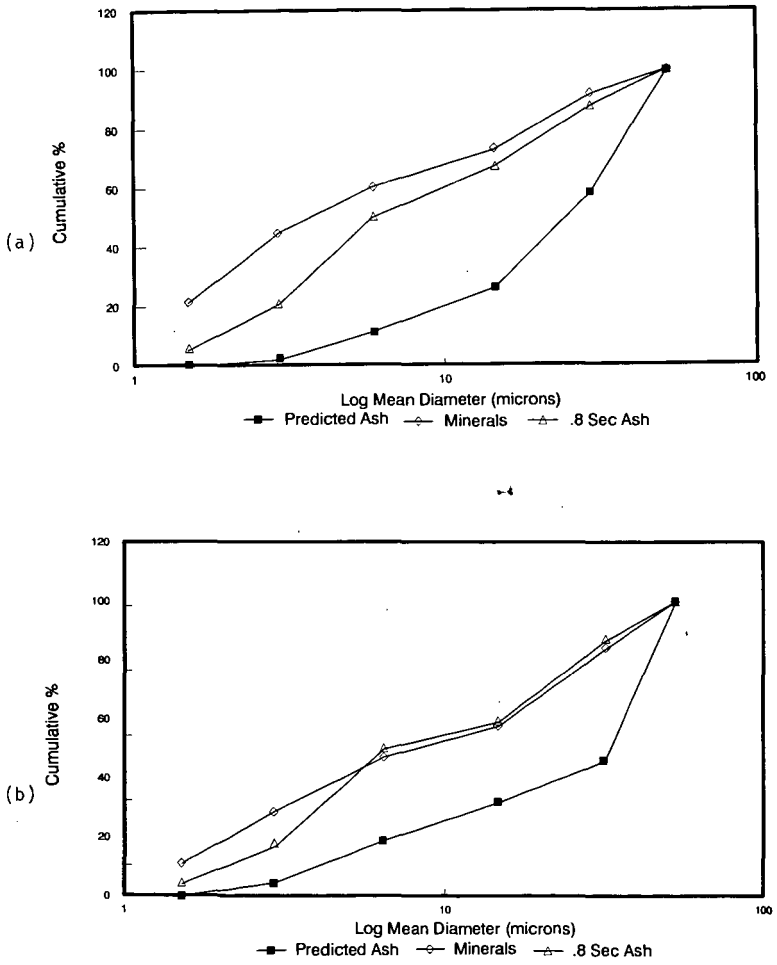

Figure 5. Cumulative particle-size distribution of predicted ash from total inorganic coalescence of each coal particle, coal minerals, and 0.8 fly ash, using CCSEM and Malvern data, for (a) Beulah and (b) Upper Freeport.

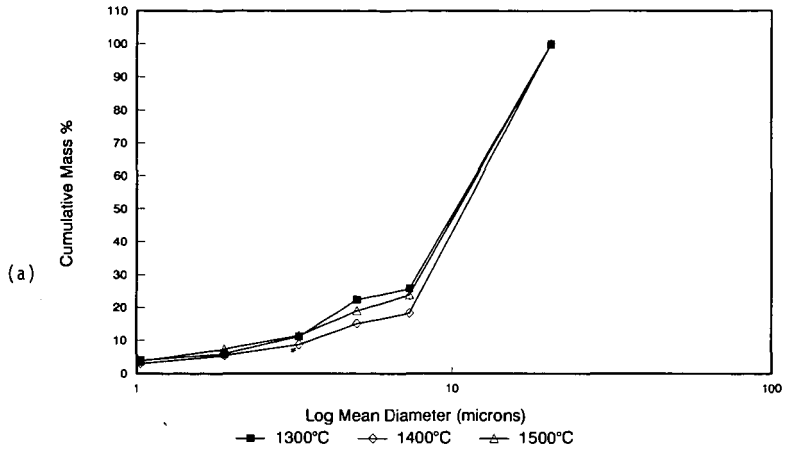

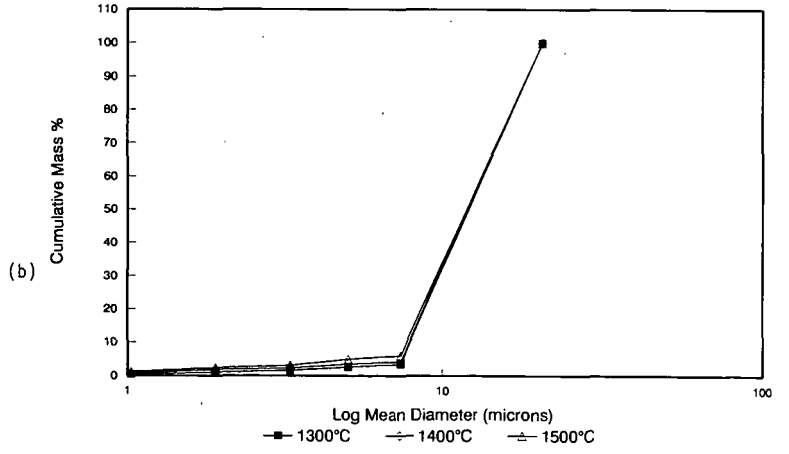

Figure 6. Fly ash particle-size distributions observed at 1300, 1400, and 1500°C after combustion of (a) Beulah and (b) Upper Freeport 53-74 μm coals.

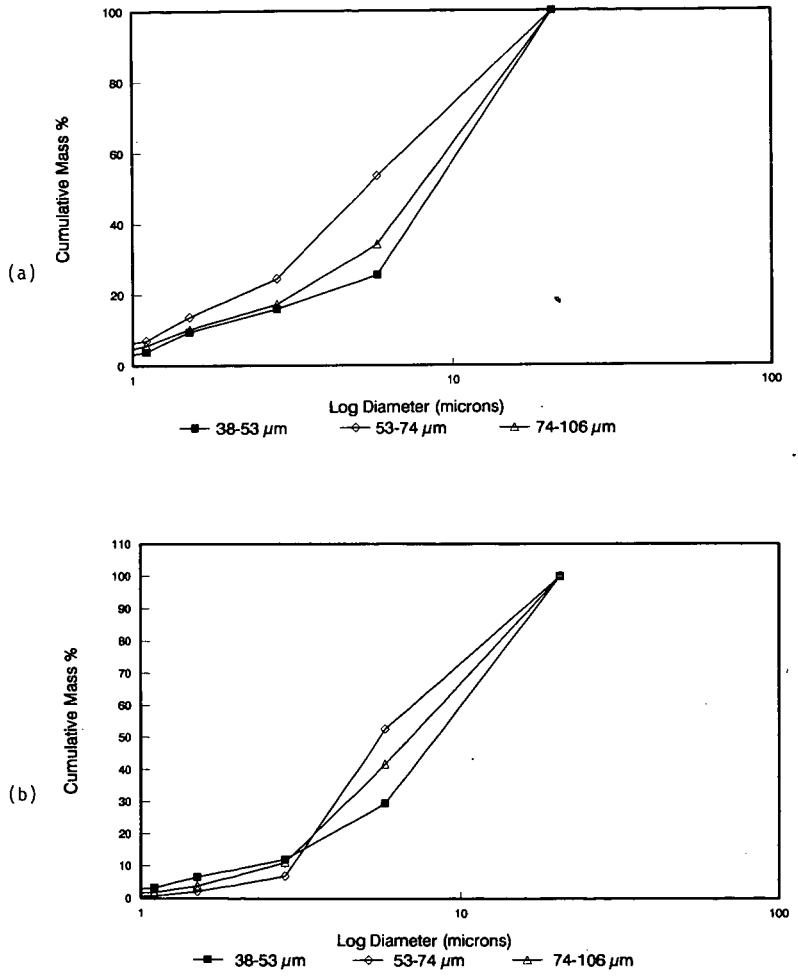

Figure 7. Fly ash particle-size distribution observed after combustion of 38-53, 53-74, and 74-106 μm coal size fractions of (a) Beulah and (b) Upper Freeport.

A Study of Ash Formation During the Combustion of Pulverized Coal

Sharon.F. Miller, Harold.H. Schobert, and Alan.W.Scaroni
The Pennsylvania State University
Fuel Science Program
University Park, PA 16802

Keywords: ash formation, particle size distribution, pulverized coal combustion.

INTRODUCTION

In order to predict the potential problems caused by ash in a pulverized coal in comparison to a coal-water fuel fired systems, it is necessary to understand the mechanism by which an ash particle acquires its particular size and compositional character. The particle size distribution (PSD) of an ash and its composition are determined by the following: the mineral matter composition and size distribution in the coal, the coal composition and particle size, the morphology of the char produced upon devolatilization of the coal particle, the local atmosphere surrounding the mineral particles, and the phase transformations of the mineral matter during combustion. When one or more of the above characteristics or conditions varies, the resulting ash size and composition may also change. In the process of preparing and burning a coal-water fuel, several or all of the above characteristics or conditions are different from those of the pulverized coal. It is the objective of this research to understand the effect that the form in which a coal is fired, pulverized versus coal-water fuel, has on the mechanisms responsible for the size and composition of the char and ash produced during combustion. Two coals, the Elk Creek bituminous and Beulah lignite, are being studied. Each coal is being fired in a pulverized form and as a coal-water fuel.

The following discussion concentrates on the preliminary results of the combustion tests on the Elk Creek and Beulah pulverized coals. The results presented show that the two pulverized coals produce distinctly different char-ash morphologies and sizes. The discussion provides comparisons between the coal PSD, the PSD of the mineral matter in the coal, and the PSDs of the char-ash samples collected at various locations down the combustor representing various degrees of burnout. The conclusions are based primarily on size data and observations of the morphologies of the various char-ash samples.

COMBUSTION SYSTEM AND ANALYTICAL TECHNIQUES

The combustion experiments were conducted in the down-fired combustor shown in Figure 1. The main radiant section of the combustor is modular and consists of four 0.46 m (18 inch) tall and 0.41 m (16 inch) diameter refractory sections. A divergent refractory cone, commonly termed a quarl, is positioned on top of the circular refractory sections. The quarl is 0.83 m (32.5 inches) high. The burner is located on top of the quarl as shown in the Figure 1. The divergent cone top has a half-angle of approximately ten degrees and was used to minimize recirculation and swirl in the combustor. Swirl was not introduced in order to minimize ash deposition on the combustor walls and to ensure an even distribution of ash flow for sampling. Below the four circular refractory sections is a constrictor segment and a flue gas exit section. The flue gas passes through the convective section and enters a spray chamber to decrease the gas temperature prior to exiting the system via the induced draft fan and the stack. The overall length of the combustor is 3.05 m (10 feet). For more detail see Hurley (1990).

A series of 7.62 cm (3 inch) sampling ports extend the length of the combustor. Sample ports are numbered 1 through 10 starting at the top of the combustor. During this study, particulate and gas sampling were conducted in Ports 1, 2, and 10. Wall temperatures were monitored using thermocouples at eight locations along the length of the combustor. The temperature profile was considered stable when the temperature in the top four ports changed at a rate of less than 0.5°C/min. The combustor was preheated using natural gas at a firing rate of 0.26 GJ/h. The preheat period typically lasted approximately three hours after which the natural gas was shut off and the pulverized coal introduced. The fuels were fed at a rate of 0.32 GJ/h corresponding to a volumetric heat release rate of 1.14 GJ/m^3-h. The Beulah lignite and Elk Creek bituminous pulverized coals were fed using an open helix dry feeder at a rate of 19.1 kg/h and 10.0 kg/h, respectively. The coal was entrained from the dry feeder and transported to the burner by the primary air which accounted for 18% of the total air required for combustion. The fuels were fired at 20% excess air. Total particle residence times within the radiant section of the combustor for the Beulah and Elk Creek coals were 2.09 and 2.13 seconds, respectively. Particle residence times for the samples collected at Ports 1, 2, and 10 are listed in Table 1. Overall carbon conversion levels of 99.4% and 99.9% were obtained at Port 10 for the Elk Creek coal and the Beulah pulverized coal, respectively.

During combustion, particulates were sampled isokinetically at a constant volumetric rate using a water-cooled sampling probe. A three-stage Anderson multicyclone and filter assembly was used to

classify the particulates during sampling. The cyclone aerodynamic diameter 50% cutpoints were 15 μm (cyclone 1), 2.7 μm (cyclone 2), and 0.46 μm (cyclone 3). The final filter was a polypropylene fiber filter which collected particles greater than 0.3 μm in diameter. Sampling isokinetically and at a constant volumetric rate ensured collecting representative samples of different sized char and ash particles by the probe and that the 50% cut sizes of the cyclones were consistent at each port. Gas sampling was conducted using a second water-cooled probe. The gas sample was withdrawn at each port and passed through a refrigeration unit to remove moisture from the gas prior to entering O_2, CO, CO_2, SO_2, and NO_x analyzers.

The ultimate analysis of each coal was determined using a Leco Corporation CHN-600 and a Leco Corporation SC-132 Sulfur Determinator. Sulfur forms of the coals were determined using ASTM D 2492. Calorific values of the coals were determined using a Parr Adiabatic Calorimeter. Proximate analysis of the coals was determined using a Leco Corporation MAC-400 proximate analyzer. Proximate analysis, ultimate analysis, and calorific value for both coals are presented in Table 2. The proximate analysis of the cyclone samples was determined thermogravimetrically with a Perkin Elmer 10 Series Thermal Analysis System. The thermogravimetric analyzer (TGA) was used for the proximate analysis of the cyclone samples because the TGA requires only 10 milligrams of sample for each analysis as compared to 1 gram for the MAC-400. TGA data was also used to determine the percent burnout, or carbon conversion, of the samples collected in the cyclones. Fuel burnout was calculated using ash as a tracer. Bulk inorganic compositional analysis for each coal ASTM ash was determined by a Spectrometrics Spectrospan 3 direct plasma spectrometer (DCP) (Table 2). The inorganic elements analyzed included silicon, aluminum, calcium, sodium, potassium, iron, magnesium, manganese, titanium, phosphorous, barium, sulfur, and strontium. Elemental analyses are reported on an oxide basis.

Computer-controlled scanning electron microscopy (CCSEM) was used to identify and quantify the size and composition of the mineral matter in the raw coal. The system is operated in conjunction with energy dispersive X-ray analysis provided by a Tracor Northern Electron Probe Microanalyzer EDS system at the University of North Dakota Energy and Environmental Center. The compositional analysis of each particle was compared with known compositional ranges of different mineral species. The computer then categorized each particle as a specific mineral phase. Mineral size data are presented in graphical form in the results section. Actual mineralogical analysis for each coal is not presented at this time. For a more detailed description of the sample preparation and procedure refer to Hurley (1990) and DeHoff and Rhines (1968). Photomicrographs were taken with a ISI ABT SX-40A SEM to study the morphology associated with the various cyclone sized fractions sampled at the different ports.

Size analysis of the coals and ash samples was conducted with a Malvern 2600 Particle Size Analyzer. The Malvern Particle Size Analyzer is an optical, nonimaging technique used to make *in situ* particle size measurements (Meyer, 1986) Composite samples from each sample port (i.e. Ports 1, 2, and 10) were used for size analysis. The particle size data are presented as cumulative volume percent as a function of the log size in microns. The data are presented in this manner in order to compare with the Malvern results which are reported on a volume distribution basis for each size category.

RESULTS AND DISCUSSION

Relation Between Coal, Mineral Matter, and Char-Ash Particle Size Distributions

Elk Creek Coal

In the case of the Elk Creek coal the data suggest that the individual mineral particles in the original coal do not form individual ash particles but rather that several mineral particles form an individual ash particle either by coalescence or agglomeration. The PSDs of the Elk Creek coal, mineral matter, and char-ash samples are shown in Figure 2. The d_{50} of the char-ash samples collected from Ports 1, 2, and 10 are 28.1, 21.1 and 8.6 μm while d_{50} of the coal is 19.4 μm. The increase in particle size at Port 1 is seen throughout the entire size range. A possible explanation for the increase in PSD is that the Elk Creek coal has a Free Swelling Index (FSI) of 6 and exhibits swelling during heating. Such coal will typically pass through a fluid or plastic phase at approximately 350 to 400°C (Scaroni et al., 1986). During the fluid phase, volatiles are evolved which result in swelling of the coal particle.

Examination of SEM micrographs indicates that samples collected at Port 1 are composed of spherical char particles which have gone through a melt phase and experienced swelling. Holes due to the release of volatiles are visible on the char surfaces. The extent of carbon conversion is approximately 59.8%. Char cenospheres are present and fragmented, suggesting rapid heating rates. According to Solomon and Hamblen (1985), char particles melt and gas is evolved into the internal micropores forming small gas pockets. With continued heating, the size of the gas pockets increases and in some cases they may coalesce. At this point, significant swelling is not usually observed. According to Solomon and Hamblen (1985), the particle changes which subsequently occur are determined by the heating rate. With

rapid heating (10^5 °C/s), the cell walls rupture, blowing multiple holes in the surface of the char. At an intermediate heating rate, some coalescence of the bubbles occurs before rupturing. At lower heating rates (i.e. 10^3 °C/s), the gas pockets expand and coalesce, eventually forming large cenospheres. In the second cyclone, ruptured char cenospheres containing individual and coalesced ash spheres are present which suggests the particles experienced rapid heating rates. The heating rate of the d_{50} (19.4 μm) Elk Creek coal particle in the combustor is estimated to be approximately 3.0×10^5 °C/s. Based on the particle size data and the char morphologies, it is reasonable to suggest that the coarser size distribution of the samples collected at Port 1 is due to the swollen char particles found in the first cyclone.

At Port 2, the char particles are 88.9% burned out. The char cenospheres are lacy in appearance and numerous ash spheres are present on the larger char surfaces. The ash spheres appear on the char surface as the surface recedes during combustion. As the char surface recedes, mineral matter particles in the char are exposed at the char surface and melt forming slag beads on the char surface. However, individual slag beads do not coalesce or spread upon the char surface due to their inability to wet a carbon surface. Eventually, as the char surface continues to recede, the ash particles will coalesce forming larger solid ash particles. Some char cenospheres are fragmented either due to impact or rupture during gas evolution.

At Port 10, the overall carbon conversion level is 99.4%. The PSD distribution of the sample collected at Port 10 approaches the PSD of the original mineral matter (Figure 3). In fact, the curves meet at approximately 48 μm, however, the mineral matter PSD consists of much finer particles than the final ash sample. The data suggest that the individual mineral particles in the original coal do not form individual ash particles but rather that several mineral particles form an individual ash particle either by coalescence or agglomeration. If each individual mineral particle were responsible for forming an individual ash particle, the PSD curves of the ash and mineral matter would be nearly identical in shape. Evidence for the coalescence of mineral matter is based on the morphology of the char and ash during combustion and the composition and size of the mineral matter in the raw coal. The individual ash particles are composed of small ash spheres which are coalesced and highly agglomerated. The char only occurs as highly fragmented lacy structures (Figure 4).

The SEM evidence supports the premise that individual mineral particles do not form individual ash particles but rather several mineral particles in the form of coalesced ash spheres comprise an individual ash particle. The result is that the ash PSD at Port 10 consists of larger particles than the mineral matter PSD in the raw coal.

Beulah Lignite

The PSDs of the Beulah coal, mineral matter, and char-ash samples are shown in Figure 4. The interpretation of the PSD data is that the char and the larger mineral matter particles in the coal undergo shedding and fragmentation during combustion. The d_{50} of samples collected from Ports 1, 2, and 10 decreases from 67.0 to 46.8 to 8.2 μm as carbon conversion increases. However, the sample collected at Port 1 has a larger volume mean diameter than the original coal mean volume diameter of 46.4 μm. The shift to a coarser PSD can be attributed to burning of the smaller coal particles thereby removing then from the total PSD. Unlike the Elk Creek coal, the Beulah coal has a FSI of 0. Therefore, the possibility of swelling as the mechanism responsible for the larger particle sizes is not reasonable. The carbon conversion at Port 1 is approximately 20%.

The samples collected from Port 2 show more extensive recession of the char surface. The surface of the char is sharply convoluted with ash cenospheres located between the ridges. The ash spheres are approximately 5 μm in diameter and are fairly uniform in size. The ash spheres represent mineral matter that has melted on the char surface as it is exposed by the receding char surface. The Beulah lignite does not pass through a fluid phase during heat up as does the Elk Creek coal and this may explain the difference in the surface appearance of the Beulah char as compared with the smooth surface of the Elk Creek char. As the char continues to burn and the char surface recedes, the char surface becomes even more jagged. Some fractured lacy carbonaceous particles and ash spheres are present in the smaller size fraction of the second cyclone where burnout is approximately 95.4%.

As with the Elk Creek coal, the size distributions for the Beulah samples collected from Port 1 through Port 10 shift to a finer overall PSD as would be expected with increasing burnout. However, unlike the Elk Creek ash PSD at Port 10, the Beulah ash PSD at Port 10 is characterized as finer than the mineral matter PSD in the original coal. The greatest difference between the PSD of the original mineral matter and the sample collected at Port 10 occurs at the coarser end of the cumulative volume percent curve. The curves actually superimpose in the size range of 4.6 μm and smaller. The interpretation of the PSD data is that the char and the larger mineral matter particles in the coal undergo shedding and fragmentation during combustion which results in the finer PSD of the ash relative to the mineral matter.

Therefore, individual large mineral particles and coal particles are actually forming several ash particles. Evidence for this is based on the morphology of the char and ash and the size and composition of the mineral matter in the pulverized coal. The mineral matter which is finely dispersed throughout the coal particle would normally form small, molten spheres on the char surface and eventually coalesce forming larger ash spheres. However, if char fragmentation occurs, the small mineral particles are unable to coalesce. The molten ash particles are released on smaller fragments of char and may coalesce but the overall increase in ash sphere size is minimized. The ash spheres may also be released into the gas stream as individual particles and retain their original size contributing to the finer size fraction of the ash. Fragmentation of ash agglomerates and cenospheres can also occur contributing to an increase in the smaller size fractions of ash. Fragmentation by either the ash particles separating from the char prior to char burnout or the fragmentation of ash cenospheres during and after char burnout are probably both occurring in the Beulah coal char and ash.

At Port 10, the overall carbon conversion is 99.88%. Micrographs of the composite sample show the ash to be composed of mostly separate individual angular ash and char particles, fragmented cenospheres, solid ash cenospheres (1.5 to 6.0 μm in diameter), and sintered spheres joined by neck structures (Figure 5). In general, there is no agglomeration of the larger ash particles suggesting that, as ash spheres are formed on the char surface they do not coalesce to form larger ash spheres or perhaps the char fragments prior to the ash spheres coalescing.

The mineral matter composition and its PSD in the Beulah coal also provide an additional explanation for the finer PSD of the ash as compared to the coal mineral matter. Thirty-four percent of the mineral matter by weight is pyrite. Ninety-seven percent of the pyrite by weight is greater than 4.6 μm in diameter and 60% is greater than 48 μm in diameter. In addition, of the 32% of the total mineral matter in the Beulah coal that is greater than 48 μm, 14.2% is pyrite. The pyrite can be considered to be mostly extraneous based on its large size when compared to the pulverized coal PSD. Large particles of pyrite are known to fracture and disintegrate when rapidly heated (Helble et al., 1989a, 1989b; Baxter and Mitchell, 1989). Some of the pyrite fragments will agglomerate upon melting; however, the resulting particle sizes of the iron-containing species are generally still smaller than the original pyrite particles. Helble et al. (1989a, 1989b) investigated the effects of oxygen levels on pyrite oxidation and subsequent fragmentation during combustion of the Beulah lignite in a drop-tube furnace. Their results showed that the ash PSD was less than the mineral matter PSD in the presence of 21% oxygen. The results from this study are in direct agreement with Helble's results in that the Port 10 sample has a finer PSD than the coal mineral matter PSD. The fragmentation of larger sized mineral particles has also been noted by Srinivasachar et al. (1989) and Bryers (1985). The fragmentation occurs primarily in pyrite particles greater than 4.6 μm based on the experimental PSD of the ash and mineral matter. Pyrite rapidly decomposes to pyrrhotite ($Fe_{1-x}S$) at 1027°C. In the presence of oxygen, pyrrhotite is converted to magnetite (Fe_3O_4). The final step in the oxidation process is the oxidation of magnetite to hematite (Fe_2O_3) (Helble et al., 1989a). Based on the evidence available at this time, the fragmentation of pyrite appears to contribute to the finer PSD of the final ash sample collected at Port 10 relative to the mineral matter in the original pulverized coal. Therefore, one larger mineral particle is actually forming several ash particles.

It should also be noted that 30% of the mineral matter in the Beulah coal was classified as unknown by the CCSEM. This mineral matter tends to be less than 2 μm in size and is composed of iron sulfur compounds and aluminosilicates. These particles are most likely finely disseminated throughout the coal particle and are therefore referred to as inherent. These mineral particles are not included in the PSD of the mineral matter shown in Figure 7. It is possible that these mineral particles may coalesce during combustion of the coal and appear as larger, although still relatively small ash particles in the PSD of the Port 10 sample. The result is an increase in the small particle portion of the PSD curve for the samples collected at Port 10 compared to the original mineral matter PSD. The fragmentation of the char and the larger extraneous mineral particles, and possible coalescence of disseminated mineral matter are the predominating mechanisms determining the PSD of the final Beulah ash sample.

CONCLUSIONS

Based on the evidence, the different mechanisms responsible for the char-ash PSDs for the Elk Creek and Beulah coals are agglomeration and fragmentation, respectively. The chars and ash particles produced during the combustion of the Beulah and Elk Creek pulverized coals exhibit very different morphologies and PSDs relative to the original coal and mineral matter PSDs. For instance, the initial Elk Creek coal char samples collected at Port 1 were coarser than the original coal PSD due to swelling of char particles. The explanation for the increase in char PSD is based on the increased internal pressure generated by volatiles released during devolatilization while the coal is fluid causing increased swelling and

the formation of large cenospheres. The result is a coarser PSD of the char samples collected at Port 1 than the original coal PSD.

The final Elk Creek ash PSD (Port 10) was coarser than that of the original mineral matter. Evidence based on particle sizing and SEM photomicrographs suggests that the individual mineral particles in the original coal do not form individual ash particles, but rather several mineral particles form an individual ash particle. The Elk Creek char passes through a fluid phase forming numerous carbonaceous cenospheres. Individual mineral matter particles form individual molten ash spheres on the exterior surface of the char as the char surface recedes during burning. The ash spheres gradually coalesce as the char surface continues to recede forming larger ash spheres. The end result is a coarser PSD for the final ash than the original PSD of the mineral matter.

A final ash PSD finer than the original mineral matter in the coal was observed during the Beulah testing. The particle size data and the SEM photomicrographs suggest that the char and the larger mineral matter particles in the coal undergo shedding and fragmentation during combustion which results in the finer PSD of the ash relative to the mineral matter. Therefore, individual large mineral particles and coal particles are actually forming several ash particles. Char samples collected from Port 1 have a fragmented appearance and the surface of the char particles tends to be very jagged. As the char surface recedes, mineral matter becomes exposed on the surface forming small ash spheres. Unlike the Elk Creek chars, the Beulah char often fragments prior to coalescing of the ash spheres. This char fragmentation results in smaller ash particle sizes.

A second source of smaller ash particles is the pyrite in the coal. The larger pyrite fragments are not present within the coal particle but rather occur as extraneous particles. These pyrite particles often fragment when heated rapidly and oxidized during combustion and form numerous smaller iron-rich particles in the final ash (Srinivasachar et al., 1989 and Bryers, 1989). In addition, finely disseminated iron-rich particles and aluminosilicate particles are present throughout the coal particle. It is possible that these mineral particles may coalesce during combustion of the coal prior to char fragmentation and appear as larger, although still relatively small, ash particles in the ash PSD. The end result of both early char fragmentation and pyrite fragmentation, as well as the agglomeration of extremely fine mineral particles, is a finer ash PSD than mineral matter PSD in the original coal.

Based on the evidence, the different mechanisms responsible for the char-ash PSDs for the Elk Creek and Beulah coals are agglomeration and fragmentation, respectively. The d_{50} values of the Beulah and Elk Creek coals are quite different being 46.4 μm and 19.4 μm, respectively and the mineral matter in the Beulah coal is coarser than that in the Elk Creek coal. However, the d_{50} values of the samples collected at Port 10 during the Beulah and Elk Creek tests are very similiar being 8.2 μm and 8.6 μm, respectively. The process of fragmentation results in the finer PSD of the Beulah ash relative to the coal mineral matter PSD. The process of coalescence and agglomeration of the Elk Creek char and ash results in a coarser ash PSD relative to the Elk Creek mineral matter PSD. The result is that the final PSDs of the two samples have similiar d_{50} values.

REFERENCES

Baxter, L.L. and R.E. Mitchell, Sixth Annual International Pittsburgh Coal Conference, v.1, pp.64-73 1989.

Bryers, R.W., Symposium on Slagging and Fouling in Steam Generators, Brigham Young University, 63 pp., January, 1987.

DeHoff, R.T. and F.N. Rhines, Materials Science and Engineering Series, McGraw Hill Book Company: New York, 422pp., 1968.

Helble, J.J., S. Srinivasachar, A.A. Boni, S.G. Kang, A.F. Sarofim, J.M. Beer, N. Gallagher, L. Bool, T.W. Peterson, J.O.L. Wendt, N. Shah, F.E. Huggins, and G.P. Huffman, Sixth Annual International Pittsburgh Coal Conference, v.1, pp.81-89, 1989a

Helble, J.J., S. Srinivasachar, C.B. Katz. and A.A. Boni, Proceedings of the 15th Biennial Low-Rank Fuels Symposium, St. Paul, MN., 15 pp., May 1989b.

Hurley, J.P., Ph.D. Dissertation, Pennsylvania State University, 247 pp., 1990.

Meyer, P. L., Ph.D. Dissertation, Carnegie-Mellon University, 219 pp., 1986.

Scaroni, A. W., M. R. Khan, S. Eser, and L. R. Radovic, "Coal Pyrolysis" in: Ullmann's Encylopedia of Industrial Chemistry, VCH Verlagsgesellschaft: Weinheim, Germany, pp. 245-280, 1986.

Solomon, P.R. and D.G. Hamblen, "Pyrolysis" in: Chemistry of Coal Conversion, R.H. Schlosberg, ed., Plenum: New York, pp. 121-252, 1985.

Srinivasachar, S., J.J. Helble, C.B. Katz, and A.A. Boni, Proceedings of the Engineering Foundation Conference on Mineral Matter and Ash in Coal, R.W. Bryers and K.S. Vorres, eds., (in press), 1989.

TABLE 1. Particle Residence Times

Port	Residence Time in Combustor (sec)	
	Elk Creek Particle (d_{50} = 19.4 μm)	Beulah Particle (d_{50} = 46.4 μm)
1	0.160	0.157
2	0.417	0.410
10	1.820	1.790

TABLE 2. Elk Creek and Beulah Pulverized Coal Analysis

Coal :	Elk Creek		Beulah	
	A.R.[a]	Dry	A.R.	Dry
Proximate Analysis, %wt.				
Moisture	0.90	---	29.99	---
Volatile Matter	30.19	30.50	30.98	44.25
Fixed Carbon	62.85	63.40	33.02	47.10
Ash	6.06	6.12	6.01	8.57
Ultimate Analysis, %wt.				
Moisture	0.90	---	29.99	---
Carbon	80.95	81.69	45.71	65.29
Hydrogen	4.89	4.94	2.98	4.26
Nitrogen	1.58	1.59	0.68	0.97
Sulfur	0.68	0.69	0.66	0.94
Oxygen	5.84	5.89	13.97	19.96
Ash	6.06	6.12	6.01	8.57
Higher Heating Value, MJ/kg	31.0	33.6	16.5	25.2
(Btu/lb)	(13,350	(14,470)	(7,116)	(10,837)
Particle Size Distribution[b], μm				
D (v, 0.9)		58.9		129.4
D (v, 0.5)		19.4		46.4
D (v, 0.1)		5.3		8.7
Ash Composition, %wt.				
SiO_2		53.70		18.00
Al_2O_3		30.00		9.96
TiO_2		1.63		0.48
Fe_2O_3		6.95		9.96
MgO		0.90		6.05
CaO		1.23		20.90
MnO		0.02		0.07
Na_2O		0.67		9.55
K_2O		1.93		0.43
SO_3		0.90		20.60
P2O5		0.19		0.67
BaO		0.22		1.40
SrO		0.16		0.80
LOI		2.05		1.32
Total		100.55		99.19

[a]As Received

[b]The D(v,0.9), D(v,0.5), and D(v,0.1) values are the particle sizes where, respectively, 90%, 50%, and 10% of the particles, by volume, are less than the indicated particle size.

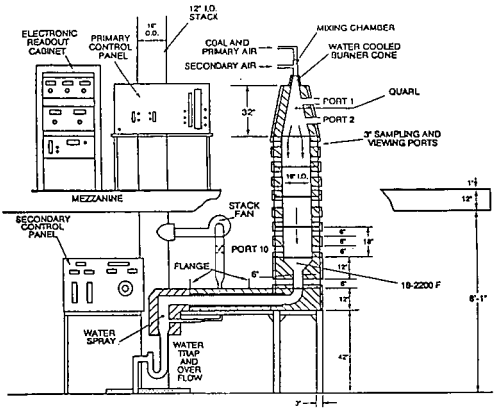

Figure 1. Down-fired Combustor

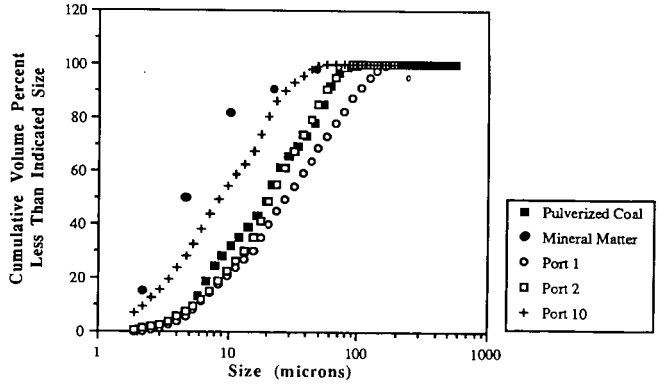

Figure 2. Comparison of PSDs of Elk Creek Coal, Mineral Matter, and Char-Ash Samples Collected from Ports 1, 2, and 10

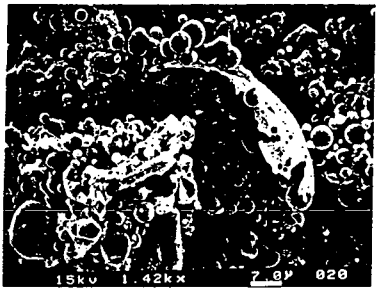

Figure 3. Elk Creek char-ash collected at Port 10.

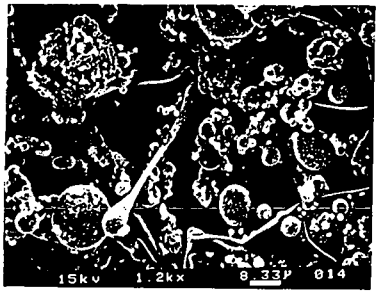

Figure 5. Beulah char-ash collected at Port 10.

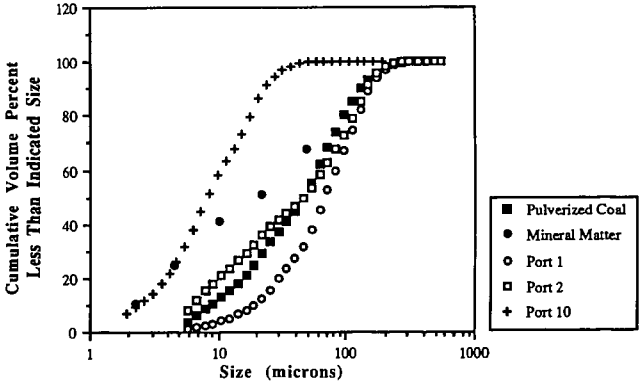

Figure 4. Comparison of PSDs of Beulah Coal, Mineral Matter, and Char-Ash Samples Collected from Ports 1, 2, and 10

A PILOT-SCALE STUDY OF THE FORMATION OF ASH DURING PULVERIZED LOW-RANK COAL COMBUSTION

John Hurley
University of North Dakota
Energy and Environmental Research Center
Grand Forks, North Dakota 58202

Keywords: char morphology, transmission electron microscopy, submicron ash

INTRODUCTION

In 1987 over 250 million tons of coal mined in the western-coal producing region of the United States was purchased by electric utilities (1,2). The goal of the utilities is to convert the chemical energy in the coal to electrical energy that can be sold at a profit. The most common conversion method involves pulverizing the coal and burning it in a boiler system. The steam produced is passed through a turbine which is used to turn an electrical generator. Unfortunately, because of the high temperatures present in a utility boiler, the ash formed during the combustion of the coal can cause a number of operational problems and can reduce the efficiency of the energy conversion process.

In an effort to delineate a portion of the process of ash formation during combustion of pulverized western U.S. low-rank coal, subbituminous coals from the Eagle Butte mine, WY, and the Sarpy Creek mine, MT, were burned in the Penn State down-fired combustor. Entrained particulate matter was collected at several stages of combustion. The particulates were analyzed by thermogravimetry, x-ray diffraction, computer-controlled scanning electron microscopy, and transmission electron microscopy (TEM) in order to discern changes in size and association of the inorganic matter during the combustion of the coal. Due to space limitations, the data and discussion presented here focus only on the TEM observations of the Eagle Butte coal as well as samples of the char and submicron ash particles produced during combustion.

EXPERIMENTAL

To properly understand the ash formation process, a knowledge of the time-temperature history and interactions of ash particles is required. Therefore, the Penn State down-fired combustor was designed for self-sustained combustion of pulverized coal in a nonrecirculating and nonswirling flame and to provide easy access for sampling at all stages of combustion. The combustor is described in depth elsewhere (3). It is illustrated in Figure 1.

Before firing with pulverized coal, the combustor was preheated on natural gas until the wall temperature profile approximated that encountered when firing the coal to be tested. During testing the coal feed rate was held at 200,000 Btu/hr which yielded a volumetric heat release rate of about 20,000 Btu/hr/ft^3. Particulate sampling commenced as soon as a stable temperature distribution occurred above the sampling point. Particulate samples were collected at three ports, the top (port 1), second

from the top (port 2), and from immediately above the accelerator at the bottom of the furnace (port 10). A four-stage multicyclone system, housed in a convective oven during sampling, was used to separate the particulates from the gas.

The morphologies of char and submicron inorganic particles were characterized by transmission electron microscopy (TEM). In order to allow analysis of particles that were included within a coal or char matrix, the samples were prepared by embedding them in LR White resin, then cutting ultrathin sections with the use of a Reichert Jung Ultracut E ultramicrotome. Only silver, gold, and violet sections were selected for analysis. The colors were an interference effect and indicated that the sections were between 0.08 to 0.2 μm thick (4). The TEM-STEM system used was a Phillips EM420 with a Link Systems 860 Series II x-ray analyzer.

RESULTS AND DISCUSSION

Coal Samples: TEM observations of ultrathin sections of the Eagle Butte coal showed that, in addition to larger irregularly shaped minerals, approximately one in four coal particles contained concentrations of small, high contrast inclusions with circular cross sections. A TEM photo of the edge of such a coal particle is shown in Figure 2. The inclusions occurred mainly in three distinct size ranges. The smallest particles had diameters of approximately 2 to 3 nanometers. They were evenly dispersed, although they were more easily visible in the thinner (lighter) portions of the coal section. A second size class of the inclusions had diameters between 20 and 30 nanometers. They did not appear to be as evenly dispersed across the coal particles as was the smallest size range. The largest size class was composed of particles with diameters greater than approximately 60 nanometers, although this size range was not completely distinct from the middle size range (i.e., there was some gradation between them).

The composition of the smallest high contrast inclusions was difficult to discern. Although the small inclusions strongly scattered the electron beam, electron diffraction was not practical because beam heating of the epoxy matrix caused the position of the particles to continually shift relative to the beam. Energy dispersive x-ray analysis of the smallest inclusions was also inconclusive because of the low signal to noise ratio in the EDS signal, although after counting times of several minutes, a signal did emerge in the EDS spectra of individual small particles or groupings. For the Eagle Butte coal the signal usually showed the presence of calcium, iron, and sulfur. Also, the source of the signals was obscured by the fact that calcium and sulfur, and possibly iron, are associated directly with the organic portion of the coal. Since the ultrathin section was approximately 100 nanometers thick, and the smallest particles were 2 nanometers in diameter, it was impossible to tell if the x-ray signal was emitted from organically associated elements or the particles. Although sodium and magnesium are also associated with the organic matrix, the detector may not have indicated the presence of those elements because they are present in lower concentrations, and the detector is not very sensitive to the K_α lines of those elements. In general, it was found that clear x-ray signals could only be obtained from particles that had diameters above several tens of nanometers, although some smaller particles gave strong x-ray signals if they were composed of high atomic number elements.

Because a strong x-ray signal from the small, high contrast inclusions was not clear, the possibility existed that the small inclusions were not inorganic. Friel and others have shown the formation of mesophase spheres upon heating of several

bituminous coals (5). The spheres they reported had the size and appearance of the medium size high contrast inclusions shown in Figure 2. However, several lines of evidence supported the conclusion that the small inclusions shown in Figure 2 were not similar to mesophase spheres. First, the coal had not been heated prior to analysis. Since mesophase usually forms on heating, one would not expect mesophase spheres to be present in the coal. However, some heating of the sample may have occurred in the TEM through absorption of energy from the electron beam. Second, the Eagle Butte and Robinson coals are subbituminous coals. Subbituminous coals do not usually form mesophase spheres upon heating. Third, and most convincing, a close examination of the boundary between the coal particles and the resin shows that some of the smallest particles have separated a small distance from the coal and reside in the resin. Mesophase spheres would not be expected to separate from the matrix.

Port 1 Samples: By the time the particulates reached the top port (port 1), the coal had undergone 50.8% burnout. The residence time of the particles in the radiant zone above that port was approximately 0.07 seconds. The maximum equilibrium temperature experienced by a nonreacting inorganic particle before sampling was approximately 1220°C.

Two main types of char particles were seen in the port 1 particulate samples: those that were highly vesicular and those that showed little internal structure. In general, the appearance of the char was essentially identical to the appearance of the char collected at port 2, so further discussion of char morphologies will be saved for the discussion of the port 2 chars.

Port 2 Samples: By the time the particulates reached port 2, the coal had undergone 96.3% burnout. The total residence time in the refractory lined portion of the combustor was approximately 0.2 seconds. The maximum equilibrium temperature reached by a nonreacting particle by the time it reached the sampling probe was approximately 1310°C. That temperature was reached immediately before the probe.

As in the case of the port 1 samples, two main types of char were evident in the ultrathin sections of the port 2 samples: highly vesicular particles and higher density particles that contained much less void space. Figure 3 is a 10,500x TEM photograph of a vesicular char particle. The thin walls of such particles suggest that they may fragment easily during combustion. The ash particles associated with such chars tend to be large globules lightly attached to either internal or external char surfaces. In addition to the large ash globules, the char particles contained high levels of the 3 and 30 nanometer particles seen in the coal. These particles are shown in Figure 4, which is a 82,000x TEM photograph of the char particle in Figure 3. The smallest inclusions underwent little change during the early stages of combustion.

The appearance of a high concentration of the small, high contrast inclusions shown in Figure 4 was an artifact of the difference in electron transmissivity of the char and the inclusions. In actuality, the thickness of the char surrounding the inclusions (the char is not obvious in the figure) was approximately 500 times the thickness of the smallest particles. Assuming that the particles had a density equal to that of quartz (2.6 g/cm^3), whereas the bulk char (i.e., carbonaceous and noncarbonaceous) had a density equal to the density of coal (1.3 g/cm^3), and that the average concentration of the particles in the char was equal to the concentration of particles shown in Figure 4 (a liberal assumption), the weight percent of the smallest inclusions can be, at most, 0.15% of the weight of the char. Assuming the concentration was the same in the coal and that the inclusions formed ash in a weight ratio of 1:1, then only about

2.5% of the weight of the ASTM ash was formed by the smallest inclusions. The mass concentration of the next larger class (30 nanometers) was approximately 0.5% of the char or 8.6% of the ash.

Figure 5 shows a TEM photograph (4,900x) of the second type of char particle, the type that showed much less void space than the highly vesicular char. Like the vesicular char, the two smallest size classes of high contrast inclusions were sometimes found in the more dense char particles. The inclusions in the higher density char collected at port 2, however, showed some coalescence which caused the distinctions between the size classes to become less pronounced. Unlike the smallest high contrast inclusions, the large globular particles of ash often associated with the highly vesicular chars were absent. This may have been because this type of char particle burned more slowly, so that particle coalescence was relatively slow and because the ash particles were shed from this type of char at a relatively high rate. Figure 5 is also interesting in that it shows two physical features of the ultrathin sections. First, grooves in the section, generally running right to left and sloping upwards slightly to the left, are caused by imperfections in the knife edge, most commonly remnants of previously cut sections. In addition, wrinkles in the ultrathin section can clearly be seen. The wrinkles generally run vertically or point toward the char section. The closeness of the wrinkles gives a visual indication of the ratio of length or width to thickness of the ultrathin sections. The typical dimensions of ultrathin sections are 0.7 mm long and 0.1 μm thick, so the length to thickness ratio is approximately 7000 to 1. The length to thickness ratio of writing paper is approximately 4000 to 1.

Port 10 Samples: By the time the particulates reached the sampling probe at port 10, the coal had undergone 99.8% burnout. The total residence time in the refractory lined portion of the combustor was approximately 2.4 seconds. The equilibrium temperature of a nonreacting particle at port 10 was approximately 1055°C.

Although uncommon, some char particles were still evident in the port 10 samples. Only the more dense char particles were seen however, indicating that the more vesicular char particles had burned out. Figure 6 is a TEM photograph (10,500x) of a portion of a char particle showing how the small, high contrast inclusions have melted. In some instances the particles coalesced to form particles with diameters in the 0.1 μm range. In other cases, the melted particles appeared to have flowed through pores within the char. The longer chain of flow regions running left to right across the photograph contained mostly iron. The large particle at the right edge of Figure 6 contained high concentrations of aluminum and silicon, with smaller amounts of nickel, chromium, and iron (possibly stainless steel). As was the case with the more dense char particles collected at port 2, no large globules of ash were seen at the surface of this type of char.

CONCLUSIONS

TEM observations of the coals indicated two main types of char form. One type was highly vesicular and burned out before the other more dense char. The thin walls of the highly vesicular char particles suggested that they may fragment easily, leading to the formation of several ash particles per char particle. However, the relatively few ash globules associated with the surfaces of the denser char particles indicated that less coalescence and more rapid shedding of ash particles occurred from the denser char than from the more vesicular char. Since the two chars most probably formed from different maceral types, a coal containing higher concentrations of the

maceral that forms the higher density char may produce more and smaller ash particles per coal grain than a coal having lower concentrations of the maceral type.

Approximately one in four coal particles contained concentrations of small, high contrast inclusions with circular cross sections. The inclusions fell into three size categories: 2 to 3 nanometers, 20 to 30 nanometers, and greater than 60 nanometers. EDS data indicated that the inclusions were composed primarily of calcium, sulfur, and iron, although the data was not conclusive. The inclusions were believed to be inorganic particles rather than organic regions such as mesophase. Calculations showed that, at most, 11% of the ash could be formed from the particles in the smallest two categories. The assumptions in the calculations were very liberal, so the actual weight was believed to be no more than 1%, within the range of the weight of fume produced during coal combustion. However, a great deal of coalescence of the inclusions occurred in later stages of particle combustion, so the importance of the inclusions in fume formation was not clear.

REFERENCES

1. U.S. Department of Energy, "Coal Production 1987", DOE/EIA0118, p 29 (1988).

2. U.S. Department of Energy, "Coal Distribution January/December 1987", DOE/EIA0125 (1988).

3. Hurley, J.P., "A Pilot-Scale Study of the Formation of Ash During Pulverized Low-Rank Coal Combustion", Ph.D. Thesis, The Pennsylvania State University (1990).

4. Peachey, L.D. "Thin Sections I. A Study of Section Thickness and Physical Distortion Produced During Microtomy", Journal of Biophysical and Biochemical Cytology, 4, 3, 233-245, 1958.

5. Friel, J.J., Mehta, S., Mitchell, G.D., Karpinski, J.M. "Direct Observation of the Mesophase in Coal", Fuel, 59, 610-616, 1980.

6. U.S. Department of Energy, "Combustion Inorganic Transformations", report for the period April 1988, to June 1989, DEFC2186MC10637 (1989).

ACKNOWLEDGEMENTS

Most of the funding for the research was provided by the U.S. Department of Energy under the Combustion Inorganic Transformations project, contract DEFC2186MC10637, Phillip Goldberg, COTR; and the Commonwealth of Pennsylvania under the Coal/Water Slurry Program. In addition, the author would like to thank Harold Schobert of Penn State and Steven Benson of the University of North Dakota Energy and Environmental Research Center for their support.

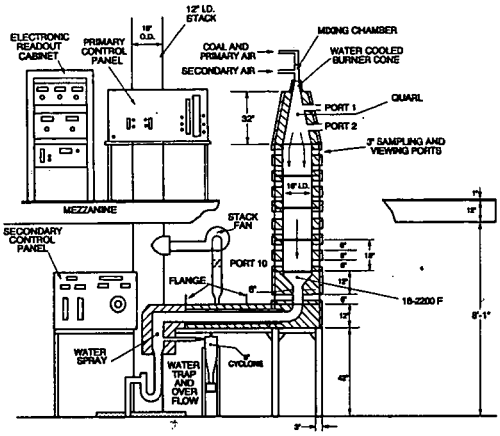

Figure 1. The Penn State down-fired combustor.

Figure 2. TEM photograph of an Eagle Butte coal particle containing high levels of high contrast inclusions.

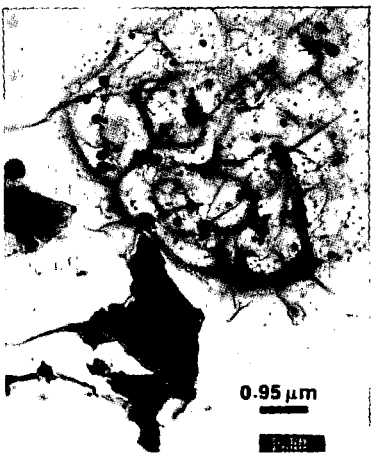

Figure 3. TEM photograph of vesicular Eagle Butte char particles showing large numbers of ash globules associated with both interior and exterior char surfaces.

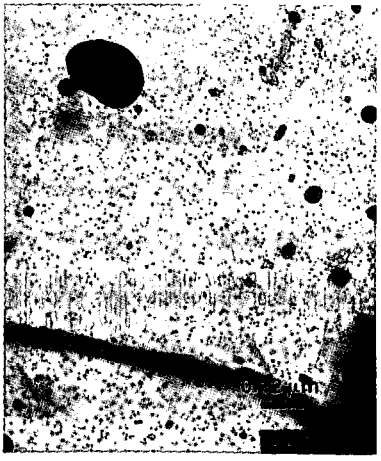

Figure 4. TEM photograph of the char particle shown in Figure 3 illustrating the unchanged nature of the 3- and 30-nanometer diameter contrast inclusions.

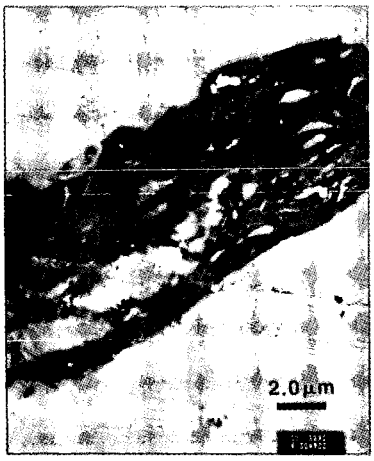

Figure 5. TEM photograph of a high density Eagle Butte char particle collected at port 2.

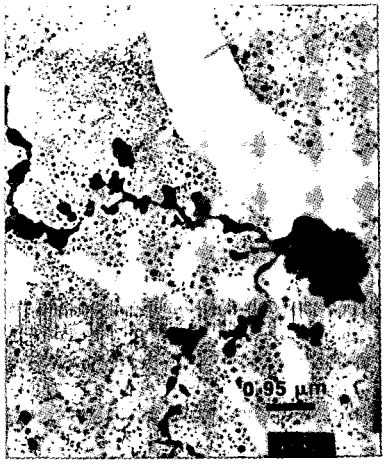

Figure 6. TEM photograph of a frozen flow of molten ash within pores in an Eagle Butte char particle collected at port 10.

THE FORM OF OCCURRENCE OF BASIC ELEMENTS IN COAL AND THEIR BEHAVIOUR DURING COMBUSTION

Anup Shah, F. E. Huggins, Naresh Shah, and G. P. Huffman
CFFLS, University of Kentucky
233 Mining & Mineral Resource Building
Lexington, KY 40506-0107

Keywords: Coal, Ash, Combustion

INTRODUCTION:

The basic elements in coal ash (alkalies,Ca,Fe) exhibit an interesting behaviour during combustion, which is closely related to the form of occurrence of these elements in the parent coal. The objective of this paper is to elucidate their evolution during combustion processes of variable time and temperature. Qualitative determinations are made from the data obtained from Computer Controlled Scanning Electron Microscopy (CCSEM), X-ray Absorption Fine Structure (XAFS) and Mössbauer spectroscopies.

Some of the data and the description of the techniques used in this paper are summarized in several publications (1-8). The main goal of this paper is to discuss some systematic trends in the behaviour of calcium, iron and the alkalies during high temperature coal combustion. It needs to be emphasized that our discussion deals only with high temperature (~1600 to 2000 K) pulverized coal combustion, and is not relevant to fluidized bed combustion.

EXPERIMENTAL PROCEDURES:

The CCSEM method measures the areas of cross-section and the energy-dispersive spectra for at least 1000 different particles in a random, polished section of the coal embedded in epoxy. The data is then reduced to derive the overall mineralogy and semi-quantitative size-distribution of individual mineral categories (9). CCSEM techniques for ash are similar to those for the coal, except that the particles are not embedded in epoxy but are mounted on Nucleopore (0.2 micrometer) filters by a process of filtration in triply-distilled acetone. The amount of material filtered is adjusted to give an optimum density of particles on the filter paper. The data reduction techniques for ash samples are similar to those used for coal minerals analysis (CMA) but the sorting program is based on the intensity of the energy-dispersive X-rays from the three most abundant elements, rather than on specific phases (9).

XAFS is used to examine specific elements and to obtain information on the bonding and structure of that element in the material at dilute concentrations (~0.1 to 1.0%). By comparing with standard materials, the phase in which the element exists is also identified.

Mössbauer spectroscopy complements the CCSEM technique by identifying the form of iron in a coal or ash. With this technique it is possible to measure the relative abundance of the major iron-bearing minerals in complex samples.

Furthermore the Mössbauer technique also provides a direct measure of the pyritic sulfur content.

RESULTS AND DISCUSSIONS:

The set of coals being investigated here are (low-rank coals) Beulah, Eagle Butte and San Miguel, (bituminous coals) Upper Freeport, Kentucky #9, Kentucky #11, Illinois #6 and (Australian brown coal) Loy Yang. These coals were combusted in different scale furnaces at Physical Sciences, Inc., M.I.T. and the University of Arizona (UA). The UA samples were collected on filter from different impactor plates of varying particle diameter.

Mössbauer data show that most of the iron in these coals is in the form of pyrite, except for Upper Freeport, in which 20% of the iron is contained in clay and siderite, and Loy Yang coals and that the pyrite contents of these coals are much higher than that of the bituminous coals. Unlike the U.S. coals, the iron in the Australian coal appeared to be present as iron oxyhydroxide (FeOOH).

If pyrite is contained in a burning coal particle that also contains clay minerals and/or quartz, it is likely to react with these minerals to form an aluminosilicate slag droplet. Isolated pyrite, either liberated or contained in a coal particle transforms into pyrrhotite by devolatilization which then undergoes exothermic oxidation, presumably to a molten Fe-O-S phase (6,7). Iron is found predominantly present as magnetite and as Fe^{+3} in glass in the ash samples of these coals. For these coals, the partitioning between iron oxide and glass appears to be simply related to amount of pyrite in the mineral matter. On this basis one would predict that the amount of iron as oxide should decrease in the order Illinois #6 > Beulah lignite > Kentucky #11 > Upper Freeport > Kentucky #9 > Eagle Butte, which is exactly the order in which iron is partitioned between iron oxide and glass in the ash samples. One would expect that how the pyrite is associated with other minerals would also play a role in determining this order, but for this particular sequence of coals, such association is apparently not an important factor or it is also dependent on the relative amount of pyrite in the sample to a first approximation (Table 1).

XANES spectra of calcium in Beulah lignite and Eagle Butte coals are very similar to the ones measured for other low-rank U.S. coals [10,11] and are characteristic of calcium bound through carboxyl groups to macerals (Fig. 1). XANES of calcium in San Miguel Texas lignite (Fig. I) also resembles that of the two low rank coals. XANES of calcium in Illinois #6 coal resembles the sum of XANES of calcite and that of a coal with carboxyl-bound calcium.

In the ash samples obtained from low rank coals, the predominant compositional classes are permutations of the three most abundant elements: Ca, Al and Si, except for the finest impactor plate where many Ca and Na sulfate particles are also present. Figures 2 show Ca-Si-Al triangular plots for each of the impactor plates of Beulah ash sample. Here each point represents an ash particle identified by the CCSEM analysis as containing > 80% Ca + Si + Al. The composition of each particle, normalized to three elements, is then plotted on the ternary diagram. The plots show a clear dependency of compositional clustering on size. These trends can be interpreted as indicating a size dependency for the reaction between CaO fume, derived from the carboxyl-bound calcium, and the kaolinite in the coal. The smaller the reactant particle, the

more probable is the formation of a Ca-Al-Si phase, and the less probable is the existence of separate Ca-rich or Al-Si particles. The fine particle compositions indicate the formation of calcium substituted glass phase. The XANES spectra (Fig. 3) are quite similar to that attributed to calcium in aluminosilicate glass [5] and indicate that the amount of CaO or $CaSO_4$ in ash is relatively minor (<10 vol%). Hence, the broader range in the Ca-Al-Si cluster observed for the coarser particles must represent the compositional range of Ca-Al-Si glass rather than mixed CaO-Al-Si particles. It should also be noted that there is a tendency for Ca enrichment near particle surfaces.

The principal alkali species in lignite is Na, believed to be molecularly dispersed through the maceral and bonded to the carboxyl group, like calcium. Sodium may also be present as hydrated Na^+ ions in the moisture associated with low-rank coals and this is probably the case with Loy Yang coal, even though appreciable NaCl was noted in the CCSEM analysis for the dried sample of this coal. Potassium is significant only for the four bituminous coals and San Miguel lignite. K in these coals is almost entirely present as illitic clays. Some KCl was noted in the CCSEM analysis of Loy Yang coal.

The behaviour of alkalies during combustion is strongly dependent on their form of occurrence in the parent coal. K, which is present as illite, is likely to remain with the aluminosilicate particle and form a molten slag droplet. Confirmed by potassium XANES (Fig.4) obtained from various ash samples, partial melting occurs because of eutectic regions in the K-Si-Al phase diagram [8,12]. The aluminosilicate glass produced by melting illite yields precisely this type of potassium XANES spectrum [8,13]. The composition of these molten particles is similar to that of the parent illite, as illustrated in Figure 5. Figure 4 shows the comparison of potassium XANES spectra of ash samples from different coals and all appear characteristic of potassium in glass. The subtle difference between the Eagle Butte spectra and the other spectra most likely reflects either its different bulk ash composition (richer in Ca, poorer in Fe) or a different mode of occurrence for potassium in the original coal.

The CCSEM analysis of Beulah lignite ash shows an abundance of sodium-aluminosilicate particles (Fig. 6). In contrast to the similar plot for calcium rich particles, the Na-rich particles cluster in the center of the Na-Al-Si ternary plot. The composition of this cluster of points corresponds to the phase nepheline ($NaAlSiO_4$). This phase must have been formed by reaction between kaolinite and Na cations volatilized in the combustion of the coal. This is an example of the efficiency of aluminosilicates derived from clays for the fixation of alkali elements in coal ash. This refutes the suggestion that alkali elements can be readily volatilized from clays or other aluminosilicates during combustion, at least to 1500 K under oxidizing conditions.

SUMMARY:

Iron (pyrite) either reacts with clay minerals to form aluminosilicate slag or devolatizes and undergoes oxidation to form oxides and sulfides, depending on whether it is associated with clay and quartz or isolated. Calcium is molecularly dispersed in coals and is bonded to carboxyl groups in the macerals. On combustion it forms CaO which may further react with clays to form aluminosilicate glass. Potassium in bituminous coals is contained in illite which melts and forms aluminosilicate glass. Finally, sodium which is believed to be molecularly dispersed in the macerals, volatilizes and reacts with clays

to form aluminosilicate glass with compositions corresponding to that of nepheline.

REFERENCES:

1. F. E. Huggins, N. Shah, G. P. Huffman, R. G. Jenkins, F. W. Lytle, and R. B. Greegor, Fuel, 67, 938-942 (1988).

2. G. P. Huffman, F. E. Huggins, and N. Shah, "EXAFS Spectroscopy: A New Technique for Investigating Impurity Elements in Coalthat Control Slagging and Fouling Behaviour", Engineering Foundation Conference on Mineral Matter and Ash in Coal, Santa Barbara, CA, 1988, Eds., K. S. Vorres and R. W. Bryers, to be published by Elsevier.

3. F. E. Huggins, G. P. Huffman, and A. A. Levasseur, "Ash Deposits from Raw and Washed Coals", ibid.

4. F. E. Huggins, G. P. Huffman, A. A. Levasseur, ACS Division of Fuel Chemistry Preprints, Vol. 33, No. 2, 73-80 (1988).

5. G. P. Huffman, F. E. Huggins, A. A. Levasseur, F. W. Lytle, R. B. Greegor, and A. Mehta, Fuel, 68, 238-242 (1989).

6. G. P. Huffman, F. E. Huggins, A. A. Levasseur, O. CHow, and S. Srinivasachar, Fuel, 68, 485-490 (1989).

7. S. Srinivasachar and A. Boni, Fuel, 68, 829 (1989).

8. G. P. Huffman, F. E. Huggins, R. W. Shoenberger, J. S. Walker, F. W. Lytle, and R. B. Greegor, Fuel, 65, 621-632 (1986).

9. G. P. Huffman, F. E. Huggins, N. Shah, and A. Shah, "Behaviour of Basic Elements During Coal Combustion", to be published in Progress in Energy and Combustion Science.

10. F. E. Huggins, G. P. Huffman, F. W. Lytle, and R. B. Greegor, "An EXAFS Investigation of Calcium in Coal", Proceedings of International Conference on Coal Science (Pittsburgh, PA), 679-682 (1983).

11. G. P Huffman, and F. E. Huggins, "Analysis of the Inorganic Constituents in low-rank Coals", ACS Division of Fuel Chemistry, Preprints, Vol. 264, 159-174 (1984).

12. E. M. Levin, H. F. McMurdie and H. P. Hall, Phase Diagrams for Ceramists, Amer. Ceramic Soc., Inc., Columbus, Ohio, 1964.

13. C. Spiro, J. Wong, F. W. Lytle, R. B. Greegor, D. H. Maylotte, S. Samson, and B. Glover, Fuel 65, 327 (1986).

TABLE 1. - Mössbauer data for ash samples from University of Arizona combustor

Coal	%Fe Distribution of Iron among Phases			
	Hematite	Magnetite	Ferric glass	Ferrous glass
Illinois #6	-	84	16	-
Beulah Lignite	-	71	24	5
Eagle Butte	-	46	54	-
Kentucky #11	8	67	12	14
Upper Freeport	3	67	18	13

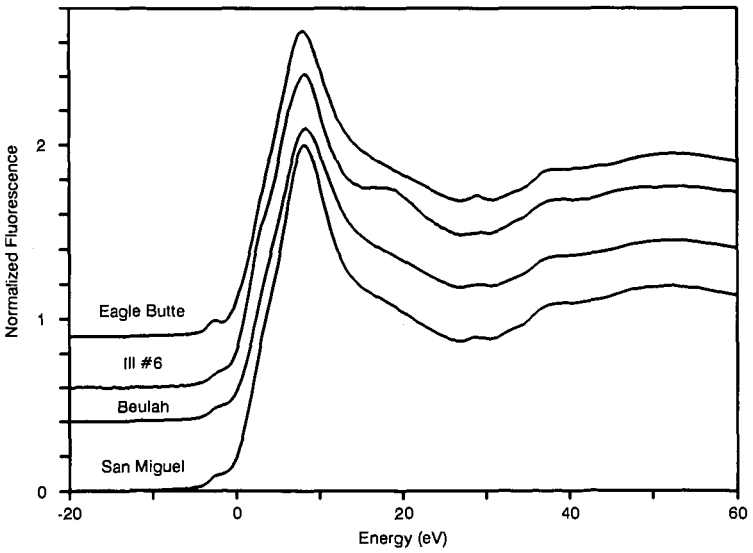

Figure 1. Ca XANES of high calcium PSI coals.

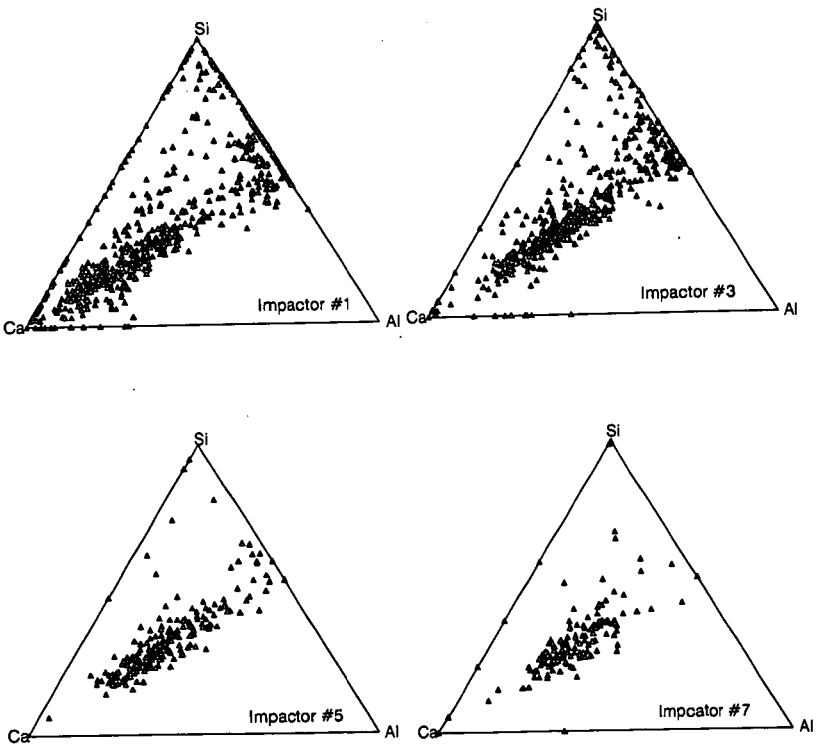

Figure 2. Ca-Al-Si triangular plots for Beulah lignite ash on different impactors in UA combustor. All particles contain Al+Si+Ca > 80%.

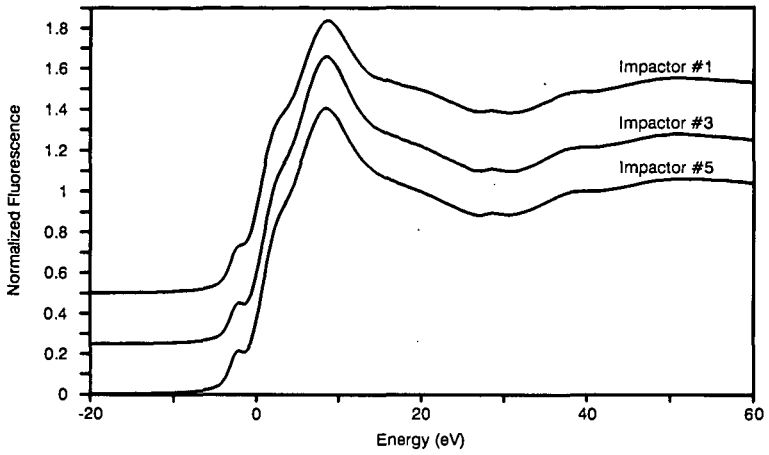

Figure 3. Ca XANES for Beulah ash from size segregated impactors of UA combustor

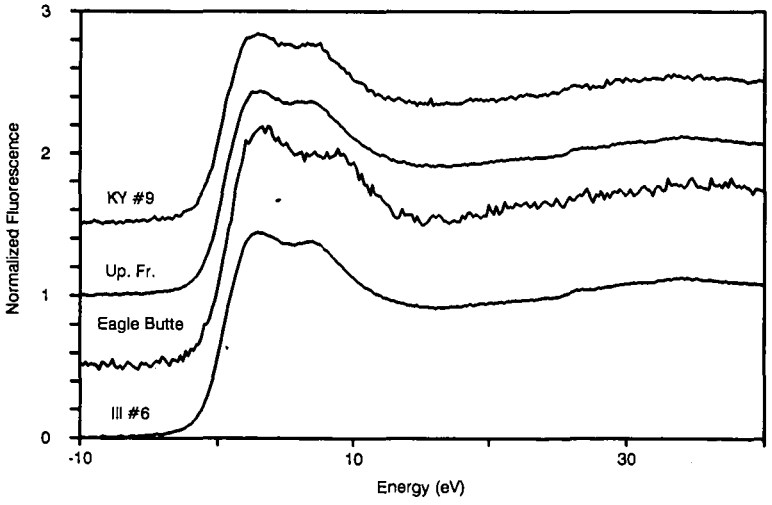

Figure 4. Potassium XANES of ash samples from MIT combustor.

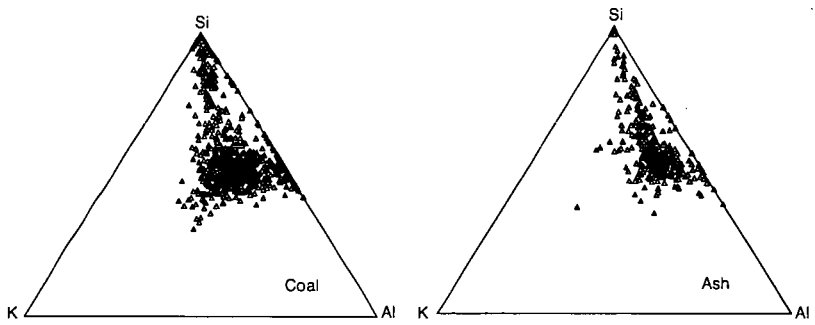

Figure 5. K-Si-Al triangular plots for Upper Freeport coal and ash

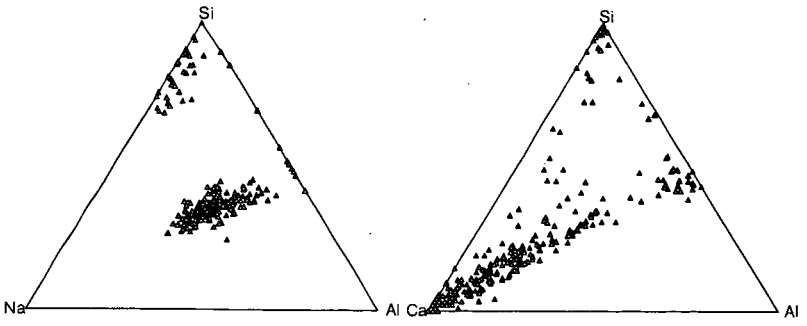

Figure 6. Triangular plots for Beulah ash from PSI drop tube furnace.
All particles contained Al+Si+Na/Ca > 80%.

FLY ASH DEVELOPMENT FROM SODIUM, SULFUR AND SILICA DURING COAL COMBUSTION

D.K. Ludlow and T.A. Erickson
Department of Chemical Engineering
University of North Dakota
Grand Forks, North Dakota 58203

S.A. Benson
Energy and Environmental Research Center
University of North Dakota

Introduction

The formation of ash during the combustion of coal is a very complex environmentally dependent reaction. Significant parameters include the combustion conditions and association and relative sizes of the inorganic constituents present. During pulverized coal combustion the inorganic constituents undergo chemical and physical transformations in the flame and during gas cooling to form inorganic vapors, liquids, and solids. These chemical and physical transformations dictate the size and composition distribution of the final ash product. Previous studies of the final ash product (fly ash) indicate that the size distribution is usually bimodal (Sarofim, 1977; Flagan and Friedlander, 1978; and Damle, 1982). The submicron size particles have an average diameter of about 0.1 microns. These small particles form as a result of the homogeneous condensation of flame volatilized species. These flame volatilized species may also condense heterogeneously on the surfaces of larger particles. The larger size fraction of the particles, referred to as the residual ash, are largely a result of the minerals present in the coal. The size and composition distributions of the larger particles are a result of the transformations and interactions of the minerals and other inorganic components in the coal. Physical processes such as coalescence, fragmentation of minerals and char, and shedding of inorganic components occur which effect the properties of the ash.

A furfuryl alcohol polymer containing Na, S, and SiO_2 was used to study the effect of combustion temperature on the formation of fly ash particles. Of specific interest to low-rank coal combustion systems is the interaction between sodium, sulfur and silica to form low melting point phases that can cause deposition problems (Jones, 1987). In order to identify key processes associated with the formation of ash in combustion systems carefully controlled combustion experiments using a laminar flow furnace system were performed. A precisely formulated synthetic coal/mineral mixture was produced, combusted in a laminar flow furnace, and the composition and size of the ash was examined. The synthetic coal was formulated to include only a specific composition of inorganic species in a specific form and size to facilitate the examination of the effects of combustion conditions on the final ash particles formed.

Experimental Approach

A furfuryl alcohol polymer was catalyzed with p-toluenesulfonic acid as outlined by Senior (1984) and modified by Erickson (1990). The coal was synthesized to include 10% by weight SiO_2 in the crystalline form of quartz. Computer Controlled Scanning Electron Microscopy (CCSEM) (Steadman et.al., 1990) and Inductively Coupled Plasma (ICP) analysis determined the synthetic coal to contain 9.3 and 11.3 % by weight

quartz, respectively. CCSEM analysis determined the quartz to range in diameter from 1 to 10 microns with the average size, based on a volume percent basis, to be 5.06 microns. Sodium (5% by weight) was added to the coal in the form of sodium benzoate in an alcohol solution. The solution was then allowed to evaporate off with the sodium remaining attached to the coal. This method gives a form of sodium which is easily volatilized (Mills, 1989) similar to the ease of the volatilization of sodium in low rank coals. Sublimed sulfur was added extraneously to comprise 1% by weight. The final coal was ground in a ball mill and sized to 46-106 microns with a sonic sieve.

The synthetic coal was combusted in a laminar flow furnace at 900, 1100, 1300, and 1500°C. The residence time of the coal was approximately 1.4 seconds with slight variations dependent upon temperature. After exiting the furnace the fly ash was cooled instantly with a quench probe and collected on a bulk filter.

After combustion the samples were mounted on a carbon plug with double stick tape, carbon coated and studied with the use of a JEOL Scanning Electron Microscope/Microprobe (SEM/EMPA). The SEM/EMPA is equipped with an ultra-thin window energy dispersive detector with a Tracor Northern 5600 processing system. The system also has the abilities of a Tracor Northern 8500 image analysis system. These three tools together create a flexible mechanism for determining the composition, size, and various characteristics of fly ash samples.

Results

Figures 1-4 show the fly ash formed at 900, 1100, 1300, and 1500°C, respectively (all four figures are at the same magnification). The particle size decreases with increasing combustion temperature. Virtually all of the particles are spherical in nature and were assumed to be for all subsequent calculations. Table 1 gives the average particle size of each of the samples. The particles were sized manually by randomly measuring 125 particles with the aid of the image analysis system. Figure 5 gives a graphical representation of the same data with the addition of: 1) the theoretical diameter of a fly ash particle assuming 100% coalescence of inorganics, and 2) the diameter of the original quartz prior to combustion. It should be noted that some of the particles at 900 and 1100°C show some evidence of either cenosphere formation or unburned carbon in the center. The combustion of the synthetic coal appears to be dominated by coalescence, i.e. formation of one fly ash particle per coal particle, at lower temperatures as shown in Figure 6, and by fragmentation followed by coalescence at higher temperatures, shown in Figure 7.

Figure 8 is a high magnification photo of the fly ash combusted at 900°C. On the surface of the larger grey particles are very small white moieties. The same phenomenon appears in all four samples but is most abundant and largest in size at the lower temperatures. Due to the small size of the moieties it is impossible to get an accurate chemical analysis of them with the SEM/EMPA (the excitation volume of the electron beam is 8 microns in diameter as compared to the submicron size of the moieties). Table 2 compares the grey area composition, moiety composition, and bulk area composition. It is important to note that SEM/EMPA analysis of the moieties includes analysis of a substantial amount of the fly ash behind and surrounding it. These analyses are averages of 3 to 5 samplings of each of the described areas. From these analyses it appears that the moieties are sodium sulfates which homogeneously condensed and impacted onto the Na-rich silicate particles.

SOLGASMIX (Erikkson and Rosen, 1973), a theoretical program based on minimization of Gibbs free energy, predicts that the abundance of sodium sulfates will decrease with increasing temperature. This corresponds to the observed results, with fewer and smaller sodium sulfate particles found at higher temperatures.

Conclusions

The formation of fly ash in the coal studied was dominated by coalescence at low temperatures (900 and 1100°C) and by fragmentation followed by coalescence at higher temperatures (1300 and 1500°C). The fragmentation during combustion may be caused by: 1) thermal breakup of the particle, 2) rapid combustion (explosion), 3) break up of pore structure, or 4) a number of other phenomena. There was increased formation of submicron sodium sulfates at lower temperatures while higher temperatures appeared to decrease both the size and abundance of the submicron sodium sulfate particles. At the higher temperatures, the sodium appears to interact with the silica to form sodium silicates.

References

Erickson, T.A., "The Fate of Flame Volatilized Sodium During the Combustion of Pulverized Coal in Reaction with Silica and Sulfur (Studied with the Aid of a Synthetic Coal)", Master Thesis, University of North Dakota, Grand Forks, N.D., 1990.

Erikkson, G., and Rosen, E., Chemica Scripta, 4, 193(1973).

Damle, A.S., Ensor, D.S. and Ranada, M.B., Aerosol Science and Technology, Vol. 1, p.119, 1982.

Flagan, R.C., and Friedlander, S.K., "Particle Formation in Pulverized Coal Combustion", Recent Developments in Aerosol Science, Ed. D.T. Shaw, Wiley, New York, Ch. 2, 1978.

Jones, M.L., and Benson, S.A., "An Overview of Fouling and Slagging in Low-Rank Coals", Conference on the Effects of Coal Quality on Power Plants, EPRI, Atlanta, Georgia, October 15-17, 1987.

Mills, M., "Sodium Release from Solids in Flames Studied using Laser Induced Fluorescence Spectroscopy", Chemistry Department, University of North Dakota, Grand Forks, N.D., 1989.

Sarofim, A.F., Howard, J.B., and Padia, A.S., Combustion Science and Technology, Vol. 16, p. 187, 1977.

Senior, C.L., "Submicron Aerosol Production During Combustion of Pulverized Coal", Ph.D. Thesis, California Institute of Technology, 1984.

Steadman, E.N., Zygarlicke, C.J., Benson, S.A., and Jones, M.L., "A Microanalytical Approach to the Characterization of Coal, Ash, and Deposit", Seminar on Fireside Fouling Problems, Brigham Young University, Provo, Utah, 1990.

Table 1

Average Particle Size of Fly Ash Formed From Synthetic Coal

Temperature(°C)	Diameter (microns)
900	27.0
1100	27.7
1300	17.6
1500	8.5

Table 2

Particle Surface Composition, Elemental %'s

Temperature	Bulk Composition			Grey Area Composition			White Moiety Composition		
(°C)	Na	S	Si	Na	S	Si	Na	S	Si
900	24	5	61	19	1	80	39	18	43
1500	80	1	19	5	0	95	6	1	93

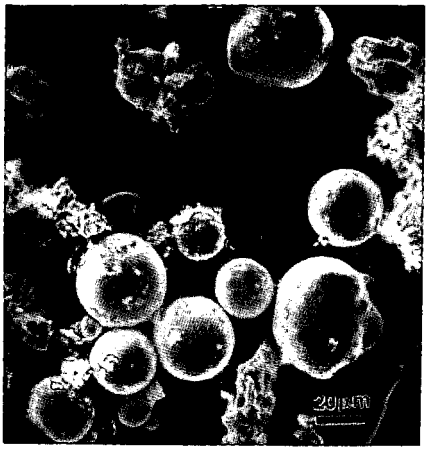

Figure 1 Fly Ash Particles Formed at 900°C, 500x.

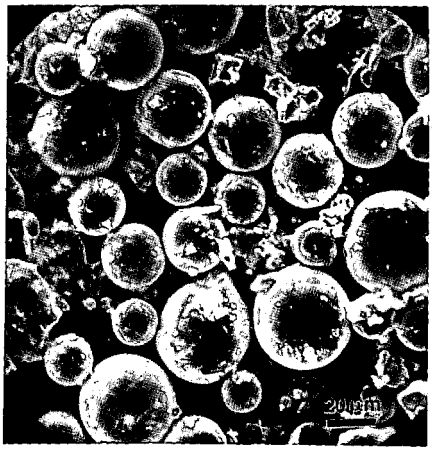

Figure 2 Fly Ash Particles Formed at 1100°C, 500x.

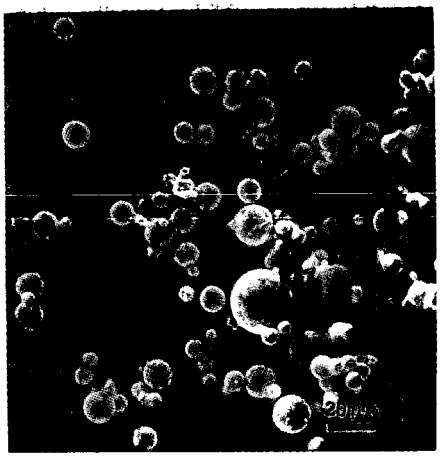

Figure 3 Fly Ash Particles Formed at 1300°C, 500x.

Figure 4 Fly Ash Particles Formed at 1500°C, 500x.

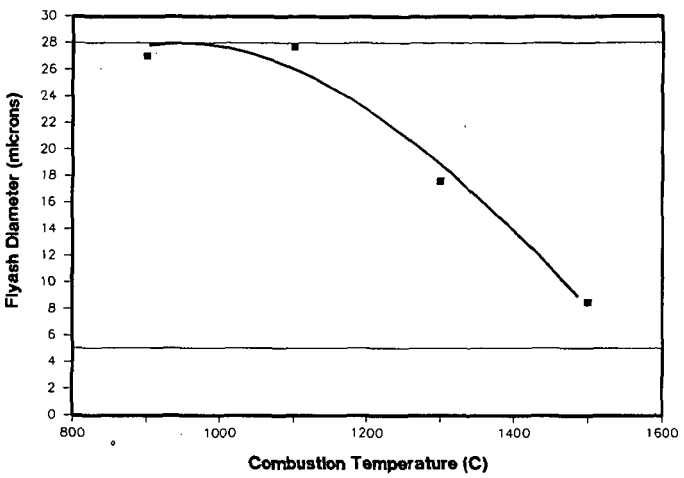

Figure 5 Particle Size versus Combustion Temperature. (upper line represents 100% coalescence and lower line represents original size of mineral grains)

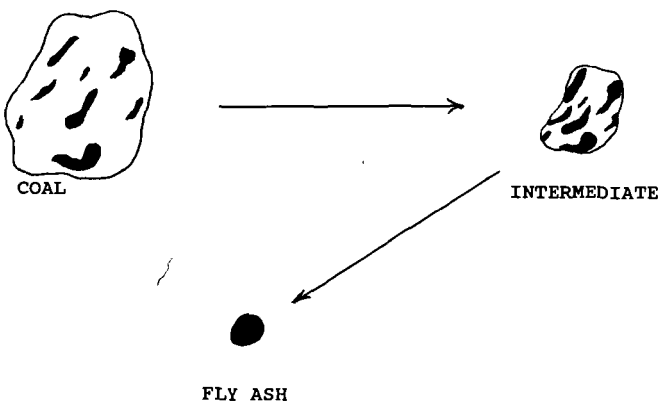

Figure 6 Diagram of the Formation of Fly Ash Particles Through Coalescence.

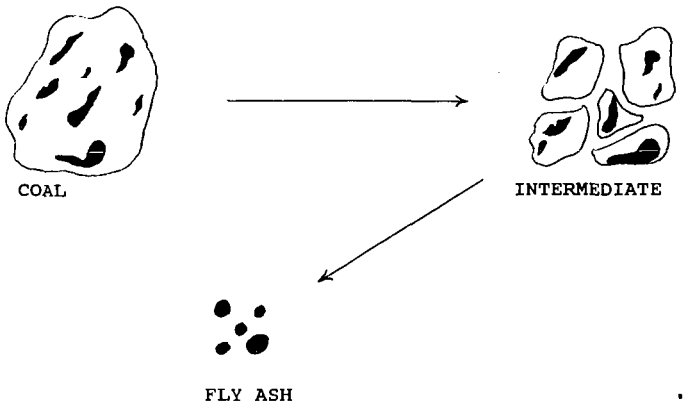

Figure 7 Diagram of the Formation of Fly Ash Particles Through Fragmentation.

Figure 8 High Magnification Photo of 900°C Fly Ash Particle Surface.

EFFECTS OF RESIDUAL CARBON ON DEPOSITION IN COAL-FIRED GAS TURBINES

Ronald G. Logan and Matthew J. Scanlon

Morgantown Energy Technology Center
United States Department of Energy
P.O. Box 880
Morgantown, WV 26505

and

Richard A. Wenglarz

Allison Gas Turbines
General Motors Corporation
P.O. Box 420
Indianapolis, IN 46206

ABSTRACT

The influence of residual carbon in coal ash on ash deposition at coal-fired gas turbine conditions has been investigated. Measurements of sticking coefficients (fraction of impacting ash particles that adhere) and ash deposit adhesion strength in a laminar-flow drop tube furnace indicate that high carbon levels in ash can decrease sticking fractions. However, high carbon levels also increased the adhesion strength of ash deposits, making them more difficult to remove. Possible mechanisms for the involvement of carbon in ash deposit formation are presented.

INTRODUCTION

The U.S. Department of Energy is currently sponsoring a program to develop direct coal-fired gas turbines. Direct coal-fired gas turbines are potentially attractive alternatives to conventional steam cycle electric power generation because of their higher efficiencies. However, the high mineral matter content of coal creates problems with deposition, erosion, and corrosion of turbine components. Ash deposits are formed in turbines by the adherence of ash particles to the surfaces of stators and blades. During combustion, components of the coal ash become molten and thus readily adhere to turbine components upon impaction. The tendency of various coals to form ash deposits during combustion is a complex function of many variables including the ash chemistry, gas temperature and pressure, gas velocity, and the temperature of the turbine components. Previous test results from this laboratory[1-2], from bench-scale combustor tests[3], and from tests on a gas turbine simulator[4-5] have indicated that unburned carbon in coal ash may affect the degree of deposit formation. The present study was initiated to further explore the effects of carbon on mechanisms of ash deposit formation.

Particulate in the products of combustion (POC) streams entering direct coal-fired gas turbines will probably contain much higher fractions of

unburned carbon than for past coal experience such as in boilers. The lower ash levels for potential turbine fuels compared to boiler fuels result in higher percentages of carbon in the POC for a given combustion efficiency. Figure 1 illustrates this effect for 99% carbon burnout of a solid fuel such as coal. This figure indicates that unburned carbon would constitute about 50% of the POC particulate for a 1% ash coal turbine fuel, but only about 15% of the POC particulate for a coal boiler plant using a 5% ash coal.

Past tests have indicated a significant effect of unburned carbon on deposition; however, data from different tests appear to be contradictory. Tests associated with an early coal-fired gas turbine program[4] showed that the presence of relatively coarse incandescent (burning) coal particles in the gas stream increased the rate and density of deposit buildup. On the other hand, more recent cascade tests at General Electric with low ash coal water fuels showed much lower deposition rates occurred when the combustion efficiency was reduced and unburned carbon levels were high[1-3]. Analyses of data from tests at General Motors Allison Division[3] resulted in the hypothesis that increased carbon levels could increase deposition at the highest temperature locations in the turbine flowpath. This was attributed to unburned carbon producing larger particle sizes and higher delivery rates, higher particle impact and surface temperatures, and locally reducing conditions with relatively low melting ash phases. For the lower temperature regions of the turbine flowpath, it was hypothesized that carbon could reduce deposition by eroding previously retained ash material on the surfaces.

The experiments described in this paper were designed to assess the effects on deposition of relatively high POC carbon-ash-ratios for conditions representative of direct coal-fired gas turbines. The data are expected to be useful in identifying parameters that need to be controlled to alleviate deposition in coal-fired gas turbines.

EXPERIMENTAL

Experiments were performed in an electrically heated, laboratory scale drop-tube combustor designed to operate at temperatures up to 1400°C. This combustor[7], the Combustion/Deposition Entrained Reactor (CDER), is shown in Figure 2. Approximately 3-10 grams per hour of -400 mesh pulverized coal was entrained in 5 standard liters per minute (lpm) of air from a circulating feeder. A water-cooled injection probe was used to introduce this particle-laden flow into the combustor where it mixed with 25 lpm of preheated primary air. The coal feed rates used in these experiments allowed long sampling times during deposition tests which resulted in excellent time resolution of the growth of the ash deposits. The residence time of coal particles in the combustor were controlled by changes in the total gas flow, or the position of the injection probe. In tests reported here, the residence time was varied over a range of 440 to 640 milliseconds by adjusting the position of the injection probe. This produced ash with a range of carbon levels from approximately 10 to 50%. The tests were conducted at gas temperatures of 1100 and 1200°C, which is representative of current and future industrial gas turbine inlet temperatures.

Experiments in the CDER were designed to simulate deposition on the leading edge of a gas turbine airfoil where the primary mode of particle delivery to the surface of the airfoil is inertial impaction. At the exit of

the combustion zone the products of combustion were accelerated through a 3.2 mm diameter nozzle, creating a jet which impinged on a flat, 12.7 mm diameter platinum disk. The resultant jet velocity of approximately 300 m/s is within the range expected in the first stage of a gas turbine. The platinum target was positioned 6 mm below the nozzle aperture (Figure 3). This nozzle/target configuration was developed according to procedures for inertial impactor design to insure that all particles larger than approximately 0.5 microns are forced by inertia to impact the target, as would occur on the leading edge of a gas turbine stator or blade. Platinum was used as an inert target material to eliminate surface reactions peculiar to a specific blade material which could affect the experimental results. The target could be cooled from the underside by an opposing jet of cooling air. Thus, a range of target temperatures were obtainable by varying the cooling air flow rate. The target temperature was measured throughout each test using a two-color optical pyrometer which monitored the temperature of the backside of the platinum target.

Sticking coefficients were measured by first passing the jet of exhaust through a filter to determine the total particle mass arrival rate. Gas flow through the filter (which was positioned in the same location as the target) was controlled via a vacuum pump and a mass flow controller. The rate of deposit buildup was determined by placing a target of known weight under the jet, and then withdrawing the target after a specified exposure period (usually ten minutes) to measure the weight gain. The sticking coefficient was calculated as the ratio of the weight gain of the target to the total mass arriving at the target (determined by the filter sample). The filter samples were quenched with cold air, resulting in unburned carbon in the samples. Since carbon was burned out of the deposits, filter samples were analyzed for carbon content to correct the ash arrival rate used to calculate the sticking coefficient.

Deposit adhesion strength (or shear strength) was measured using a device shown in Figure 4. The device consists of an alumina rod attached to a translation stage and linear actuator. A load cell is used to measure the force required to dislodge deposits from the targets using the blunt tip of the rod. The device is attached to the CDER, and the measurements are conducted at temperature. The measurements are in pounds of force, and are adjusted for the area of contact between the deposit and target to produce units of pounds per square inch.

DISCUSSION

The coal used in these tests was an Arkwright Pittsburgh bituminous containing approximately 7% ash and 2% sulfur. Ultimate and elemental analyses for the coal are shown in Table 1. Figure 5 shows measurements of sticking coefficients as a function of carbon levels in the ash at two gas temperatures. The data points are averages of a number of measurements collected on the same day at identical conditions. In Figure 6, the high and low data points are plotted along with the average to show the degree of scatter in the data. Figure 7 shows the trend in the sticking coefficient data compared to measurements of adhesion strength as a function of carbon.

The data show several significant effects of unburned carbon:

- Sticking fractions were highly sensitive to unburned carbon, decreasing by a factor of about seven when unburned carbon levels increased from 10 to 50%.
- Increased unburned carbon increased deposit adhesion strength.
- Carbon levels more significantly affected sticking fractions than changes in gas temperature from 1100 to 1200°C.

The following are proposed as possible mechanisms for the observed effects of unburned carbon. Unburned carbon may have a short term effect on sticking, and a long term effect on deposit strength. Some of the carbon may be captured by other molten material on the surface and oxidize under subsequent layers of deposits over longer periods of time (seconds or minutes) compared to the time frame of particle impacts (milliseconds). The increased temperatures and locally reducing conditions within the deposit could produce increased levels of molten phases and sintering to result in higher deposit strengths with increased carbon levels.

The sticking fraction of particles impacting at the outer deposit surfaces may be predominantly affected by the competition between capture of molten particles and erosion by harder particles. The ultimate sticking fraction may depend on factors affecting the balance of levels of molten phases versus hard materials (both the particles, and at the deposit outer surface). The levels of molten versus hard phases may be affected by the ash composition and local temperatures. The elevation in local temperature of both the impacting particles and the outer deposit surface due to oxidizing carbon may ultimately be limited by the local oxygen levels. In that case, additional carbon in the POC would not increase levels of molten ash phases, but would increase the amount of hard material to erode the deposit surface. This would cause a decrease in deposition with an increase in carbon levels as was observed in these experiments. And, since the local temperatures and levels of molten phases would be predominantly affected by local oxygen levels rather than gas temperature, the sticking fraction would not be strongly influenced by gas temperature as was observed in these experiments.

The increase in deposition with increased carbon levels mentioned previously for tests in an early direct coal-fired turbine program[1] may have involved changes in carbon fractions below levels where local oxygen concentrations limit the degree of melting. In that case, molten ash levels and sticking may be controlled by carbon fractions and would increase with increasing carbon levels.

SUMMARY AND CONCLUSIONS

Particulate in the POC streams entering direct coal-fired gas turbines will probably contain much higher fractions of unburned carbon than for past coal experience because of the use of beneficiated, low ash fuels. Measurements of ash sticking fractions and ash deposit adhesion strength in a

drop tube combustor indicate that high levels of carbon in ash can reduce sticking fractions significantly, while also increasing the deposit strength. It is suggested that increased carbon levels may increase the amount of hard material relative to molten phases in the particulate when carbon oxidation is limited by local oxygen concentrations. However, heat generation from the burning carbon in deposited particulate in a locally reducing environment may cause increased levels of molten species and sintering, creating deposits that are more difficult to remove.

REFERENCES

1. Logan, R. G., G. A. Richards, C. T. Meyer, and R. J. Anderson, "A Study of Techniques for Reducing Ash Deposition in Coal-Fired Gas Turbines," Accepted for publication in Progress in Energy and Combustion Science, 1990.

2. Richards, G. A., R. G. Logan, C. T. Meyer, and R. J. Anderson, "Ash Deposition at Coal-Fired Gas Turbine Conditions: Surface and Combustion Temperature Effects," Accepted for publication in Transactions of the ASME, 1990.

3. Wenglarz, R. A. and R. G. Fox, Jr., "Physical Aspects of Deposition from Coal Water Fuels Under Gas Turbine Conditions," Journal for Gas Turbines and Power, Vol. 112, January 1990.

4. Kimura, S. G., C. L. Spiro, and C. C. Chen, "Combustion and Deposition in Coal-Fired Turbines," Journal of Engineering for Gas Turbines and Power, Vol. 109, July 1987.

5. Staub, F. W., S. G. Kimura, C. L. Spiro, and M. W. Horner, "Coal-Water Slurry Combustion in Gas Turbines," Journal of Engineering for Gas Turbines and Power, Vol. 111, January 1989.

6. Morley, W. J. and J. C. Wisdom, "Brown Coal Ash Deposition in the Open-Cycle Gas Turbine," Journal of the Institute of Fuel, Vol. 37, No. 280, May 1964.

7. Anderson, R. J., R. G. Logan, C. T. Meyer, and R. A. Dennis, "A Combustion/Deposition Entrained Reactor for High Temperature/Pressure Studies of Coals and Coal Minerals," Accepted for publication in Review of Scientific Instruments, 1990.

Table 1. Coal Analyses

	Arkwright	Blue Gem
ULTIMATE ANALYSES		
% Ash	6.93	0.56
% Carbon	75.90	78.06
% Hydrogen	5.34	5.67
% Nitrogen	1.45	1.98
% Sulfur	2.03	0.99
ASH ANALYSES		
% SiO_2	48.09	16.86
% Al_2O_3	25.07	22.75
% Fe_2O_3	10.95	29.57
% TiO_2	1.27	1.95
% P_2O_5	0.18	0.48
% CaO	5.78	7.03
% MgO	1.25	2.46
% K_2O	1.16	0.53
% Na_2O	0.90	1.54
% SO_2	5.34	8.07
ASH FUSION TEMPERATURE (+/- 40°C)		
Initial Deformation	1,190	1,238
Softening	1,316	1,308
Hemispherical	1,356	1,371
Fluid	1,383	1,427

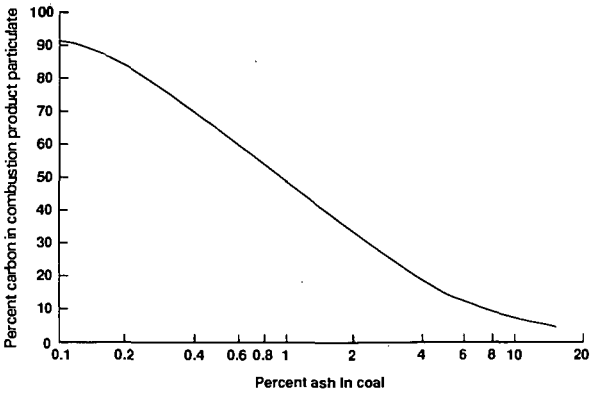

Figure 1: Percent of carbon in combustion particulate versus percent of ash in coal for 99% carbon burnout efficiency during combustion

Item	Test Section
PRESSURE, ABSOLUTE, atm	1-12
FLOW RATE, slpm	10-350
VESSEL LENGTH, cm	152
VESSEL OUTSIDE DIAMETER, cm	61
WALL THICKNESS, mm	95 (sch 40-304LSS)
PROCESS STREAM EXIT TEMPERATURE, °C	1,400
VESSEL SKIN TEMPERATURE, °C	< 150
ELEMENTAL TEMPERATURE (maximum), °C	1,650
HEATING ELEMENTS	KANTHAL SUPER 33 9/18
HEATER OUTPUT, watts	7,060
POWER SUPPLY, V/A	35/350
EXHAUST FLOW COMPOSITION	DILUTE COAL POC/ FILTERED
EXHAUST FLOW PRESSURE/TEMPERATURE	< 2 atm; < 200°C

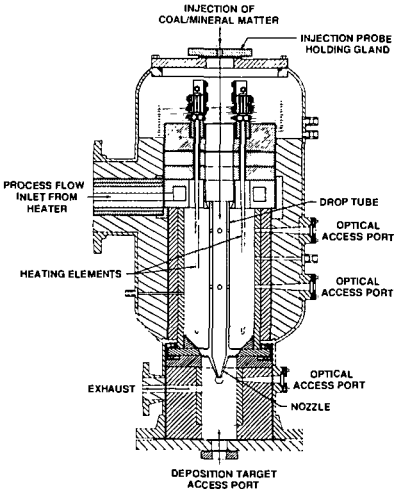

Figure 2: CDER System Design Specifications

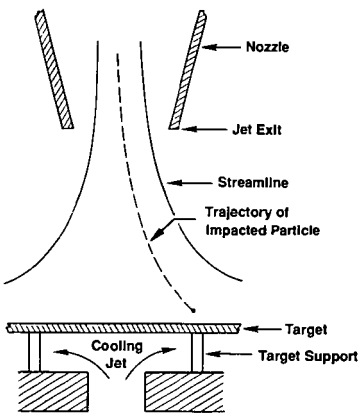

Figure 3: CDER Nozzle/Target Assembly

M90001853

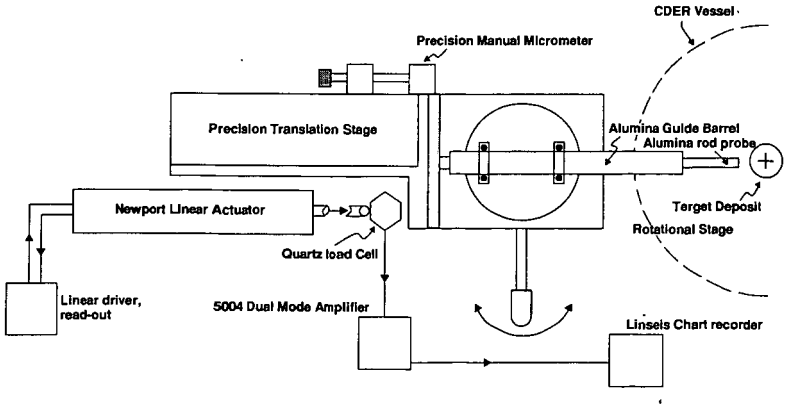

Figure 4: Adhesion Strength Meter

M90001854

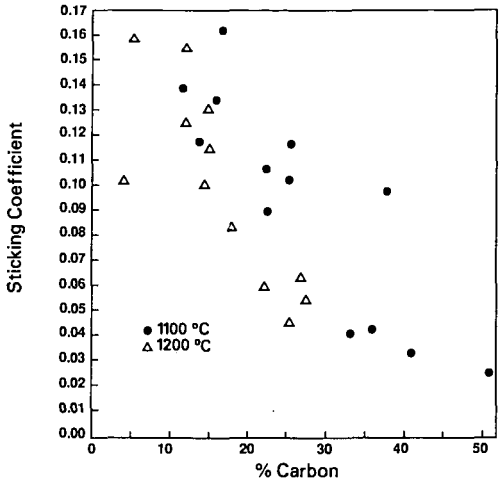

Figure 5: Sticking Coefficient vs % Carbon in Ash, Arkwright Bituminous Coal

M90001370

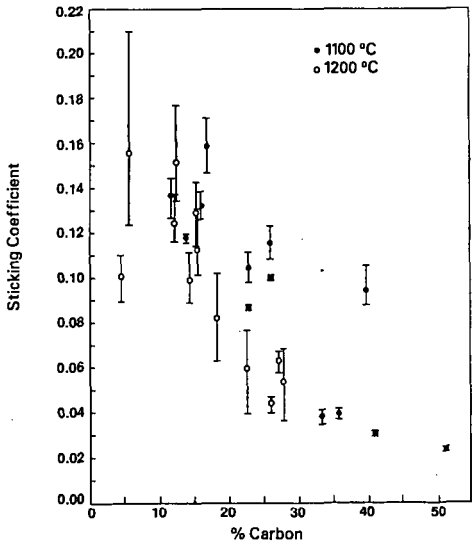

Figure 6: Sticking Coefficient vs % Carbon in Ash, Arkwright Bituminous Coal

M90001371

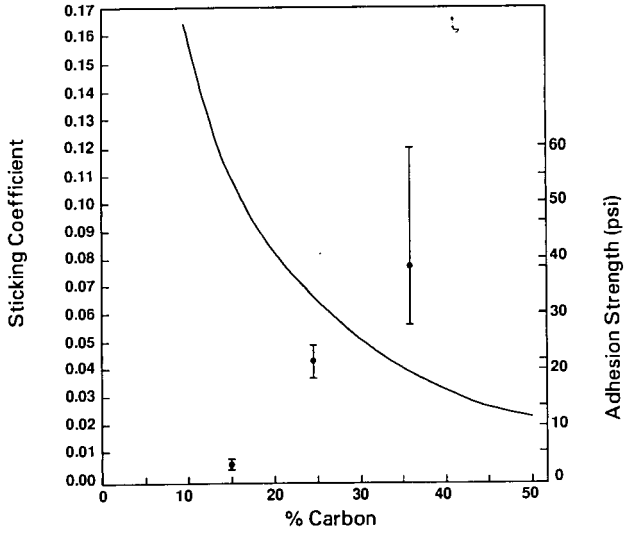

Figure 7: Adhesion Strength vs % Carbon in Ash Arkwright Bituminous Coal, T = 1100 °C

M90001376

EFFECTS OF INORGANIC CHANGES CAUSED BY NATURAL WEATHERING ON THE COMBUSTION BEHAVIOR OF BITUMINOUS COALS

SARMA V. PISUPATI and ALAN W. SCARONI
The Combustion Laboratory, 404 Academic Activities Bldg.
The Pennsylvania State University, University Park, PA 16802

Key words: Weathering; Mineral Matter; Combustion

INTRODUCTION

Weathering/oxidation is a process that can occur when coal is exposed to the atmosphere following mining and, in some instances, while it is still in the seam (outcropping). Weathering causes changes in the organic, inorganic and physical structure of coals. These structural changes can alter significantly the utilization behavior of the coals [1,2]. The most adverse effect of oxidation is probably experienced in the coking industry. Although attempts have been made to understand the mechanism of oxidation, and to elucidate the structural changes to the organic phase accompanying oxidation, [3,4,5] the reactions are still poorly understood and methods to suppress oxidation are often rather primitive [6]. Even though 70% of the coal mined in U.S is burnt in electric utility boilers, very little attention has been paid to the effects of weathering/oxidation/storage on combustion behavior. A few published studies[7,8] indicate that weathering/oxidation is detrimental to combustion in terms of carbon conversion. In addition, acid rain legislation is expected to increase the demand for low sulfur coals and therefore, electric utilities have begun to test blending strategies. As a result, coal suppliers have started blending fresh and naturally weathered/oxidized coals, because the latter generally have lower sulfur contents (for the reasons discussed later in the paper) than their fresh counterparts. Although desulfurization by weathering/oxidation may be desirable from an emissions point of view, the effects of the accompanying structural changes on combustion are not well established.

The structural differences between the organic phases and the relative combustion behavior of five outcrop coals and their fresh companions have been reported elsewhere[9]. The mineral matter is important from at least two aspects; its role in the combustion process itself and the operation and maintanence of combustion equipment (slagging, fouling and ash handling). It is known that inorganic species have a significant effect on the reactivity of coal chars to air depending on the amount, type and state of the species and rank of the coal. In this paper some of the changes in the inorganic species accompanying natural weathering, and their influence on the combustion process are discussed. A brief discussion on the likelihood of operational consequences due to these changes is also provided.

Unique Nature of Naturally Weathered Crop Coals

Inorganic matter in coals is basically present in two forms - as discrete mineral matter which are particles of micron size or larger and as inorganic metal cations bonded to organic matter. It is known that low rank coals contain as much as 30 - 40% of the inorganic matter bound to the organic structure. On the other hand high rank coals contain mostly discrete mineral matter. Compositionally, a decrease in oxygen content is accompanied by a change in the relative amounts of the various oxygen containing functional groups. Oxidation, a process by which oxygen is introduced into the coal structure, may therefore reinstate some coal properties and behavior which were eliminated by progressive coalification. A decrease in carbon content and heating value and an increase in volatile matter, oxygen content and oxygen functional groups, and loss of coking properties lead to a lower apparent rank of a weathered coal compared to its fresh companion. On the other hand an increase in the aromaticity and sometimes a small increase in reflectance give the appearance of increasing the rank of a coal upon oxidation.

The samples used in this study were obtained from two active mines in Pennsylvania (Fort Palmer and N.S.M #2) and their companion crop coals were taken from the same seams. The naturally weathered samples are termed " crop" coals in keeping with practical mining terminology. These samples were ground to utility grind specifications (80% through 200 mesh) and then sealed under a nitrogen atmosphere in polyethylene bags until used. The time - temperature history during weathering for these samples is not known. Two other samples were obtained from the Penn State/DOE Coal Data Bank . The fresh sample was PSOC 1448 (York Canyon seam, New Mexico) and the corresponding weathered sample was from a surface of the same seam partially mined and exposed to the atmosphere for about 20 years.

EXPERIMENTAL

Proximate analyses were performed on a Leco MAC 400 analyzer using the standard procedure. For carbon, hydrogen and nitrogen measurements, a Leco CHN 600 analyzer was used. Total sulfur was measured on a Leco Sulfur Analyzer.

Char Preparation and Measurement of Reactivity

Preparation of the chars and measurement of the reactivity were performed in a thermogravimetric analyzer (Perkin Elmer Series 7 Thermal Analyzer). The sample size used was 5 ± 0.5 mg. The experiments involved a multistep procedure. The furnace was purged with nitrogen for one hour and heated from room temperature to 110°C at the rate of 20°C/min and held at 110°C for 5 minutes. The temperature was then ramped to 930°C at the rate of 40°C/min and held at 930°C for 7 minutes in order for devolatilization to take place. The temperature of the furnace was reduced to 450°C at 50°C/min and allowed to thermally stabilize at 450°C for 10 minutes. The heating sequence above was conducted in a nitrogen atmosphere. The reactivity of the char thus produced was determined at 450°C (723 K) in one atmosphere of air. The change in the weight of the sample with time was recorded.

To determine the effect of mineral matter on the reactivity of the companion fresh and crop coal samples, about 10 grams of each coal were acid washed with 100 ml of 10% HCl for 24 hours at about 60°C. The samples were then filtered and washed thoroughly with distilled water until the filtrate was free of chloride ions (i.e. produced no precipitate with $AgNO_3$ solution). The residue was then dried overnight in a vacuum oven at 50°C and stored for subsequent reactivity measurements.

Chemical Analyses of the Inorganic Species

Chemical analyses were performed on the samples of ash produced by ashing coals in a Leco proximate analyzer (MAC 400) at 750°C. Determination of all the major elements was performed using the atomic absorption technique described by Meddlin et al.[10]. SO_3 was determined using a Leco Sulfur titrator. The acid wash extracts were analyzed for sodium, potassium, calcium, barium, magnesium and iron by spectrochemical - Lithium metaborate fusion into solution on a Spectrometrics Spectraspan III D.C. plasma Spectrometer with a CDAC 360 Data Acquisition System.

Qualitative mineralogical analysis was performed using a Rigaku X - ray Diffractometer with the low temperature ashes produced from the coals. Ash fusion temperatures were determined using a Leco - AF600 Ash Fusion Determinator.

RESULTS AND DISCUSSION

Proximate and elemental analyses of the samples are given in Table 1. The N.S.M.#2, Fort Palmer and New Mexico fresh coals have ranks of low volatile, medium volatile and high volatile bituminous (ASTM), respectively. Differences in chemical composition between the fresh and the crop coals have been discussed in detail elsewhere[9]. The most important difference pertaining to inorganics is the lower sulfur content of the crop coals relative to their fresh companions by about 20 - 80%. This is due mainly to the oxidation of pyrite in the coals. The difference in sulfur content between the N.S.M.#2 fresh and crop coals was about 80% (3.24 versus 0.68%), whereas it was only about 20% (0.51 versus 0.41%) for the New Mexico samples because of a very low pyritic sulfur content of this coal (0.05%). The sulfatic and organic sulfur contents were 0.01 and 0.45% respectively. Table 2 lists the qualitative mineralogical analysis of the fresh and the crop coals. The data confirmed the absence of pyrite in the Fort Palmer and New Mexico weathered samples. Similarly, a lower pyrite content was observed for N.S.M.#2 crop coal relative to its fresh companion. Desulfurization by oxidation of pyrite has been reported in the literature[11]. Chandra et al.[11] reported a 93% decrease in pyritic sulfur (from 0.89 to 0.06%) accounting for 92% of the total sulfur reduction due to weathering over a four year period. This desulfurization process is believed to take place as follows[12]

$$2FeS_2 + 7O_2 + 2H_2O \text{ --------> } 2FeSO_4 + 2H_2SO_4 + \text{Heat}$$

and

$$2\,Fe^{2+} + 3H_2O + 0.5\,O_2 \text{ -------> } Fe_2O_3.H_2O + 4H^+$$

$$2Fe^{2+} + SO_4^{2-} + x\,H_2O \text{ -------> } FeSO_4.x\,H_2O$$

(various hydrated ferrous sulfates)

Some of the ferrous sulfates, being soluble in water, and sulfuric acid are responsible for acid mine drainage. However, iron sulfates such as szolmolnokite are insoluble in water.

It can be seen from Table 1 that the ash contents of the weathered coals are lower and higher than their fresh companions, i.e. there is not a definite trend. This can be explained as follows. The weight of the oxidized minerals depends on the form of iron after oxidation (for example $FeSO_4$ or Fe_2O_3) and the extent of oxidation. The acidic water may also lead to leaching of some of the acid soluble components such as calcite and depending on the acidity, some of the clay minerals may also be leached. It can be seen from Table 2 that the New Mexico Fresh sample contained calcite but the oxidized companion did not and that the ash content of the crop coal was lower than that of fresh sample due to leaching. Table 3 gives the compositional analysis of the ash samples of the fresh, crop and acid washed samples. It is noted from Table 3 that the amount of iron per unit weight of coal in the Fort Palmer and N.S.M.#2 weathered samples is higher than in their fresh companions as is their ash contents (dry basis). This suggests that the iron sulfates formed by the oxidation of pyrite in these coals are insoluble (such as szolmolnokite) and therefore the iron was not leached out. The reduction in sulfur in the two Pennsylvania crop coals was due to sulfuric acid drainage. A reduced iron content in the New Mexico weathered sample is probably due to the formation of soluble iron sulfates.

Reactivity of the Fresh and the Crop Coals

The coal samples were pyrolyzed in a nitrogen atmosphere as described earlier. The resultant chars were stabilized thermally at 450° C for 10 minutes and were then reacted with air at 450°C until at least 50% burnoff (d.a.f. basis). The first derivative of the weight versus time curve was plotted as a function of time and a typical curve is shown in Fig.1 for the Fort Palmer fresh, crop and acid washed coals. Various parameters have been used in the literature to express the reactivity of coal chars[13,14,15]. Since the burnoff time of the particle is the ultimate indicator of its reactivity, the time for 50% burnoff (d.a.f. basis) of the char was used in this study as a measure of reactivity. The time required for 50% burnoff of the fresh, crop and acid washed fresh and crop coal chars is listed in Table 4. The times required for 50% burnoff were reproducible to within $\pm$ 3 min. In all cases, the time for 50% burnoff for the crop coal chars was found to be lower than that of the corresponding fresh sample. The higher reactivity of crop coals cannot be explained by the increase in the total and accessible surface areas as discussed elsewhere[9]. Therefore, an alternative explanation is provided here.

Possibility of Catalytic Activity in the Crop Coal Chars

It has been reported that mineral matter plays an important role in the reactivity of coal chars to various gases[14,16-18] depending on the rank of the coal precursor and the state and type of inorganic species present. Jenkins et al.[14] correlated reactivity with CaO and MgO contents although the state in which the elements were present was not reported. No correlation was obtained between the reactivity and the potassium, sodium and iron contents.

Depending on the local environment, oxygen partial pressure, moisture content, the chemical nature of the overburden, the concentration of ion - exchangeable cations and pH of the percolating water, there is a possibility of some cations being bound to the carboxylic functional groups produced during weathering. Since there was an indication of the presence of salts of carboxylic acids in the DRIFT spectra of the crop coals[9] and also a significantly higher CaO content in the Fort Palmer crop coal ash (16.5%) compared to that in its fresh companion coal ash (0.81%), and a substantially higher iron content in the N.S.M#2 crop coal ash (38.6%) compared to that in its fresh coal ash (23.9%), some catalytic activity due to these differences was suspected.

Figure 2 shows a plot of the time required for 50% char burnoff (d.a.f. basis) as a function of the calcium oxide content in the coal. It can be seen that there is a trend of increasing reactivity with increasing calcium oxide content in the coal for both the weathered and fresh coals. This is similar to the trend observed by Jenkins et al.[14].

A separate reactivity test was conducted to determine the influence of catalytic activity on the reactivity of the samples. Times required for 50% burnoff on d.a.f. basis ($T_{50\%}$) were obtained for the acid washed fresh and crop coal samples and are listed in Table 4. On examining the effect of acid washing on the reactivity of the fresh coals, in which no catalytic activity is expected, it was observed that there was an increase in the reactivity of N.S.M.#2 and Fort Palmer fresh coal chars upon acid washing. This shows that the reactivity of a char is a complex phenomenon which depends on the combined effects of the change in physical structure and the chemical nature of the coal. The ranks of these two coals are low and medium volatile bituminous, respectively. For such high rank coals with low porosity, the alteration of the pore system by acid washing increases the accessibility of oxygen into the pore structure. The effect of an increase

in the number of 'feeder pores' is significant compared to the reduction of the catalytic activity due to the removal of inorganic species upon acid washing, and hence, there is a net increase in the reactivity of the N.S.M.#2 and Fort Palmer fresh coals. Jenkins et al.[14] reported such a phenomenon for a low volatile bituminous coal (PSOC 127). Also, Mahajan and Walker[19]found an increase in the nitrogen and carbon dioxide surface areas for a low volatile bituminous coal char (from PSOC 127) by factors of 2 and 3, respectively upon removing the mineral matter from the coal. From Table 4 it is also noted that for the New Mexico coal the $T_{50\%}$ of fresh sample increased marginally upon acid washing. This is again in concurrence with the observations of Mahajan and Walker[19] of no significant difference in the surface areas of raw and acid washed, high volatile bituminous coal chars. The marginal decrease in the reactivity of the New Mexico fresh sample upon acid washing, could also be due to the removal of catalytically active inorganic species.

It was also observed that acid washing reduced the reactivity and thereby increased the $T_{50\%}$ for all the crop coals reported. The $T_{50\%}$ for the acid washed crop coal was almost twice that of the crop sample for the Fort Palmer coal (59 compared to 26 min) and the Mew Mexico coal (75 compared to 46 min), whereas the $T_{50\%}$ for N.S.M.#2 acid washed crop sample was only 13% higher (119 compared to 105 min) than that of the crop coal. In light of the above discussion, this significant decrease in the reactivity of the acid washed Fort Palmer crop char was a result of the removal of inorganic species, despite the likely attendant increase in the number of 'feeder pores'. This indicates a significant contribution by the inorganic species to the reactivity of the Fort Palmer crop sample. The reactivity of the New Mexico crop sample also decreased upon acid washing and this is attributed to the removal of catalytic species during acid washing since the surface area change was found to be negligible for the high volatile bituminous coal chars[19]. The reactivity decrease or the increase in the $T_{50\%}$, in the case of the N.S.M.#2 acid washed crop sample was not very high. This is attributed to the type of catalytic species present in the coal. Table 5 gives the spectrochemical analysis of the acid extracts. The species present in significant proportions relative to those in the fresh coal extracts were calcium, magnesium and iron in the case of the Fort Palmer coal. Although some minerals such as calcite and gypsum are acid soluble, such minerals are known to be catalytically inactive[20]. Hence, the catalytic activity in the Fort Palmer and New Mexico crop coals was attributed mainly to the presence of ion-exchangeable calcium since this cation is known to be highly catalytic towards gas - carbon reactions[17,21]. In the case of the N.S.M.#2 crop coal acid washing extract, a significant proportion of iron was found compared to that in the extract from the fresh coal and since some of the iron was present in sulfate form, the catalytic activity could be due to iron in ferrous form. However, during the carbon - oxygen reaction, iron is oxidized to ferric oxide and looses its catalytic activity quickly. The slope of the weight change curve for the N.S.M.#2 crop coal was initially high and then dropped off to a lower value as can be seen from Fig. 3. The slope of the curve for the N.S.M.#2 acid washed sample tended to be more linear. As previously noted, the catalytic activity of iron depends on the ratio of ferrous to ferric and how quickly ferrous is oxidized to ferric. This explains the smaller decrease in reactivity (only 13%) on acid washing the N.S.M. #2 crop sample.

Effect of Changes in Mineral Matter on Operational and Handling aspects

The nature and amount of inorganic matter in coal are important considerations in the design of a coal fired boiler. These influence fouling of convective heat transfer surfaces and affect heat transfer characteristics. The potential for slagging and fouling depends on the inorganic constituents and the temperature they attain during combustion. A reduction in acidic oxides (SiO_2, Al_2O_3 and TiO_2) and an enrichment in CaO (from 0.8 to 16.5%) was observed for Fort Palmer crop coal ash compared to the ash from the fresh sample. Other alkali oxides such as K_2O and Na_2O did not show any significant change. Similarly, a higher iron content was noted in the N.S.M.#2 weathered sample (23.9 to 38.6%). The New Mexico ash samples did not indicate any major differences that could affect the behavior of the ash in a boiler. An increase in the basic oxides in an ash usually indicates an increased potential for fouling and slagging. Many empirical indices have been proposed to predict slagging and fouling[22]. The ASTM fusion temperature determination, although purely empirical, was developed to measure the clinkering tendency of coal ash on a grate, but it is still widely used as a method for determining ash fusibility. The ash fusion temperatures for the fresh and crop coal samples are listed in Table 6. The initial deformation temperature (I.D.T.) of the Fort Palmer crop ash is about 430° F lower than for the corresponding fresh coal ash. Similarly, the Hemispherical Temperature (H.T.) is about 250° F lower than for the corresponding fresh coal ash. Although the I.D.T of the crop coal ash is relatively low it is still high enough for use in a dry bottom furnace. The fusion temperature for the New Mexico crop sample is also lower than that of its fresh companion ash by about 250° F. The difference in fusion temperatures for N.S.M.#2 crop and fresh samples is not significant. The slagging and fouling indices defined by Attig and Duzy[23] (base/acid ratio times coal sulfur and base/acid ratio times sodium content,

respectively) were also calculated and are listed in Table 7. They are within the values generally recommended for trouble free operation.

CONCLUSIONS

Weathering causes desulfurization of coals primarily through oxidation of pyrite and the reduction in sulfur has a direct impact on SO_x emissions from combustors. Some of the metal cations are incorporated into the organic structure as ion-exchangeable cations which catalyze the combustion reactions and thereby increase the heat release rate. The composition of the ash from weathered coals indicates a significant concentration of fluxing agents such as CaO and Fe_2O_3 which is reflected in the relatively low fusion temperatures. Although the empirical parameters used to predict slagging and fouling are within safe limits, caution should be exercised when burning these crop coals.

REFERENCES

1. Huggins, F. E., Huffman, G. P., Dunmyre, G. R., Nardozzi, M. J. and Lin, M. C., Fuel Processing Technology, 1987,vol. 15, pp. 233 - 244.
2. Gray, R. J., Rhoades, A. H. and King, D. T., Trans. Of Soc. of Min. Engrs., AIME, 1976, Vol. 260, pp. 334 - 341.
3. Wachowska, H. M., Nandi, B. N. and Montgomery, D. S., Fuel, 1974, Vol. 53, p. 212.
4. Liotta, R., Brons, G. and Isaacs, J., Fuel, 1983, Vol. 62, p. 781.
5. Rhoads, C. A., Senftle, J. T., Coleman, M. M., Davis, A. and Painter, P., Fuel, 1983, Vol. 62, p. 1387.
6. Gaines, A. F., in "New Trends in Coal Science", NATO Series, Kluwer Academic Publishers, The Netherlands, 1988, p. 206.
7. Nandi, B. N., Brown, T. D. and Lee, G. K., Fuel, 1977, Vol. 56, No. 4, pp. 125-130.
8. Lee, G. K. and Whaley, H., J. of Inst. of Energy, 1983, Vol. 12, pp. 191-197.
9. Pisupati, S. V., Scaroni, A. W. and Stoessner, R. W., " Combustion Characteristics of Naturally Weathered (Insitu) Bituminous Coals", submitted to Fuel Processing Technology
10. Meddlin, J. H., Suhr, N. H. and Bodkin, J. B. Atom. Abs. News, 1969, vol. 8, p. 25.
11. Chandra, D., Chakrabarti, J. N. amd Swamy, Y. V., Fuel, 1982, Vol. 61, pp. 204 - 205.
12. Berkowitz, N., in " Sample Selection, Aging and Reactivity of Coal", Klen, R. and Wellek, R (eds), John Wiley & Sons, N.Y., 1989, P. 226.
13. Walker, P. L., Jr., and Hippo, E. J., Div. of Fuel Chem., Am. Chem. Soc., 1977, Vol 20, pp. 45 - 51.
14. Jenkins, R. G., Nandi, S. P. and Walker, P. L., Jr., Fuel, 1973, Vol. 52, pp. 288 - 293.
15. Tomita, A., Mahajan, O. P. and Walker, P. L., Jr., Fuel, 1977, Vol.56, pp. 137 - 144.
16. Walker, P. L., Jr., Shelef, M. and Anderson, R. A., "Chem. and Phy. of Carbon", Walker, P.L., Jr., (Ed.), 1969, Vol. 4, Marcell Dekker Inc., N.Y., pp. 287 - 383.
17. Morgan, B. A. and Scaroni, A. W., "Pulverized Lignite Combustion", Int. Conf. on Coal Sci., Int Energy Agency, Sydney, Australia, 1985.
18. Radovic, L. R., Walker, P. L., Jr. and Jenkins, R. G., Fuel, 1983, Vol. 62, pp. 209 -212.
19. Mahajan, O. P. and Walker, P. L.,Jr., Fuel, 1979, Vol. 58, pp. 333 - 337.
20. Tomita, A., Mahajan, O. P. and Walker, P. L.,Jr., Div. of Fuel Chem., Am. Chem. Soc., 1977, Vol. 22, pp. 4 - 6.
21. Hippo, E. J., "The Effect of Cation Exchange on the Subsequent Reactivity of Lignite Chars to Steam", Ph.D Thesis, 1977, The Pennsylvania State University.
22. Sondreal, E. A., Tufte, P. H. and Beckering, W., Comb. Sci. and Tech., 1977, Vol. 16, pp. 95 - 110.
23. Attig, R. C. and Duzy, A. F., " Coal Ash Deposition Studies and Application to Boiler Design", Am. Power Conf., April 1969.

TABLE 1
Proximate Analysis (as determined) Wt%

Mine	Moisture	Ash	F.C. (d.m.m.f)	V.M. (d.m.m.f)	Rank (A.S.T.M)
N.S.M. #2 Fresh	0.54	8.70	79.06	20.94	l.v.bit.
N.S.M. #2 Crop	4.44	9.19	75.50	24.50	m.v.bit.
Fort Palmer Fresh	0.72	13.43	75.94	24.06	m.v.bit.
Fort Palmer Crop	8.34	15.91	67.19	32.81	sub.bit.A
New Mexico Fresh	1.48	11.27	60.17	39.82	h.v.A.b
New Mexico Crop	7.29	6.07	60.83	39.16	h.v.A.b

Elemental Analysis on dry, mineral matter free basis

Mine	Carbon	Hydrogen	Nitrogen	Sulfur	Oxygen(by diff.)
N.S.M. #2 Fresh	90.23	4.68	1.56	3.24	0.29
N.S.M. #2 Crop	86.11	4.04	1.47	0.68	7.70
Fort Palmer Fresh	89.61	5.04	1.83	2.09	1.43
Fort Palmer Crop	82.05	3.90	1.66	1.24	11.15
New Mexico Fresh	87.29	5.63	1.64	0.51	4.93
New Mexico Crop	78.66	4.24	1.70	0.41	14.99

TABLE 2
Qualitative Mineralogical Analysis

Mineral	N.S.M.#2 Fr	N.S.M.#2 Cr	F.P. Fr	F.P. Cr	N.M. Fr	N.M. Wea.
Kaolinite	X	X	X	X	X	X
Quartz	X	X	X	X	X	X
Pyrite	X	X	X	--	X	--
Illite			--	X		
m.l.c			X	--		
Calcite					X	--
Bassanite			--	X		
Fe sulfates	--	X	--	X		
Feldspars			X	--		

Fr = Fresh, Cr = Crop and Wea = Weathered

TABLE 3

Analyses of the Ashes (wt%)

Oxide	FPF	FPW	NSMF	NSMW	NMF	NMW	FPFAW	FPWAW	NMFAW	NMWAW
SiO_2	55.9	38.3	43.2	34.5	40.5	37.2	61.0	58.0	65.0	57.4
Al_2O_3	26.9	20.2	25.6	22.1	23.9	29.0	27.8	29.4	29.6	32.4
TiO_2	1.42	0.96	1.46	0.98	1.06	1.36	1.45	1.57	1.68	1.84
Fe_2O_3	10.3	9.31	23.9	38.6	7.00	9.02	6.89	5.99	1.88	2.55
MgO	0.59	1.33	1.12	0.48	2.11	2.97	0.48	0.7	0.49	0.96
CaO	0.81	16.5	2.71	1.24	15.7	11.0	0.26	1.53	0.48	2.17
MnO	0.02	0.03	0.03	0.02	0.01	0.02	0.01	0.01	0.01	0.01
Na_2O	0.57	0.45	0.22	0.22	1.09	2.13	0.61	0.85	0.74	1.41
K_2O	2.08	1.65	2.11	2.11	0.54	0.79	2.09	2.63	0.85	0.61
P_2O_5	0.38	0.41	0.3	0.18	1.39	1.67	#	#	#	#
SO_3	0.1	10.9	<0.05	<0.05	5.5	*	<0.05	<0.05	<0.05	<0.06
Total	99.1	100.0	100.7	99.4	98.8	95.2	100.6	100.7	100.7	100.0

FPF : Fort Palmer Fresh FPW: Fort Palmer Crop NSMF: N.S.M.#2 Fresh NSMW: N.S.M. # 2 Crop
NMF: New Mexico Fresh NMW: New Mexico Weathered FPF AW : Fort Palmer Fresh, Acid Washed FPW AW: Fort Palmer Crop, Acid Washed
NMF AW: New Mexico Fresh, Acid Washed NMW AW: New MexicoWeathered, Acid Washed

TABLE 4
Times for 50% Burnoff of Char (d.a.f. basis, min)

Sample	Original Coal Char	Acid Washed Coal Char
Fort Palmer Fresh	345	242
Fort Palmer Crop	26	59
N.S.M.#2 Fresh	668	572
N.S.M.#2 Crop	105	119
New Mexico Fresh	98	102
New Mexico Crop	46	75

TABLE 5
Spectrochemical Analysis of the Acid Extracts

Cation	Concentration (μ g / g of daf coal)					
	F.P. Fr.	F. P. Cr.	N.S.M.#2 Fr.	N.S.M.#2 Cr.	N.M. Fr.	N.M. Cr
Barium	82	181	47	144	555	580
Calcium	660	16634	608	1616	11786	4323
Iron	3690	9826	5891	13464	4853	3396
Potassium	260	470	140	287	372	438
Magnesium	140	1184	NA	NA	1450	988
Sodium	188	140	65	45	693	618

TABLE 6
Ash Fusion Temperatures (°F)

Sample	Initial Deformation	Softening	Hemispherical	Fluid
Fort Palmer Fresh	2775	2805	2830	2845
Fort Palmer Crop	2340	2375	2470	2590
N.S.M. # 2 Fresh	2540	2570	2595	2600
N.S.M. # 2 Crop	2540	2555	2560	2565
New Mexico Fresh	2435	2465	2480	2500
New Mexico Crop	2215	2405	2420	2425

TABLE 7
Slagging and Fouling Indices *

Sample	Slagging Index	Fouling Index
Fort Palmer Fresh	0.35	0.10
Fort Palmer Crop	0.61	0.22
N.S.M.#2 Fresh	1.39	0.10
N.S.M.#2 Crop	0.50	0.16
New Mexico Fresh	0.20	0.44
New Mexico Crop	0.16	0.94

* Attig and Duzy [23]

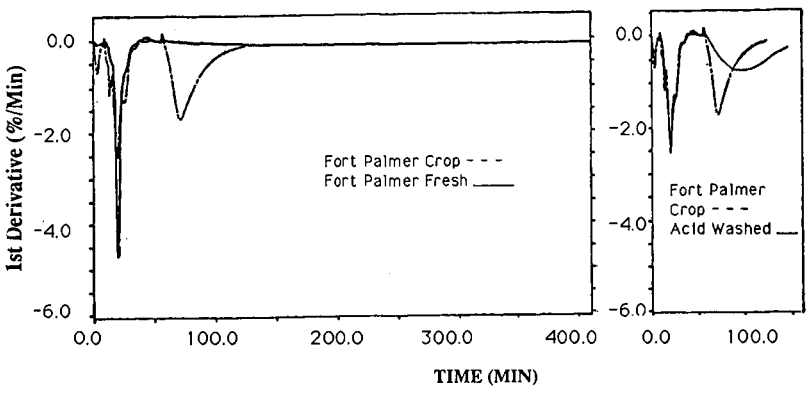

FIG.1. RATE OF WEIGHT LOSS (DERIVATIVE) AS A FUNCTION OF TIME FOR FORT PALMER FRESH, CROP AND ACID WASHED COALS

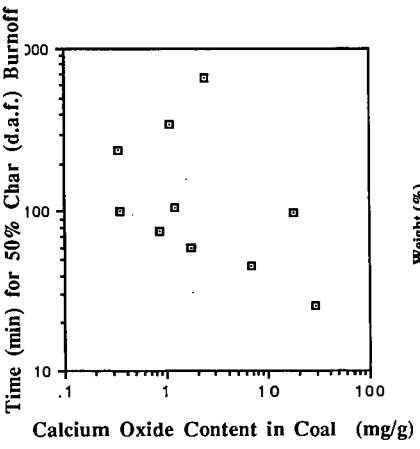

FIG.2. TIME FOR 50% BURNOFF (D.A.F.) AS A FUNCTION OF CALCIUM OXIDE CONTENT IN COAL

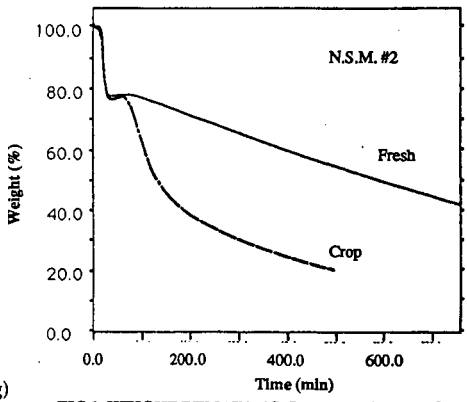

FIG.3. WEIGHT REMAINING CURVES AS A FUNCTION OF TIME FOR N.S.M. #2 FRESH AND CROP COALS

ENERGETIC DISTRIBUTIONS OF OXYGEN SURFACE COMPLEXES ON POROUS CARBONS AND CHARS

P.J. Hall and J.M. Calo
Chemical Engineering Program
Division of Engineering
Brown University
Providence, Rhode Island 02912

Keywords: Carbon-oxygen surface complex energetics; temperature programmed desorption; TPD spectra deconvolution.

INTRODUCTION

When an oxidized coal char is subjected to a program of increasing temperature, the surface oxides desorb primarily as the oxides of carbon, CO and CO_2 (e.g., [1]). This process produces TPD spectra which can be interpreted in terms of the energetic state of chemisorbed surface complexes and interaction phenomena occurring within the char structure during the TPD process. The latter have been shown to be [2]: (1) the desorption of rechemisorbed CO released at lower temperatures, appearing primarily as a feature centered typically *ca.* 1200K; and (2) secondary CO_2 evolution which appears as a reflection or satellite peak under primary CO desorption features. We have attributed the latter to:

$$CO(g) + C(O) \Leftrightarrow C_f + CO_2(g) \qquad [R.1]$$

where: CO(g) represents "free," gaseous CO resulting from the desorption of a surface oxygen complex; C(O) is a surface oxygen complex; and C_f is an unoccupied surface active site.

From the perspective of previous work, including our own, there appear to be two principal obstacles to the direct application of TPD to the understanding of the behavior of oxygen surface complexes: (1) a more quantitative interpretation of the data; (2) deconvolution of secondary interactions from TPD spectra in order to enable the analysis of such data in terms of the energetics of the surface complexes. These issues are addressed in the current communication.

EXPERIMENTAL

Chars were prepared from Pittsburgh #8 and Wyodak coals obtained from the Argonne Premium Coal Sample Bank *via* pyrolysis in ultrahigh purity helium at 1273K with a soak time of 1 hour.

The TPD apparatus and methods have been described elsewhere [2]. The most salient experimental details are as follows. Char oxidation/gasification was performed in a TGA

apparatus in 0.1 MPa O_2 at the temperatures noted. Following cooling to room temperature in the TGA apparatus, the samples were transferred to a TPD reactor. Tests involving comparisons of TPD spectra obtained using this procedure with those following *in situ* oxidation in the TPD reactor have shown that transfer of the sample does not affect the resultant spectra.

The TPD reactor was constructed from a high-purity silica tube, 1-cm inside diameter, within which a close-fitting, circular silica sinter is used to support the sample. Ultrahigh purity helium carrier gas is passed over the sample in downflow. Heating is accomplished electrically via nichrome wire wrapped around the outside of the silica tube, powered by a high current variable transformer. The heating regimen is controlled by a microcomputer. The resultant TPD reactor has a low thermal capacitance which allows linear heating rates of up to 500K/min.

Detection of desorbed species is accomplished with a quadrupole mass spectrometer (MS) which samples a small portion of the carrier flow. The MS output is fed to a microcomputer which also provides for multiple species detection via mass programming.

Typical sample sizes for the TPD measurements were ~10 mg. This size resulted in less than a monolayer coverage on the silica frit that was used as the sample holder in the TPD reactor. This, when combined with high helium carrier gas sweep rates, insured the absence of secondary interactions between the bulk gas species and the char samples.

Repeated experiments with char samples obtained from the same batch indicate that the reproducibility of gas desorption rates is approximately ±10%. This error is attributable to a combination of effects arising primarily from sample inhomogeneity, sample size and MS calibration. For this reason, the spectra reported are representative, rather than averages.

RESULTS AND DISCUSSION

Deconvolution of TPD Spectra.

Over the course of examining many TPD spectra from oxygen-oxidized chars, it was noted that the leading edge of the *total oxygen* (i.e., $CO+2CO_2$) desorption feature centered *ca.* 1000K always seems to be reasonably well approximated by a Gaussian distribution. For this reason, it was decided to investigate the deconvolution of the total oxygen production rate into two contributions - one as a Gaussian centered at the maximum rate of production, with the variance determined from the leading edge of the 1000K peak, and the other as a higher temperature residual difference peak. The results of such a deconvolution for spectra obtained from an oxidized Wyodak coal char are presented in Figure 1. As shown, the Gaussian approximation is quite reasonable for describing the leading edge of the total oxygen distribution, and the residual peak appears to be relatively smaller and non-Gaussian.

As it stands, such a deconvolution is nonunique, and thus we are faced with the question of whether the high temperature end of the 1000K oxygen peak remains near-Gaussian in the region

where it cannot be directly observed. There is some experimental evidence in support of this hypothesis.

One such piece of evidence is provided by a set of previously reported experiments with Wyodak coal char [3] in a slightly different context, and re-analyzed here. The coal char was gasified to 15.2% burn-off (in 0.1MPa oxygen at 623K) in the TGA apparatus. In the current analysis only the CO data are analyzed, although similar results were found for total oxygen spectra as well, due to the relatively minor contribution of the CO_2 in this case. A sample of the gasified char was *partially cleaned* by heating to 1100K at 100K/min, and was then quickly cooled (at a rate exceeding 200K/min) in ultrahigh purity helium. This was done not only to remove complexes stable below 1000K, but also as an attempt to effectively "titrate" the high temperature sites suspected of involvement in CO re-adsorption that give rise to the 1200K peak in TPD spectra. A second sample of the same coal char, oxidized under the same conditions, was subjected to TPD to 1100K and quick cooling in He to room temperature. Then, a TPD was carried out to 1400K. The result of this experiment is the "high temperature - clean" CO spectrum [HT] presented in Figure 2. The "partially cleaned" sample, with high temperature CO remaining on the surface, was then re-oxidized in the TPD apparatus under non-gasifying conditions in 0.1MPa of oxygen at 473K for 12 hours. We have shown that this treatment effectively reoxidizes practically all the surface sites created during the original gasification for the Wyodak coal char [3]. TPD was then carried out on this partially cleaned and reoxidized char, and this result is designated as the [PC] spectrum in Figure 2. The difference between the "high temperature - clean" TPD [HT] and the "partially cleaned/reoxidized" TPD [PC] then represents the surface oxygen added during reoxidation. This is designated as [HT-PC] in Figure 2. From the arguments presented above, this difference spectrum should be uncomplicated by CO re-chemisorption, and the resultant distribution should, therefore, be reflective of the original state of the oxygen chemisorbed during reoxidation. As shown in the figure, a Gaussian distribution seems to fit the difference spectrum reasonably well. This agreement suggests that the *intrinsic* 1000K peak for oxygen production may indeed be Gaussian over its entire range.

Energetic Distributions.

In view of the available evidence in support of a Gaussian distribution for the 1000K feature, the question naturally arises as to what the physical basis may be for this type of distribution. In considering this question, it is useful to transform the TPD spectra from a temperature to a desorption energy basis, using a procedure derived from the original work of Redhead [4]. A brief outline of the derivation follows.

For a *continuous* distribution of *i* species on a *heterogeneous* surface, each obeying a first order desorption rate law characterized by a single desorption activation energy, E_i, there must also be a *continuous* distribution of maximum desorption temperatures, $T_{p,i}$, one for each of the *i* species. These are related to the E_i *via* a familiar expression derived by Redhead [4]. Since the relationship between desorption activation energy and temperature is very nearly linear over

a large range of parameter values, this is closely approximated by the expression:

$$E_i/RT_{p,i} = \ln [\nu_o T_{p,i}/\beta] - 3.64, \qquad [1]$$

which for $10^{13} > \nu_i/\beta > 10^8$ (K^{-1}), was shown to be accurate to within $\pm$ 1.5% [4].

If the $T_{p,i}$ are described by a continuous probability density function, then each instantaneous temperature, T, during a heating regimen must also correspond to some $T_{p,i}$. As a consequence, an expression like Eq. [1] provides a direct transformation between the observed experimental desorption temperature, T, and the desorption activation energy distribution, $S(E_i)$. Furthermore, since Eq.[1] is evaluated at the peak temperature, $T_{p,i}$, then the heating rate, β, is rigorously defined as the local *instantaneous* heating rate at $T_{p,i}$, or, more generally, at temperature T. Therefore, Eq. [1] applies to a first order desorption process for any monotonic heating regimen exhibiting a maximum in desorption rate.

An analysis of the continuity expression for surface oxygen complexes can be shown to yield the following expression for the total desorption rate of CO from the surface:In this expression,

$$d[CO]/dt = [C\text{-}O]_o \, S(E^*) \, dE^*/dt \qquad [2]$$

where $[C\text{-}O]_o$ is the total amount of oxygen surface complex initially on the char surface, $S(E^*)$ is the probability density function of desorption activation energies, and dE^*/dt is the time derivative of the desorption activation energy during the heating regimen. In deriving this expression, the resultant integral over the distributed desorption rate constant was approximated as a step function occurring at a critical activation energy, E^* (*cf.* [5,6]), since it increases over a very narrow energy range from zero to unity. Since a TPD experiment yields the instantaneous d[CO]/dt directly, then knowledge of E^* and dE^*/dt defines the initial energetic distribution of surface complex, $[C\text{-}O]_o S(E^*)$, experimentally. Differentiating Eq. [1]:

$$dE^*/dt = R\beta \, [E^*/RT] = R\beta \, [\ln (\nu_o T/\beta) - 3.64]. \qquad [3]$$

Combining Eqns. [2] and [3], then yields the energetic distribution of surface complexes as:

$$[C\text{-}O]_o S(E^*) = \{d[CO]/dt\}/\{R\beta \, [\ln (\nu_o T/\beta) - 3.64]\}. \qquad [4]$$

From this expression, the energetic distribution of oxygen surface complexes can be determined experimentally from TPD spectra. Eq. [4] indicates that this transformation is practically linear for constant heating rate, β; i.e., the logarithmic term does not vary appreciably over the TPD temperature range. Thus, for *linear* TPD, if the distribution of the surface complex desorption in temperature is Gaussian, then the distribution of desorption activation energies will be close to

Gaussian as well.

One interpretation of a Gaussian energetic distribution is that the oxygen surface complexes exhibit a continuum, random distribution of binding energies. For many typical coal chars, most of the surface area and, consequently, most of the oxygen complexes, are present in micropores. In these small pores of molecular dimensions, the effective binding energies of the complexes would be strongly influenced by the local environment, the presence of neighboring complexes etc., and thus may be randomly distributed. For example, an oxygen atom could be bound to opposing walls of a micropore (e.g., an ether linkage). The binding energy of such a complex would vary according to the local width of the micropore, and, ultimately, in a very wide micropore, or a mesopore, the complex could be bound to only one wall, thereby assuming a semiquinone or carbonyl character. In other words, oxygen functional groups that may otherwise be chemically distinct on an "open" surface, may ultimately "blend" into one another in a multi-surface environment of molecular dimensions, as in micropores.

This *rationale* for a Gaussian distribution of desorption activation energies suggests that the resultant energetic distribution should be a characteristic property of the char and its porosity, and *not* a function of heating rate. In order words, once the distribution of desorption activation energies is known, it should enable the prediction of desorption spectra obtained under any heating regimen. In addition, the fact that it is the *total oxygen* distribution that appears to be Gaussian supports the hypothesis that the secondary interaction features arise primarily from the same source as the "1000K CO." These points are demonstrated below using TPD data obtained from Pittsburgh #8 coal char.

In Figure 3 is presented a 100K/min total oxygen TPD spectrum from a sample of Pittsburgh #8 coal char gasified to 10% burn-off at 723K in 0.1MPa of O_2, along with a Gaussian fit to the leading edge of the principal desorption feature. As discussed above, the high temperature peak/shoulder is believed to originate primarily from CO originally liberated during desorption of the 1000K oxygen complexes and re-chemisorbed to be liberated once again as "1200K CO." Therefore, in order to be consistent in reconstructing the original state of the oxygen complex distribution on the char surface, the additional oxygen represented by the difference between the integral over the total oxygen desorption and the Gaussian fit to the 1000K peak should be added to the latter to yield a "corrected" Gaussian, as shown in Figure 3. For example, for the Pittsburgh #8 coal char sample this amounted to an amplitude correction (increase) of 20%.

The "corrected" Gaussian distribution was then transformed into an energetic distribution using Eq. [4]. As indicated above, for a linear heating rate, the transformation between the TPD spectrum with respect to temperature and the energetic distribution is practically linear, so that the resultant S(E*) distribution is also quite close to Gaussian as well. The construction of this distribution requires the assumption of values for the pre-exponential frequency factor, ν_o. Originally we tried using ν_o=kT/h, the frequency factor predicted by transition state theory.

However, this did not result in the best fits to total oxygen TPD spectra obtained at different heating rates for the same char. In any case, these values are simply estimates. Therefore, it was decided to vary ν_o in such a manner as to obtain the best fit to TPD spectra obtained at the nominal heating rates of 20, 100, and 300K/min. The calculations were, therefore, iterative, and were performed using a spreadsheet program. Essentially, the procedure involved assuming a value of ν_o to obtain an energetic distribution from the 100K/min data. This distribution was then used to predict the 20 and 300K/min total oxygen TPD spectra, "corrected" for rechemisorbed oxygen as described above. The final energetic distribution, arrived at in this manner, was approximately Gaussian with a mean of 48.8 kcal/mol and a standard deviation of 6.9 kcal/mol. The total amount of surface oxygen was 2.4 mmol/g. A value of $\nu_o = 10^{11}$ min^{-1} yielded the best predictions, although reasonable results were also obtained over a range of ν_o of about an order of magnitude in either direction, so this value is not necessarily unique. A summary of the final TPD curves, predicted from the energetic distribution, for the three heating rates used, along with the corresponding "corrected" data, are presented in Figure 4.

CONCLUSIONS

Based on these results, it is concluded that Gaussian deconvolution of the 1000K peak from total oxygen TPD spectra seems to be a reasonable approximation. The amount of rechemisorbed CO may be estimated using this procedure. The resultant Gaussian spectra can be transformed to obtain the probability density distribution function of desorption activation energies which is related to the energetic state of oxygen complexes on coal char surfaces. This distribution is a characteristic property of the char and can be used for kinetic predictions involving the thermal desorption rates of such complexes, and/or as a diagnostic of the nature of the active sites.

The authors believe that the quantitative description of char surfaces *via* energetic distributions represents a new and more fundamental approach to all issues related to char reactivity. It is anticipated that techniques arising from such descriptions will eventually supplant more empirical methods.

Acknowledgement. This work was supported by the Morgantown Energy Technology Center of the Department of Energy under Contract No. DE-AC21-MC23284.

REFERENCES

1. Tremblay, G.; Vastola, F.J.; Walker, P.L., Jr., *Carbon* **1978,** *16,* 35.
2. Hall, P.J.; Calo, J.M., *Energy & Fuels* **1989,** *3,* 370.
3. Hall, P.J.; Calo, J.M.; and Otake *Proc. Nineteenth Biennial Conf. Carbon,* **1989,** p. 594.
4. Redhead, P.A. *Vacuum* **1962,** *12,* 203.
5. Suuberg, E.M. , *Comb. Flame* **1983,** *50,* 243.
6. Du, Z., Sarofim, A.F., and Longwell, J.P. *Energy & Fuels* **1990,** in press.

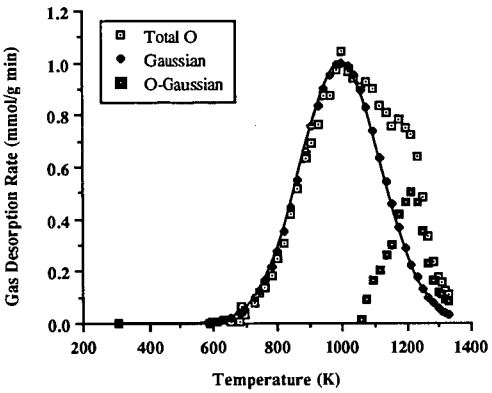

Figure 1. Deconvolution of 100K/min total oxygen TPD spectra from Wyodak coal char gasified to 15.2% burn-off in 0.1MPa of O_2 at 350°C into a Gaussian and a residual.

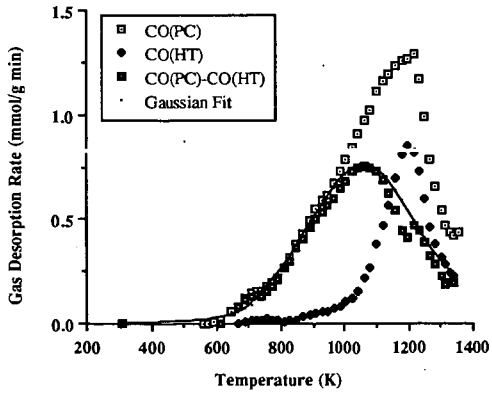

Figure 2. 100K/min CO TPD spectra from Wyodak coal char, originally burned-off to 15.2% in 0.1MPa O_2. CO(PC): after partial cleaning to 1100K and re-oxidation in 0.1MPa O_2 at 200°C for 12h; CO(HT): residual high temperature surface complexes after partial cleaning to 1100K; CO(PC)-CO(HT): difference spectrum.

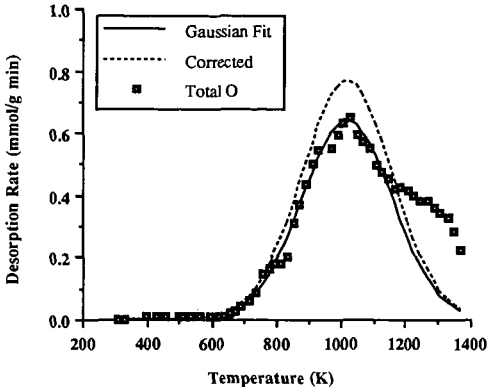

Figure 3. 100K/min total oxygen TPD spectrum from Pittsburgh #8 coal char gasified to 10% burn-off in 0.1MPa of O_2 at 723K, and Gaussian fits; both direct and "corrected."

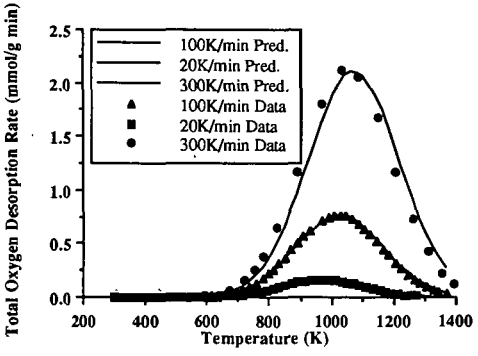

Figure 4. Total oxygen TPD spectra as a function of linear heating rate for Pittsburgh #8 coal char burned-off to 10% in 0.1MPa O_2 at 723K; both "corrected" data and predictions.

MASS SPECTROMETRIC STUDIES OF THE CHEMICAL COMPOSITION OF COAL TARS PRODUCED IN A LAMINAR FLOW REACTOR

Robert Lo, Ronald J. Pugmire*, Thomas H. Fletcher**,
and Henk L.C. Meuzelaar

Center for Micro Analysis and Reaction Chemistry
*Department of Fuels Engineering
University of Utah, Salt Lake City, UT 84112
**Sandia National Laboratories, Livermore, CA

ABSTRACT

Curie-point desorption in combination with Gas Chromatography/Mass Spectrometry (GC/MS) and, alternatively, with direct Low Voltage Mass Spectrometry (LV-MS) was used to investigate the chemical composition and structure of condensed tar vapors produced during rapid devolatilization (heating rate ~ 10,000 K/sec) of carefully sized coal particles representing the Beulah Zap, Big Blue, Illinois #6, Pittsburgh #8, and Pocahontas #3 seams, respectively, using the laminar flow reactor described by Fletcher et al [1]. at two gas temperatures (1050 K and 1250 K).

Tar samples were collected by means of a special probe [1] at different points downstream of and corresponding to residence times between 70 and 250 msec. GC/MS analyses of the corresponding tars indicate that the degree of aromaticity increased rapidly as a function of residence time at the 1250 K gas temperature condition. Moreover, at 1250 K devolatilization is complete within 70 msec and beginning secondary gas phase reactions of tar vapors (viz. marked increases in PNAH content and corresponding decreases in phenolic components) are observed within less than 100 msec. However, at 1050 K the coal devolatilization process appears to be barely complete after 250 msec and little or no evidence of secondary gas phase reactions is found.

INTRODUCTION

Recent devolatilization studies [1-5] have identified the rates and the temperature regimes of pulverized coal devolatilization as a function of heating rate, final temperature, and coal type. Careful particle temperature measurements during devolatilization at rapid heating conditions [1-2] have eliminated many uncertainties caused by estimations of particle temperatures in early studies.

Current devolatilization models have advanced beyond one-step Arrhenius kinetics to descriptions of the bonding structure in the coal, metaplast, and tar [6-9]. Other models include detailed empirical correlations to estimate yields of tar products from elemental compositions of the parent coal [10], as well as mechanism to describe the evolution of the physical structure of char particles [11]. Most of these models presume a mechanisms for generation of metaplast during pyrolysis, followed by release of lighter fractions of the metaplast as tar vapor, where tar is commonly defined as pyrolysis products that condense at room temperature and pressure. It is clear that quantitative experimental investigations of the evolution of the chemical structure of solid and condensible pyrolysis products (char and tar) are critical to the understanding of coal devolatilization mechanisms.

The present study addresses the characterization of condensible tar vapors, produced by rapid (~10^4 K/sec) heating of pulverized coals in a laminar flow reactor. Curie-point desorption GC/MS and

direct Low Voltage MS methods were used to characterize tar samples at the molecular level and to elucidate some of the underlying reaction mechanisms.

EXPERIMENTAL

Reactor and Sample Collection System:

Experimental details regarding the particle temperature measurements and sample collection system were previously published [1], and hence only a brief discussion will be given here. The pyrolysis studies were performed in 100% nitrogen in a laminar flow reactor [1]. Transparent (quartz flass) flow reactor walls allow radiant emission from the coal particles to be monitored at any axial location. Two gas temperature conditions were used in this study, with maximum centerline gas temperatures of 1050 and 1250 K.

An infrared sizing pyrometer system was used to measure size, temperature, and velocity of individual particles in the flow reactor at different axial locations. Typical standard deviations in measured particle temperatures are 5 K for pure carbon spheres (Spherocarb) and 30 K for coal particles. A water-cooled, helium-quench probe was used to collect solid samples iso-kinetically. A virtual impactor and three-stage Andersen cyclone system were used to aerodynamically separate char particles from condensed tar vapors and aerosols. Tars were collected on polycarbonate filters following the separation system [1].

Collected tars were shipped overnight to the analytical facility frozen in an ice chest and stored at -90 C. Five milligrams of the tar samples were suspended in 1 ml of Spectrograde methanol and the homogeneity of each suspension enhanced with a vibrating mixer.

Curie-Point GC/MS and Low Voltage MS Analyses:

GC/MS analyses of the tar samples were performed using a Hewlett-Packed 5890 chromatograph with a 15 m x 0.25 mm i.d. x 0.25 μm film thickness DB-5 column (J&W Scientific). The conditions used in GC/MS were as follows : electron energy 70 eV, Ion Trap Dector (ITD, Finnigan MAT) scanned from m/z 40-450 at 1 scan/sec, pyrolysis time 2 sec, 610 C Curie-point wires in an inlet set at 250 C. The column was temperature programmed from 40-300 C at 15 C/min.

LV-MS experiments were carried out using an Extranuclear Model 5000-1 Curie-point pyrolysis MS system. Twenty five microgram quantities of tar sample were coated on ferromagnetic wires from methanol suspensions. The wires were inserted into borosilicate glass reaction tubes and introduced into the vacuum system of the mass spectrometer. The ferromagnetic wires were inductively heated at approx. 100 C/s to an equilibrium temperature of 610 C. Total heating time was 10 s. LV-MS conditions were as follows : electron ionization at 12 eV (set value), scanning rate 1000 amu/s, total scanning time 20 s, mass range scanned m/z 40-260.

RESULTS AND DISCUSSION

Low Voltage mass spectra of tars obtained by Curie-point desorption directly in front of the ion source and representing two different coals are shown in Figure 1a-e. Comparison of the Beulah Zap tar sample produced at 1250 K and collected after 70 msec with the corresponding 250 msec sample shows major changes characterized by a marked decrease in hydroxyaromatic signals (e.g., alkylsubstituted phenols, dihydroxybenzenes and naphthalenes) accompanied by a strong increase in polycondensed aromatic hydrocarbons, e.g., phenanthrenes and pyrenes, in the 250 msec sample. Apparently, this marked change is due to secondary reactions. Especially the dominance of unsubstituted

pyrene among the various alkylsubstituted homologs is a telltale sign of high temperature gas phase reactions and may perhaps be seen as a first step in the direction of soot formation.

The Beulah Zap tar pattern at 70 msec, on the other hand, compares well with direct Curie-point pyrolysis mass spectra of North Dakota coal [12], indicating that at 70 msec primary pyrolysis products (e.g., dihydroxybenzenes) still dominate, although the yield of polycondensed aromatic hydrocarbons e.g., (alkyl) phenanthrenes, is already higher than would be observed under vacuum micropyrolysis conditions. The tar patterns of Pittsburgh #8 coal at 1250 K (Figures 1c and d) are in excellent agreement with these observations. Again the short residence time pattern (80 msec) corresponds quite well with the Curie-point pyrolysis mass spectrum, e.g. as reported by Chakravarty et al. [13], whereas the long residence time (250 msec) tar shows a pronounced shift towards polycondensed aromatic hydrocarbon. Due to the higher rank (hvAb) of the Pittsburgh #8 coal, however, the short residence time spectrum (Figure 1c) is clearly different from that of the Beulah Zap lignite, e.g., with regard to the lower (alkyl) dihydroxybenzene intensities and increased (alkyl) naphthalene series. This is in agreement with trends observed in earlier Py-MS studies of coals of different rank [14].

Finally, the effect of temperature is briefly illustrated in Figure 1e (Pittsburgh #8, 1050 K). In spite of the long residence time (250 msee) the MS pattern in Figure 1e is highly simlar to that in Figure 1c, indicating the absence of marked secondary reactions at this lower temperature.

The usefulness of Curie-point desorption GC/MS techniques for confirming and further elucidating the above discussed trends and effects is illustrated in Figures 2 and 3. Illinois #6 tars produced at 1250 K and collected after 70 msec (Figure 2) and 250 msec (Figure 3), respectively, show an approx. 100 X reduction in the relative abundance of (alkyl) phenols accompanied by a 10 X increase in selected polycondensed (4-6 ring) aromatic hydrocarbons.

Although in the current experimental set-up absolute tar yields cannot yet be established with sufficient certainty to enable precise quantitative studies, e.g., for determining the kinetics of the gas phase condensation reactions, changes in the relative composition as a function of residence time are illustrated for Big Blue tars at 1050 K in Figure 4 and for Beulah Zap, Illinois #6 and Pittsburgh #8 tars in Figures 5a, b and c, respectively. At 1050 K fragment ions of aliphatic hydrocarbons (e.g., at m/z 85, 57, 43, see Figure 4c) dominate the short residence time (120 msec) tar. Based on previous, time-resolved pyrolysis field ionization MS studies [15], early evolution of aliphatic hydrocarbon moieties during devolatilization of low rank coals is likely to represent the desorption of low MW biomarker type compounds, e.g., branched and/or alicyclic terpenoids. At 150 msec the relative intensities of the aliphatic hydrocarbon moieties are starting to decrease due to the strong increase in hydroxyaromatics. e.g., dihydroxybenzenes at m/z 110 and 124 (Figure 4b). Finally, at 250 msec, the relative abundance of compounds such as naphthols, are still increasing suggesting that the devolatilization process may not yet be fully completed. On the other hand, suspected secondary reaction products such as pyrenes and perylenes are starting to increase slightly. Nevertheless, the relative abundance of the highly reactive dihydroxybenzenes appears to be more or less stable. Altogether, our tentative conclusion is that at 1050 K the devolatilization process of Big Blue coal is close to being complete after 250 msec.

A drastically different picture is obtained at 1250 K, as illustrated for the three coals in Figure 5. Compounds such as pyrenes, perylenes and even picenes appear to be increasing right from the start, whereas the relative abundances of naphthols and even phenanthrenes are decreasing after approx. 100-150 msec., suggesting the occurrence of marked secondary gas phase reactions. Unfortunately, at the time of writing no tar samples had been produced at intermediate temperatures, e.g., 1150 K. If the above observations at 1050 and 1250 K are correctly interpreted, devolatilization at 1150 K should be completed within 100-200 msec and the onset of secondary gas phase reactions should become clearly visible at longer residence times.

CONCLUSIONS

Based on the Curie-point GC/MS and Low Voltage MS analyses of the tar formed during devolatilization of Beulah Zap, Big Blue, Illinois #6, Pittsburgh #8, and Pocahontas #3 coals, the following conclusions are reached:

1. The degree of aromaticity increases rapidly as a function of residence time at the 1250 K gas temperature.
2. However, little increase in aromaticity can be detected at the 1050 K gas temperature.
3. At a gas temperature of 1250 K devolatilization is complete within 70 msec and secondary gas phase reactions of tar vapors can be observed within 100 msec.
4. At 1050 K, the devolatilization process appears to be more or less complete after 250 msec.
5. In order to study complete devolatilization process and the possible onset of secondary reactions, further experiments should be conducted at an intermediate temperature, e.g., 1150 K.

ACKNOWLEDGEMENTS

This work was sponsored by the Advanced Combustion Engineering Research Center (funds for this Center are received from the National Science Foundation, the State of Utah, 23 industrial participants and the U.S. Department of Energy) and by the Consortium for Fossil Fuel Liquefaction Science (DOE grant no. UKRF-4-23576-90-10).

REFERENCES

1. Fletcher, T.H., Comb & FLame, 78, pp.223-226, 1989.
2. Solomon, P.R., Serio, M.A., Carangelo, R.M., and Markham, J.R., Fuel 65, pp.182, 1986.
3. Freihaut, J.D., and Proscia, W.M., Energy & Fuels, 3, pp. 625, 1989.
4. Gibbons-Matham, J., and Kandiyoti, R., Energy & Fuels, 2, pp. 505, 1988.
5. Serio, M.A., Hamblen, D.G., Markham, J.R., and Solomon, P.R., Energy & Fuels, 1, pp. 138, 1987.
6. Niksa, S., and Kerstein, A.R., Comb & Flame, 66, pp. 95, 1986.
7. Solomon, P.R., Hamblen, D.G., Carangelo, R.M., Serio, M.A., and Deshpande, G.V., Energy & Fuels, 2, pp. 405, 1988.
8. Grant, D.M., Pugmire, R.J., Fletcher, T.H., and Kerstein, A.R., Energy & Fuels, 3, pp. 175, 1989.
9. Fletcher, T.H., Kerstein, A.R., Pugmire, R. J., and Grant, D.M., accepted for publication, Energy & Fuels, 1989.
10. Ko, G.H., Sanchez, D.M., Peters, W.A., and Howard, J.A., Twenty-Second Synp. (Int.) on Comb., The Combustion Institute, pp. 115, 1988.
11. Oh, M.S., Peters, W.A., and Howard, J.B., AIChE Journal, 35:5, pp. 775, 1989.
12. Metcalf, G.S., Windig, W., Hill, G.R.,and Meuzelaar, H.L.C., Internatioanl Journal of Coal Geology, 7, pp. 245-268, 1987.
13. Chakravarty, T., Windig, W., Taghizadeh, K., and Meuzelaar, H.L.C., Energy & Fuels, 2, pp. 191-196, 1988.
14. Meuzelaar, H.L.C., Harper, A.M., Hill, G.R., and Given, P.H., Fuel, 63:5, pp. 640-652, 1984.
15. Yun, Y., Meuzelaar, H.L.C., Simmleit, N., and Schulten, H.-R., "The Mobile Phase in Coal Viewed from a Mass Spectrometric Perspective", ACS Symp. Series, 1990, in press.

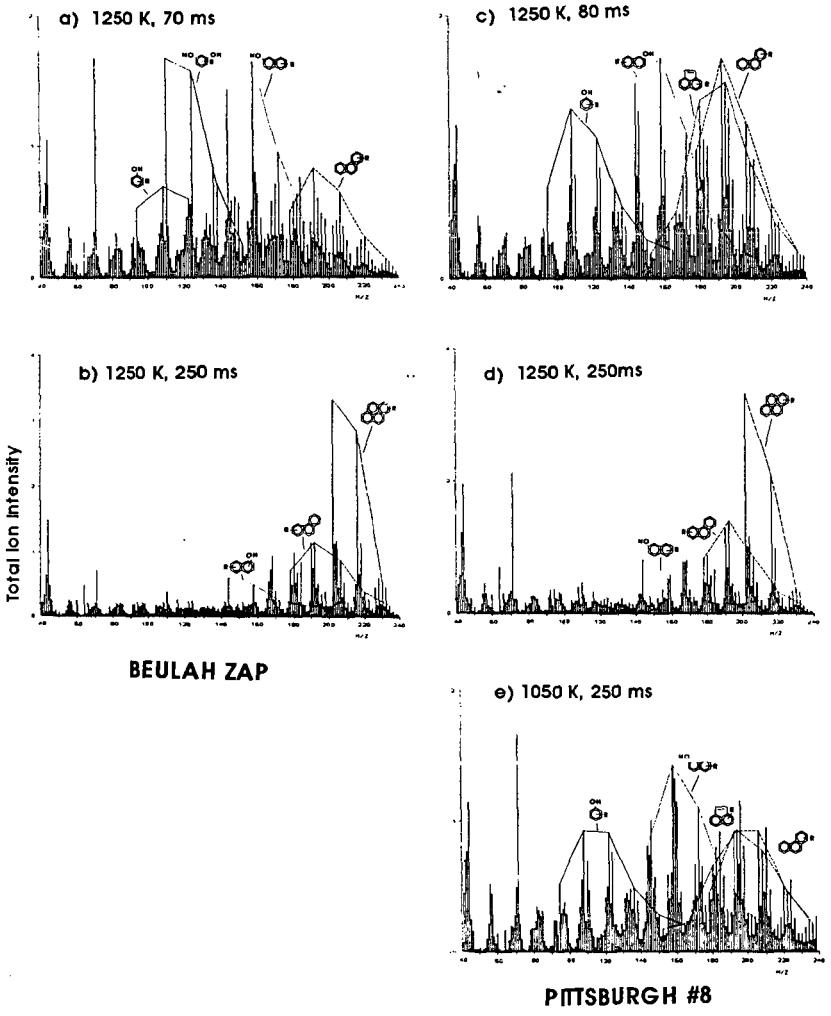

Figure 1. Curie-point desorption mass spectra of Beulah Zap and Pittsburgh #8 tars showing the effects of coal rank (a and b vs. c, d and e), residence time (a and c vs. b, d and e) and gas temperature (c vs. a, b, c and d).

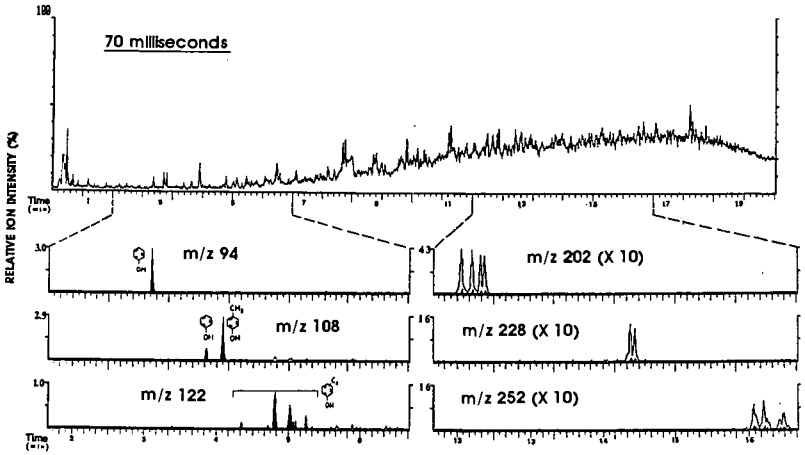

Figure 2. Curie-point desorption GC/MS profiles of Illinois #6 tar obtained at 1250 K after 70 msec. Total ion chromatogram (upper profile) and selected ion chromatograms (lower profiles) show relative abundance of (alkyl) phenols vs. pyrenes, perylenes and picenes.

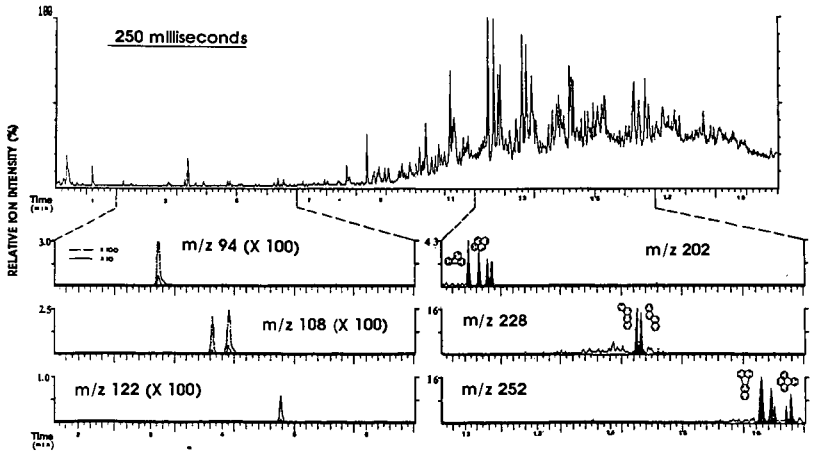

Figure 3. As Figure 2 but obtained after 250 msec. Note 100-fold decrease in (alkyl) phenol as opposed to 10-fold increase in polynuclear aromatic hydrocarbons.

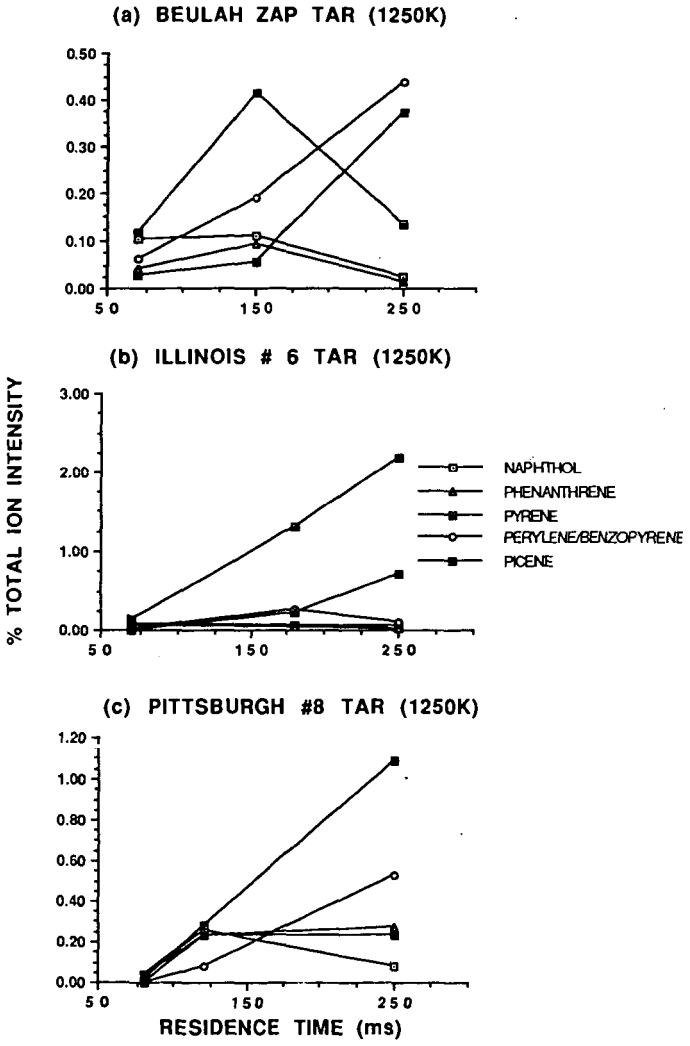

Figure 5. As Figure 4 but representing tars from 3 different coals obtained at 1250 K.

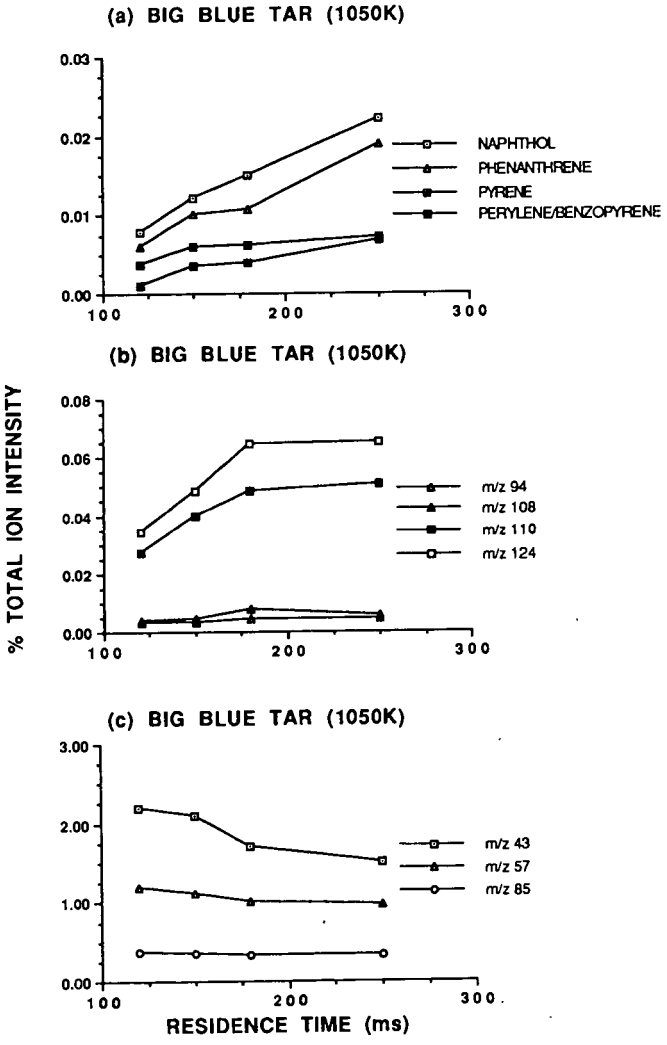

Figure 4. Relative abundance of selected ion profiles in Curie-point desorption GC/MS data on Big Blue tar samples obtained at 1050 K and at different residence times.

THE INTERPRETATION OF SECONDARY INTERACTIONS DURING TEMPERATURE PROGRAMMED DESORPTION OF OXYGEN COMPLEXES IN TERMS OF CHAR POROSITY MORPHOLOGY

P.J. Hall and J.M. Calo
Chemical Engineering Program
Division of Engineering
Brown University
Providence, RI 02912

Keywords: Coal char gasification; secondary interactions; coal char porosity development.

INTRODUCTION

Our recent work [1] concerning temperature programmed desorption (TPD) of oxygen complexes from oxidized coal char surfaces has demonstrated that secondary interactions during the thermal desorption process can convolute the resultant spectra. Their effects are generally enhanced by the presence of inorganic mineral matter impurities and seem to be influenced by the nature of the char porosity [2]. However, the relationship between pore morphology and the behavior of these secondary interactions was not systematically explored in our previous work performed on coal chars at constant burn-off [1]. In the current communication we investigate the variation of the extent of secondary interactions with char burn-off in oxygen. As shown, the results of this work suggest that the behavior of secondary interactions during TPD exhibit some potential as a diagnostic technique for monitoring the variation and development of char porosity; perhaps as a complement to other methods such as gas adsorption.

We have identified two different types of secondary interactions [1]. One involves the reaction of desorbed "free" CO in the process of out-transport to the bulk gas phase with other oxygen surface complexes to produce CO_2. This is primarily manifested as a reflection or satellite peak under primary CO desorption features, the largest of which is typically centered *ca.* 1000K. The other type of secondary interaction involves rechemisorption of "free" CO onto unoccupied active sites to form more stable complexes [1]. This is usually manifested as a high temperature peak or shoulder in TPD spectra, typically centered *ca.* 1200K. It will be demonstrated here that secondary CO_2 production appears to take place in the smaller pores of the char (i.e., the microporosity), while CO rechemisorption takes place primarily in the larger pores.

EXPERIMENTAL

Samples of two precursor coals -- Wyodak and Pittsburgh #8 -- were obtained from the Argonne Premium Coal Sample Bank. The coals were pyrolyzed in ultrahigh purity helium at 1273K with a soak time of one hour. Care was taken to insure that the coals did not come into contact with

oxygen during handling.

The chars from this treatment of the two coals exhibit distinct pore morphologies. During slow carbonization, and in the complete absence of oxygen, Pittsburgh #8 passes through a fluid state during which most of its original microporosity is lost [3]. The resultant char has a very low surface area and develops porosity during subsequent gasification. Conversely, Wyodak is a subbituminous coal which does not proceed through a fluid phase upon carbonization. Consequently, much of the original porosity present in the coal is preserved or enhanced during carbonization. A number of studies indicate that the original porosity consists of a random network of pores with extensive "ink-bottle"-type restrictions and a significant amount of "closed" porosity [3,4]. Our conclusions support these observations. Therefore, gasification of the Wyodak coal char not only develops new porosity, but also tends to enlarge restrictions and render previously closed pores accessible.

Details of the TPD apparatus and the experimental procedures are described elsewhere [1]. The typical sample size was ~10 mg, and ultrahigh purity helium was used as the carrier gas. A heating rate of 100K/min was used for the experiments reported here because this gave good peak resolution [2] and reasonable gas desorption rates. Also, our results [2] suggested that this heating rate tended to maximize the effects of secondary interactions for a number of different coal chars. Char gasification was performed in a TGA apparatus in 0.1 MPa of O_2 at the selected temperature. The 77K N_2 isotherms were measured in a Quantachrome Quantasorb gas adsorption apparatus. No significant differences were observed between N_2 isotherms and CO_2 isotherms obtained at higher temperatures for these chars.

RESULTS AND DISCUSSION

In a companion paper in this symposium [5], it is demonstrated that total oxygen TPD spectra from coal chars can be deconvoluted from secondary interactions by fitting the leading edge of the principal desorption feature to a Gaussian distribution. The residual spectrum, typically centered *ca.* 1200K, is believed to be primarily due to rechemisorbed CO. Typical total oxygen TPD spectra for Wyodak coal char gasified to varying extents are presented in Figure 1. The CO desorption spectra can also be fit to Gaussians in a similar fashion, since CO accounts for the majority of the total oxygen desorbed. For our purposes here, the resultant integral under the CO Gaussian will be termed "1000K CO," and that under the residual CO will be termed "1200K CO." Due to the relatively low amounts of primary CO_2 formed at the lower temperatures, all the CO_2 will be referred to as secondary CO_2.

Figures 2 and 3 show how the three contributions to total oxygen desorption -- "1000K CO," "1200K CO," and "secondary CO_2" -- vary as a function of burn-off for Wyodak and Pittsburgh #8 coal chars, respectively. These figures reveal some interesting behavior. Consider for example the analysis of these data presented in Figure 4. As shown, the "1200K CO/secondary CO_2"

ratio increases continuously with increasing burn-off for the Wyodak char, while it remains essentially constant for the Pittsburgh #8 coal char. This will be shown to be consistent with the expected porosity development for these chars with burn-off.

The available evidence suggests that the 1200K oxygen complexes arise primarily from "free" CO rechemisorbed during the TPD process, and not from just chemically different (i.e., from the 1000K complexes) oxygen complexes formed during steady-state gasification/oxidation. If these complexes did arise from the latter source, their population would tend to *increase* relative to the "low temperature" complexes with exposure under gasification conditions, rather than *decrease,* as generally observed. In fact, for both Wyodak and Pittsburgh #8, the 1200K CO shoulder actually decreases at high burn-off. Product CO formed during isothermal, steady-state gasification is not appreciably chemisorbed because CO chemisorption has been shown to be a highly activated process with a low sticking probability [6]. As a consequence, at the relatively low temperatures used for oxygen gasification, the rate of rechemisorption of product CO is too low to occupy the high energy sites available under gasification conditions. Moreover, any sites that may be accessible under these conditions would react preferentially with oxygen, which is present in considerably greater amounts and exhibits much greater reactivity towards the formation of stable complexes. During TPD, however, the high temperatures experienced during the nonisothermal heating process in the absence of oxygen serves provides the conditions necessary to "fix" a certain fraction of the desorbed CO.

The available evidence suggests that secondary CO_2 formation is a phenomenon associated with the smaller pores (e.g., the micropores) rather than the larger pores. For example, it has already been shown in Figure 4 that the "1200K CO-to-secondary CO_2" ratio is a minimum for zero burn-off Wyodak, which exhibits a "Type I" N_2 adsorption isotherm (as shown in Figure 5), characteristic of microporous materials. Further evidence derives from other oxidation studies where, for example, it has been reported that, due to the large size of the nitrate ion, nitric acid does not oxidize the surface within the microporosity, but rather only that accessible in the meso- and macroporosity, as well as the external surface [7]. TPD spectra on such nitric acid oxidized chars exhibit no secondary CO_2 in comparison to gas oxidized chars [7]. We obtained similar results from hydrogen peroxide-oxidized chars [8]. If secondary CO_2 production did take place appreciably in the larger pores, then significant amounts of secondary CO_2 would be expected from such chars. On the other hand, significant, discernible 1200K CO, which is believed to be due to CO rechemisorption, was evident upon TPD for both nitric acid and hydrogen peroxide-oxidized chars [8]. The reasons for this behavior are still a matter for speculation, but it may be that secondary CO_2 production takes place primarily in micropores for the same reason that a normal distribution of bond energies occurs [5]; that is, the low temperature, less stable complexes would also tend to be more reactive towards attack by "free" CO as they would be towards desorption. In a similar fashion, there is as yet no definitive evidence as to whether CO rechemisorption can occur in micropores to an appreciable extent. However, it is noted that the zero burn-off Wyodak which is known to have significant microporosity does not exhibit any

1200K CO. It may be that CO rechemisorption cannot compete with the more favorable secondary CO_2 production in the micropores. In any case, any CO that might be rechemisorbed in micropores may also participate in secondary CO_2 formation, and thus may not survive to desorb in the higher temperature peak *ca.* 1200K.

In summary then, it is hypothesized that secondary CO_2 formation takes place primarily in the more restrictive porosity, such as the microporosity, whereas CO re-chemisorption is favored in the larger pores. Therefore, the two secondary interactions are in a sense complementary and sensitive to different aspects of the char porosity. In this manner, the decrease in the relative magnitudes of both secondary interactions at high burn-off for Wyodak, as indicated in Figure 2, is consistent with a reduction in total porosity as a result of pore collapse at high burn-off.

It is of interest to compare these observations with information available from adsorption isotherms. 77K N_2 adsorption isotherms for gasified Wyodak and Pittsburgh #8 coal chars are presented in Figures 5 and 6, respectively. Examination of Figure 5 shows that at zero burn-off, the Wyodak char exhibits a classical "Type 1" isotherm [9], characteristic of a microporous material. Figure 2 shows that the secondary CO_2 is relatively high, and that there is virtually no 1200K CO for this char. Therefore the interpretations of both isotherm and TPD spectra are consistent for this char. At 15.2% burn-off, the isotherm appears to have evolved into something in between a "Type 1" and "Type 2". This suggests that at this stage micropores are still a significant part of the Wyodak porosity, but that larger porosity is also developing with burn-off [9]. Again, this is consistent with the increase in the relative amount of 1200K CO to secondary CO_2, as shown in Figure 4. At 48.6% and 61.8% burn-off, the isotherms appear to more closely approach "Type 2" behavior, indicative of larger porosity, and, consistently, secondary CO_2 decreases and 1200K CO increases significantly in this range. The corresponding N_2 surface area goes through a maximum between 15.2% and 48.6% burn-off. Following the maximum, the general tendency is for microporosity to be lost at the expense of larger pores.

For the Pittsburgh #8 char, the isotherms shown are similar for all degrees of burn-off, with some definite "Type 2" behavior characteristic of materials with significant mesoporosity. This is consistent with the even maintenance of the relative contributions of the two different types of oxygen over the entire burn-off range, as shown in Figure 4.

Proper interpretation of the TPD spectra may give additional insight into the nature of the porosity. For example, the isotherms for Wyodak burned-off to 61.8% at 623K and Pittsburgh #8 burned-off to 46% at 723K in Figures 5 and 6 are quite similar in shape, except that the Wyodak isotherm is about a factor of two greater in amplitude.. Therefore, if one were to draw conclusions on the pore morphology based upon this evidence alone the conclusion would be that they were chars of similar pore structure. However, Figure 4 reveals that for the 61.8% gasified Wyodak, the ratio of 1200K CO to secondary CO_2 is 1.47, compared to 0.36 for the 46% gasified Pittsburgh

#8. This suggests that a much higher proportion of the surface area is present in restrictive porosity for the Pittsburgh #8 coal char in this particular case.

At this point it should be noted that integral measures of the various contributions to desorbed oxygen may not be a good indicator of total surface area or pore volume. This is especially evident for the Pittsburgh #8 coal char for which the total oxygen coverage increases steadily with burn-off in Figure 3, whereas the N_2 surface area goes through a maximum between 25 and 46% burn-off (*cf.* Figure 6). It has been well established that total surface area, as measured by gas adsorption techniques, is generally not as good an indicator of char reactivity as is active surface area, as measured by oxygen chemisorption. The oxygen complexes that give rise to secondary interactions are obviously more related to active surface area and thus may behave in a similar fashion. However, it has also been shown that for some chars the amount of oxygen adsorbed under chemisorption conditions can be a fraction of that adsorbed under gasification conditions [10], and also that the amount of chemisorbed oxygen can yield larger apparent surface areas than the total surface area measured by gas adsorption [11]. Therefore, it is not clear at this stage exactly how the integrated amounts of the three contributions to desorbed oxygen are related to the absolute amount of macro-, meso-, and microporosity. In any case, the principal point to be made here is that the *relative* magnitudes of these contributions seem to be related to the char porosity morphology, and, moreover, seem to be quite sensitive to morphological changes during gasification.

CONCLUSIONS

The kinetics of secondary interactions during thermal desorption processes are not yet sufficiently well understood to allow a more quantitative treatment of pore morphology at this time. However, we have demonstrated that the *relative* magnitudes of secondary interactions appear to be sensitive to pore morphology. Although the total amount of surface complex may not be a good indicator of total surface area, the *relative* extents of secondary interactions can reveal information about the pore morphology that is difficult to derive from adsorption isotherm analysis. Thus, the two methods are complementary.

Acknowledgement. This work was supported by the Morgantown Energy Technology Center of the Department of Energy under Contract No. DE-AC21-MC23284.

REFERENCES

1. Hall, P.J.; J.M. Calo *Energy & Fuels* **1989,** *3,* 370.
2. Hall, P.J.; Calo J.M.; Lilly W.D. *Proc. Intl. Conf. Carbon, Carbon'88,* **1988,** McEnaney, B., Mays, T.J., eds.; IOP Publishing Company, Bristol, UK, p. 78.
3. Mahajan, O.P. in *Coal Structure* **1982,** Meyers, R.A., ed., Academic Press, NY, Ch. 3.
4. Larsen, J.W.; Wernett, P. *Energy & Fuels***1988,** *2,* 719.
5. Hall, P.J.; Calo, J.M. *ACS Div. Fuel Chem. Prepr.* **1990,** "Energetic distributions of oxygen

surface complexes on porous carbons and chars," this symposium.
6. Marchon, B., Carrazza, J., Heinemann, H. and Somorjai, G.A *J. Phys. Chem.* **1988,** *92,* 5447.
7. Otake, Y., Ph.D. Dissertation, **1986,** The Pennsylvania State University.
8. Hall, P.J., J.M. Calo, H. Teng, E.M. Suuberg, J.A. May, and W.D. Lilly, *ACS Div. Fuel Chem. Prepr.* **1989,** *34,* No. 1, 112.
9. Gregg, S.J.; Sing K.S.W. *Adsorption, Surface Area and Porosity* **1982,** 2nd ed., Academic Press London, UK.
10. Hall, P.J.; Calo, J.M.; and Otake *Proc. Nineteenth Biennial Conf. Carbon,* **1989,** p. 594.
11. Taylor, R.L., Ph.D. Dissertation, **1982,** The Pennsylvania State University.

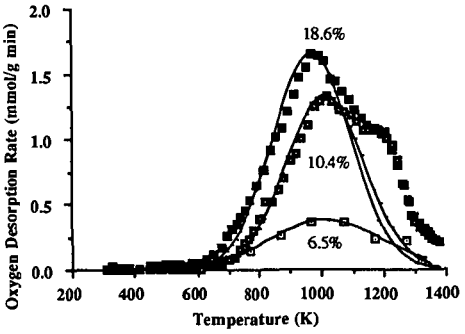

Figure 1. 100K/min TPD spectra total oxygen desorption spectra from Wyodak coal char gasified to varying extent in 0.1MPa oxygen at 573K and their Gaussian fits.

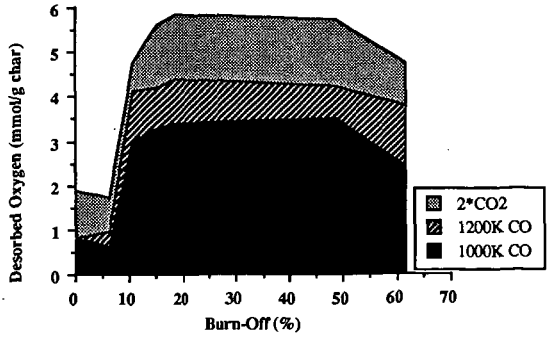

Figure 2. Desorbed oxygen distribution vs. burn-off for Wyodak coal char.

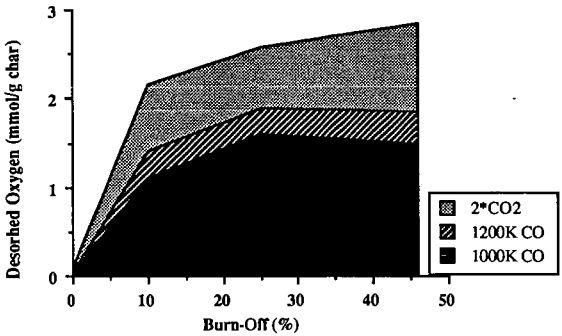

Figure 3. Desorbed oxygen distribution vs. burn-off for Pittsburgh #8 coal char.

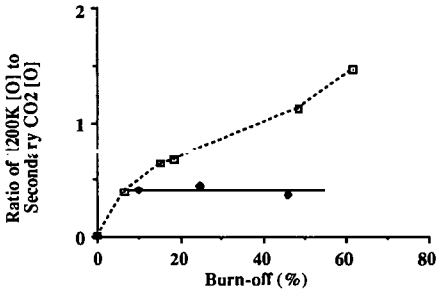

Figure 4. Variation of the ratio of [O] from 1200K CO to [O] from secondary CO_2 production as a function of char burn-off. --- Wyodak coal char; — Pitsburgh #8 coal char.

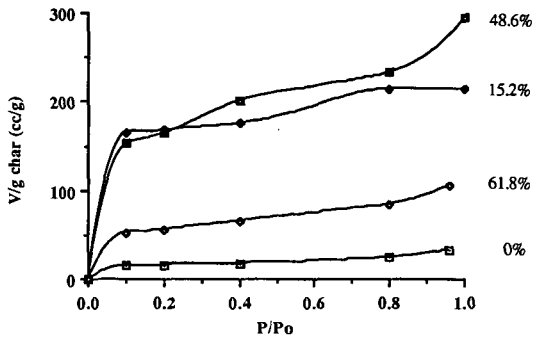

Figure 5. 77K nitrogen adsorption isotherms for Wyodak coal char gasified to varying extents in 0.1MPa O_2 at 623K.

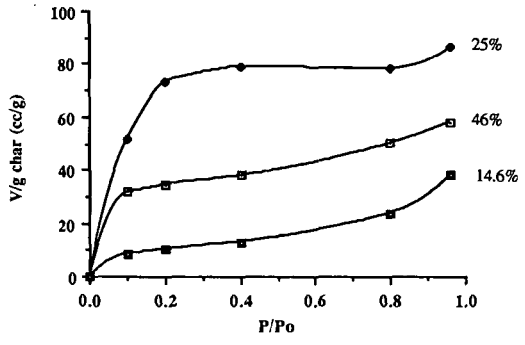

Figure 6. 77K nitrogen adsorption isotherms for Pittsburgh #8 coal char gasified to varying extents in 0.1MPa O_2 at 623K.

LASER PYROLYSIS-TRANSFER LINE CHROMATOGRAPHY/MASS SPECTROMETRY OF SINGLE, LEVITATED COAL PARTICLES

Waleed Maswadeh, Neil S. Arnold and Henk L.C. Meuzelaar
Center for Micro Analysis & Reaction Chemistry
University of Utah, Salt Lake City, UT 84112

Keywords: coal devolatilization, laser pyrolysis, mass spectrometry

INTRODUCTION

A laser pyrolysis transfer line gas chromatograph/mass spectrometry (laser Py-TLGC/MS) system based on the combination of an electronically pulsed CW CO_2 laser with an electrodynamic balance (EDB), a heated capillary ("transfer line") GC column and an ion trap mass spectrometer (ITMS) was constructed (Figure 1), as described previously [1].

The main purpose of the system is to study the devolatilization behavior of single, levitated coal particles at very high heating rates, e.g., 10^5-10^6 K/sec, while comparing the composition of the devolatilization products to those observed at much lower heating rates, e.g., 10^{-2}-10^2 K/sec. At the lower heating rates, several different time-resolved Py-MS techniques, including vacuum thermogravimetry/mass spectrometry (TG/MS) [2], Curie-point Py-MS [3] and pyrolysis Field Ionization mass speetrometry (Py-FIMS) [4] are available to provide kinetic information on coal devolatilization processes. Although kinetic parameters obtained at these lower heating rates may be directly applicable to fixed bed or even fluidized bed coal processes, the usefulness of these parameters for pulverized coal combustion processes at heating rates in the 10^4-10^5 K range remains to be determined. The laser Py-TLG/MS system shown in Figure 1, although not suitable for determining kinetic parameters at these high heating rates, enables us to verify the mechanistic aspects of coal devolatilization reactions. If the main coal devolatilization mechanisms remain unchanged at 10^5-10^6 K/sec, it may be argued that it should be possible to extrapolate the kinetic parameters obtained by the abovementioned TG/MS, CuPy-MS and Py-FIMS experiments.

CO_2 laser devolatilization experiments on single levitated coal particles using EDB type particle trapping devices have previously been described by several authors [5-7]. However, although successful in measuring particle temperatures and/or weight loss profiles as a function of time none of these prior studies addressed the characterization and identification of the complex mixture of devolatilization products generated during these experiments. To the best of our knowledge, the work reported here represents the first successful attempt to do so.

EXPERIMENTAL

The experimental set-up (Figure 1) consists of an EDB, a 50 w CW CO_2 laser and a Finnigan MAT ITMS system. The particle levitation cell was constructed in such a way as to provide line-of-sight access to the center of the cell for the CO_2 laser beam as well as for visual observation by means of a stereo microscope and for a two-color optical pyrometer (under development). Typical cell operating parameters for levitating a 120 μm dia. Spherocarb particle are: ring electrode 3000 V (60 Hz ac), upper end cap +100 V dc, lower end-cap -100 V dc.

The CO_2 laser (Apollo 3050 OEM) is capable of electronic pulsed beam operation. The 8 mm dia. beam is split equally into 2 opposing beams focussed at the center of the levitation cell (beam waist ca. 400 μm, power density ca. 4-10 MW/m^2). A co-linear parfocal HeNe laser beam permits positioning the levitated particle in the optical and electrical center of the cell. Two IR detectors measure the integrated pulse and time-resolved pulse energy.

A heated transfer line column (2m x .18 mm DB5) equipped with a special air sampling inlet [8] enables intermittent sampling of volatiles from the center of the levitation eell into the ITMS vacuum system.

Feasibility studies were performed on 120-150 μm Spherocarb particles impregnated with ng amounts of an alkylnaphthalenes mixture and other selected model compounds. Finally, a series of experiments was performed with actual coal particles in the 100-130 μm size range, prepared by careful sieving of coals from the Argonne National Laboratory Premium Coal Sample (ANL-PCSP) program.

RESULTS AND DISCUSSION

Before applying the laser Py-TLGC/MS technique to coals, we measured the shot-to-shot reproducibility of the electronically pulsed CW CO_2 laser system. As illustrated in Figure 2 overall linearity of the laser pulse energy in the 1-35 msec range is quite good. However, the cause of the unexpectedly large variation in pulse energy at 20 msec is being investigated further.

System performance was further tested with 120-130 μm sized Spherocarb particles loaded with known quantities of a well characterized mixture of alkylnaphthalenes and related aromatic compounds. Figure 3 shows the time-resolved TLGC/MS profiles obtained by using the 6 ft long heated transfer line between EDB and ITMS as a short capillary column. Various alkylnaphthalene homologs and isomers are readily separated and identified. Moreover, repeated laser pulse heating of the same Spherocarb particle shows that the devolatilization process is virtually complete within the duration of the first pulse (10 msec).

This encouraged us to perform laser Py-TLGC/MS analyses on real coal particles. The resulting TLGC/MS profiles shown in Figures 4 and 5 demonstrate a surprising level of chemical detail. Repeat analyses of Pittsburgh #8 coal shown in Figure 4 demonstrate an acceptable level of shot-to-shot reproducibility in spite of the unavoidably high heterogeneity of 100-150 μm dia. coal particles, Figure 4c illustrates the fact that, at these high heating rates oxygen does not markedly influence the devolatilization process. Apparently, the rapidly expanding and cooling cloud of devolatilization products surrounding the particle effectively protects the hot particle surface from severe oxidative changes.

As mentioned earlier, the main goal of the EDB-ITMS experiment is to verify the effect of high heating rates on devolatilization mechanisms. Assuming that any significant shift in mechanisms should be reflected in changes in the relative abundances of various structural isomers, e.g., alkylsubstituted phenols or naphthalenes, Figure 5 enables a side by side comparison of laser Py-MS profiles and more conventional Curie-point Py-GC/MS profiles obtained on samples of Pittsburgh #8 coal. Obviously, little if any changes in product distributions are observed, when

allowing for interparticle heterogeneity as well as for differences in chromatographic techniques. A high degree of correspondence between coal devolatilization products observed at 10^2 K/sec and at 10^5 K/sec was also found to exist for other ANL-PCSP coals (not shown here).

However, due to the inherently low tar yields of both the Beulah Zap lignite (see Figure 6) and the low volatile bituminous Pocahontas coal satisfactory laser pyrolysis mass spectra of single, levitated particles of these coals proved difficult to obtain. Therefore, it is too early to conclude that no significant mechanistic changes are observed at these high heating rates. Moreover, careful examination of the laser pyrolysis TLGC/MS profiles revealed the absence (or strongly reduced intensity) of dihydroxybenzenes and of long chain (e.g., C_{10}-C_{20}) n-alkane/alkene pairs. Whether these compounds are lost by secondary condensation reactions in the hot outer layers of the particle or by some other chemical or physical process is currently the focus of further investigations.

As noted earlier, a marked degree of interparticle heterogeneity is expected to exist in pulverized coals. Provided that a high level of shot-to-shot reproducibility can be achieved, the laser Py-TLGC/MS approach could become a powerful tool for studying interparticle heterogeneity. A preliminary indication of the effects of interparticle heterogeneity on successive laser Py-TLGC/MS profiles can be obtained from the bivariate plot in Figure 7. The clustering trends observed in the intensities of the peaks at m/z 94+108 and m/z 142+156 appear to be relatively independent of pulse length (except for very short laser pulse deviations which result in incomplete devolatilization reactions). At this point, differences in maceral and mineral composition between different particles are thought to be primarily responsible for the clustering behavior observed in Figure 7.

CONCLUSIONS

In conclusion, laser Py-TLGC/MS appears capable of producing a detailed chemical profile of the devolatilization products from single, levitated coal particles at very high heating rates (~10^5 K/sec), especially when using coals which produce relatively high tar yields. Most devolatilization products detected at these high heating rates appear to be identical to those observed at much lower heating rates, e.g., 10^{-2}-10^2 K/sec, indicating that coal devolatilization mechanisms remain essentially unchanged over some 7 orders of magnitude difference in heating rates!

A few compound classes found to be missing or strongly reduced, e.g., dihydroxybenzenes and long chain aliphatic hydrocarbons, are though to be lost by secondary condensation reactions. Another interesting observation is the absence of marked oxidative phenomena when performing laser pyrolysis TLGC/MS experiments in air rather than under inert atmospheric conditions. Apparently, the rapidly expanding and cooling vapor cloud protects the hot surface of the particle. Finally, it is concluded that interparticle heterogeneity has a marked effect on laser Py-TLGC/MS profiles and that this technique therefore offers a unique opportunity to study the effect of interparticle heterogeneity on coal devolatilization processes.

ACKNOWLEDGEMENTS

This work was sponsored by the Advanced Combustion Engineering Research Center. Funds for this Center are received from the National Science Foundation, the State of Utah, 23 industrial participants, and the U.S. Department of Energy.

REFERENCES

1. Maswadeh, W.M., Roberts, K.A., McClennen, W.H., Meuzelaar, H.L.C., "Laser Pyrolysis Mass Spectrometry of Single Levitated Coal Particles," Proc. 37th ASMS Conf. Mass Spectrom. All. Topics, Miami, FL, 1989.
2. Yun, Y., Meuzelaar, H.L.C., "Simultaneous Thermogravimetric and Mass Spectrometric Observations on Vacuum Pyrolysis of Argonne PCSP Coals," ACS Preprints, Div. of Fuel Chem., Vol. 33, #3, Sept. 1988, pp. 75-84.
3. Chakravarty, T., Windig, W., Hill, G.R., Meuzelara, H.L.C., "Time-resolved Pyrolysis Mass Spectrometry of Coal: A New Tool for Mechanistic and Kinetic Studies", Energy & Fuels, Vol. 2, 1988, pp. 400-405.
4. Yun, Y., Maswadeh, W., Meuzelaar, H.L.C., Simmleit, N., Schulten, H.-R., "Estimation of Coal Devolatilization Modeling Parameters from Thermogravimetric and Time-Resolved Soft Ionization Mass Spectrometric Data," ASMS, Miami, FL 1989
5. Phuoc, T.X., Maloney, D.J., "Laser Pyrolysis of Single Coal Particles in An Electrodynamic Balance," 22nd Symp. (Intl.) on Combustion (The Combustion Institute), 1988, pp. 125-134.
6. Smith, M.W., McMillen, D.F., Malhotra, R., Platz, R., "Laser Pyrolysis of an Entrained Stream of Coal Particles", ACS Preprints, Div. of Fuel Chem., Vol. 35, #2, April 1990, pp. 455-466.
7. Spjut, R.E., Sarofim, A.F., Longwell, J.P., "Laser Heating and Particle Temperature Measurement in an Electrodynamic Balance," Langmuir, Vol. 1, #3, 1985.
8. Arnold, N.S., Roberts, K.A., McClennen, W.H., Meuzelaar, H.L.C., "Direct On-line Vapor Mounting by Transfer Line GC/MS," 37th ASMS Conf. Mass Spectrom. All. Topics, Miami, FL, 1989.

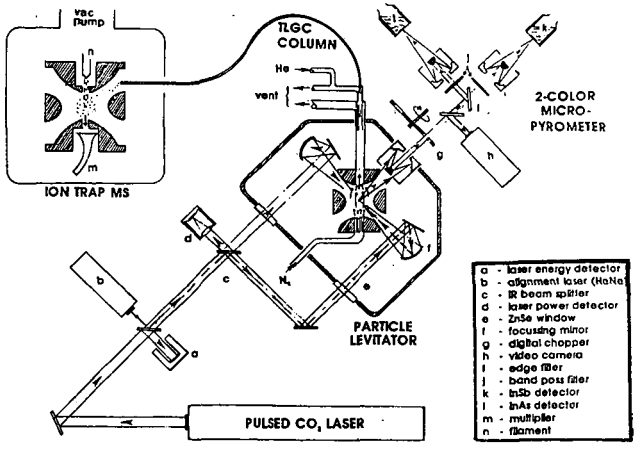

Figure 1. Schcmatic diagram of CO_2 laser pyrolysis TLGC/MS system consisting of a pulsed CO_2 laser, an electrodynamic balance ("particle levitator), a transfer line GC column and an ion trap mass spectrometer. The 2 color micropyrometer is currently under development.

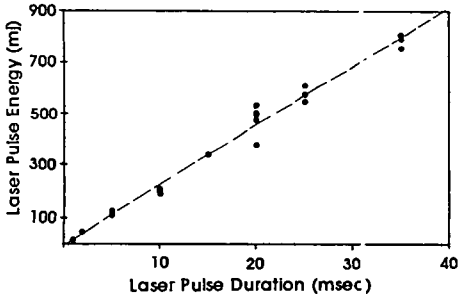

Figure 2. Variability in laser pulse energy at different pulse lengths.

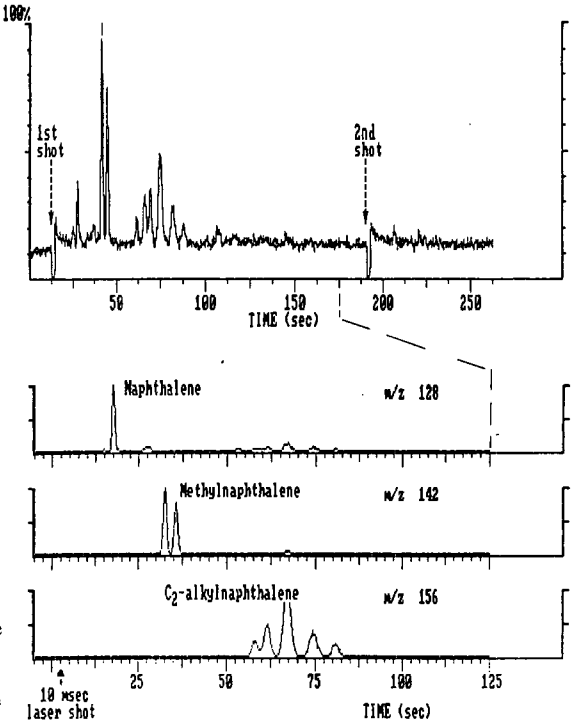

Figure 3. Total ion chromatogram (top) shows 2 consecutive laser shots at same Spherocarb particle (impregnated with alkylnaphthalenes mixture). Selected ion chromatograms illustrate TLGC separation of alkylnaphthalene homologs and isomers. Column temp: 50-200 C in 2 minutes.

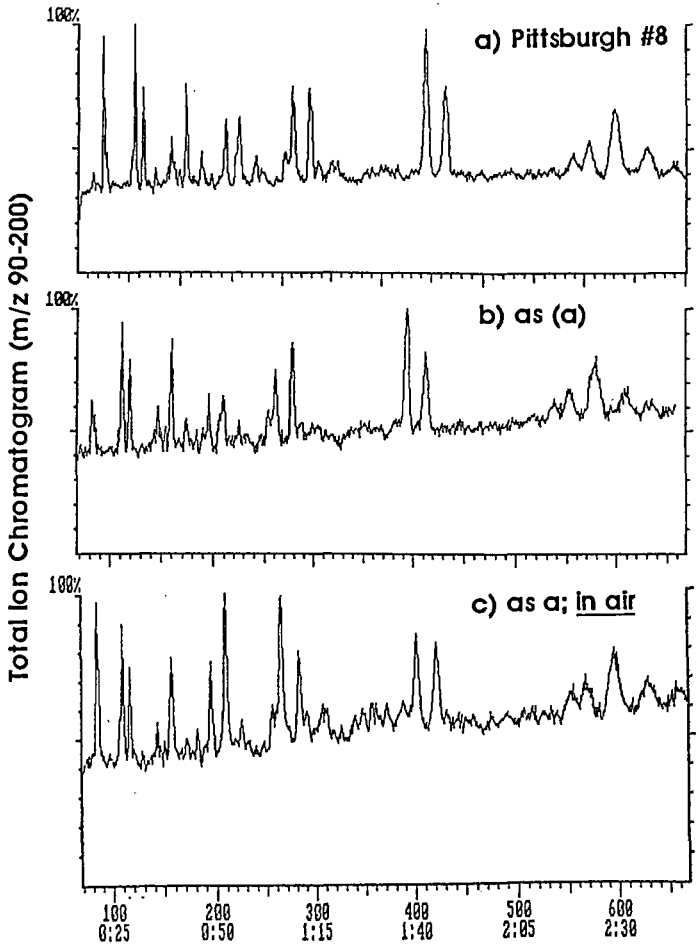

Figure 4. Repeatability of Laser Py-TLGC/MS profiles of single Pittsburgh #8 coal particles. Profile (c) falls within normal range of variation!

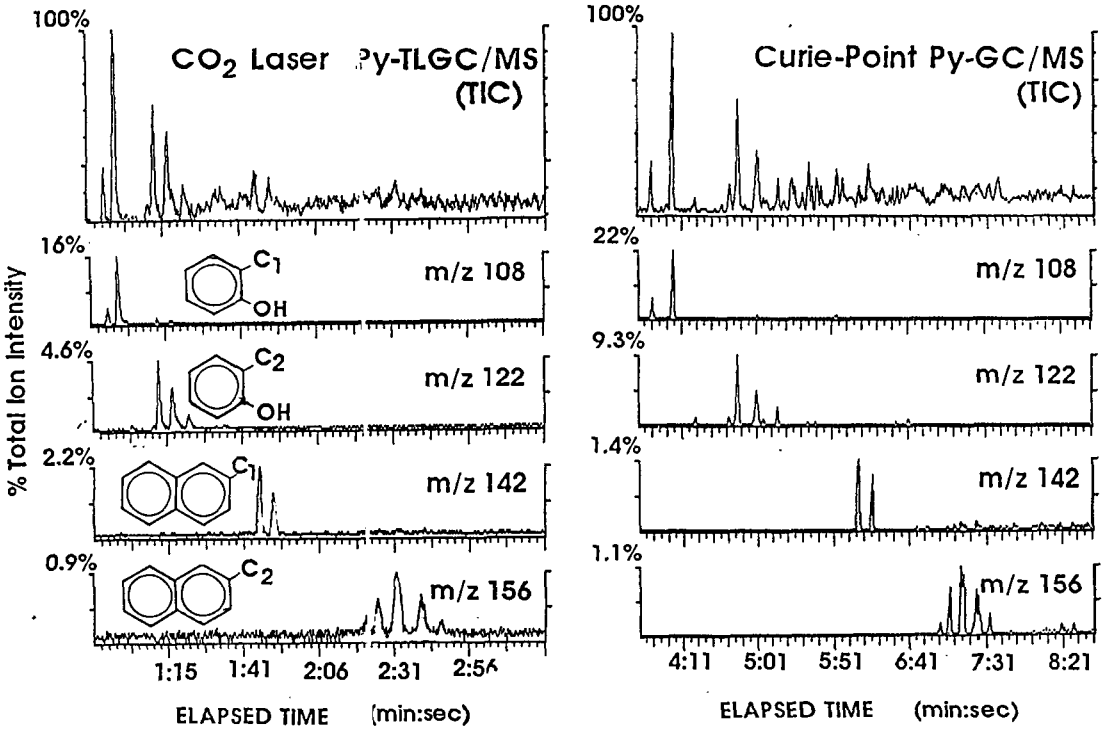

Figure 5. Comparison of CO_2 Laser Py-TLGC/MS profiles obtained at high heating rates (~10^5 K/sec) with Curie-point Py-GC/MS profiles obtained at lower heating rate (~10^3 K/sec). Note similar relative abundances of major tar components.

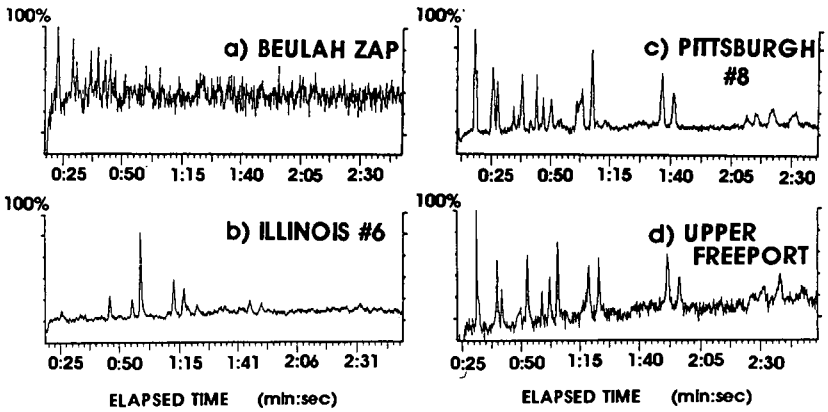

Figure 6. Comparison of laser Py-TLGC/MS profiles of 4 ANL-PCSP coals of different rank. Note lower signal-to noise ratio for Beulah Zap lignite and Upper Freeport, mvb coal compared to hvCb Illinois #6 and hvAb Pittsburgh #8 coals.

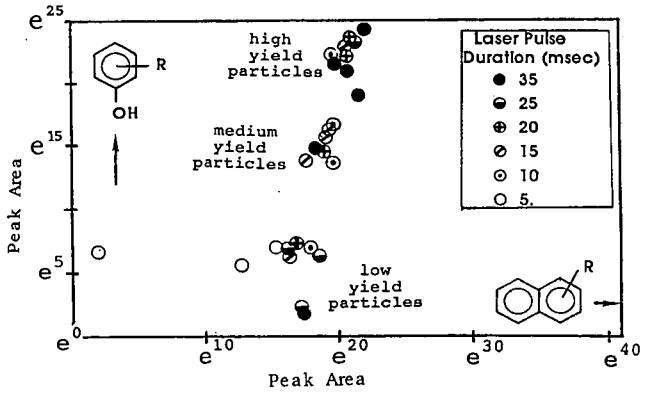

Figure 7. Scatter plot of peak areas at m/z 142 + m/z 156 (x-axis) vs. m/z 94 + m/ 108 (y-axis) from TLGC/MS profiles of 26 Illinois #6 coal particles analyzed at 6 different pulse lengths. Note variable naphthalene response at 5 msec (due to incomplete devolatilization) and presence of 3 phenol yield levels independent of pulse length (thought to be due to differences in maceral content).

TEMPERATURE MEASUREMENTS OF SINGLE COAL PARTICLES DURING THE EARLY STAGES OF HEATING AND DEVOLATILIZATION

Daniel J. Maloney, Esmail R. Monazam, Steven D. Woodruff and Larry O. Lawson
Morgantown Energy Technology Center
P. O. Box 880
Morgantown, West Virginia 26507-0880

Keywords: coal devolatilization, temperature measurement, combustion

ABSTRACT

Unique instrumentation was applied to measure changes in coal particle size and temperature during the early stages of heating and devolatilization. The system incorporated an electrodynamic balance and a pulsed radiation source with a high-speed photodiode array and single wavelength radiation pyrometer. Single coal and carbon particles were pulse heated to simulate the rapid heating rates experienced in high intensity combustion environments (10^5 K/s). Measured temperature histories for 135 μm diameter carbon spheres were in excellent agreement with theoretical predictions of the temperature response of radiatively heated spheres using heat capacity and thermal conductivity property correlations commonly applied in modeling coal devolatilization and combustion. Measured temperature histories of 115 μm coal particles, however, greatly exceeded (on the order of 50 percent) theoretical predictions of the temperature response using the same assumptions and property correlations. Potential causes for the high heating rates observed include uncertainty in assigning thermodynamic and heat transfer properties as well as failure to account for particle shape factors. It is concluded that heat transfer analyses employing spherical particle assumptions and commonly used coal property correlations can lead to significant underestimation of temperature histories and corresponding errors in associated devolatilization rates.

INTRODUCTION

The large discrepancies in observed temperature sensitivities for coal devolatilization are well documented.[1,2] with variations in reported rate constants at a given temperature of several orders of magnitude being common. These variations can in large part be attributed to the experimental techniques used to study rapid devolatilization because estimation and/or measurement of coal particle temperatures in these systems is difficult. Recent attempts to overcome these limitations have concentrated on in-situ temperature measurement or careful characterization of heat transfer fields. For example, Solomon and coworkers[3,4] developed and applied an FTIR emission/transmission technique to measure average temperatures for clouds of devolatilizing coal particles in an entrained flow reactor. Fletcher[5,6] recently reported using a two-color particle sizing pyrometer to characterize the temperature history of single devolatilizing particles in an entrained flow reactor. Friehaut and Proscia[7] performed a detailed characterization of the temperature rise in a screen heater system which was then applied to study rapid devolatilization. Results from these investigations suggest that coal devolatilization rates may be significantly faster and have a stronger temperature sensitivity than implied from many previous studies. The importance of accurate temperature measurements in future devolatilization studies is clear.

In the present paper a novel system is described for monitoring rapid changes in particle size and temperature during coal devolatilization at heating rates representative of high intensity combustion environments (on the order of 10^5 K/s).

The objective was to time and temperature resolve tar evolution and particle swelling that accompany devolatilization and thereby provide data needed to develop more accurate predictions of coal combustion behavior. Initial measurements are reported along with a discussion of the implications for predicting coal devolatilization in combustion systems.

EXPERIMENTAL

Single coal or carbon particles were statically charged and captured in an electrodynamic balance (EDB). Details of the design and operation of the EDB system are published elsewhere.[8,9] The captured particles were balanced at the EDB null position and then heated radiatively from opposite sides by well characterized pulsed Nd:YAG laser beams of equal intensity. Delivered energy fluxes were varied from 500 to 1200 W/cm^2 giving rise to heating rates on the order of 10^5 K/s. Heating pulse times were varied from 3 to 10 ms. The ambient gas was 1 atmosphere of air.

Photographic records of the volatile evolution and particle swelling that accompany devolatilization were obtained using a high-speed 16 mm movie camera which was operated at 5000 frames per second. Timing marks were recorded on the film to accurately determine the film speed and to mark the initiation of the heating pulse. As reported elsewhere,[10] these movies provided excellent time resolution of the particle response including rotation and swelling, and definition of distinct stages of the devolatilization process such as heavy (condensible) volatile evolution.

Changes in particle size and temperature that accompany rapid heating were measured using a novel imaging system and a single wavelength radiation pyrometer. The imaging system was developed around a 16 x 62 element silicon photodiode array. Particles were backlit with a HeNe laser and a magnified shadow image was projected onto the detector array. The full array was scanned at 6300 Hz yielding an analog output proportional to the particle cross-sectional area. A 7 percent reflecting beam splitter was placed in line between the focussing optic and the imaging system array to deflect part of the particle image onto a video camera detector. The video camera was employed to facilitate particle capture and positioning in the EDB.

The radiant power emitted from hot particles was measured using a single wavelength optical pyrometer which was filtered to provide a 100 nm bandpass centered at 1.5 μm wavelength. These measurements were made along the same line of sight as the particle size measurements by employing a set of dichroic beam splitters to separate the HeNe backlight laser from the near infra-red radiation required for the pyrometer. Particle temperatures were determined based on measurements of particle size and radiant emission intensity with application of the Wien approximation to Plank's law. Emissivities used in these calculations were estimated based on measurements' and on available literature.[11] Details of the temperature measurement system including pyrometer calibration, data analysis and associated measurement errors are published elsewhere.' A schematic of the measurement system is provided in Figure 1.

Analog outputs from the imaging system, the pyrometer and a heating beam synchronization pulse were acquired using a Data Translation DT2828 interface card in an AT compatible PC. Data acquisition was triggered from the movie camera, when a framing rate of 5000 per second was achieved, and continued at a rate of 10 kHz per channel for a period of 50 ms. Heating pulses were initiated 15.5 ms after initiation of data acquisition. Measurements were made on individual particles of Spherocarb (Foxboro, Analabs), a spherical, microporous molecular sieve carbon and PSOC 1451D a HVA Pittsburgh seam bituminous coal. Ultimate analysis for the carbon sample yielded 95.2 percent carbon, 0.4 percent hydrogen, and 0.7 percent nitrogen.

Ultimate analysis of the coal yielded 83.3 percent carbon, 5.4 percent hydrogen, and 1.6 percent nitrogen on a dry ash free basis.

ANALYSIS

Measured temperature histories were compared with theoretical estimates of the temperature response of radiatively heated particles. Temperature histories were modeled assuming that particles were spherical, heat flow was in the radial direction only, and the incident heating pulses were absorbed and distributed uniformly at the particle surface. Under these assumptions, the transient temperature distribution in the particles was obtained by solution of the Fourier equation for a sphere:

$$\rho_p C_p \frac{\partial T}{\partial t} = K \left(\frac{\partial^2 T}{\partial r^2} + \frac{2}{r} \frac{\partial T}{\partial r} \right) \qquad (1)$$

where ρ_p, C_p, T, K, and r represent particle density, heat capacity, temperature, thermal conductivity and radius, and t represents time. In solving equation 1, the following boundary conditions were applied:

(i) The initial condition at t = 0:

$$T(r,0) = T_0 \qquad 0 \le r \le R \qquad (2)$$

(ii) The symmetry condition at the center r = 0:

$$\frac{\partial T(0,t)}{\partial r} = 0 \qquad t \ge 0 \qquad (3)$$

(iii) The energy delivered at the surface r = R:

$$K \frac{\partial T}{\partial r} = \frac{\alpha I}{2} - [\, h(T_s - T_\infty) + \sigma\varepsilon(T_s^4 - T_\infty^4) \,] \qquad (4)$$

where α, I, h, σ and ε represent particle absorptivity, incident radiation flux, heat transfer coefficient, Stefan-Boltzman constant and particle emissivity respectively. The subscripts s and ∞ denote the particle surface and ambient environment.

Equation 1 was solved numerically using an implicit Crank-Nicholson scheme. Calculations were performed using the Merrick model[12] to estimate particle heat capacities. Thermal conductivities were estimated using the temperature data for coals and chars of Badzioch and coworkers.[13] The heat transfer coefficient at the particle surface was calculated assuming a Nusselt number of 2. Calculations were performed employing both a constant particle size assumption and using the measured particle size history as input to the model.

RESULTS

Experiments were conducted with carbon spheres to evaluate the capabilities of the measurement system and to test the validity of the heat transfer analysis. Previous experience with Spherocarb particles indicated sufficient temperature measurement accuracy and response to enable heat capacity measurements of individual particles in the EDB system.[7] Temperature traces for replicate experiments with three different Spherocarb particles are presented in Fig. 2. Heating pulse intensities

for the three experiments varied from 1100 to 1160 W/cm^2 with particle diameters ranging from 135 to 140 μm. The temperatures reported were determined using the pyrometer output and the measured particle size data assuming a particle emissivity of 0.85. The measured temperature histories for the three particles were all very similar with less than 50 K deviation at any given time during the particle heat up. The temperature histories showed a steady rise from 850 K (low temperature limit of pyrometer) up to a temperature around 1200 K and then exhibited a marked decrease in the rate of temperature rise at about 6.5 ms into the heating pulse. Analysis of the corresponding high speed movie records indicated that each of the particles passed through a plastic transition during heat up and showed clear signs of volatile evolution and fragmentation from the surface. The observed change in heating rate coincided with the initiation of volatile evolution and particle fragmentation.

The solid line in Fig. 2 represents the calculated temperature history at the surface of a 135 μm particle exposed to an incident flux of 1160 W/cm^2. Excellent agreement was obtained between temperature measurements and predictions with less than 50 K temperature difference being observed over the first 6.5 ms of particle heating. Beyond 6.5 ms the model predictions exceeded the measured temperature rise. Possible causes for the marked decline in the observed particle heating rate and the corresponding deviation from the predicted temperature rise include; a) thermochemical or thermophysical heat requirements which may be associated with volatile evolution and particle fragmentation, but were not accounted for in the calculations; b) attenuation of the particle emission due to the presence of the volatile aerosol cloud and/or small particle fragments; and, c) attenuation of the heating pulse due to the presence of the volatile cloud or particle fragments around the particle. Efforts are in progress to resolve this issue. The data shown in Fig. 2 are typical in terms of measurement reproducibility and agreement between model predictions and measurements for experiments conducted over a range of Spherocarb particle sizes (125 to 150 μm) and incident heat fluxes (500 to 1200 W/cm^2).

Measured temperature histories from six independent experiments with PSOC 1451D coal are presented in Fig. 3. Initial particle diameters for these experiments ranged from 110 to 127 μm , with heating pulse intensities and times varying from 1040 to 1100 W/cm^2 and 3 to 10 ms respectively. The temperatures reported represent data collected before the particles began to move out of the measurement focal volume. The six data sets, recorded at essentially identical heat input rates, but for different heating times, illustrate that the temperature rise was very similar in each case. The data indicate an initial heating rate on the order of 2.5 x 10^5 K/s to a temperature around 1400 K. For the particles that remained in the detection volume through the duration of the heating pulse, the temperature remained at a plateau value near 1400 K for the last several ms of heating. Analysis of the corresponding high speed movies showed rotation of particles beginning between 1.6 and 1.8 ms into the heating pulse at measured surface temperatures around 900 K. Similar observations of particle rotation were reported previously by Phuoc and Maloney[10] and are most likely associated with the inception of light (non-condensible) volatile evolution. Between 3 and 4 ms into the heating pulse, the first indications of a condensed volatile cloud were observed around the particles, afterwhich intense volatile evolution proceeded. Figure 4 illustrates particle size histories showing the swelling behavior of three particles. These data correspond with three of the temperature records shown in Fig. 3. Most of the observed particle swelling occurred between 3 and 5 ms with the maximum swelling values varying from 10 to 30 percent for the particles studied. During the last 5 or 6 ms of heating, in the longer pulse time experiments, the measured temperatures remained fairly constant at about 1400 K. At the present time it is not clear if this behavior is real or the result of interference from the volatile cloud that forms around the particle during the latter stages of devolatilization. This matter is

the subject of an ongoing investigation. The discussion below, therefore, is limited to the first 4 ms of the particle heat up until this issue can be resolved. It should be noted that intense volatile evolution continued during the last half and for several ms beyond the completion of the heating pulse in the 10 ms duration experiments.

Comparisons of one of the temperature records presented in Fig. 3 with temperature history predictions based on the heat transfer analysis described above are presented in Fig. 5. The base case for the analysis included an initial coal density of 1.2 g/cm^3, and particle emissivity and absorptivity of 0.8. The base case analysis gave poor agreement with the measured temperature histories using the same coal property correlations and initial assumptions that gave good agreement for the carbon spheres heating under similar incident heat flux conditions. A second comparison was made assuming an emissivity of one for the coal particles. As shown in Fig. 5 this modification did improve the agreement between the predicted temperature rise and the measurements, however, the agreement was still poor when compared with the results obtained for carbon spheres. The comparisons in Fig. 5 have significant implications because they suggest that the coal particles heated much faster than predicted based on commonly employed approaches to modeling heat transfer using assumptions routinely applied to coal. Fletcher[3] recently reported that the same coal studied here heated as much as 40 percent faster in an entrained flow reactor than predicted using a fairly comprehensive heat transfer analysis. He used a "corrected" characteristic heat transfer time to obtain good agreement between model predictions and particle temperature measurements. The results presented in Fig. 5 are similar to Fletchers observations and suggest significant errors in the assumed particle properties or model assumptions because, even when assuming all of the incident energy was absorbed by the particle, the measured temperature rise greatly exceeded the model predictions. This observation implies one or more of the following; a) significant temperature gradients existed in the particle, i.e. assumed thermal conductivities for the coal were too high; b) assumed particle thermal mass was too high, i.e. particle density and/or heat capacity were overestimated; and, c) the spherical particle assumption was inadequate to model heat transfer for coal particles, i.e. surface to mass ratios for coal particles significantly exceed that of a sphere.

Additional calculations were performed to evaluate the sensitivity of temperature history predictions to changing particle properties such as heat capacity and thermal conductivity. Some improvements were obtained in the model predictions relative to the measurements when lower heat capacity and thermal conductivities were employed in the analysis. However, there were still significant differences between measurement and prediction if coal property values were held within a range that is generally accepted. Additional improvements in the model predictions might be obtained if mass loss during particle heat up were accounted for in the particle energy balance. No attempt was made to do so, however, because there was no evidence of significant mass loss from the coal particles during the first 3 to 4 ms of particle heating. Attempts were made to estimate the relative contribution to the energy balance due to particle oxidation. Based on these calculations it was concluded that heat release due to oxidation during the initial 4 ms of particle heating was insignificant and should have little influence on the observed particle temperatures. This conclusion is supported by other evidence as well because, if the high heating rates observed resulted from oxidation the associated heat release would lead to particle ignition. No evidence of particle ignition was observed and following the heating pulse, the particles were observed to cool rapidly.

An alternative explanation for the high heating rates observed in the experiments arises from the irregular shape of the coal particles. As is typical when modeling coal behavior, the heat transfer analysis was based on an assumption of spherical particle shape. This analysis gave good agreement with experiments performed on

spherical particles. The mass per unit surface area is an important factor in the analysis and irregular shaped particles may not be dealt with adequately. For example, a cube has a mass per unit surface area approximately 40 percent less than a sphere of equivalent surface area. This may have a significant impact on the energy balance and could account for some of the errors in the predicted particle heating rate.

CONCLUSION

A novel imaging system was developed and applied to study changes in coal particle size and temperature during the early stages of devolatilization at heating rates representative of high intensity combustion processes. Based on these measurements, it is concluded that coal particles heat significantly (on the order of 50 percent) faster than is predicted using commonly employed approaches to model heat transfer. Potential causes for the differences between measured and predicted temperature histories include inadequate understanding of the temperature dependence of relevant coal thermodynamic and heat transfer properties and failure to account for particle shape factors. Regardless of the cause, heat transfer analyses employing spherical particle assumptions and widely accepted coal property correlations may yield significant errors in temperature histories and corresponding errors in the associated devolatilization time scales. Efforts are now in progress to address some of these issues.

ACKNOWLEDGEMENT

This work was funded through the U. S. Department of Energy Advanced Research and Technology Development Direct Utilization Program. E. R. Monazam would like to acknowledge Oak Ridge Associated Universities for their support in the form of a post-doctoral fellowship. The authors also wish to acknowledge the contributions of G. E. Fasching, K. Renner, J. D. Thornton and H. Lemley.

REFERENCES

1. Howard, J. B.: Chemistry of Coal Utilization (M. A. Elliot, Ed.) Second Supplementary Volume, p. 665, John Wiley, 1981.

2. Solomon, P. R. and Hamblen, D. G.: Chemistry of Coal Conversion (R. H. Schlosberg, Ed.) pp. 121-251, Plenum Press, 1985.

3. Solomon, P. R., Serio, M. A., Carangelo, R. M. and Markham, J. R.: Fuel **65**, 182 (1986).

4. Best, P. E., Carangelo, R. M., Markham, J. R. and Solomon, P. R.: Combustion and Flame **66**, 47 (1986).

5. Fletcher, T. H.: Combust. Sci. and Tech. **63**, 89 (1989).

6. Fletcher, T. H.: Combustion and Flame **78**, 223 (1989).

7. Freihaut, J. D. and Proscia, W. M.: Energy and Fuels **3**, 625 (1989).

8. Maloney, D. J., Fasching, G. E., Lawson, L. O. and Spann, J. F.: Rev. Sci. Instrum. **60**, 450 (1989).

9. Monazam, E. R., Maloney, D. J. and Lawson, L. O.: Rev. Sci. Instrum. **60**, 3460 (1989).

10. Phuoc, T. X. and Maloney, D. J.: Twenty-Second Symposium (International) on Combustion, p. 125, The Combustion Institute, 1988.

11. Baxter, L. L., Fletcher, T. H. and Ottesen, D. K.: Energy and Fuels **2**, 423 (1988).

12. Merrick, D.: Fuel **62**, 540 (1983).

13. Badzioch, S., Gregory, D. R. and Field, M. A.: Fuel **43**, 267 (1964).

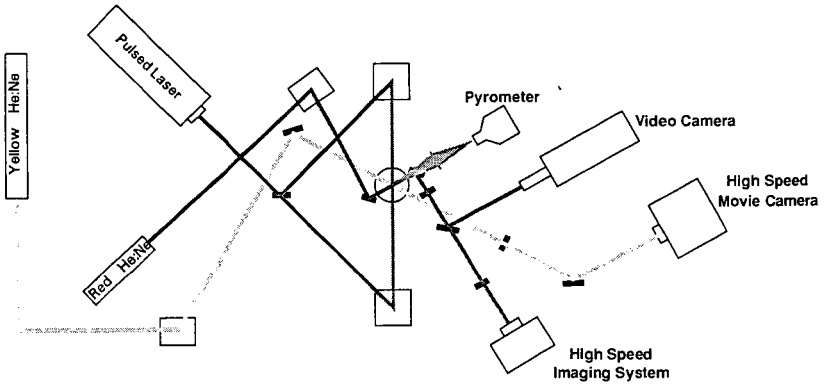

Figure 1. Diagram of EDB Measurement System

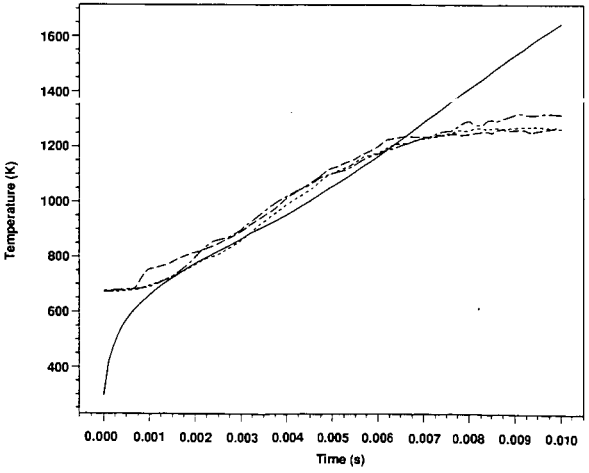

Figure 2. Comparison of Measured Temperature Histories and Model Predictions for Carbon Spheres

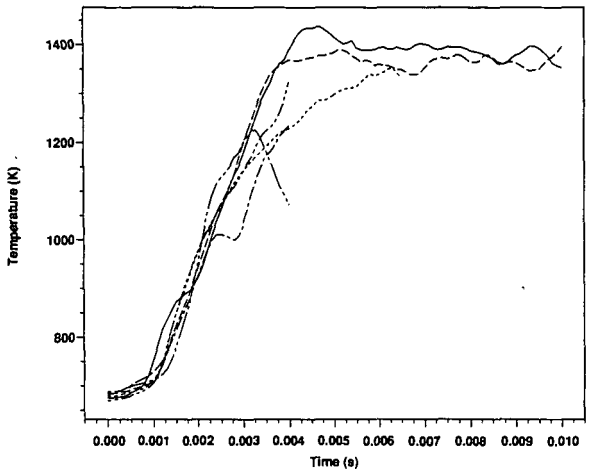

Figure 3. Measured Temperature Histories for Six Coal Particles at Similar Incident Heat Flux Conditions.

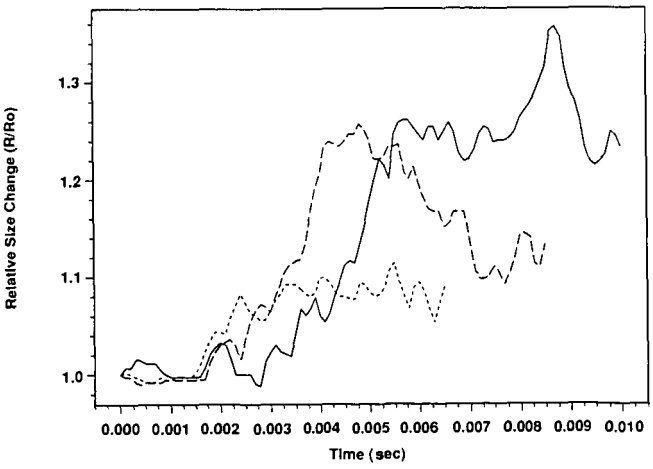

Figure 4. Measured Particle Size Histories for Three Coal Particles at Similar Incident Heat Flux Conditions.

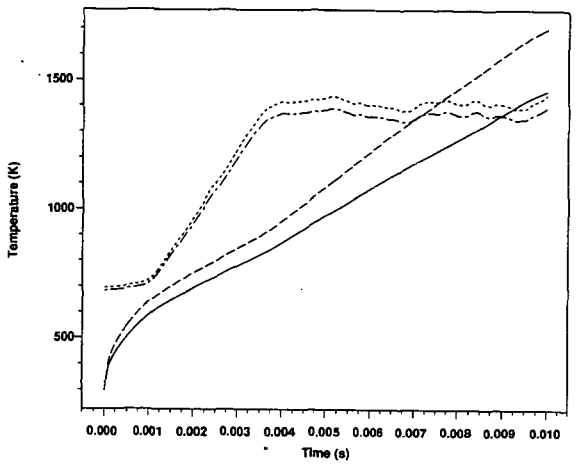

Figure 5. Comparisons of Measured and Predicted Temperature Histories for a Coal Particle as a Function of Assumed Particle Emissivity.
ε = 0.8: ------- Measured, ——— Predicted
ε = 1.0: —·—·— Measured, — — — Predicted

TRANSIENT HEATING OF COAL-WATER SLURRY DROPLETS

Phuoc X. Tran and Mahendra P. Mathur
Pittsburgh Energy Technology Center
Pittsburgh, PA. 15236

1. INTRODUCTION

Although many advantages can be derived from the use of CWF, the relatively large quantities of water in these fuels causes difficulties with ignition and flame stability. In addition, agglomeration of coal particles within the fuel droplets has been commonly observed to result in reduced combustion efficiency. Therefore, it is necessary to investigate the behavior of a CWF droplet undergoing heating and evaporation and the transient processes occurring in the interior of a CWF during this period so that processes such as disruptive burning, volatile release, combustion characteristics etc... are reliably predicted.

Theoretical model for the present analysis is illustrated in Fig. 1. For this droplet, the solid loading is initially large so that as the liquid component vaporizes, the evaporation front propagates into the interior of the droplet. In the wake of the evaporation front, coal particles support each other to form a porous shell keeping the droplet size constant during the evaporation history. The droplet now contains two different regions of consideration: the inner binary core whose surface is regressing with time and the porous shell which is thickening as the evaporation front moves. Thus the problem involves heating of the inner binary core, diffusion transport of the water vapor produced at the moving interface, and the diffusion transport of heat from an outer spherical boundary through the spherical porous shell of coal particle agglomerate. In addition to the complex phenomena, the inherent difficulties in the analysis are also due to the nonlinear nature of the moving interface and the transient behavior of the boundary conditions. Because of these difficulties any attempt to formulate any analytical solution must be accompanied with various model assumptions [1,2]. Such an attempt will obtain only relatively simple solutions in parametric forms and, therefore, many complicated phenomena associated with a slurry droplet during heating and evaporation will not be resolved. The main purpose of the present analysis is to develop numerical procedures to calculate the temperature distributions in both regions and the motion of the evaporation front under various conditions of heating rates, particle sizes.

2. FORMULATION OF THE PROBLEM

The present analysis is carried out under following assumptions: (i) spherical symmetry is valid, (ii) thermal properties are constant, (iii) internal mass transport is neglected, (vi) evaporation during the initial heat-up is neglected, (iv) surface absorption of the radiative heat flux is assumed and (v) the droplets behave like single phase with following properties:

$$\rho_d = (1-\phi)\,\rho_c + \phi\rho_w \quad ; \; m_d = \sum_i m_i \tag{1}$$

$$c_{p,d} = \sum_i Y_i \, c_{p,i} \quad ; \quad Y_i = \frac{m_i}{m_d} \tag{2}$$

where i is for coal and water; ϕ is the liquid volume fraction and it relates to m_c and m_w as:

$$m_c = (1-\phi)\, \rho_c V_d \quad ; \quad m_w = \phi\, \rho_w V_d \tag{3}$$

and the droplet thermal conductivity is calculated using Lee and Taylor analysis [3] as:

$$\frac{\lambda_d}{\lambda_w} = \frac{2\phi + (2-\phi)\, \lambda_c/\lambda_w}{3 - \phi\, (1-\lambda_c/\lambda_w)} \tag{4}$$

We define the following dimensionless groups for the present analysis:

$$\theta_i = \frac{T_i - T_o}{T_b - T_o} \quad ; \quad U_i = r\theta_i \quad ; \quad i = d,c \tag{6}$$

$$\tau = \alpha_d t / r_s^2 \quad ; \quad \xi = r/r_b \quad ; \quad \eta = (r-r_b)/(r_s-r_b) \tag{7}$$

$$\sigma = r_b/r_s \quad ; \quad \beta = \alpha_c/\alpha_d \quad ; \quad \kappa = \lambda_c/\lambda_d \tag{8}$$

$$\gamma = \varepsilon\, I_o r_s \,/\, \lambda_d\, (T_b - T_o) + \lambda_g\, (\theta_{g,e} - \theta_{d,s}) \,/\, \lambda_d \tag{9}$$

$$\nu = \rho_d\, c_{p,d}\, (T_b - T_o)/\rho_w\, \phi\, \Delta H \tag{10}$$

The process of the droplet heating and evaporation are described as:

At $0 \le \tau < \tau_p$

$$\frac{\partial U_d}{\partial \tau} = \frac{\partial^2 U_d}{\partial \xi^2} \tag{11}$$

At $\tau \ge \tau_p$

for the binary core

$$\frac{\partial U_d}{\partial \tau} = \frac{1}{\sigma^2} \frac{\partial^2 U_d}{\partial \xi^2} + \frac{\xi}{\sigma} \frac{\partial U_d}{\partial \xi} \frac{d\sigma}{d\tau} \tag{12}$$

for the porous shell

$$\frac{\partial U_c}{\partial \tau} = \frac{\beta}{(1-\sigma)^2} \frac{\partial^2 U_c}{\partial \eta^2} - \left(\frac{\eta-1}{1-\sigma}\right) \frac{\partial U_c}{\partial \eta} \frac{d\sigma}{d\tau} \tag{13}$$

and the droplet surface regression rate is calculated by:

$$\frac{d\sigma}{d\tau} = \frac{\nu}{\sigma} \left[\frac{1}{r_b} \left(\frac{\partial U_d}{\partial \xi}\right)_{\xi=1} - \frac{\kappa}{r_s - r_b} \left(\frac{\partial U_c}{\partial \eta}\right)_{\eta=0} + \kappa - 1\right] \tag{14}$$

These equations are subjected to the following conditions:

$$\text{At } \tau < 0 : \quad U_d = 0 \tag{15}$$

$$\text{At } 0 \leq \tau < \tau_p : \quad \sigma = 1 \; ; \quad U_d(0) = 0 \; ; \quad \left(\frac{\partial U_d}{\partial \xi}\right)_{\xi=1} = r_s \left(\gamma + \theta_{d,s}\right) \tag{16}$$

$$\text{At } \tau \geq \tau_p : U_d(0) = 0 \; ; \quad U_c(0) = U_d(1) = r_b \tag{17a}$$

$$\left(\frac{\partial U_c}{\partial \eta}\right)_{\eta=1} = (r_s - r_b) \left(\frac{\gamma}{\kappa} + \theta_{c,s}\right) \tag{17b}$$

3. NUMERICAL CALCULATIONS

Numerical procedures developed by Tran and Mathur [4] are used. The spatial coordinate of Eqs. (11), (12) and (13) are discretized employing the usual central difference approximation. These discretized equations are used to transform these equations into a system of ordinary differential equations in temporal coordinates as:

At $0 \leq \tau < \tau_p$

$$\left(\frac{\partial U_d}{\partial \tau}\right)^i = \frac{U_d^{i+1} - 2U_d^i + U_d^{i-1}}{\Delta \xi^2} \tag{18}$$

At $\tau \geq \tau_p$

for the binary core:

$$\left(\frac{\partial U_d}{\partial \tau}\right)^i = \frac{U_d^{i+1} - 2U_d^i + U_d^{i-1}}{\sigma^2 \Delta \xi^2} + \frac{\xi}{\sigma} \left(\frac{U_d^{i+1} - U_d^{i-1}}{2\Delta \xi}\right) \frac{d\sigma}{d\tau} \tag{19}$$

for the porous shell:

$$\left(\frac{\partial U_c}{\partial \tau}\right)^i = \frac{\beta\left(U_c^{i+1} - 2U_c^i + U_c^{i-1}\right)}{(1-\sigma)^2\,\Delta\eta^2} - \left(\frac{\eta-1}{1-\sigma}\right)\left(\frac{U_c^{i+1} - U_c^{i-1}}{2\Delta\eta}\right)\frac{d\sigma}{d\tau} \tag{20}$$

where i = 0 to k, k = $1/\Delta\xi$ for the binary core and $1/\Delta\eta$ for the porous shell.

The interface motion is now evaluated at i= k for the binary core and i = 0 for the porous shell as:

$$\frac{d\sigma}{d\tau} = \frac{\nu}{\sigma}\left[\frac{U_d^{k+1} - U_d^{k-1}}{2r_b\Delta\xi} - \frac{\kappa\left(U_c^1 - U_c^{-1}\right)}{2\Delta\xi\left(r_s - r_b\right)} + \kappa - 1\right] \tag{21}$$

To calculate the interface motion represented by Eq. (21), values of U_d^{k+1} and U_c^{-1} must be determined. Using conditions at the interface given by Eq. (17a), one can get:

$$\left(\frac{\partial U_d}{\partial \tau}\right)^k = \left(\frac{\partial U_c}{\partial \tau}\right)^0 = r_s\,\frac{d\sigma}{d\tau} \tag{22}$$

introducing Eq. (22) into Eq. (19) for i = k and into Eq. (20) for i = 0 to obtain U_d^{k+1} and U_c^{-1} as:

$$U_d^{k+1} = \frac{\left(r_s + \frac{U_d^{k-1}}{2\sigma\Delta\xi}\right)\frac{d\sigma}{d\tau} + \frac{2U_d^k - U_d^{k-1}}{\sigma^2\Delta\xi^2}}{\frac{1}{\sigma^2\Delta\xi^2} + \frac{d\sigma}{d\tau} \,/\, 2\sigma\Delta\xi} \tag{23}$$

$$U_c^{-1} = \frac{\left(r_s - \frac{U_c^1}{2(1-\sigma)\Delta\eta}\right)\frac{d\sigma}{d\tau} - \frac{\beta\left(U_c^1 - 2U_c^0\right)}{(1-\sigma)^2\,\Delta\eta^2}}{\frac{\beta}{(1-\sigma)^2\,\Delta\eta^2} - \frac{1}{2(1-\sigma)\Delta\eta}\,\frac{d\sigma}{d\tau}} \tag{24}$$

Hence value of $d\sigma/d\tau$ can be determined implicitly from Eqs. (21), (23) and (24) using method of halving of the interval. Using varying dimensionless time interval, and $\Delta\xi = \Delta\eta = 0.2$ these above equations are integrated using Adams-Moulton integration subroutine.

4. RESULTS AND DISCUSSION

The calculation was made for CWF droplet with 70 percent coal loading by weight heating and evaporation in an environment with $\lambda_g = 2.6\times10^{-4}$

cal/cm-s-K. Additional data for water are: ρ_w = 1.0 g/cm^3; $c_{p,w}$ = 1.0 cal/g-K; λ_w = 0.00146 cal/cm-s-K; ΔH = 540 cal/g and T_b = 373 K. For coal: ρ_c = 1.3 g/cm^3; $c_{p,c}$ = 0.35 cal/g-K and λ_c = 0.0003 cal/cm-s-K.

Shown in Fig. 2 are the typical temperature profiles in the interior of the CWF droplet i.e. the profiles of both the inner binary sphere and the porous coal agglomerate shell for I_o = 400 W/cm^2, r_s = 25 μm, ν = 1.326. In this figure the intersection of the temperature profiles and $\theta_d = \theta_c = 1$ gives the location of the evaporation front while the thickness of the developed porous shell is given by the width between these locations and σ = 1. For this CWF droplet, the temperature profile that exists when the droplet surface temperature increases to the boiling temperature of the water is far from uniform. As the surface temperature reaches the boiling temperature of the water, two regions of temperature distributions within the CWF droplet ensue: the inner binary core, whose surface is regressing with time and the porous shell which is thickening as the evaporation front moves.

The effects of radiation heat flux, I_o, droplet size, r_s, on the dimensionless temperature profiles of the binary core and of the porous shell are illustrated in Figs. 3a and 4a. To increase I_o and r_s leads to an increase in the heating rate, the surface temperature will rise rapidly and the droplet temperature deep inside will lag further behind the surface temperature. Eventually large temperature gradient is established and the intra-droplet temperature does not have enough time to keep pace with the motion of the evaporation front which depends strongly on the internal temperature gradient as describe by Eq. (14). As a result, the inner binary core is heated essentially by the thermal wave moving with the evaporation front. To decrease I_o and r_s results in lowering the heating rate, the surface temperature rises slowly and the internal temperature has enough time to keep pace with the surface temperature. In this instance, the internal temperature gradient is less significant leading to slow motion of the evaporation front. As a result, the heating of the binary core is due to thermal diffusion from the outer boundary.

The dimensionless temperature profiles of the porous shell of the coal particles agglomerate for various values of I_o and r_s were also illustrated in Figs . 3b and 4b. As shown, the temperature of the porous shell is distributed linearly across the porous shell for values of I_o and r_s used in the present analysis. Under opposite condition, such a linear distribution, however, was found only in the region closed to the droplet surface. As shown, the surface temperature is substantially higher than the boiling temperature of the liquid component and is also higher at higher radiant heat flux , I_o, large particle size, r_s.

5. CONCLUSION

A simple analysis has been made to investigate the transient processes occurring in the interior of a CWF droplet undergoing heating and evaporation. Two heating mechanisms have been obtained: at low heating rate the rate of heat diffusion is faster than the rate of the evaporation front motion, the transient heating of the inner binary core is controlled by diffusion and vanishes quickly after the evaporation begins. However, under opposite conditions, the rate of the motion of the evaporation is faster than the rate of the energy diffusion, the transient heating of the inner binary core occupies the entire period of evaporation and is controlled by the thermal wave moving with the evaporation front. The present numerical

technique is powerful for this kind of moving boundary and phase change problem.

NOMENCLATURE

c_p	-	specific heat
ΔH	-	heat of evaporation
I_o	-	radiant heat flux
r	-	r-coordinate
r_b	-	evaporation front location
r_s	-	droplet radius
T	-	temperature
T_b	-	temperature
T_o	-	initial particle temperature
t	-	time

Greek Symbols

α	-	thermal diffusivity
ε	-	emissivity
λ	-	thermal conductivity
ρ	-	density

Subscripts

b	-	evaporation front location
c	-	coal
d	-	droplet
e	-	ambient condition
g	-	gas phase
p	-	pyrolysis
s	-	surface
w	-	water

REFERENCES

1. P. Antaki, Transient Processes in a Rigid Slurry Droplet During Liquid Vaporization and Combustion, Combustion Science and Technology, 46, 113-135, (1986).

2. G. F. Carey and P. Murray, Perturbation Analysis of The Shrinking Core, Chem. Eng. Sci., 44, 979-983, (1989).

3. T. Y. R. Lee and R. E. Taylor, Thermal Diffusivity of Dispersed Material, J. of Heat Transfer, 400, 720-724, (1978).

4. P. X. Tran and M. P. Mathur, "Transient Heating of Coal Particles Undergoing Pyrolysis," 23rd Symposium (International) on Combustion, in press.

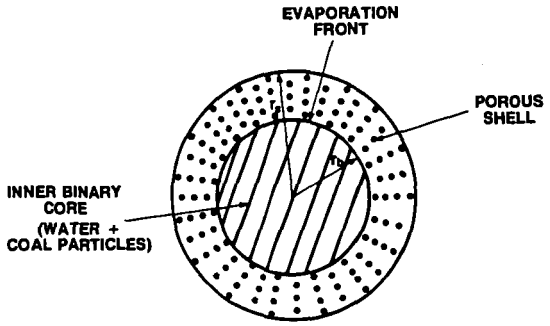

Figure 1. Theoretical Model.

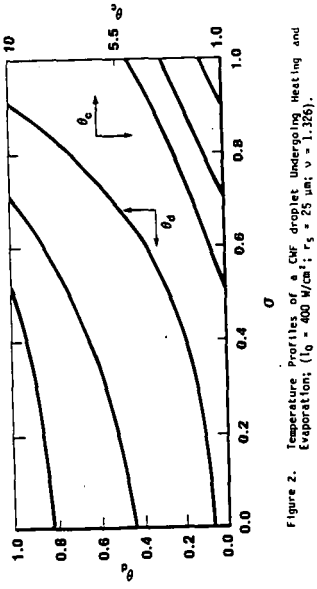

Figure 2. Temperature Profiles of a CWF droplet Undergoing Heating and Evaporation; (I_0 = 400 W/cm²; r_s = 25 μm; ν = 1.326).

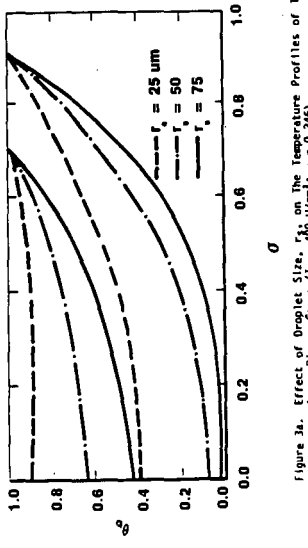

Figure 3a. Effect of Droplet Size, r_s, on The Temperature Profiles of The Inner Binary Core; (I_0 = 400 W/cm²; ν = 0.246).

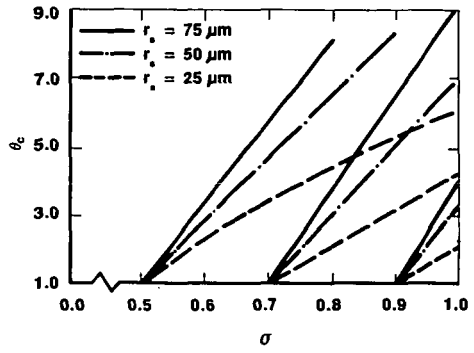

Figure 3b. Effect of Droplet Size, r_s, on The Temperature Profiles of The Porous Shell; (I_o = 400 W/cm²; ν_s = 0.246).

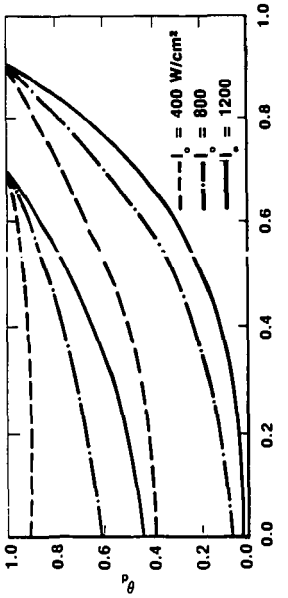

Figure 4a. Effect of Heat Flux, I_o, on The Temperature Profiles of The Inner Binary Core; (r_s = 25 μm; ν_s = 0.246).

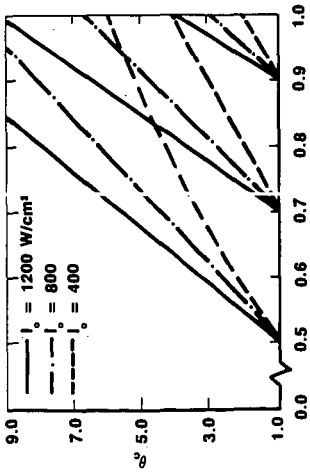

Figure 4b. Effect of Heat Flux, I_o, on The Temperature Profiles of The Porous Shell; (r_s = 25 μm; ν_s = 0.246).

Gas Stream Temperature Measurements Via Fourier Transform Infrared Spectroscopy

M. Shahnam*, S.D. Woodruff**, I. Celik* and R.G. Logan**

* Mechanical and Aerospace Engineering Department
West Virginia University, Morgantown, WV 26505

** U.S. Department of Energy, Morgantown Energy Technology Center
P.O. Box 880, Morgantown, WV 26507-0880

Abstract

A temperature measuring technique utilizing a Fourier Transform Infrared spectrometer (FT-IR) is reviewed and tested by applying it to a natural gas/air flame and to a hot gas (air) stream. The numerous problems encountered in using this technique are elucidated. Preliminary temperature measurement results based upon the intensity of the absorption spectrum of the ν_3 band of carbon dioxide is encouraging when compared to the standard thermocouple readings. Temperature measurements at different locations in a flame indicate that accurate temperature values can be obtained if there is sufficiently large amount of carbon dioxide present compared to the background carbon dioxide concentration.

Introduction

The problems in measuring the temperature and composition of hot, luminous, and particle-laden flows (i.e. inside coal combustors) have received increasing attention lately (Ottesen and Thorne, 1983). Particle temperature can often be measured by two color pyrometry. Gas phase information, however, is difficult to obtain in these dirty environments. FT-IR spectroscopy is a non-intrusive, in situ optical technique which can determine gas phase composition and temperature (Thorne and Ottesen, 1983). This technique does not perturb the chemical or flow characteristics of the combustion processes. Furthermore, the large spectral region sampled using FT-IR spectrometers permits quantitative determination of low molecular weight gases (CO, CO_2, H_2O, etc.) and hydrocarbons, as well as qualitative determination of heavier hydrocarbons. The temperature of the absorbing species can be determined if the individual vibration-rotation transitions of carbon dioxide, carbon monoxide, or low molecular weight hydrocarbons can be resolved. The aim of this study was to further the development of a procedure for measuring the temperature of hot combustion products based upon the individual vibration-rotation transitions of carbon dioxide. This paper reports on the preliminary results obtained from measurements in a natural gas/air laminar flame. Quantitative information such as temperature and concentration can be obtained from the observed absorption intensities. Ottesen and Thorne [1985] indicated that the characteristics of CO and CO_2 vibrational and rotational energy spectra are the most suitable for temperature measurements. They have mostly used CO spectra for this purpose. However for coal combustion, CO is usually an unstable reactive compound and may not be readily present for detection. Carbon dioxide will always be present in sufficient concentrations

in any coal combustion system. Therefore, a procedure has been developed to calculate the temperature of a natural gas/air diffusion flame based upon the υ_3 band of CO_2 absorption spectrum of the combustion products.

Theory

The flame temperature is obtained by resolving the vibrational-rotational transitions of CO_2 as pointed out by Herzberg [1939]

$$I = c_1 (J' + J'' + 1) \, EXP[-E(J'')/(kT)] \qquad (1)$$

where I = transition intensity, c_1 = a constant dependent on the vibrational transition, J', J'' = principal rotational quantum numbers for the upper and lower states respectively, $E(J'')$ = energy of the lower state, k = Boltzmann's constant and T = absolute temperature. Equation (1) can be rearranged as

$$\ln[I/(J' + J'' + 1)] = C - E(J'')/(kT) \qquad (2)$$

Assuming that the peak absorbance , H, of each transition is proportional to its transition intensity, a plot of $\ln[H/(J' + J'' + 1)]$ Vs. $E(J'')$ should give a straight line with a slope equal to $-1/(kT)$ according to (2). The rotational temperature, T, can then be obtained by calculating this slope. The energy levels of the lower state, E(J), of the υ_3 band of CO_2 (i.e. $00^0 1 - 00^0 0$) were tabulated by Air Force Geophysical Laboratory (AFGL) and are available upon request, Rothman [1989].

Experimental Setup and Procedure

The experimental apparatus consisted of four major components: the FT-IR spectrometer, transfer optics, the flame source, and an infrared detector. The FT-IR spectrometer was manufactured by Mattson Instruments, Inc. An Infrared beam was produced from the output of the interferometer and sent across the sample to an MCT infrared detector via transfer optics. Temperature measurements were taken in a flame and in a hot gas stream. The flame was created by burning natural gas with air in a bunsen burner, Figure 1. The hot gas stream was produced by heating the air inside a ceramic reactor, Figure 2. The high velocity jet emanating from the 1/8 inch ID nozzle fitted to the end of the reactor constituted the measuring section. The infrared beam traversing the flame or the hot jet measured the absorption spectra of carbon dioxide. Temperature measurements were based upon 100 scans at a resolution of 0.125 cm^{-1} of the background and the sample (i.e. flame). More details of the governing equations and procedure can be found in Celik et al. [1990].

Results and Discussion

Temperature measurements were taken at three different locations of (1) in the diffusion flame, Figure 1, (2) in the premixed flame, Figure 1, and (3) two inches away from the exit of a jet discharging hot air, Figure 2.

Location (1)

Figure 3 illustrates the absorption spectrum of the combustion gases in the outer cone of a natural gas/air flame, location (1). The various combustion species are evident based upon their absorption frequencies. Figure 4 shows the absorption spectrum of the υ_3 R-branch band of CO_2. The flame temperature is calculated based upon the intensity of each line, H, in this region. A plot of ln [H/(J + J + 1)] Vs. E(j) should yield a straight line whose slope is equal to -1/(kT) according to equation (2). This plot is shown in Figure 5. Since the slope of the straight line in Figure 5 is equal to -9.982E-04 , the flame temperature at the point of measurement should be 1441.37 K. A thermocouple reading of 1394.11 K was obtained at the same point in flame. The difference between the thermocouple reading and the FT-IR measured value can be attributed to the interference of the carbon dioxide absorption spectrum of flame by the amount of carbon dioxide already existing in the room (i.e. background). This is evident from comparison of Figures 6 and 7 which are the absorption spectrum of carbon dioxide at the point of measurement with and without the flame. The difference between these two distributions is the population distribution of carbon dioxide in the flame at the point of measurement. The larger this difference, the less interference exists. Since there is a significant population of the ν_3 vibration in the flame at this point compared to the population at room temperature, the temperature measured via FT-IR is close to the thermocouple measured value.

Location (2)

Temperature measurements based upon the υ_3 band of CO_2 absorption spectrum in the inner cone of the flame, approximately 10 mm above the surface of the burner Figure 8, resulted in erroneous values, location (2). The slope of the straight line in Figure 9 was -1.209E-03, that resulted in a temperature of 1190° K. A thermocouple reading of 589 K was obtained at the same point in the flame. This discrepancy is possibly due to the nonlinear distribution of carbon dioxide in the inner cone of the flame. Figures 10 and 11 illustrate the ν_3 population distribution of carbon dioxide at the point of measurement with and without the flame. A comparison of the difference between υ_3 band of CO_2 in Figures 10 and 11 with Figures 6 and 7, location (1), indicates a smaller distribution in location (2) compared to location (1); i.e. at the wavenumber of 2400.09, this difference is about 12.57 for location (1) and it is about 6.19 for location (2). This seems to indicate that for location (2) there was more interference from the existing amount of carbon dioxide in the room, causing much less accurate temperature readings.

Location (3)

Attempts were made to measure the temperature of hot gases in a heated air jet with an exit velocity of approximately 50 m/s, location (3). Figure 12 illustrates the absorption spectrum of carbon dioxide at 2 inches away from the exit of the jet. Carbon dioxide free air was purged through optical access holes on both sides of the jet in order to minimize the pollution of the jet by an external carbon dioxide source. The thermocouple reading was

560 F for this location. However the υ_3 band of carbon dioxide absorption spectrum was not sufficiently resolved to yield any temperature information. The background and the sample population distributions of the υ_3 band of carbon dioxide were virtually identical. This meant that there was a significant amount of interference from the carbon dioxide in the room, resulting in wrong temperature values.

Conclusions

A technique for measuring temperature using FT-IR spectroscopy based upon the ν_3 band of CO_2 absorption spectrum was evaluated in a flame and in a heated air jet. Since the intensity of the absorption spectrum of the υ_3 band of carbon dioxide was the basis for measuring the temperature, any interference of the infrared beam by an outside source (in this case background) seems to cause erroneous results. In the high temperature region of the diffusion flame, there was sufficient population distribution of CO_2 resulting in an accurate temperature measurement. However, since the population distribution of the ν_3 band of CO_2 in the premixed flame region and the hot air stream was comparable to that of the background, inaccurate results were obtained.

Acknowledgement

Support for this project was provided by Department of Energy, Morgantown Energy Technology Center under contract No. DE-FC21-87M24207, project A.2.

REFERENCES

Celik, I., Shahnam, M., Katragadda, S., and Usmen, R., "Deposition, Corrosion, Erosion and Sulfur Emission Studies Related to Coal Combustion", Final Report, No.: MAE/90/IC2, Mechanical and Aerospace Engineering Department, West Virginia University, February 1990.

Herzberg, G., "Molecular Spectra and Molecular Structure," V. I, Prentice-Hall. Inc.. 1939.

Herzberg, G., and Herzberg, L., "Rotation-Vibration Spectra of Diatomic and Simple Polyatomic Molecules with Long Absorbing Paths," Journal of Optical Society of America, Vol. 43, Number 11, November 1953, pp. 1037-1044.

Mavrodineanu, R., and Boiteux, H., "Flame Spectroscopy," Wiley, 1988.

Rothman, L., Private Communications, 1989.

Ottesen D.K. and Thorne L.R., International Conference on Coal Science, Pittsburgh, PA, p. 621 (August 15-19, 1983).

Ottesen, D.K. and Thorne, L.R., "In Situ Studies of Pulverized Coal Combustion by Fourier Transform Infrared Spectroscopy" International Conference on Coal Science, Sydney, NSW, Australia, p. 351 (Oct. 28-31, 1985).

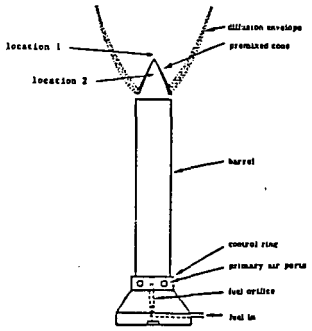

Figure 1 Schematic of a Bunsen Burner.

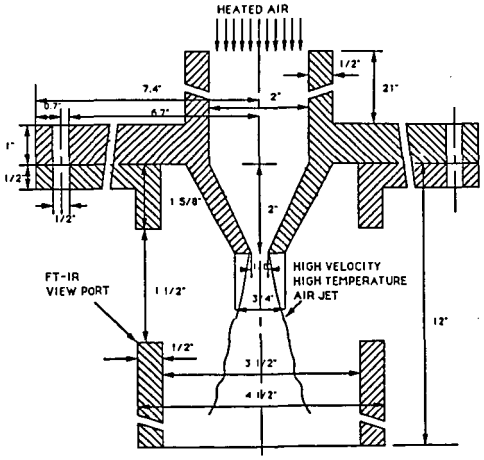

Figure 2 Side View of the Entrained Flow Reactor with the Nozzle.

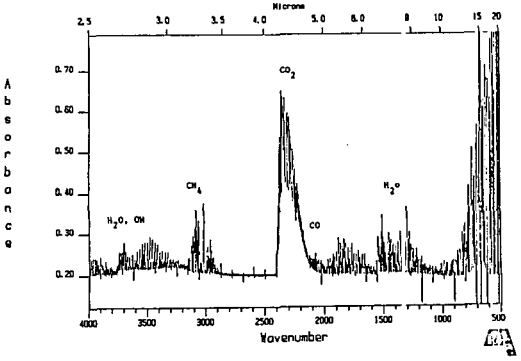

Figure 3 Absorption Spectra of Flame.

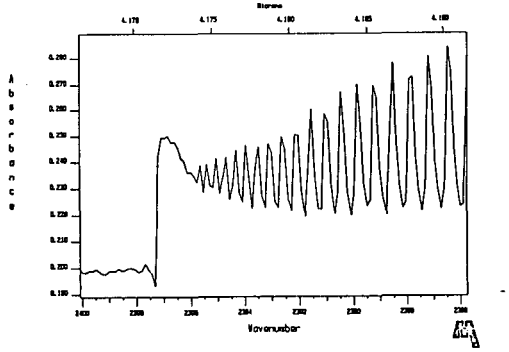

Figure 4 Absorption Spectra of the ν_3 Band of CO_2 (R-branch).

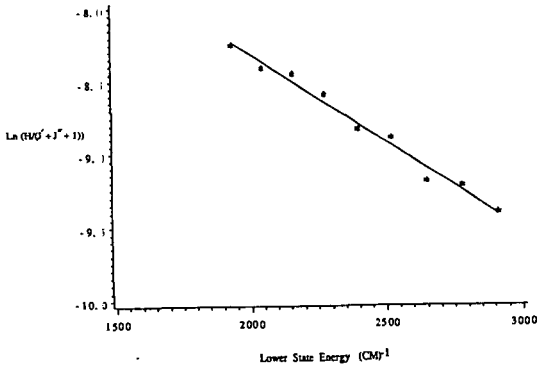

Figure 5 Rotational Temperature of Carbon Dioxide.

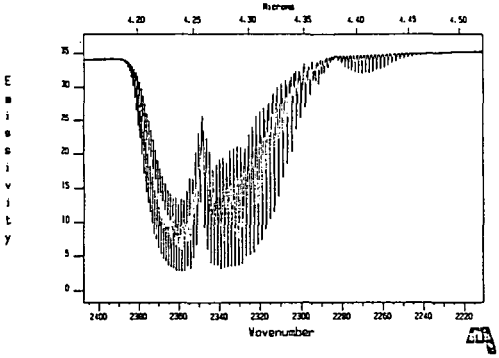

Figure 6 Background Single Beam.

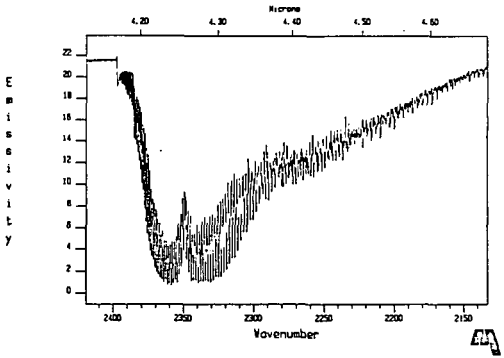

Figure 7 Sample Single Beam.

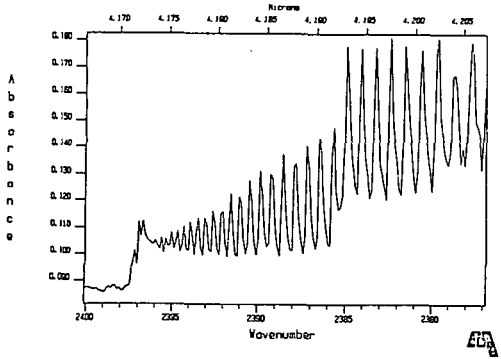

Figure 8 Absorption Spectra of the ν_3 Band of CO_2 (R-branch).

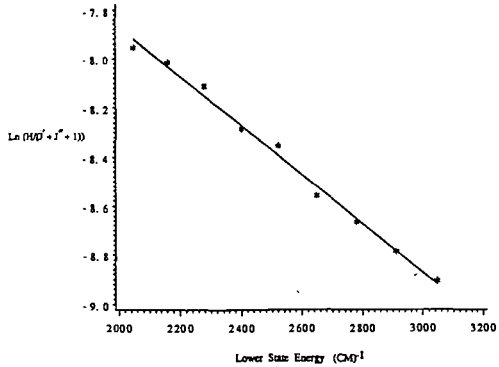

Figure 9 Rotational Temperature of Carbon Dioxide.

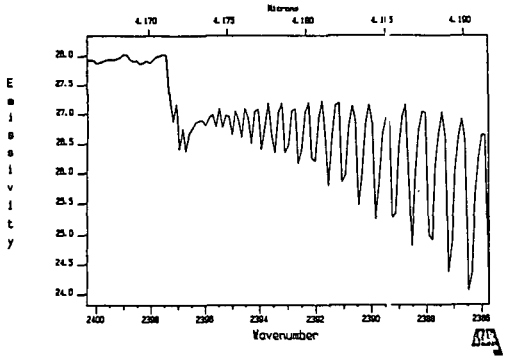

Figure 10 Sample Single Beam.

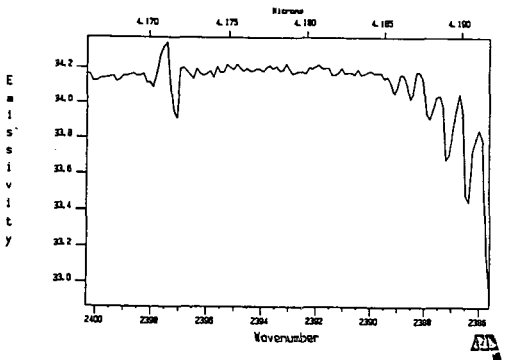

Figure 11 Background Single Beam.

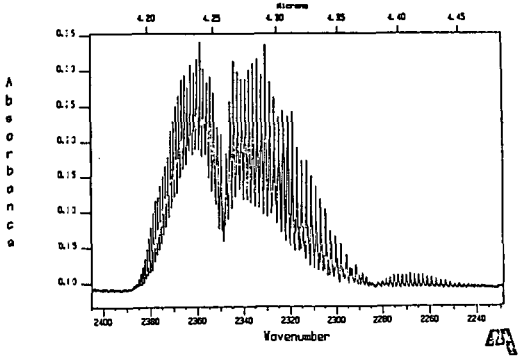

Figure 12 Absorption Spectra of CO_2 in a Hot Air Jet.

FT-IR EMISSION/TRANSMISSION TOMOGRAPHY OF COAL FLAMES

P.R. Solomon, J.R. Markham, Y.P. Zhang, and R.M. Carangelo
Advanced Fuel Research, Inc.
87 Church Street
East Hartford, CT 06108

INTRODUCTION

Fourier Transform Infrared (FT-IR) Emission/Transmission (E/T) spectroscopy has recently been shown to be a versatile technique for coal combustion diagnostics by allowing for measurements of particle concentrations and temperatures, and gas compositions, concentrations, and temperatures (1). These measurements are for the ensemble of particles and gases along a line-of-sight in the flame.

To correct the shortcoming of the line-of-sight measurements, tomography techniques have been applied to both the FT-IR emission and transmission spectra to obtain spatially resolved spectra from which local flame properties can be obtained. This method has been applied to a stable, well defined co-annular laminar ethylene diffusion flame (2,3). From the spatially resolved spectra, point values for species temperature and relative concentrations were determined for CO_2, H_2O, alkanes, alkenes, alkynes, and soot. Temperatures (for CO_2 and H_2O), and soot concentrations were found to be in good agreement with measurements performed on the same flame by coherent-anti-stokes Raman spectroscopy (CARS) (4) and laser scattering (5), respectively.

The technique was recently applied to a coal flame produced in a transparent wall reactor (TWR) using a Rosebud subbituminous coal (6). From these spectra, spatially resolved point values have been obtained for particle and CO_2 temperatures, relative particle, soot and CO_2 concentrations, the fraction of ignited particles, and the relative radiance intensity.

To study the effect of these conditions on coal type, two more flames have now been characterized. These are a second Rosebud subbituminous coal flame produced using a slower flow of preheated gas and a flame using Pittsburgh Seam coal produced under the same conditions. This paper compares the results from these three flames.

EXPERIMENTAL

Apparatus

The TWR facility has been described previously (1,6). The coal is injected upwards into the center of a 10 cm diameter upward flowing preheated air stream in the center of a 20 cm diameter x 70 cm tall glass enclosure. A flow of room temperature air along the perimeter of the reactor keeps the enclosure cool. Radial thermocouple measurements show that the preheated air stream provides a stable hot environment for the coal up to a height of about 30 cm. Our coal feeding system uses a carrier gas which exits the feeder through a tube as it is slowly lowered through a bed of coal particles. Mechanical vibration helps to displace and entrain particles into the tube. A steady feed results in a flame that is stable in shape and position except for the ignition point, where rapid verticle fluctuations of $\pm$ 5 mm are observed. The gas flows used for the high flow case were 2.9 l/sec in the preheated gas and 4.2×10^{-3} l/sec in the carrier gas. The gas flows used for the low flow case were 1.7 l/sec in the preheated gas and 3.6×10^{-3} l/sec in the carrier gas. The coal feed rate was 0.91 g/min for both cases.

The enclosure has movable KBr windows to allow access to the flame by the FT-IR spectrometer (a modified Nicolet 20SX). As discussed in Ref. 7, emission measurements are made by directing the radiation emitted by the hot sample stream through an interferometer to an "emission" detector. Transmission measurements are made by replacing this detector with a high intensity globar source which, after passing through the interferometer, is directed through the sample area to a "transmission" detector. The emission and transmission measurements are made along the same 1 mm wide by 4 mm high optical path defined with apertures. With this optical geometry, twenty-one parallel line-of-sight emission and transmission spectra were collected across the coal stream at 1 mm increments along the radius for each slice. Several slices were obtained for each flame.

The spatially resolved "point" values correspond to an average within 1 mm x 1 mm x 4 mm high volumes. In this work the data were smoothed by co-adding data from eight adjacent wavenumber bands. This results in degraded resolution from the 8 cm^{-1} used, although still sufficient to quantitatively measure the gas species.

Sample

The samples used in this experiment were sieved fractions (200 x 325 mesh) of dry Montana Rosebud subbituminous coal and dry Pittsburgh Seam coal. The characteristics of these coals have been published previously (1,8).

ANALYSIS

The analysis for the line-of-sight FT-IR E/T measurement pertaining to multi-phase reacting streams has been presented previously (1,6,7,9-11). The relative concentration and temperatures for individual components (gas, soot, and particles) are obtained from the transmission and normalized radiance spectra, respectively, as discussed in Refs. 1,6,7,9-11.

The reconstruction of spatially resolved FT-IR spectra from multiple line-of-sight spectra was first introduced elsewhere (2,3,6). We have employed the standard Fourier image reconstruction technique (12) which is capable of handling data from systems of arbitrary shape. Our flame, however, was cylindrically symmetric. The computer program published by Shepp and Logan was used for this work (12) by applying the reconstruction one wavelength at a time to determine spatially resolved spectra.

A straight-forward application of the reconstruction technique to radiance spectra is not possible, because of self-absorption in the sample. In the case of small absorbance encountered in this work (percent transmission > 80%), an emission measurement can be directly corrected by an absorption measurement made along the same path. A self-absorption correction corresponding to that used by Freeman and Katz was employed for the thin sample studied (13). The Fourier reconstruction program can be applied directly to the emission thus corrected, to obtain local radiances. These are then converted to normalized radiance and the analysis proceeds as for the line-of-sight spectra.

RESULTS

Flame Characteristics

The three flames are presented in Fig. 1. All three flames are characterized by a bright ignition zone followed by a region of lower intensity where burnout is occurring. Photographs show the high intensity zone to contain burning volatile clouds which are 3 to 5 times the diameter of the particles. The Pittsburgh Seam coal shows a region of distinct dimness after ignition which may occur after the initial oxygen is consumed by the volatiles.

Measurements were made of the particle velocities by measuring the length of tracks recorded with a video camera using a 1/250 shutter speed. The results are presented in Fig. 2. The particles accelerate as they leave the nozzle due to the heating of the carrier gas, the influence of the faster hot gas surrounding the carrier gas stream, and buoyancy effects. At ignition, the acceleration is increased as the center stream is rapidly heated. The data show the velocities increasing to above the hot gas velocity. The heating of the central stream appears to dominate the particle velocity as the two cases where the hot gas velocity is lowest (Fig. 2b and 2c) produces a higher particle velocity then in Fig. 2a where the hot gas velocity is higher. Based on these velocities, the particle residence times (given in Fig. 1) were computed.

The tomography data for these three flames are presented in Figs. 3 to 5. The seven parameters which were measured are: a) relative particle and soot concentration, b) the multiplier M which is the emissivity times the fraction of particles at the measured temperature, c) the spectral radiance at 4500 cm^{-1}, d) the particle and CO_2 temperatures, and e) the CO_2 concentration.
The tomography data for the Rosebud fast flow case are presented in Fig. 3. These data were presented previously (6) but are reproduced here for comparison. Figure 3a presents the height of

the continuum blockage determined from the transmittance spectra as percent blockage of the incident IR beam. The blockage is divided into particles and soot. Soot is observed to appear at ignition as inferred by the change in shape of the continuum as described below. Below the ignition (6 cm above the 4 mm diameter nozzle) there are particles only (no soot) confined to a radius of about 6 mm. This is in agreement with the boundaries as determined by scattering of a He-Ne laser beam. The multiplier, M (the product of emissivity times the fraction of ignited particles in Fig. 3b shows a few particles (up to 10%) have ignited at the edge of the coal stream. Such ignited particles can also be seen in Figs. 1b and 1c.

Just above ignition (10.5 cm above the nozzle), the particles appear to be forced inward into a more dense central stream at the same time that some particles are spread outward. The spreading of the stream is confirmed visually. This spreading is consistent with the location of the ignition zone centered at about 2 mm radius, indicated by the 0.35 M value in Fig. 3b (i.e., approximately one-third of the particles ignite). Considerably less material is ignited at the center and outer region of the ignition zone. The increase in gas volume in this zone acts to compress the stream inward and expand the stream outward. The total particle blockage (number in parentheses in Fig. 3a) determined by integrating the blockage times area indicates that the blockage is increased from 1.0 (by definition) at 6 cm to 1.7 at 10.5 cm to 1.5 at 12 cm. This suggests that the devolatilization which appears complete at this point may swell or fragment the particles to increase the blockage. Swelling is observed in SEM photographs of collected particles. Above 12 cm, the particle blockage is reduced as the material burns out (Fig. 3a).

The multiplier, M (Fig. 3b), indicates that the ignition zone quickly collapses to the center axis (compare 10.5, 12, and 14 cm). From 14 cm through 16 cm M again drops near the center region, but this may be caused by a build-up of ash in the center region, as evidenced by a corresponding drop in the relative amount of soot compared to particles at these positions. At 20 cm, an increase in blockage at radiuses above 4 mm is observed (ash dispersion) with a corresponding decrease in M above 4 mm and an increase in M at the center.

Figure 3c presents the local radiance determined at 4500 cm^{-1}. At 6 cm, high frequency radiance is detected from the previously mentioned few particles that are observed to ignite at the edge of the coal stream. Just above the ignition point (10.5 cm), the high values of radiance along the center result from the high density of particles blockage, even though M may be low. The radiance from 10.5 cm to 12 cm is observed to increase along the center, as was observed for M.

Figure 3d presents the temperature of CO_2 (dashed line) and total continuum, both particles and soot (solid line). Also presented are measurements with a Pt + PtRh thermocouple obtained in the flame at the 12, 16, and 20 cm positions. The particles have a relatively constant temperature between 1800 and 1900 K at 10.5 and 12 cm. The cooler center region at 10.5 cm (in agreement with M and radiance) is observed. Particle temperature increases from 1900 K to 2000 K at 14 cm, and to 2200 K to 2400 K through 16 to 20 cm. Above 20 cm the temperature falls.

The maximum CO_2 temperatures (2200 to 2600 K) occur in the regions of high particle radiance where the maximum combustion is occurring, although the center temperature at 12 and 16 cm are puzzling. In the beginning region of the flame, CO_2 is 400 to 700 K hotter than the particles in the same region suggesting that CO is burning to CO_2 away from the particles. CO_2 temperatures are generally closer to the particle temperatures above 14 cm. At the edge of the stream the CO_2 temperature is always lower due to rapid heat transfer to the surrounding air. At 20 cm the CO_2 and particle temperatures are within 100 K except along the axis where the CO_2 is hotter.

The CO_2 concentrations are presented in Fig. 3e. Below ignition the CO_2 concentration is very small. Above ignition the CO_2 level jumps drastically and spreads with increasing height. These data present a picture of the coal burning in a shrinking region which collapses to the center at the tip of the flame.

The results for the two other flames are presented in Figs. 4 and 5. The trends are qualitatively similar. There are, however, differences in the soot formation, swelling, ignition, particle temperatures, burnout, and CO_2 concentrations, and these will be discussed below.

Soot Formation - As described previously (1) the shape of the continuum spectra can be employed to separate the contributions from particles and soot. Two spectra for the Pittsburgh Seam coal are presented in Fig. 6. Figure 6a presents $1-\tau$, where τ is the transmittance, prior to ignition where no soot is present. The upward slope toward low wavenumbers (long wavelengths) is due to diffraction. Figure 6b presents a spectrum above ignition in the region of high soot. The spectrum now slopes in the opposite direction due to soot. To resolve the spectrum into particle and soot contributions, the frequency dependent extinction efficiency, F'_ν, for the particles (which is proportional to $(1-\tau)$) is assumed to have the same shape as prior to ignition, and the particle transmittance is assumed to be equal to the measured transmittance extrapolated to 0 cm^{-1} (where the attenuation from soot goes to zero). A straight line extrapolation is made below 3500 cm^{-1} excluding the region of the spectrum containing CO_2 and H_2O bands. The soot contributions is the difference between the particle attenuation and the total as shown in Fig. 6c.

The relative amounts of soot can be seen in Figs. 3a, 4a, and 5a. The soot concentration is highest just above ignition. The highest soot concentrations are observed for the Pittsburgh Seam coal followed by the Rosebud slow case and then the Rosebud fast case. For Pittsburgh Seam, the highest attenuation from soot is about three times that from the particles. For Rosebud (slow flow) the highest value is only 2.3 times and for Rosebud (fast flow) only a little over 1 times. The variation in soot concentration comes from two factors: 1) tar, which is the soot precursor (1) is higher for Pittsburgh Seam coal than for Rosebud, and 2) the better mixing in the fast flow increases the oxygen to the central core which reduces the soot.

Swelling and Fragmentation - The swelling or fragmentation of the particles is indicated by the integrated particle blockage values as a function of position. The 6 cm case of the Rosebud and the 4 cm case for the Pittsburgh provide the baseline before ignition. Both cases show a flat distribution over the center 2 mm and goes to zero between 4 and 5 mm. The integrated blockage is given in parenthesis on each of the figures.

If there was no swelling or fragmentation, the blockage would decrease due to the gas heating. For the Pittsburgh Seam coal, the integrated blockage more than triples. Photomicrographs of samples collected in the flame show both swelling of coal and the appearance of small ash particles. Both changes would increase the blockage. For the Rosebud coal, the increases are more modest. While swelling was observed for the fast flow case, the slow flow case does not indicate an obvious swelling or rounding.

Ignition - Ignition for all three cases occurs with the outside of the particle stream (which is in best contact with the hot gases) igniting first. This can be seen in the multiplier M, which is the fraction of ignited particles, in Figs. 3b, 4b, and 5b. At ignition, M is highest at the edge of the particle stream. A photograph in Fig. 7 looking at the ignition zone of the Rosebud slow case clearly shows the ring of ignition. The Pittsburgh which is also a slow flow case exhibits a similar ring while the faster flow case which appears to have better mixing shows the same effect but to a lesser degree. Ignition at the edges is consistent with the particle temperatures below ignition (Fig. 5d) which indicate that the particles at the edge of the stream have reached 800 K while those in the center are as low as 600 K.

Temperatures - The following observations can be made about particle temperatures. 1) Particle temperatures are highest at the edge of the flame where the concentration of oxygen is highest. 2) The lowest temperatures are observed for the Pittsburgh Seam coal, while the highest temperatures are observed for the fast flow Rosebud case. Particle temperatures are generally in the range 1400 to 2200 K.

CO_2 temperatures are always higher than the particle temperatures in the combustion region suggesting that most CO_2 is produced away from the particle surface (e.g., by CO oxidation). The highest CO_2 temperatures were observed in the fast flow case and approached 2600 K.

Burnout - The percent weight loss as a function of distance above the nozzle for the three flames is indicated in Fig. 1, and plotted in Fig. 8. Both slow flow cases display a transient plateau in their burnout profiles which begin within 5 cm past their respective ignition points. Rapid oxygen consumption and inadequate mixing of the surrounding air is believed to cause this effect, which is not displayed for the fast flow (better mixing) case. Both Rosebud flames exhibit essentially 100%

DAF burnout by 50 cm above the nozzle. The Pittsburgh flame, however, seems to contain - 10% char which displays a very low reactivity.

CO_2 Concentration - The concentration of CO_2 for all cases generally decreased with distance away from the centerline for each slice. The slow flow Rosebud case showed an overall larger amount of CO_2 in the combustion region than the fast flow Rosebud case, but this may be attributed to less mixing (and hence, less dilution) for the slow flow condition.

CONCLUSIONS

Tomographic reconstruction techniques have been applied to FT-IR E/T measurements to derive local values for species temperatures and concentrations within three laboratory scale coal flames. Values for particle temperature, relative particle density, relative soot concentration, the radiance intensity, the relative CO_2 concentration and the CO_2 temperature have been obtained as functions of distance from the flame axis and height above the coal injector nozzle. The spectroscopic data are in good agreement with visual observations and thermocouple measurements. These data present a picture of the coal burning in a shrinking region which collapses to the center at the tip of the flame. CO_2 temperatures are highest in the rapid burning zone (2200 to 2600 K). The highest particle temperatures in this zone are 1900 to 2000 K, with temperatures up to 2400 K outside the zone. The three flames showed both coal and flow dependent phenomena. The slow flow cases showed reduced mixing (more soot and more variations in flame properties with radius) compared to the fast flow case. The Pittsburgh Seam coal showed higher soot, higher swelling, lower particle temperatures, and lower char reactivity compared to the Rosebud coal.

ACKNOWLEDGEMENT

This work was supported under the U.S. Department of Energy, Morgantown Energy Technology Center Contract No. DE-AC21-86MC23075. Richard Johnson is the METC Project Manager.

REFERENCES

1. Solomon, P.R., Chien, P.L., Carangelo, R.M., Best, P.E., and Markham, J.R.: Twenty-Second Symposium (International) on Combustion, p. 211, The Combustion Institute, (1988).
2. Chien, P.L., Best, P.E., Carangelo, R.M., and Solomon, P.R., "Tomographic Reconstruction of Fourier Transformed Infrared (FT-IR) Spectra at Points within a Coannular Flame", poster session 22nd Symposium (Int) on Combustion, Seattle, Washington, DC, (Aug. 1988).
3. Best, P.E., Chien, P.L., Carangelo, R.M., Solomon, P.R., Danchak, M. and Ilovici, I.: "Tomographic Reconstruction of FT-IR Emission and Transmission Spectra in a Sooting Laminar Diffusion Flame: Species Concentrations and Temperatures", Combustion and Flame, submitted for publication (1989).
4. Boedeker, L.R., and Dobbs, G.M., Comb. Sci. Technol., **46**:301, (1986).
5. Santoro, R.J., Semerjian, H.G., and Dobbins, R.A., Combustion and Flame, **51**:203, (1983).
6. Markham, J.R., Zhang, Y.P., Carangelo, R.M., and Solomon, P.R., "FT-IR Emission/Transmission Tomography of a Coal Flame", 23rd Symposium (Int) on Combustion, France, (July 1990).
7. Best, P.E., Carangelo, R.M., and Solomon, P.R.: Combustion and Flame **66**, 47, (1986).
8. Serio, M.A., Hamblen, D.G., Markham, J.R., and Solomon, P.R.: Energy & Fuel, **1**, 138, (1987).
9. Solomon, P.R., Carangelo, R.M., Best, P.E., Markham, J.R., and Hamblen, D.G.: Twenty-first Symposium (International) on Combustion, p. 437, The Combustion Institute, (1987).
10. Solomon, P.R., Best, P.E., Carangelo, R.M., Markham, J.R., Chien, P.L., Santoro, R.J., and Semerjian, H.G.: Twenty-first Symposium (International) on Combustion, p. 1763, The Combustion Institute, (1987).
11. Solomon, P.R., Carangelo, R.M., Best, P.E., Markham, J.R., and Hamblen, D.G.: Fuel **66**, 897, (1987).
12. Shepp, L.A. and Logan, B.F.: IEEE Trans. Nucl. Science, NS-21, (1974).
13. Freeman, M.P. and Katz, S.J.: Optical Society of Am., 50, (8), 826, (1960).

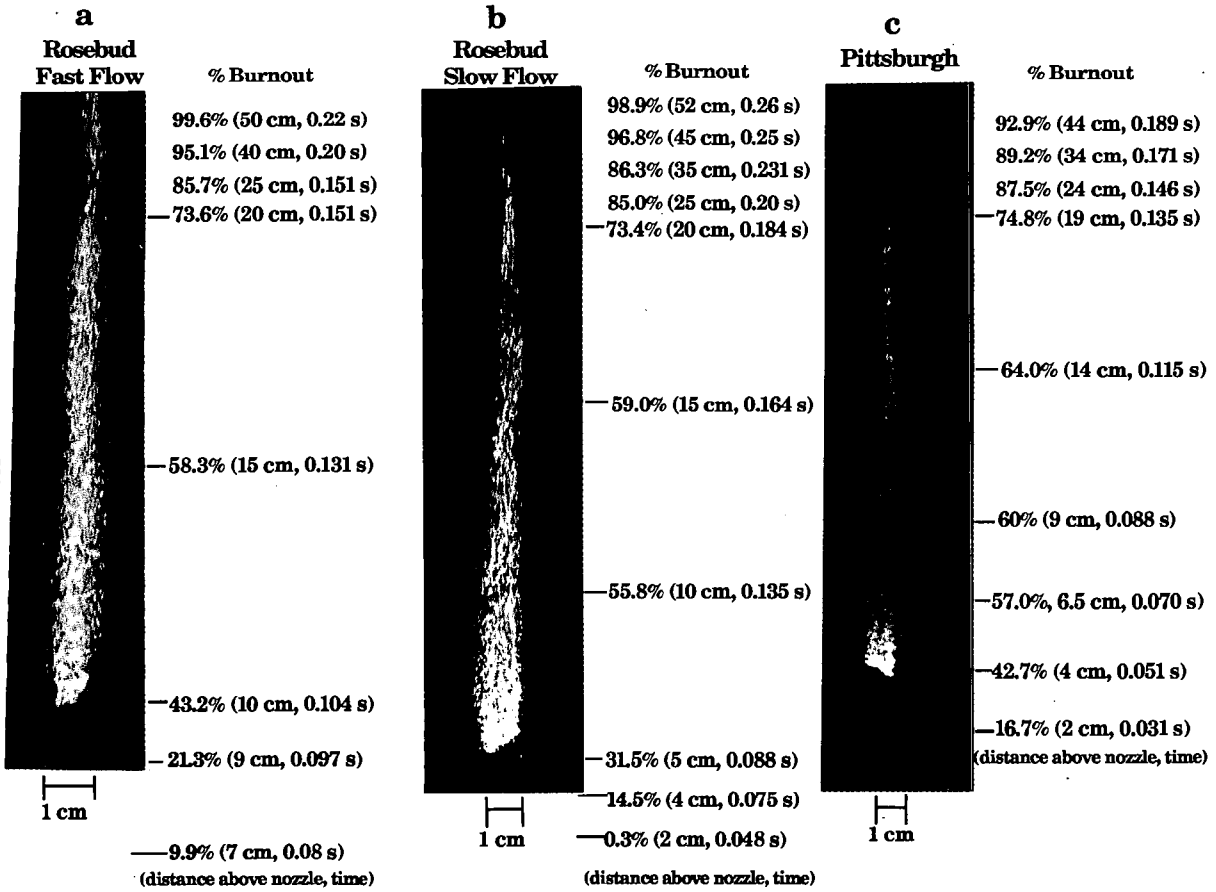

Figure 1. Photographs of Coal Flames in the TWR. a) Rosebud Subbituminous - Fast Flow, b) Rosebud Subbituminous Coal - Slow Flow, and c) Pittsburgh Seam Bituminous - Slow Flow. % Burnout as Determined from Particle Collections in each Flame is Indicated.

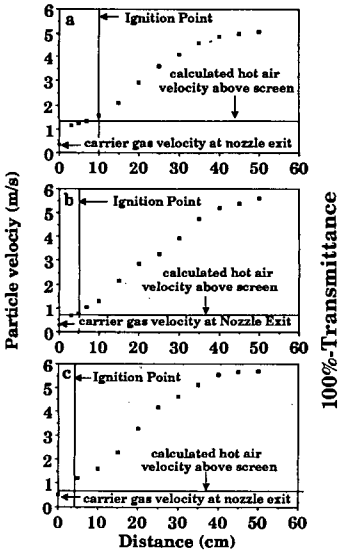

Figure 2. Particle Velocities as a Function of the Distance Above the Nozzle. a) Rosebud Subbituminous Coal - Fast Flow, b) Rosebud Subbituminous Coal - Slow Flow, and c) Pittsburgh Seam Bituminous Coal - Slow Flow.

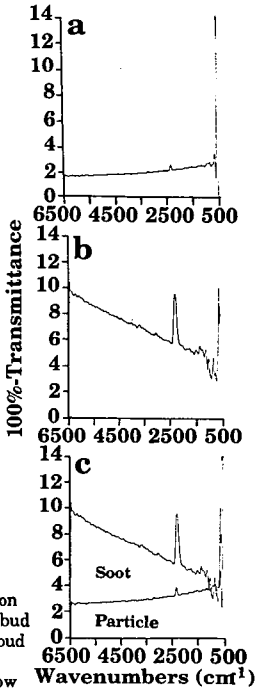

Figure 6. Analysis to Resolve Continuum Blockage Spectrum into Particle and Soot Contributions. a) Particle Blockage Below Ignition, b) Total Particle and Soot Blockage above Ignition, and c) Contribution of Each Component to Total Blockage.

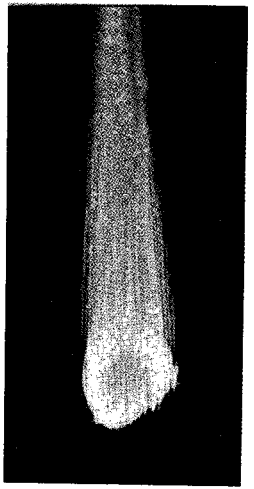

Figure 7. Photograph of Rosebud Subbituminous Coal - Slow Flow Flame Taken from Above the Ignition Region.

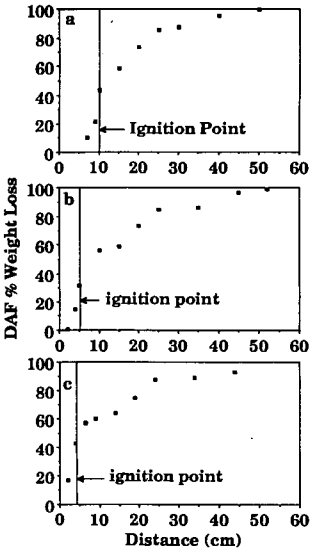

Figure 8. DAF % Weight Loss (burnout) as a Function of Distance Above the Nozzle for a) Rosebud Coal - Fast Flow, b) Rosebud Coal - Slow Flow and c) Pittsburgh Coal - Slow Flow.

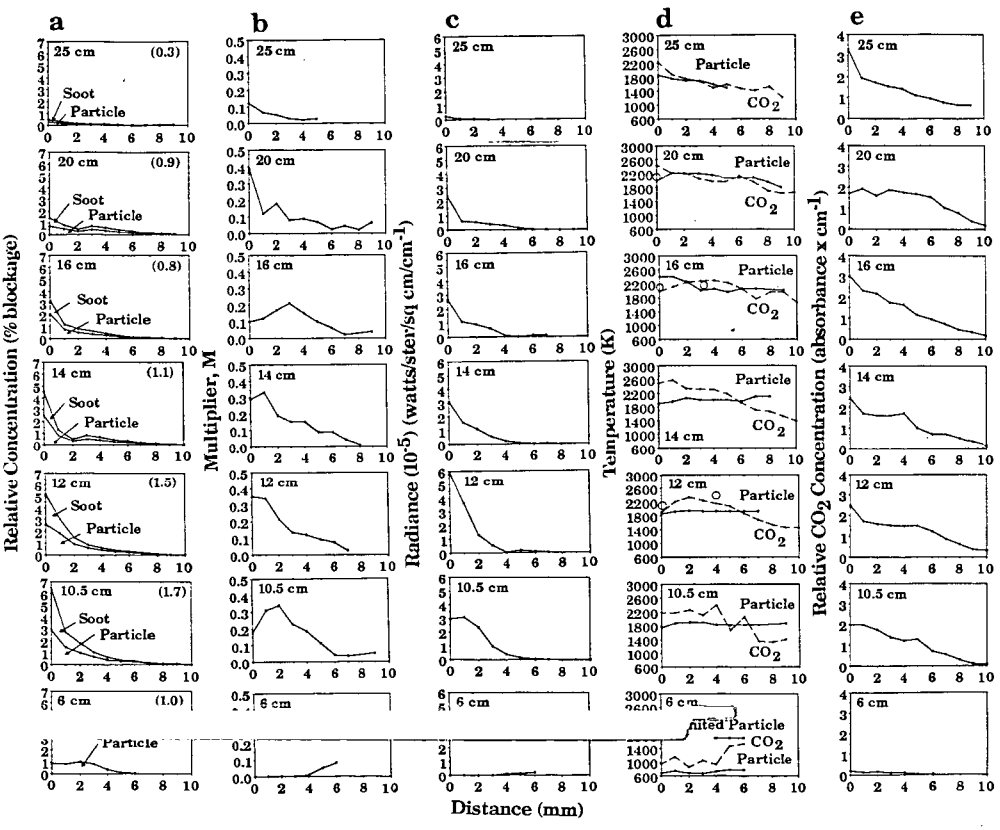

Figure 3. Data for Rosebud Subbituminous Coal - Fast Flow Flame. Radial Distributions of a) Particle and Total (particle + soot) Concentration. Integrated Particle Blockage is Indicated in Parenthesis; b) Multiplier for IgnitedParticles (Black-body intensity); c) Spectral Radiance at 4500 cm^{-1}; d) Particle (solid) and CO_2 (dashed) Temperature; e) CO_2 Concentration at Indicated Distances above the Nozzle for a Rosebud Coal Flame in the TWR.

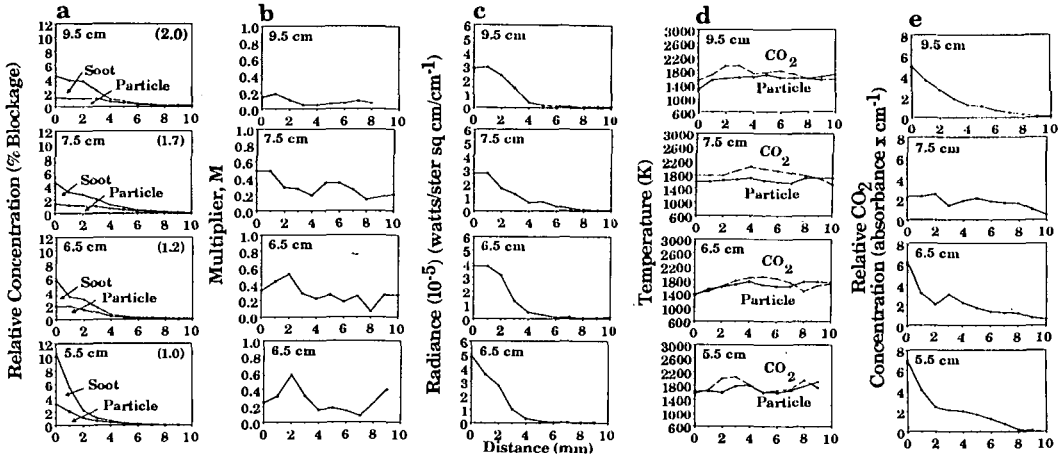

Figure 4. Data for Rosebud Subbituminous Coal - Slow Flow Flame. Radial Distributions of a) Particle and Total (particle + soot) Concentration. Integrated Particle Blockage is Indicated in Parenthesis; b) Multiplier for *IgnitedParticles (Black-body intensity)*; c) *Spectral Radiance at 4500* cm^{-1}; d) Particle (solid) and CO_2 (dashed) Temperature; e) CO_2 Concentration at Indicated Distances above the Nozzle for a Rosebud Coal Flame in the TWR.

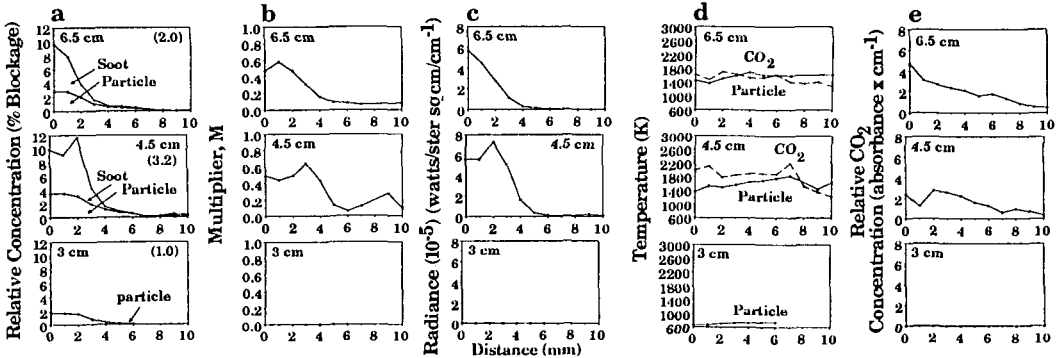

Figure 5. Data for Pittsburgh Seam Bituminous Coal - Slow Flow Flame. Radial Distributions of a) Particle and Total (particle + soot) Concentration. Integrated Particle Blockage is Indicated in Parenthesis; b) Multiplier for Ignited Particles (Black-body intensity); c) Spectral Radiance at 4500 cm^{-1}; d) Particle (solid) and CO_2 (dashed) Temperature; e) CO_2 Concentration at Indicated Distances above the Nozzle for a Rosebud Coal Flame in the TWR.

DEVELOPMENT OF NOVEL, MASS SPECTROMETRIC COMBUSTION MONITORING TECHNIQUES

William H. McClennen, Neil S. Arnold, Sue Anne N. Sheya, JoAnn S. Lighty* and Henk L.C. Meuzelaar

Center for Micro Analysis and Reaction Chemistry
University of Utah
Salt Lake City, UT 84112

*Chemical Engineering Department, University of Utah
Salt Lake City, UT 84112

KEYWORDS: combustion monitoring, gas chromatography, mass spectrometry

ABSTRACT

An on-line gas and vapor analysis method has been developed to monitor combustion products by short column ("transfer line") Gas Chromatography/Mass Spectrometry. An automated vapor sampling inlet with only inert materials (quartz and fused silica) in the sample path is utilized to introduce flue gases into a 1 m long "transfer line" capillary GC column for rapid, repetitive chromatographic separation of products. The column effluent is introduced directly into the source of an ion trap type mass spectrometer. Combustion products from a gas fired rotary kiln were monitored by this method using a standard Ion Trap Detector (ITD). Detection limits of 20 to 50 ppb were obtained for various substituted benzenes. Monitoring of polycyclic aromatic hydrocarbons (PAHs) from the thermal desorption of contaminated soils in a fixed bed reactor utilized a modified Ion Trap Mass Spectrometer (ITMS). Varying isothermal column temperature allowed analysis of PAHs from naphthalene through 6 ring PAHs. The ITMS system provides higher sensitivity (~4 ppb for benzene) in addition to tandem MS and chemical ionization capabilities for unambiguous identification of combustion products incompletely resolved by the transfer line GC approach.

INTRODUCTION

With the decreasing availability of hazardous waste disposal landfills, new technologies must be utilized for the permanent and proper elimination of these wastes. Of the approximately 265 million metric tons (MMT) of hazardous wastes generated yearly in the United States, at least 47 MMT per year could be incinerated [1]. In addition to the yearly generation of hazardous waste, the cleanup of uncontrolled hazardous waste sites must also be considered. The National Priority List (NPL) contains nearly 1000 sites which have been identified as hazards to public health and the environment and must be remediated. In addition there are estimated to be 10,000 sites which are presently uncontrolled [2]. Among the as yet uncontrolled sites are the widespread contaminated soils of former coal gas plant sites [3]. At these sites one may expect to encounter a broad range of polynuclear aromatic hydrocarbons (PAH's).

The importance of incineration technology for primary treatment of various types of industrial, medical, urban and agricultural waste as well as for remedial treatment of toxic waste dumps, landfills, chemical stockpiles, or accidental spill sites is widely recognized. Thermal treatment

is presently an effective way of removing organic contaminants from soil [4]. Generally, a two stage process is used in which the first stage is represented by a fixed bed or rotary kiln reactor [5] in which the organic contaminants are desorbed and/or pyrolyzed followed by a second stage, high temperature "afterburner" in which the volatile products of the first stage are effectively destroyed. Especially, the heaviest PAH components are likely to desorb very slowly from the soil matrix.

Continuous monitoring is needed to ensure that the incineration or thermal desorption system is operating properly at any given time [6]. Currently, unwanted emissions due to faulty equipment or operational procedures are generally detected (if at all) weeks or even months after the fact, when laboratory test data become available. Modern, on-line chromatographic and spectroscopic monitoring techniques offer the potential of near instantaneous feedback, thereby enabling immediate detection and correction of problems before significant levels of unwanted emissions have occurred. In view of their high sensitivity, specificity and speed, mass spectrometric methods play an important role among candidate monitoring techniques.

As shown by McClennen et al. [7,8] and Arnold et al. [9,10] a transfer line gas chromatography/mass spectrometry (TLGC/MS) technique, using the heated 1 m long coated fused silica capillary transfer line of a Finnigan-MAT Ion Trap Detector (ITD) as a short GC column, constitutes a powerful detection and characterization method for volatiles evolving from combustion reactors. In combination with a specially developed direct vapor sampling inlet [10] vapor detection levels in the low ppb range, corresponding to subpicogram quantities, can be achieved on an array of volatiles.

EXPERIMENTAL

The transfer line chromatography is performed using a 1 m fused silica capillary column which is contained and heated in the ITD transfer line. The inlet of the column is at ambient pressure, while the exit is evacuated in the ion trap. Using a .18 mm ID column, the carrier gas (helium) velocity is 2.7 m sec^{-1} (at 4400 ft elevation), which is close to optimum for the column length and pressure drop.

For both the fixed bed and kiln experiments a direct vapor sampling transfer line GC/MS method was used. The direct atmospheric vapor sampling inlet, shown in Figure 1, consists of three concentric tubes with appropriate flow control plumbing and electronics. The inlet system is made from deactivated fused silica, quartz and glass, or glass lined metal tubing. The sample path contains no moving parts. When sampling, the gas is exposed to the column inlet for a controlled period of time (0.5 to 2 s) while 30 to 200 μL of sample is admitted to the column. Helium carrier gas flow is then restored for the rest of the sampling cycle and GC separation of the sample takes place.

This inlet is coupled to fixed a pressure column drop transfer line chromatography. The 1 m long transfer line fused silica capillary GC column, provides both a nominal GC separation of components and a pressure drop to the ion source of the mass spectrometer. With the fixed pressure drop, the chromatographic conditions are controlled primarily by the column length, radius and temperature [11].

This transfer line inlet system was used with both a regular Finnigan MAT ITD and a modified ITMS system (termed MINITMASS) with axial modulation and Selective Mass Storage to allow for tandem mass spectrometry [12]. In addition to tandem capabilities, this second system permitted higher flow rates by using the axial modulation feature. The combination of increased resolution and increased flow rates resulted in higher sensitivity.

Rotary Kiln - The (GC/MS) system was used to monitor the evolution of trace amounts of hydrocarbons evolving from a material combusted in a rotary-kiln simulator. The rotary-kiln simulator is a useful tool for determining the transient emission of hydrocarbons from a control volume of waste. The simulator replaces the variable of kiln distance in a full-scale incinerator for that of time in the simulator; hence, the gas-phase concentrations of hydrocarbons are given as a function of combustion time for various combustion parameters. Approximately 11 g samples of a polymeric material were loaded into the kiln and incinerated at two different temperatures, 600 C and 760 C.

Rapid on-line analysis of rotary kiln combustion was obtained using the ITD based system. A sample flow of 25-50 ml/min of kiln gases were sampled from the transition area to the afterburner (see Figure 2). Samples were taken at 10 sec intervals to follow the concentration fluctuations following sample introduction into the kiln. The transfer line column was a 1 m long, .15 mm ID methyl silcone (DB-1) coated capillary column. The film thickness was 1.2 μm thick and for the present results the column was operated at ambient and 82 C. Carrier gas flow conditions were 250 cm/s or 1.7 ml/min. For these analyses the mass spectrometer was scanned at 4 scans/second from m/z 35 to 120 for the ambient column temperature runs and from m/z 50 to 148 for the 82 C runs.

Bed Characterization Reactor - The bed characterization reactor (BCR, see Figure 3) is used to study the thermal desorption of compounds from contaminated soils and is described in detail elsewhere [13]. Contaminated and uncontaminated clay soil samples were obtained from several undisclosed sites. The contaminated samples were air dried and designated simply as "soil A" and "soil B." Approximately 200 grams of soil were placed beneath the BCR radiant heaters with a 3 cm/sec gas stream flowing across the bed, and were monitored for temperature change and weight loss. The exhaust gas was monitored 25 cm beyond the bed by a quartz tube drawing ~25 ml/min of gas past the vapor inlet. Samples of these gases were taken at 60 sec intervals to monitor the release of volatiles from the soil. The transfer line separation was performed using a 1 m long, .18 mm ID methyl-phenyl silicone (DB-5) coated capillary column. A .4 μm thick stationary phase provided the separation of compounds in vapor phase. The larger column ID had carrier gas flows of 360 cm/sec or 3.5 ml/min. The modified ITMS (MINITMASS) system accommodated these higher flows with axial modulation. The spectra were scanned from m/z 50 to 200 or m/z 60 to 300 depending on the compounds of interest. Various boiling point ranges of compounds from naphthalene to 6 ring PAHs were monitored by isothermal operation of the transfer line at 125 or 230 C.

RESULTS AND DISCUSSION

Figure 4 shows the chromatograms for repetitive GC/MS sampling of the kiln exhaust gases at 10 s intervals as indicated; the column temperature was 82°C and the kiln temperature was 600°C. The top trace represents the total ion chromatogram while selected chromatograms of ions with mass to charge ratios (m/z) 78 and 92 show the individual peaks for benzene and toluene, respectively. Note that the chromatogram of Figure 4 consist of a series of short chromatograms with peak areas of the separate compounds being proportional to the exhaust gas concentrations at each sampling time. Higher boiling compounds which do not elute within the 10 s sampling interval overlap with subsequent sampling, but can still be resolved by separate ion chromatograms and related back to the correct sample time.

Concentration profiles for separate compounds, determined by the GC/MS data illustrated in Figure 4, are shown in Figure 5 for a kiln temperature of 600 C. The data show the concentrations (ppb) of benzene, toluene, C_2-benzenes, phenol, and styrene as a function of time, with peaks at 30 s (20 s into combustion) and 85 s (75 s into combustion). The polymeric material would initially melt and pyrolyze, releasing high concentrations of organic compounds which then ignited and burned to form water and carbon dioxide. The two peaks in organic products came prior to the flame totally engulfing the samples, and after the local flame began to burn out. During higher temperature kiln tests, at 760 °C, only the most stable products such as benzene were observed above the 20-40 ppb detection limits as the organics were more quickly and completely oxidized.

Figure 6 shows the total ion chromatograms and several selected ion chromatograms for a single vapor analysis during BCR thermal treatment in N_2 of soil B. C_1, C_2 and C_3 alkylnaphthalene peaks are indicated by selected ion traces of m/z 142, 156, 170, respectively. For these vapor analyses, data were not acquired for the first 2 s after sampling to allow elution of the major gas and vapor components which were essentially non-retained on the GC column. With the short column operated isothermally at 125 C, naphthalene was completely separated from the N_2 and other light gases while the combined phenanthrene/anthracene eluted less than 45 sec later.

By integrating the areas of specific molecular ion peaks within each 1 min segment, composite evolution curves were produced such as those shown for soil B in the BCR in Figure 7. Figure 7a compares the time evolution profiles for naphthalene at m/z 128, the combined phenanthrene/anthracene peaks at m/z 178, and their methyl homologs at m/z 142 and 192 respectively. In all cases a major evolution maximum is observed at approximately 10 minutes followed by a second minor peak at approximately 45 minutes into the run. The second evolution peak is larger relative to the first peak for the unsubstituted compounds than for the methyl homologs. In other words, a larger proportion of methyl homologs desorbed within the first 30 minutes or so when water is being desorbed from the soil bed.

The desorption of tar components from the BCR soil bed is further represented in Figure 7b where the heteroatomic compounds dibenzofuran at m/z 168, and dibenzothiophene at m/z 184, are compared to the PAH fluorene at m/z 166. As expected, the higher boiling dibenzothiophene (b.p. 332-333) has a slightly broader and later second peak than the dibenzofuran (b.p. 287). However, both of these have much larger second evolution peaks than the fluorene, similar to unsubstituted PAHs relative to their methyl homologs as in Figure 7a. One interpretation is that the four planar, fully aromatic compounds, namely naphthalene, phenanthrene/anthracene, dibenzofuran and dibenzothiophene, might be more strongly bound to the soil and less completely released in the first thermal desorption or "steam stripping" process than the alkyl substituted or non-planar (fluorene) compounds. A second possibility is that a larger fraction of the fluorene and methyl-aromatics might have reacted to form other products due to their greater ease of oxidation. This latter explanation is supported by the observation of aldehyde and ketone oxidation products such as 9-fluorenone in extracts from incompletely desorbed soils run at lower temperatures or shorter times.

CONCLUSIONS

The broad range of boiling points and polarities of the organic vapors produced during incineration or the thermal treatment of contaminated wastes and soils mandates the use of sophisticated instrumentation for monitoring their production, evolution, and destruction, especially during the design of new facilities. The results of this work have demonstrated that the on-line, short-column GC/MS approach is capable of reliably obtaining qualitative and quantitative data on the products evolving from two types of incinerators.

The on-line short column GC/MS systems are shown to be powerful instruments for measurement of transient concentrations (30-60 sec interval) of a broad range of aromatic compounds. Short column gas chromatography separates the organic vapors away from the major ambient atmospheric constituents and also provides some separation of isomers indistinguishable by MS. The mass spectrometer provides a rapid and sensitive method of compound identification and specific quantitation. A standard Ion Trap Detector is an economical MS system with 20-40 ppb detection limits for aromatics while the MINITMASS system offers improved sensitivity and the added selectivity of MS^n capability.

ACKNOWLEDGEMENTS

This work was sponsored by the Advanced Combustion Engineering Research Center. Funds for this Center are received from the National Science Foundation, the State of Utah, 23 industrial participants, and the U.S. Department of Energy.

REFERENCES

1. Oppelt, E.T., *J. Air Pollut. Control Assoc.*, **37**, 558 (1987).
2. Wentz, C.A., *Hazardous Waste Management*, McGraw-Hill, New York, 1989, p. 84.
3. de Leer, E.W.B., Bass, M., Erkelens, C., Hoogwater, D.A., de Leeuw, J.W., Schutl, P.J.W., de Leer, L.C. and Graat, J.W., *Proc. of Conf. on New Frontiers for Hazardous Waste Management, USEPA*, Cinn, OH, EPA/600/9-85025, (1985).
4. Troxler, W.L., Alperin, E.S. and Fox, R.D., *Proc. 8th Intl. Conf. on Thermal Destruction of Hazardous, Radioactive, Infectious and Mixed Wastes*, Knoxville, TN (1989).
5. Oppelt, E.T., *J. Air Pollut. Control Assoc.*, **37**, 558 (1987).
6. Lee, K.-C., *J. Air Pollut. Control Assoc.*, **38**, 1542 (1988).
7. McClennen, W.H., Arnold, N.S., Lighty, J.S., Eddings, E.G., Lindgren, E.R., Roberts, K.A. and Meuzelaar, H.L.C., *Proc. ACS, Div. of Fuel Chem.*, Miami, FL, **34**:3, p. 1028 (1989).
8. McClennen, W.H., Arnold, N.S., Roberts, K.A., Meuzelaar, H.L.C., Lighty, J.S., Lindgren, E.R., Fast, Repetitive GC/MS Analysis of Thermally Desorbed Polycyclic Aromatic Hydrocarbons (PAHs) from Contaminated Soils, *Combustion Science & Technology*, in press, 1990.
9. Arnold, N.S., McClennen, W.H., and Meuzelaar, H.L.C., *Proc. ACS, Div. of Environmental Chem.*, Miami, FL, Vol. 29, No. 2, p. 426. (1989).
10. Arnold, N.S., Roberts, K.A., McClennen, W.H., Meuzelaar, H.L.C., *Proc. of the 37th Annual Conf. on Mass Spec. and All. Topics*, Miami, FL, 1425 (1989).
11. Arnold, N.S., McClennen, W.H., Meuzelaar, H.L.C., Development of an On-line Transfer Line GC/MSn Sampling Method for Direct Atmospheric Vapor Analyses at Low PPB Levels, submitted to *Analytical Chemistry*, 1990.
12. Meuzelaar, H.L.C., McClennen, W.H., Arnold, N.S., Reynolds, T.K., Maswadeh, W., Jones, P.R., Urban, D.T., *Proc. 1st Intl. Symp. Field Screening Methods for Hazardous Waste Site Investigations*, Las Vegas, NV, 195 (1988).
13. Lighty, J.S., Silcox, G.D., Pershing, D.W., Cundy, V.A. and Linz, D.G., *Environ. Progress*, **8**, 57 (1989).

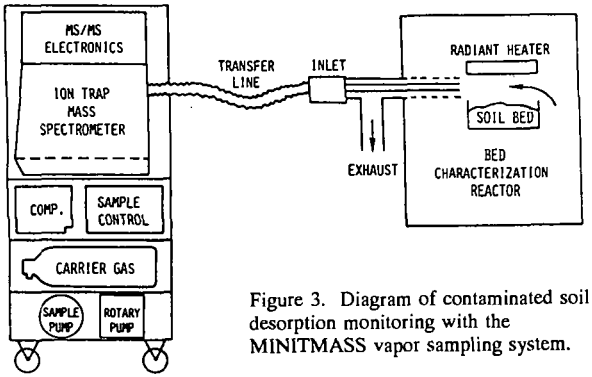

Figure 3. Diagram of contaminated soil desorption monitoring with the MINITMASS vapor sampling system.

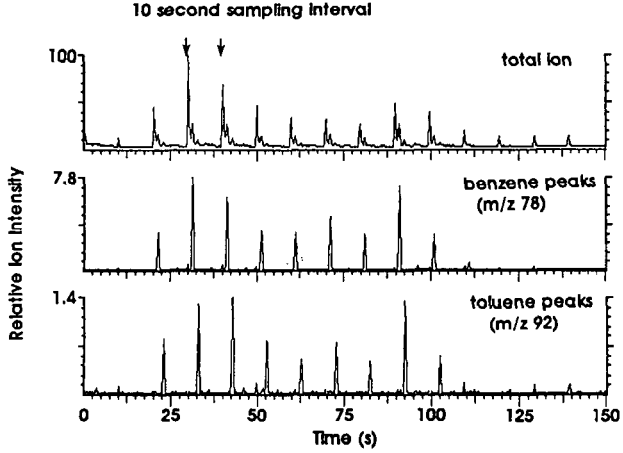

Figure 4. Total and selected ion chromatograms from 16 repetitive GC/MS vapor samples during incineration of disposable medical supplies in the rotary kiln simulator.

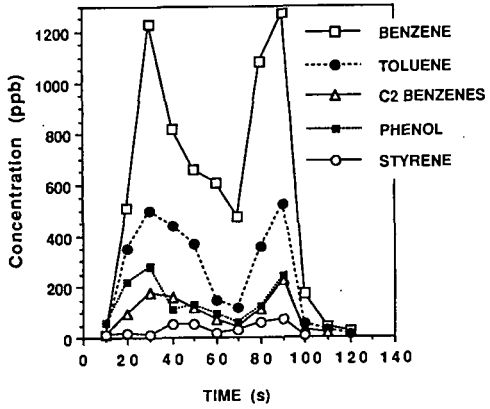

Figure 5. Time evolution of organic compounds during incineration of medical supplies at 600 C in a rotary kiln simulator.

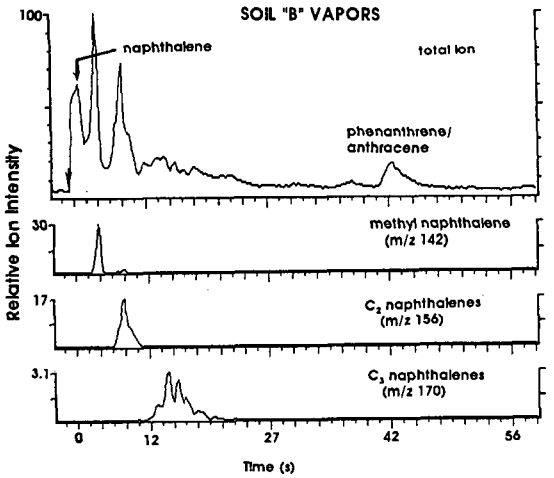

Figure 6. Total and selected ion chromatograms for a single on-line vapor sample GC/MS analysis during a 400 C BCR run on soil B.

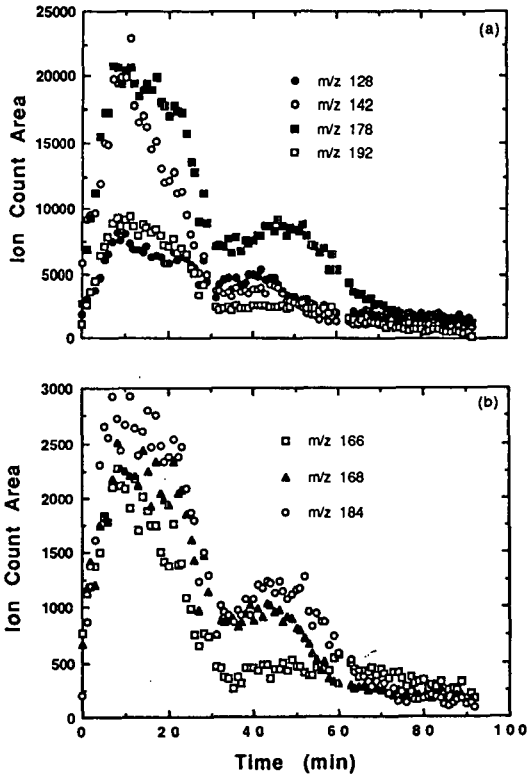

Figure 7. Time evolution profiles for several compounds from vapor sampling of the thermal treatment of soil B in the BCR at 400 C. Each point is from the integrated area of a specific peak in the molecular ion chromatogram for the 90 vapor samples. The ions represented are: in a) m/z 128, naphthalenes; m/z 142 methylnaphthalenes; m/z 178, phenanthrene/anthracene; m/z 192, methyl-phenanthrenes and anthracenes; in b) m/z 166, fluorene; m/z 168, dibenzofuran; and m/z 184, dibenzo thiophene.

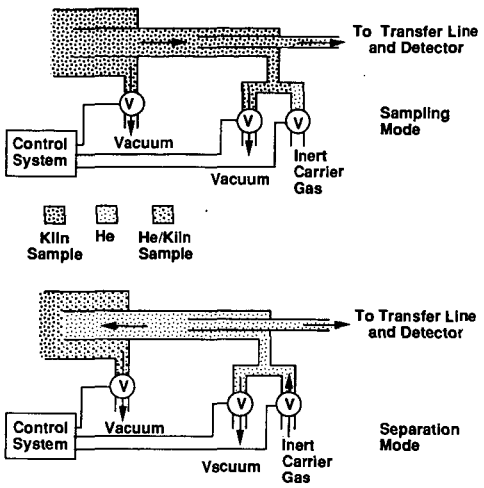

Figure 1. Schematic diagram of vapor sampling inlet operation.

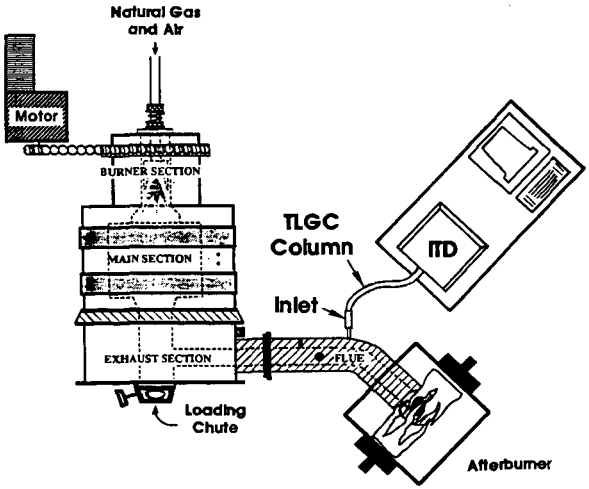

Figure 2. Top view of rotary kiln simulator with on-line GC/MS system using an Ion Trap Detector (ITD).

TRANSIENT EMISSIONS ASSOCIATED WITH VARIOUS FURNACE CYCLIC PATTERNS IN RESIDENTIAL OIL COMBUSTION - A LABORATORY STUDY

S. Win Lee

Energy Research Laboratories, CANMET
Energy, Mines and Resources Canada
555 Booth St. Ottawa. Canada. K1A 0G1

INTRODUCTION

Environmental considerations dictate that combustion processes increase energy efficiency, reduce pollutant emissions from fossil fuels and utilises alternate fuels that generate fewer particulates and volatile organics. These considerations will receive greater attention than the operational costs as the environmental awareness of a concerned public increases. All combustion processes are potential air pollution sources and most of the major fuel consuming units are covered by government regulations, the residential heating appliance being one of the few exceptions. In Canada, with its cold winter climate, energy in the form of electricity and heating fuel for domestic requirement makes up for about one-fifth of the total national energy consumption. Energy conservation in the residential sector is encouraged nationally and an average homeowner sees its direct effects as immediate dollar savings. However, there is a need to increase the public awareness on the environmental impact of reduced energy consumption since it is not as evident as in cost reduction.

The Combustion and Carbonization Laboratory, a federal research facility long associated with research programs to promote efficient use of energy, provides technical information including publications on conservation strategies and pollution emissions in residential oil heating (1, 2). Data from field studies revealed that the most effective strategies for both fuel saving and emission reduction are the use of a high efficiency low excess air burner, lowering the overnight thermostat setting significantly, and by reducing the burner firing rate. As for reduction of seasonal emissions of carbon monoxide and particulates, a combined strategy of reduced fuel consumption and reduced cycling frequency was suggested. The authors observed that these emissions were contributed equally by cyclic emissions and steady-state emissions at combustion air levels giving steady-state smoke numbers close to one.

Keywords: cyclic combustion, emissions, residential heating

A similar study by other researchers reported that particulates, carbon monoxide, and hydrocarbons decrease in concentration as the excess air level increases and that hydrocarbons tend to increase once excess air level reaches a certain level and beyond (3). An apparent linear correlation between particulate emissions and final boiling point of the fuel at low excess air conditions was also suggested. The present study focuses on laboratory measurements of startup transient emission levels at different burner on/off cyclic operations. The purpose is to determine the effect of burner cyclic pattern, especially "off" period on emission concentrations. This work is part of the ongoing research program on fuel quality and combustion characteristics of middle distillates at the Combustion and Carbonization Research Laboratory.

MATERIALS AND METHODS

Fuel Types and Properties

Eight specific fuels with different characteristics (Table 1) were selected for this work. Fuels N, Q, HH, and FF are commercial No. 2 heating fuels purchased locally. Three other fuels (OO, CC, PP, EE) were contributed by various Canadian oil companies. The origin of crudes and the refinery processes utilized to produce the fuels vary depending on the company and location. They were specially blended to obtain a wide range of properties especially varying aromatic concentrations. Fuel FF was used in combustion tests with variable cyclic pattern and the rest were used in simulation tests for reduced overnight thermostat cut-back (lowering of setting) situations.

Combustion Experiments

All combustion experiments were carried out using the procedure and facilities developed at the Combustion and Carbonization Research Laboratory (4). The schematic of the experimental facilities is shown in Figure 1. The experimental procedure can simulate the actual usage pattern of residential oil heating in Canadian homes. A typical experimental run starts with an initial burner startup (cold start) lasting one hour (steady state), immediately followed by five consecutive cyclic operations with selected on/off time pattern. Flue gas emissions and temperatures at specified locations of the test rig are continuously monitored over the entire run. The following experimental equipment and operating conditions were used.

Fuel temperature:	15 ± 2 °C
Nozzle oil temperature:	17 - 20 °C for cold start
Fuel pump pressure:	100 psi
Oil nozzle:	0.65 US gph, 80° spray angle
Combustion air:	Set to obtain a No 2 smoke at steady-state with Bacharach tester for each fuel

Cold air return temp:	15 ± 1 °C
Burner:	Beckett domestic gun type burner with Areo AFC-2 flame retention head
Furnace:	Forced air type. Brock model LO-1M, 74,000-120,000 Btu/h, with concentric tube type heat exchanger.
Furnace draft:	1 mm (0.04 in) of water column

Equipment for Emission Monitoring

The oxygen analyzer was a paramagnetic type instrument while the carbon dioxide and carbon monoxide analyzers used the infrared detection principle. Nitrogen oxides in the flue gas were measured by a chemiluminescent type instrument. Particulates were measured manually with a Bacharach smoke tester and continuously with a Celesco model 107 in-line smoke opacity meter. Temperature of the oil in the nozzle line was measured continuously using a "K" type thermocouple inserted through a hole in the nozzle adaptor located as close as possible to the nozzle.

The burner cold-start operation was simulated in the laboratory by cooling the appliance, especially burner and combustion chamber by a blast of chilled air until they attained temperatures comparable to those of a residential basement environment. Based on the actual readings from homes, oil temperature in the nozzle line was lowered to 17-20 °C.

RESULTS AND DISCUSSION

No two homes will have the same appliance on/off cyclic operation pattern since it varies depending on numerous factors. The appliance type and condition, level of home insulation, climate, location, user comfort level and life style, thermostat anticipator setting, and overnight temperature setting all determine the operation mode of a residential burner. The cyclic pattern strategy described in Table 1 attempts to simulate some of the possible situations but by no means represents the numerous real life conditions in homes. These patterns are selected to reflect the usage pattern of most Canadian homes where lowering the thermostat setting before retiring at night is the accepted practice for energy conservation.

The degree of severity in overnight thermostat cut-back, however, controls the length of the burner cycles and consequently the burner performance at the cold-temperature conditions. The performance may be adversely affected in the case of fuels with slightly lower grade specifications and of high aromatics as have been predicted for marketing, before the fall of oil prices in 86. Four special blends were selected to represent this senerio.

Transient emissions from cyclic combustion of a No. 2 fuel at variable on/off cyclic patterns

As reported in the literature, gaseous and particulate emissions of a residential burner are higher at transient startups and shutdowns than steady-state conditions. The peaking of emissions at startup is due to the cold temperature conditions, mainly low fuel volatility leading to a poor fuel/air mixing, before the combustion zone temperature rises. Immediately upon shutdown, incomplete combustion products result due to an excess fuel condition created by the high pressure oil pump and lack of combustion air supply. These emission peaks are difficult to reproduce by a burner and concentrations between five consecutive cycles show variations with a relative standard deviation of 5% to 20%. The reproducibility of emission data from controlled cyclic operations is much better for typical commercial fuels than those of lower grade fuels.

Data in Table 3 show particulate and gaseous emissions at different transient startup conditions. Each value represents the average of data from a minimum of three experimental runs, each run having five consecutive cycles. Opacity % reported in Table 3 represents the average maximum opacity reading at the peak of transient particulate emissions as recorded by the smoke opacity meter. The reproducibility of opacity, calculated as relative standard deviation, between each run ranges from 7% to 26%. Despite this moderate error margin, there appears to be a gradual trend to increasing particulate levels with the increase in burner cooling-down time. A noticeable increase in particulate emissions was noted after a 7 to 10 hours burner "off" period (simulation of an extreme overnight thermostat cut-back condition). A gradual decrease in the oil temperature in the nozzle line was noted as the burner off period increased. This cooling- down process is dependent of the combustion chamber design among other variables. Similar variable cyclic tests in a different appliance may or may not find the same observations. Data indicate that severe thermostat cut-back could increase pollution emissions from a residential oil burning unit. However, this emission increase is compensated, by several magnitudes, by the total emission reduction resulted from the long burner "off" period.

These combustion tests were carried out using Fuel FF under identical steady-state particulate concentrations of Bacharach smoke number 2. This condition provided an steady-state efficiency of 84% and an excess air of 36% (equivalence ratio of about 1.4). During a one hour steady-state run before cycling, the CO emissions were between approximately 30 ppm and no detectable hydrocarbons were recorded. CO and hydrocarbon emissions at transient startups are significantly higher than steady-state levels. They appear to be similar in magnitude for all variable cyclic operations. Nitrogen oxides concentrations are consistent in all steady-state and transient emissions.

Transient emissions from cold-start and cyclic combustion of different distillate oils

The difference in transient particulate emissions from cold-start and cyclic combustion experiments using different fuels is seen in Table 4. Data indicate that cold-start particulates are higher than cyclic emissions for all fuels. This could be mainly due to the combustion temperature differential between the two operations. The actual thermocouple reading recorded during an experimental run showed that the oil temperature in the nozzle line was between 17-21 °C at cold-start and between 35-65 °C during cyclic operations following a one hour steady-state run. The significant effect of oil temperature at ignition on particulate emissions of residential burners was reported elsewhere (5). Favourable warm temperatures of the oil and combustion zone allows efficient burner ignition and reduced incomplete combustion products.

Data in Table 4 also indicate that, using the same burner, higher cold-start smoke emissions resulted from fuels with higher aromatics. Cyclic transients of the fuels are comparable (Fig.2). Smoke opacity, resulting mainly from soot in the flue gas, is an indicative combustion parameter since other incomplete combustion products exhibit similar emission trends. Although the fuel aromatics are not included in current specifications, volumetric concentrations of aromatics of No. 2 heating fuels fall within 20 to 40%. Special blends have aromatics concentrations higher than 40 %. 90% boiling point of the fuels appear to be proportioal to aromatics. Data suggests that cold-start emissions may be of concern if the fuel aromatics reaches about a 60 % level. The strong influence of fuel viscosity and aromatics on burner performance have been reported previously by the author (6). It was shown that off-spec, low quality fuels generate higher emissions of incomplete combustion products such as particulates, carbon monoxides and hydrocarbons than normal fuels. A complex relationship among fuel properties such as aromatics, viscosity, boiling point range, carbon residue, and gravity influences combustion emissions. This paper is limited to the scope of burner performance at various cyclic patterns.

The following conclusions can be drawn from this study;

1. Transient emissions from varying burner on/off cyclic patterns show a slight increasing trend of particulate emissions as the burner cooling-down period increases.
2. Cold-start ignition after a burner cooling-down period of more than 7 hours, simulating a severe thermostat cut back situation generates higher emissions than cyclic operation.
3. Cold-start transient emissions increase with increasing fuel aromatics and final boiling point but cyclic emissions are less affected by fuel properties.

ACKNOWLEDGEMENT

The author thanks D.E. Barker and N. Rioux for combustion experiments and Canadian oil companies for contribution of fuels.

REFERENCES

1. Hayden, A.C.S, Braaten, R.W., and Brown, T.D. ASME Transactions. 1976. Paper No.76-WA/Fu-8.
2. Hayden, A.C.S, Braaten, R.W., and Brown, T.D. JPCCA. 1978. 28(7), 653-758.
3. Kraus, B.J. and Coburn, J.F. Prep. Am. Chem. Soc. 1974. 19(5), 49-58.
4. Lee, S.W. and Hayden, A.C.S. ASHRAE Transactions. 1986. 92. Part 1B, 667-682.
5. Lee, S.W. and Hayden, A.C.S. 1989. Prep. Am. Chem. Soc. Div. Fuel. Chem. 1989. 34(3), 1000-1007.
6. Lee, S.W. and Hayden, A.C.S. 1986. ASHRAE Transactions. 92. Part 2B, 223-238.

Table 1. Basic Properties of Fuels

Fuel	Density Kg/L @ 15°C	Viscosity c St @ 38°C	Aromatics Vol %	90% BP °C	Calorific Value MJ/kg
N	0.845	2.09	30.3	322	44.3
Q	0.846	2.59	30.6	325	45.5
FF	0.855	2.52	31.4	311	44.5
HH	0.861	2.82	39.2	308	45.1
CC	0.902	2.70	54.2	315	43.9
OO	0.914	2.56	55.2	304	43.7
PP	0.916	2.61	60.0	327	43.2
EE	0.912	2.90	68.0	368	43.2

Table 2. Laboratory Furnace Cyclic Operation Pattern to Simulate Various Periods of a Heating Season

ON time (m)	OFF time (m)	ON/OFF ratio	Approximate period
5	15	0.33	Fall and spring months
5	10	0.5	Fall and spring months
5	5	1.0	Most of winter days
10	10	1.0	Most of winter days
3.8	13.3	0.29	ASHRAE 103 standard average
10	30	0.33	At lower thermostat settings
10	overnight		Under extreme thermostat cut-back conditions

ASHRAE is American Society of Heating, Refregeration & Air-Conditioning Engineers

Table 3. Maximum Transient Emissions Resulting from Different Cyclic Combustion Processes of Fuel FF

on/off time (m)	Opacity (%) & BSN[a]	Carbon monoxides (ppm)	Hydrocarbons (ppmc)	Nitrogen oxides (ppm)
10/5	1.1 (6)	235	14	75
10/10	1.2 (6)	250	20	73
5/5	1.2 (6)	260	15	73
5/10	2.2 (7)	265	30	75
5/15	2.6 (8)	190	20	76
3.8/13.5	2.1 (8)	330	25	72
10/60	2.9 (8)	325	23	75
overnight	3.1 (9)	360	32	72

[a] BSN represents Bacharach smoke number

Table 4. Startup Transient Particulate Emissions from Different Fuels

Fuel	Maximum Cold-start Opacity %	Maximum Cyclic startup Opacity %
N	1.7	0.2
Q	1.6	0.4
FF	3.1	1.2
HH	1.4	0.9
CC	4.7	2.3
OO	2.8	1.3
PP	3.9	1.8
EE	26	2.9

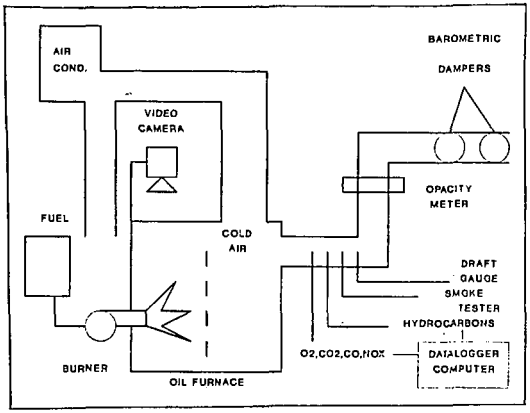

Figure 1. Schematic of equipment for combustion experiments.

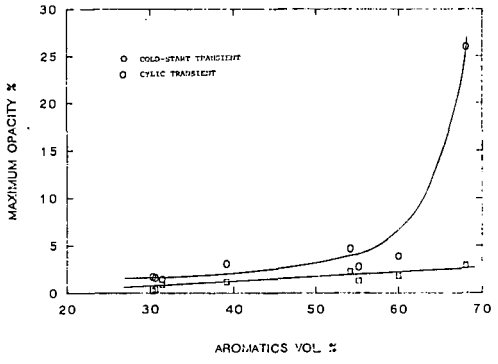

Figure 2. Startup transient particulate emissions from different fuels.

A CONTINUUM THEORY FOR THE FLOW OF PULVERIZED COAL IN A GASIFIER

M. Massoudi and P.X. Tran
U.S. Department of Energy
Pittsburgh Energy Technology Center
P.O. Box 10940
Pittsburgh, PA 15236

ABSTRACT

Multiphase flows have increasingly become the subject of considerable attention because of their importance in many industrial applications, such as fluidized beds, pneumatic transport of solids, coal combustion, etc. For example, coal conversion in an entrained flow reactor has received much attention as an important process for transforming coal into fuel gas [cf. Phuoc and Durbetaki (1987)]. In this work the behavior of coal particles in a down flow reactor is modeled using the theory of interacting continua (or mixture theory). The mixture is considered to be made up of saturated granular materials (coal particles) infused with a linearly viscous fluid (gas). Appropriate constitutive relations for stresses and interactive forces are motivated and proposed [Massoudi (1988)]. The conversion of coal particles is studied in terms of chemical kinetics, fluid dynamics flow of volatiles and the heat transfer mechanism at the interface.

INTRODUCTION

The flows of a mixture of solid particles and a fluid have relevance to several important technologies. Pneumatic transport of solid particles, fluidized bed combustors, and flow in a hydrocyclone are but a few examples. In many processes, such as coal conversion in an entrained flow reactor, coal is transformed into clean fuel gas. A fundamental understanding of the behavior of dense flow of coal particles and the interaction between the gas and the coal particles is extremely important.

In general, developing models capable of describing various multiphase flow regimes has attracted considerable attention due to their significant applications in many chemical and transport processes. These mathematical models or theories may be roughly classified into two categories. In one class, the basic conservation laws are postulated and the ideas in continuum mechanics are used to arrive at appropriate constitutive relations with proper restrictions. In the other class, averaging techniques are used to derive the fundamental balance laws. Whichever approach is used, constitutive relations are needed which would supply connections among kinematic, mechanical, and thermal fields which are compatible with the balance laws and which, in conjunction with them, provide a theory which can be solved for properly posed problems.

In this work the behavior of coal particles in a down flow reactor is modeled using the theory of interacting continua (or mixture theory). This theory is a means for the mathematical modeling of multicomponent systems by generalizing the equations and principles of the mechanics of a single continuum. This theory, which traces its origins to the work of Fick (1855), was first put into a rigorous mathematical format by Truesdell (1957). The theory is, in a sense, a homogenization approach in which each component is regarded as a single continuum and at each instant of time, every point in space is considered to be occupied by a particle belonging to each component of the mixture. That is, each component of the mixture is homogenized over the whole space occupied by the mixture. A historical development of the theory can be found in the review articles by Atkin and Craine (1976), Bowen (1976), and the book by Truesdell (1984). We assume the mixture is made up of saturated granular materials (coal particles) infused with a linearly viscous fluid (gas). Appropriate constitutive relations for stresses and interactive forces are

motivated and proposed. The conversion of coal particles is studied in terms of chemical kinetics, fluid dynamics flow of volatiles and the heat transfer mechanism at the interface. The specific assumptions in the theory of interacting continua, and the constitutive models are presented in the next section.

MODELING

In almost all the modeling of solid particles and a fluid, the solid particles are assumed to behave like a linearly viscous fluid [for a review of this, see Rajagopal, et al. (1990)] with a viscosity μ_s and an associated pressure field p_s. A fundamental shortcoming of assuming a fluid-like behavior for the solid phase is that, theoretically, in one limit, as the volume fraction of solids becomes zero, the mixture of fluid and solid particles should behave as a fluid; in the other limit, as the volume fraction of fluid becomes small, the mixture should behave as a granular material. This second limiting case is not described if the particles are assumed to behave like a Newtonian fluid. Indeed, rheological behavior of granular materials is quite different from that of Newtonian fluids. For example, phenomena such as normal stress effects which are observed experimentally, in the shearing motion of dense flow of granular materials, cannot be predicted using a Newtonian model [Massoudi and Boyle (1987)]. Recently, Massoudi (1988) advocated the modeling of the stress in the solid constituent of the mixture by a constitutive expression appropriate to flowing granular solids, and the stress in the fluid constituent of the mixture by a linearly viscous fluid. Therefore, we assume that the stress tensors ${}^{s}\underline{T}$ and ${}^{f}\underline{T}$ of a granular material and a fluid are, respectively [cf. Rajagopal and Massoudi (1990)].

$$ {}^{s}\underline{T} = [\beta_0(\rho_1) + \beta_1(\rho_1)\, \nabla\rho_1 \cdot \nabla\rho_1 + \beta_2(\rho_1)\, \mathrm{tr}\, {}^{s}\underline{D}]\, \underline{1} + \beta_3(\rho_1)\, \nabla\rho_1 \otimes \nabla\rho_1 + \beta_4(\rho_1)\, {}^{s}\underline{D} \,, \tag{1} $$

$$ {}^{f}\underline{T} = (1-\nu)\, \{[-p_f + \lambda_f(\rho_2)\, \mathrm{tr}\, {}^{f}\underline{D}]\, \underline{1} + 2\mu_f(\rho_2)\, {}^{f}\underline{D}\} \,, \tag{2} $$

where β_i's are material properties of the granular solid*, ν is the volume fraction of solid particles defined through

$$ \nu \equiv \rho_1/\rho_s \,, \tag{3} $$

in which ρ_s denotes the reference density for the granular solid. Notice that if the total stress tensor of the mixture is defined as the sum of the two stresses, ${}^{s}\underline{T}$ and ${}^{f}\underline{T}$, then indeed the two limiting cases (i.e., $\nu \to 0$ and $\nu \to 1$), mentioned earlier, are recovered with the present forumlation. In Equations (1) and (2) ${}^{s}\underline{D}$ and ${}^{f}\underline{D}$ denote the stretching tensor for the solid and fluid phases, respectively; λ_f and μ_f are coefficients of the viscosity of the fluid; p_f the pressure; ρ_2 the density of fluid; ∇ designates the gradient operator; $\otimes$ denotes the outer product; and $\underline{1}$ is the identity tensor.

CONSERVATION EQUATIONS

A detailed description of the conservation laws for mixtures is given in the review articles by Bowen (1976), Atkin and Craine (1976), and the book by Truesdell (1984). Associated with each constituent is its mass supply $\hat{c}_a$, momentum supply $\hat{m}_a$, and an energy supply $\hat{e}_a$, where all these quantities are assumed to be continuous functions. The balance laws are then expressed as

---

*For the meaning of material properties β_0 through β_4 and especially how they can be measured experimentally, we refer the reader to Rajagopal and Massoudi (1990).

$$\partial \rho_a / \partial t + \operatorname{div} (\rho_a \underset{\sim}{v}_a) = \hat{c}_a \tag{4}$$

$$\rho_a \underset{\sim}{v}'_a = \operatorname{div} \underset{\sim}{T}_a + \rho_a \underset{\sim}{b}_a + \hat{\underset{\sim}{m}}_a - \hat{c}_a \underset{\sim}{v}_a \tag{5}$$

$$\rho_a e'_a = \underset{\sim}{T}_a \cdot \operatorname{grad} \underset{\sim}{v}_a + \operatorname{div} \underset{\sim}{q}_a + \rho_a r_a - \hat{\underset{\sim}{m}}_a \underset{\sim}{v}_a - \hat{c}_a (e_a - 1/2\, v_a^2) + \hat{e}_a \ , \tag{6}$$

$$a = 1, 2$$

where prime denotes material time derivative following the motion of the constituent a, $\underset{\sim}{v}_a$ is the velocity of the constituent a, $\underset{\sim}{T}_a$ the stress tensor, $\underset{\sim}{q}_a$ the heat flux vector, r_a external heat sources, and e_a is the specific internal energy. Equation (4) is a statement of conservation of mass, Equation (5) conservation of linear momentum, and Equation (6) conservation of energy.

The modeling of $\underset{\sim}{T}_a$ (a=1,2), was explained in the previous section. In addition, constitutive relations for $\hat{c}_a$, $\hat{\underset{\sim}{m}}_a$, and $\hat{e}_a$, would also have to be provided so that the system of Equations (4) - (6) can be used to study this problem.

In this problem, we will study the downflow of coal-gas mixtures in a gasifier. Specific models for $\hat{c}_a$, $\hat{\underset{\sim}{m}}_a$, and $\hat{e}_a$ will be proposed and motivated. Appropriate boundary conditions will be provided. The basic numerical scheme is that of Phuoc and Durbetaki (1987). Restrictions and assumptions concerning the material properties appearing in the constitutive relations will also be discussed. Quantities and fields of interest which will be calculated and plotted are velocity, temperature, density fields, and pressure distribution.

REFERENCES

Atkin, R.J., and R.E. Craine, Q. J. Mech. Appl. Math., 29, 290 (1976).

Bowen, R.M., in Continuum Physics, III, Academic Press (1976).

Fick, A., Ann-der Physik, 94, 56 (1855).

Massoudi, M., Int. J. Engng. Sci., 26, 765 (1988).

Massoudi, M., and E. Boyle, Technical Note DOE/METC-88/4077, U.S. Department of Energy (1987).

Phuoc, T.X., and P. Durbetaki, Int. J. Numerical Methods Engng., 24, 203 (1987).

Rajagopal, K.R., and M. Massoudi, Topical Report, DOE/PETC/TR-90/3, U.S. Department of Energy.

Rajagopal, K.R., M. Massoudi, and J.M. Ekmann, in Recent Developments in Structured Continua II, Longman Scientific (1990).

Truesdell, C., Lincei-Rend. Sc. Fis. Mat. E. Nat., Series 8, 22, 33 (1957).

Truesdell, C., Rational Thermodynamics, 2nd Ed., Springer-Verlag (1984).